

A Thesis Submitted for the Degree of PhD at the University of Warwick

Permanent WRAP URL:

<http://wrap.warwick.ac.uk/144873>

Copyright and reuse:

This thesis is made available online and is protected by original copyright.

Please scroll down to view the document itself.

Please refer to the repository record for this item for information to help you to cite it.

Our policy information is available from the repository home page.

For more information, please contact the WRAP Team at: wrap@warwick.ac.uk

Nanostructured Copper Window and Reflective Electrodes for Organic Photovoltaics

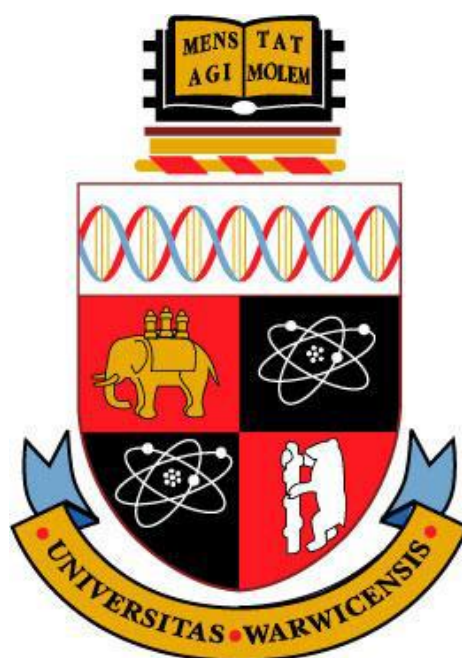
by

Harriotte Jessica Pereira

A thesis submitted in partial fulfilment of the requirements

for the degree of

Doctor of Philosophy



Supervised by Dr. Ross A. Hatton

Department of Chemistry

University of Warwick

July 2019

*Dedicated to my beloved father, mother and sister, for everything they have done for me
throughout my life.*

I could not have done it without them.

Table of Contents

| | |
|---|-------------|
| Acknowledgements | v |
| Declaration | vi |
| List of Publications | vii |
| Abstract | viii |
| List of Abbreviations and Acronyms | ix |
| 1. Introduction | 1 |
| 1.1 Background..... | 1 |
| 1.2 The Solar Resource..... | 1 |
| 1.3 Photovoltaic Technologies | 3 |
| 1.4 Organic Photovoltaics | 4 |
| 1.5 Semiconductors | 5 |
| 1.5.1 Organic Semiconductors | 6 |
| 1.6 Work Function | 8 |
| 1.7 The Metal – Semiconductor Interface..... | 10 |
| 1.8 Excitons | 11 |
| 1.9 Working Principle of an OPV | 12 |
| 1.10 Key Device Performance Parameters | 15 |
| 1.11 Materials | 18 |
| 1.11.1 Substrate | 18 |
| 1.11.2 Photo-active Material | 19 |
| 1.11.3 Charge transport Layers | 21 |
| 1.11.4 Reflective Electrode | 22 |
| 1.12 Device Architectures | 22 |
| 1.13 Transparent Electrodes..... | 23 |
| 1.14 Copper | 27 |
| 1.14.1 Optical properties of Copper | 27 |
| 1.15 Surface Plasmons..... | 31 |
| 1.16 Polymer Blends | 34 |
| 1.17 Project Overview | 39 |
| 1.18 References | 40 |
| 2. Experimental Techniques | 50 |
| 2.1 Substrate Cleaning | 50 |
| 2.2 UV Ozone Treatment..... | 50 |

| | |
|--|------------|
| 2.3 Monolayer Deposition | 52 |
| 2.4 Thermal Evaporation | 53 |
| 2.4.1 Evaporation of metals | 54 |
| 2.4.2 Evaporation of inorganic oxides and organic semiconductors | 55 |
| 2.5 Spin Coating | 56 |
| 2.6 Sheet Resistance Measurements | 57 |
| 2.7 Atomic Force Microscopy | 58 |
| 2.8 Conductive Atomic Force Microscopy | 60 |
| 2.9 Scanning Electron Microscopy | 61 |
| 2.10 Energy Dispersive X-ray Spectroscopy | 62 |
| 2.11 Integrating Sphere | 62 |
| 2.12 Kelvin Probe | 65 |
| 2.13 Tube Furnace | 66 |
| 2.14 X-ray Diffraction | 67 |
| 2.15 X-ray Photoelectron Spectroscopy | 68 |
| 2.16 OPV Fabrication | 70 |
| 2.17 OPV Device Testing | 71 |
| 2.18 Quantum Efficiency | 72 |
| 2.19 Optical Simulations | 74 |
| 2.19.1 Essential MacLeod (Version 9.7) | 74 |
| 2.19.2 COMSOL Multiphysics 5.2a | 74 |
| 2.20 References | 75 |
| 3. Fabrication of Copper window electrodes with $\sim 10^8$ apertures per cm^2 | 77 |
| 3.1 Background..... | 77 |
| 3.2 Experimental Methods..... | 80 |
| 3.3 Results and Discussion | 82 |
| 3.4 Conclusion | 100 |
| 3.5 References | 102 |
| 4. High Figure-of-merit Transparent Copper Window Electrodes for Organic Photovoltaics..... | 109 |
| 4.1 Background..... | 109 |
| 4.2 Experimental Methods..... | 110 |
| 4.3 Results and Discussion | 112 |
| 4.4 Conclusion | 121 |
| 4.5 References | 123 |

| | |
|--|------------|
| 5. Copper Substrate Electrode for Efficient Top-illuminated Organic | |
| Photovoltaics | 126 |
| 5.1 Background..... | 126 |
| 5.2 Experimental Methods..... | 128 |
| 5.3 Results and Discussion | 129 |
| 5.4 Conclusion | 138 |
| 5.5 References | 139 |
| 6. Copper Light-catching electrodes | 143 |
| 6.1 Background..... | 143 |
| 6.2 Experimental Methods..... | 147 |
| 6.3 Results and Discussion | 148 |
| 6.4 Conclusion | 156 |
| 6.5 References | 157 |
| 7. Optically Thin Copper Films as Top Electrodes for Top-illuminated Organic | |
| Photovoltaics | 160 |
| 7.1 Background..... | 160 |
| 7.2 Experimental Methods..... | 161 |
| 7.3 Results and Discussion | 162 |
| 7.4 Conclusion | 170 |
| 7.5 References | 171 |
| 8. Future Work | 173 |
| 8.1 Fabrication of a Plasmon-active Transparent Copper Electrode Using Polymer Blend Lithography..... | 173 |
| 8.2 Fabrication of a Plasmon-active Reflective Copper Electrode Using Polymer Blend Lithography | 175 |
| 8.3 References..... | 178 |

Acknowledgements

I would like to extend sincere gratitude and thanks to my PhD supervisor Dr. Ross A. Hatton for the continuous support, guidance, encouragement and advice given to me throughout the entire period of study. I feel privileged to have conducted this research under his proficient supervision. I am also thankful to the University of Warwick for the award of a Chancellor's International Scholarship which has enabled me to pursue postgraduate studies in the United Kingdom.

Thanks is also extended to all members of the Hatton group, both past and present especially Dr. Martin Tyler, Dr. Dinesha Dabera, Dr. Kenneth Marshall, Dr. Silvia Varagnolo, Dr. Jaemin Lee, Philip Bellchambers, Anjana Wijesekara, Joseph Reed and Max Martin for the help, fun and excellent companionship which made this journey very pleasant and entertaining.

Gratitude is also extended to late Prof. J.N.O Fernando, Mevan Peiris, Dr. Dilushan Jayasundara, Dr. Nicola Gurusinghe, friends and family for their advice, motivation and encouragement especially in the early stages of this study.

Last but not least, heartfelt gratitude is warmly extended to my beloved father, mother and sister, for their endless love, care, motivation, encouragement and unwavering confidence in me. I am truly indebted for all the support they have provided from miles away, for I know I could not have done it without them.

Declaration

This thesis is submitted to the University of Warwick in support of my application for the degree of Doctor of Philosophy. The work presented in this thesis has been conducted at the Department of Chemistry at University of Warwick with the exception of X-ray photoelectron spectroscopy, scanning electron microscopy, energy dispersive X-ray spectroscopy, X-ray diffraction measurements and optical measurements using the integrating sphere which were conducted at the Department of Physics. Data collection for X-ray diffraction (Figure 3.9 and 6.10) and scanning electron microscopy with a built-in heating stage (Figure 6.4) was carried out with the assistance of Dr. Dinesha Dabera and Steve York respectively. Data collection for conductive atomic force microscopy (Figure 3.10) and X-ray photoelectron spectroscopy (Figure 3.11) was carried out with the assistance of Dr. Jaemin Lee. Data collection for all other experiments were performed by myself. Design of experiments, execution and the analysis of resulting data were performed by me under the guidance of Dr. Ross. A. Hatton. Parts of the work presented in this thesis, particularly sections in chapter 3, 4, 5, 6 and 7 have been published in scientific journals and presented at national and international scientific conferences. All schematics and illustrations have been created by myself using Microsoft PowerPoint and 3dsMax drawing tools. I confirm that none of the work included in this thesis has previously been submitted for a higher degree.

List of Publications

- H. J. Pereira, O. S. Hutter, G. D. M. R. Dabera, L. A. Rochford and R. A. Hatton, Copper light-catching electrodes for organic photovoltaics, *Sustain. Energy Fuels*, **2017**, 1, 859–865.
- H. J. Pereira, J. Reed, J. Lee, S. Varagnolo G. D. M. R. Dabera and R. A. Hatton, Fabrication of copper window electrodes with $\approx 10^8$ apertures cm^{-2} for organic photovoltaics, *Adv. Funct. Mater.* **2018**, 28 (36), 1802893.
- H. J. Pereira and R. A. Hatton, Copper substrate electrode for efficient top-Illuminated organic photovoltaics, *ACS Appl. Mater. Interfaces*, **2019**, 11 (1), 43-48
- H. J. Pereira and R. A. Hatton, High Figure-of-merit transparent copper window electrodes for organic photovoltaics, *Front. Mater.*, submitted.

Abstract

The work reported in this thesis is focused on developing Cu electrodes for organic photovoltaics (OPVs). At present indium tin oxide (ITO) coated glass is the dominant transparent electrode used in OPVs owing to its high optical transparency and electrical conductivity. However, there are some significant drawbacks in ITO, most notably the use of indium which is a costly rare earth metal and poor compatibility with flexible substrates. Consequently, more sustainable alternative electrode materials are needed for application in OPVs and thin metal films particularly silver has attracted attention for this purpose because of the high electrical conductivity and low optical losses. However, silver is a costly metal, thus more cheap alternatives are essential in order to reap the full cost benefit of energy generation from OPVs.

Cu is an abundant metal with comparable electrical properties to that of silver but has received very little attention as an alternative electrode material due to its susceptibility to oxidation in air. However, in the recent past, a number of passivation techniques have been developed that enable retardation of Cu oxidation without electrical isolation, imparting increased stability under ambient conditions.

This thesis highlights Cu as a viable alternative to conventional ITO and silver metal electrodes, describing in detail the fabrication and characterization of Cu electrodes and their application in conventional, inverted and top-illuminated OPV device architectures. A comprehensive investigation of the application of Cu as a transparent window electrode, reflective substrate electrode and a plasmon-active light catching electrode is discussed.

As research pertaining to the use of Cu electrodes in OPVs is extremely limited, it is anticipated that the concepts and results discussed in this thesis will be useful in the inevitable transition to low cost-alternatives enabling the exploitation of the full potential of OPVs in energy harvesting.

List of Abbreviations and Acronyms

| | |
|------------|--------------------------------------|
| AFM | Atomic force microscopy |
| AM | Air mass coefficient |
| AO | Atomic orbitals |
| APTMS | 3-aminopropyltrimethoxysilane |
| AZO | Aluminium doped zinc oxide |
| A_s | Electron affinity |
| BCP | Bathocuproine |
| BHJ | Bulk heterojunction |
| C - AFM | Conductive atomic force microscopy |
| CB | Conduction band |
| CIGS | Copper indium gallium diselenide |
| ClAlPc | Chloro aluminium phthalocyanine |
| CPD | Contact potential difference |
| CTL | Charge transport layer |
| DMD | Dielectric/metal/dielectric |
| DOS | Density of states |
| e | Charge on an electron |
| EDXS | Energy dispersive X-ray spectroscopy |
| E_f | Fermi level |
| E_g | Band gap |
| EQE | External quantum efficiency |
| ETL | Electron transport layer |
| ϵ | Complex dielectric constant |

| | |
|--------------|---|
| ϵ' | Real part of the complex dielectric constant |
| ϵ'' | Imaginary part of the complex dielectric function |
| f | Composition |
| f_A | Overall fraction of component A |
| $f(E)$ | Probability of occupancy |
| FF | Fill factor |
| FoM | Figure-of-merit |
| FTO | Fluorine doped tin oxide |
| HOMO | Highest occupied molecular orbital |
| HOPG | Highly oriented pyrolytic graphite |
| HTL | Hole transport layer |
| I_p | Ionisation potential |
| IPCE | Incident photon to converted electron ratio |
| IQE | Internal quantum efficiency |
| ITO | Indium tin oxide |
| J | Total current density |
| J_D | Current density across the diode |
| J_0 | Reverse bias saturation current density |
| J_{MPP} | Current density at maximum power point |
| J_{ph} | Photo-generated current density |
| J_{sc} | Short circuit current density |
| J_{SH} | Current density across the shunt resistor |
| k_B | Boltzmann constant |
| LSPR | Localized surface plasmon resonance |
| LUMO | Lowest unoccupied molecular orbital |

| | |
|---------------------|---|
| <i>m</i> -ITIC | 3,9-bis(2-methylene-((3-(1,1-dicyanomethylene)-6/7-methyl)-indanone))-5,5,11,11-tetrakis(4-hexylphenyl)-dithieno[2,3-d:2',3'-d']-s-indaceno[1,2-b:5,6-b']dithiophene |
| <i>m</i> * | effective mass of an electron |
| MO | Molecular orbitals |
| MPP | Maximum power point |
| MPTMS | 3-mercaptopropyltrimethoxysilane |
| μ | Bulk chemical potential |
| N | Number of segments per polymer molecule |
| OLEDs | Organic light emitting diodes |
| OPV | Organic photovoltaics |
| PC ₇₀ BM | [6,6]-Phenyl-C71-butyric acid methyl ester |
| PCE | Power conversion efficiency |
| PCE10 | Poly[4,8-bis(5-(2-ethylhexyl)thiophen-2-yl)benzo[1,2-b;4,5-b']dithiophene-2,6-diyl-alt-(4-(2-ethylhexyl)-3-fluorothieno[3,4-b]thiophene-)-2-carboxylate-2-6-diyl] |
| PCE12 | Poly[(2,6-(4,8-bis(5-(2-ethylhexyl)thiophen-2-yl)-benzo[1,2-b:4,5-b']dithiophene))-alt-(5,5-(1',3'-di-2-thienyl-5',7'-bis(2-ethylhexyl)benzo[1',2'-c:4',5'-c']dithiophene-4,8-dione)] |
| PEDOT: PSS | Poly(3,4-ethylenedioxythiophene) polystyrene sulfonate |
| PEI | Polyethylenimine |
| PEIE | Ethoxylated polyethylenimine |
| PEN | Polyethylene naphthalate |
| PET | Polyethylene terephthalate |
| PMMA | Poly(methyl methacrylate) |
| PS | Polystyrene |
| ϕ | Work Function |

| | |
|------------|---|
| ϕ_B | Schottky barrier potential |
| ϕ_M | Work function of metal |
| ϕ_S | Work function of semiconductor |
| QCM | Quartz crystal microbalance |
| R_s | Series resistance |
| R_{sh} | Sheet resistance |
| R_{SH} | Shunt resistance |
| ρ | Electron density |
| SEM | Scanning electron microscopy |
| SPP | Surface plasmon polariton |
| SPR | Surface plasmon resonance |
| T | Temperature |
| T_{avg} | Average transmission |
| TCO | Transparent conductive oxides |
| VB | Valence band |
| V_{bi} | Built-in potential |
| V_L | Vacuum level |
| V_{MPP} | Voltage at maximum power point |
| V_{oc} | Open-circuit voltage |
| XPS | X-ray photoelectron spectroscopy |
| XRD | X-ray diffraction |
| χ | Surface potential |
| χ_s | Flory-Huggins segment-segment interaction parameter |
| ω | Frequency of the applied field |
| ω_p | Plasmon frequency |

| | |
|--------------|---------------------------------------|
| ΔG_m | Change in Gibbs free energy of mixing |
| ΔH_m | Change in enthalpy of mixing |
| ΔS_m | Change in entropy of mixing |

Chapter 1

Introduction

1.1 Background

The search for sustainable, reliable and affordable energy sources is a growing global concern especially with the escalating global population predicted to increase from 7.7 billion as of March 2019 to 8.5 billion in 2030. Access to energy is therefore mandatory in order to meet the needs and wants of this growing population. In the recent past there has been continuous research focused on harnessing energy from renewable sources motivated by the need to reduce carbon dioxide emissions, which are primarily produced by burning coal, natural gas and oil. Carbon dioxide, which is currently 410 ppm in the atmosphere,^{1,2} is a greenhouse gas and the main contributor to global warming. The rise in atmospheric temperature increases the frequency of extreme weather conditions, increases ice mass loss from polar regions which results in rising in sea levels affecting coastal areas, causes loss of biodiversity and ecological damage.^{1,3,4} Additionally, fossil fuels are a limited resource, therefore several alternative renewable sources such as wind, geothermal, solar, ocean and hydro power have been developed over the years to support the ever increasing energy demand. Considering the current international agreements on climate change, air quality and access to modern energy the International Energy Agency (IEA) forecasts a growth of the renewable energy capacity by 43 % or 920 GW by 2022, of which solar energy will be the highest.⁵ Photovoltaics (PV) are attractive as an alternative means of electricity generation in many parts of the world because of their low cost, sustainability and short energy payback times.⁶ The performance of PV devices depends on the availability of sunlight which they convert directly into electricity. The sun deposits a large amount of energy onto the earth's surface in the form of solar radiation which, if harnessed, will be adequate to fulfil the energy demand of all humanity. Nevertheless, all PV technologies depend on the availability of sunlight, therefore, energy generation using this technology must be used in conjunction with other means of renewable energy generation and energy storage.

The Solar Resource

The sun is a star located at the centre of the solar system and is the primary source of energy for all life on earth. Sunlight consists of the infrared (IR), visible and ultraviolet (UV) parts of the electromagnetic (EM) spectrum. The solar spectrum can be modelled

as a black body at a temperature of ~ 5800 K.⁷ The amount of EM radiation incident on the earth's outer atmosphere per unit area on a plane perpendicular to the incoming rays is referred to as the solar constant and is ~ 1366 W m². However, the actual radiation that arrives at the earth's surface is lower than this value because it is attenuated when passing through the atmosphere due to interaction between water vapour in the atmosphere, dust particles, carbon dioxide, oxygen and other gases which absorb and scatter the incoming radiation. Therefore, a parameter known as the air mass coefficient (AM) is defined to quantify the solar spectrum after the radiation has passed through the atmosphere. The AM is a measure of the optical path length through the atmosphere and is defined as,

$$AM = \frac{L}{L_0} = \frac{1}{\cos \theta}$$

Equation 1.1

where L is the path length through the atmosphere, L_0 is the path length normal to the earth's surface (zenith path length) and θ is the zenith angle in degrees.⁸

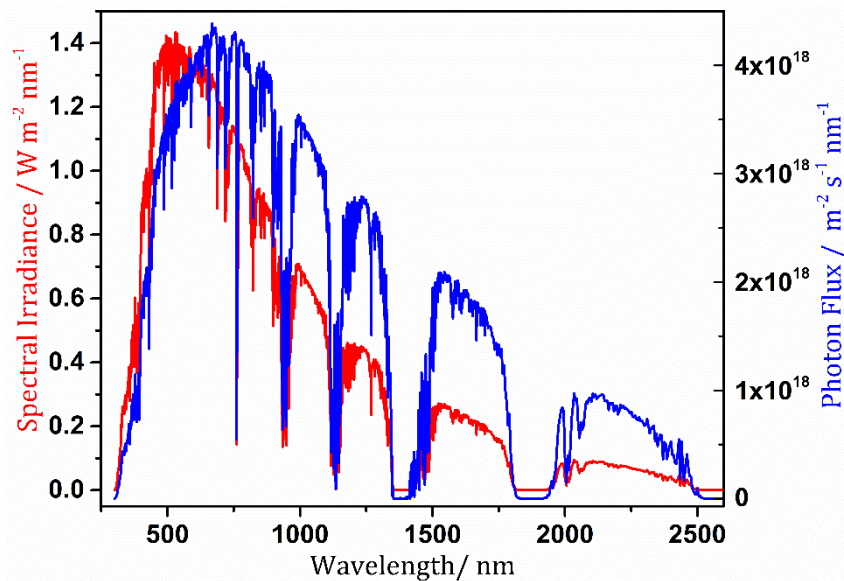


Figure 1.1: American Society for Testing Materials (G173-03) AM 1.5 reference spectra of the spectral irradiance and Photon flux adapted from ref. [10].

When the sun is located directly above the earth's surface and the radiation passes directly through the atmosphere, it is referred to as air mass 1 Direct (AM 1D). The notation AM 1G is given when both direct and diffuse radiation is considered where G means Global. The standard spectrum at the earth's surface is known as AM 1.5G where θ is 48° and solar radiation is incident at 48° angle from the normal to the earth's surface. The AM

1.5G spectrum (Figure 1.1) is the standard spectrum used to compute PV device performance and has an intensity of 1kW m^{-2} .^{9,10}

1.3 Photovoltaic Technologies

Many advances have been made in the field of PVs, since the invention of silicon (Si) PVs in 1954, when scientists at Bell laboratory demonstrated the first practical Si PV device.¹¹ Si PVs (first generation PV), which include monocrystalline, polycrystalline and amorphous Si PVs, are the dominant PV technology with a record power conversion efficiency (PCE) of $\sim 26\%$.^{12,13} Si PVs dominate the PV market because they are relatively efficient, very stable and because they are the oldest PV technology there is a widespread knowledge and know-how within the scientific community. However, Si PVs have the following drawbacks^{11,14,15} which has motivated the development of alternative PV technologies:

- Their rigid flat plate design limits utility in certain important application areas;
- Fabrication of Si wafers require high temperatures and therefore it is an energy intensive process;
- Relatively long energy payback times (i.e. the operating life of a PV device needed to produce the amount of energy invested during manufacturing, installation and maintenance): 1-1.5 years;
- Si is an indirect band gap material at long wavelengths (λ) so there is poor light absorption at long wavelengths, which requires the use of thick layers of the order of $100 - 300\ \mu\text{m}$ to attain maximum efficiency.

Second generation PVs comprise thin film PVs.¹¹ Thin film based PV offer reduced material cost by decreasing the thickness of materials used and by reducing the energy consumption during the manufacturing process. CdTe PV and Copper Indium Gallium Diselenide (CIGS) are the dominant types of thin film PV and have reported a PCE of 21.7% and 21% respectively.¹³ Third generation PVs aim to combine the advantages of the former types of PV and comprise all emerging PV technologies including hybrid inorganic – organic PVs such as perovskite PV which have grown rapidly in the recent years. Third generation PV also include polymer and organic PVs (OPVs) as well as multi-junction PVs which are capable of breaking the theoretical upper limit for the efficiency of a single junction PV given by the Shockley-Queisser efficiency limit, by using several complementary light harvesting layers to absorb light across different regions of the spectrum.

1.4 Organic Photovoltaics

OPV devices convert sunlight directly into electricity using thin films of organic semiconductors (conjugated organic molecules) as the photo-active material and are considered to be one of the most promising emerging thin film PV technologies. OPVs have several advantages over conventional Si PVs:^{11,16,17}

- Organic semiconductors have a large optical absorption coefficient; hence, a small thickness of material is sufficient to absorb all of the incident light. Thus, typical high performance OPV devices are relatively thin (≤ 200 nm) requiring less material;
- Low fabrication cost which stems from the low processing temperature of organic semiconductors (< 150 °C);
- Solution processing and printing techniques enable high speed roll-to-roll production which is low cost;
- Tunable electrical properties; molecular engineering permits the alteration of the band gap and frontier orbital energies providing higher material flexibility
- Short energy payback times: ~ 1 week;
- Compatibility with flexible light weight substrates, renders them useful in applications such as transportation and building integration where rigid flat plate PVs are not a possibility.

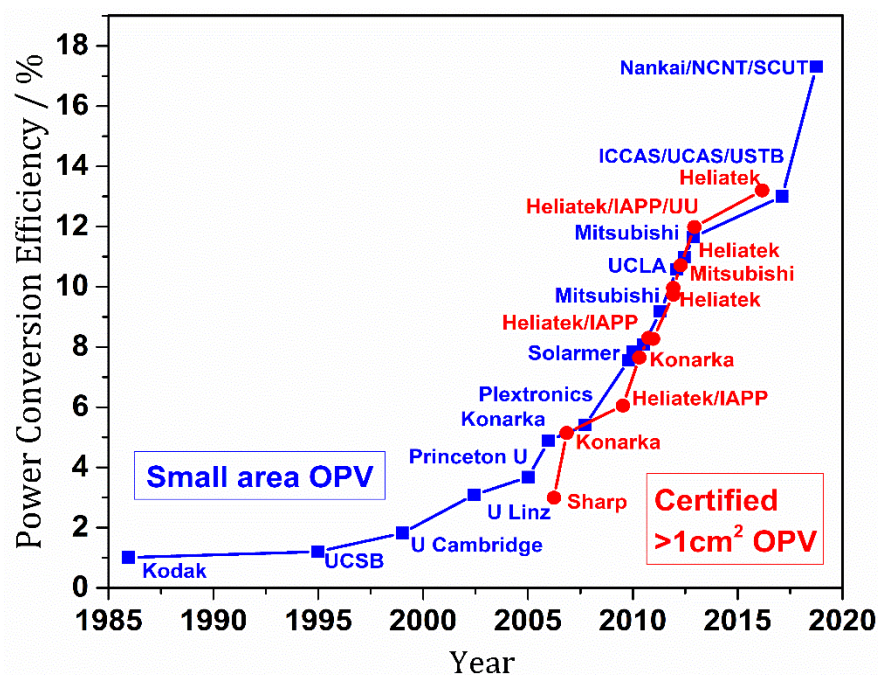


Figure 1.2: Progress of OPV device performance from 1985 – 2019 adapted from ref. [18].

The major drawback in OPVs is the relatively low PCEs compared to that of Si PV and the lower long term stability. However, it is important to note that over the years OPVs have progressed rapidly¹⁸ and together with scientific and technological improvements have recently achieved a PCE 16%¹⁹ for a single junction device and 17 %²⁰ for a multi-junction OPV. Therefore, OPVs have strong potential as a low cost environmentally friendly and sustainable means of energy generation provided the advantages are fully exploited and the shortcomings are addressed in the years to come.

1.5 Semiconductors

Semiconductors are materials that have an electrical conductivity intermediate to that of a metal and an insulator. Pure semiconductors possess few free charge carriers but can be made conductive under specific conditions. Addition of impurity atoms into the lattice in small proportions (10^{13} - 10^{18} atoms cm^{-3}) to the base material is a versatile way to engineer the electrical conductivity by increasing the concentration of free charges. This deliberate addition of impurities is referred to as doping. Commonly known examples of crystalline semiconductors include Si, germanium (Ge) and Gallium arsenide (GaAs).

The electrical conductivity in materials can be understood by considering the electronic band structure of the material. Atoms consist of atomic orbitals (AO) with discrete energies occupied by pairs of electrons with opposite spin. When the inter-atomic distance of two such AOs with unpaired electrons is sufficiently small they interact forming a molecular orbital (MO) having a bonding orbital with an energy lower than the AOs and an anti-bonding orbital with a higher energy. When a very large number of identical AOs overlap the high density of bonding and anti-bonding orbitals give rise to continua of energy levels called bands. The highest occupied bonding MOs form the valence band (VB) whilst the lowest unoccupied anti-bonding MOs give rise to the conduction band (CB). The gap between the VB and CB is known as the band gap (E_g) and denotes the energy range in which there are no electronic states. Electrons can be promoted from the VB to the CB only by absorbing energy $\geq E_g$. The vacancy in the VB left behind by the photo-excitation of an electron is called a hole. These positively charged vacancies in an otherwise filled band can move in response to an applied electric field and so contribute to current flow. When a material becomes conductive due to the generation of free charge carriers (electrons and holes) by absorption of light, it is known as photoconductivity. Absorption of energy $> E_g$ will result in the excited electron rapidly relaxing to the CB edge by a process known as thermalisation. Consequently, band

diagrams only include the VB and CB edges indicated by the blue lines in Figure 1.3(b) and (c).

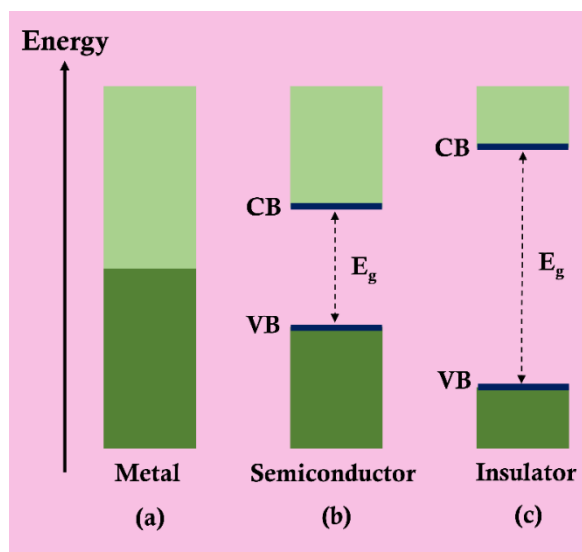


Figure 1.3: Electronic band diagrams of a typical (a) metal; (b) semiconductor and (c) insulator. The dark regions indicate filled states and the light regions depict unfilled states.

As depicted in Figure 1.3(a) metals have a half-filled band and materials with a $E_g \leq 3$ eV are referred to as semiconductors and those with a larger E_g as insulators. When the E_g is large, in addition to it being difficult to excite electrons from the VB to the CB it is also difficult to inject charge carriers into the VB and CB edges, due to the small electron affinity and large ionisation potential.

1.5.1 Organic Semiconductors

Organic semiconductors can range from simple small molecules to complex polymers and are primarily composed of carbon (C) and hydrogen (H) but can also include other heteroatoms such as oxygen (O), nitrogen (N) and sulphur (S).

Organic semiconductors consist of hybrid orbitals resulting from the hybridisation of 2s and one or more 2p atomic orbitals. These hybrid orbitals give rise to highly directional strong sigma bonds which form the backbone of the molecule, whereas electrons remaining in unhybridized 2p orbitals lead to weak π bonding. The latter are delocalised and can move along the molecule in response to an electric field when the p orbital is partially filled.^{21,22}

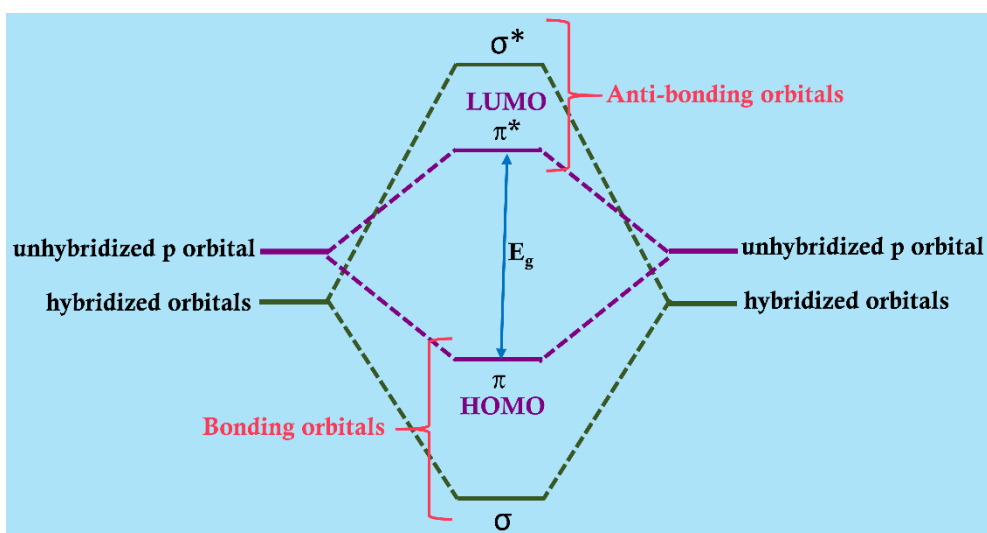


Figure 1.4: Molecular orbital diagram showing the positioning of bonding and antibonding orbitals responsible for sigma and π bonding.

In inorganic crystals, the charge carriers (electrons or holes) are delocalised over a few lattice sites in the 3-dimensional crystal lattice. In organic semiconductors (molecular solids) the situation is quite different, since the charges are highly localised on individual molecules or in the case of conjugated polymers, on segments of the polymer chain. The weak interaction between adjacent molecules in an organic semiconductor leads to very narrow bands and therefore the electronic structure is best described in terms of weakly interacting potential wells rather than a conventional band structure which only apply for few exceptional highly ordered molecular solids.

The highest occupied molecular orbital (HOMO) and the lowest unoccupied molecular orbital (LUMO) are equivalent to the VB and CB in a crystalline inorganic semiconductor (Figure 1.4). The energy gap between these two energy levels corresponds to the E_g similar to the inorganic semiconductor discussed in section 1.5. According to the potential well model, the electronic structure of the molecules comprising a molecular solid are highly preserved due to the weak interactions between adjacent molecules, so the valence electrons are in deep potential wells. Therefore, if the electrons are to move from one molecule to the next, the potential barrier between them must be overcome and they must hop from one potential well to the next. This is a thermally activated process that is also electric field assisted.^{21,23} Consequently, in this type of solid, charge transport is achieved by means of hopping between potential wells as depicted by the arrows in Figure 1.5.^{17,23}

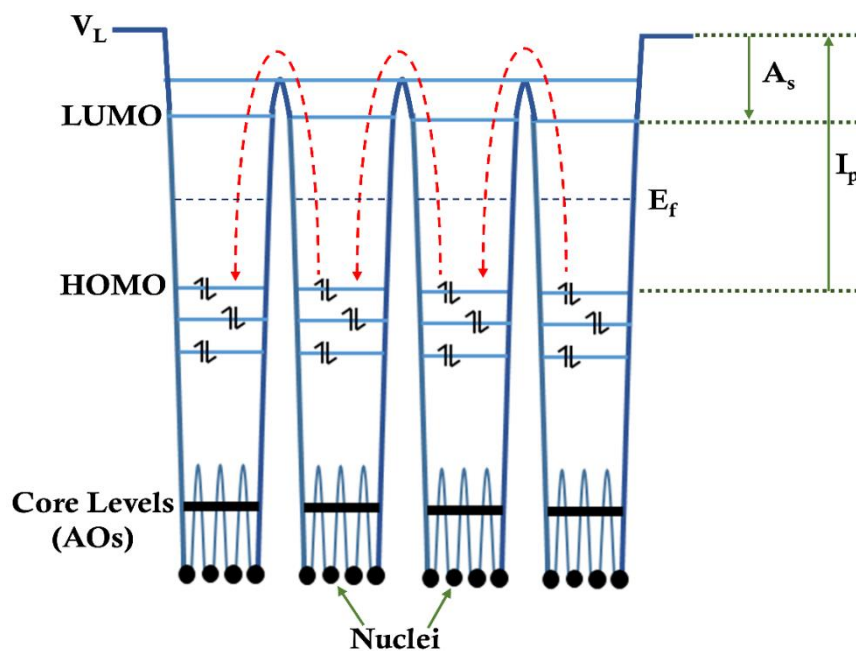


Figure 1.5: Potential well model for a molecular solid adapted from ref. [18].

The potential well model shown in Figure 1.5 includes other energy levels which are key to understanding the operation of an OPV: The vacuum level (V_L) refers to a region immediately outside the surface of the solid where the electron is at rest and the energy at V_L is considered to be zero; The Fermi level (E_f) is a precisely defined thermodynamic quantity that refers to the energy level at which the probability of electron occupancy is 0.5. The Fermi-Dirac distribution function, given by equation 1.2 below, is the probability that (at thermodynamic equilibrium) an electron will occupy a state having an energy, E .

$$f(E) = \frac{1}{e^{\frac{(E-E_f)}{k_B T}} + 1} \quad \text{Equation 1.2}$$

where $f(E)$ is the probability of occupancy of a state of energy E , T is the temperature and k_B is the Boltzmann constant. The energy needed to remove an electron from the HOMO to the V_L is known as the ionisation potential (I_p), and the energy dissipated when an electron moves from the V_L to the LUMO is the electron affinity (A_s).

1.6 Work Function

Work function (ϕ) is defined as the amount of energy needed to take an electron from the E_f to the V_L . The ϕ is made up of two components; the bulk chemical potential (μ) and the surface potential (χ).

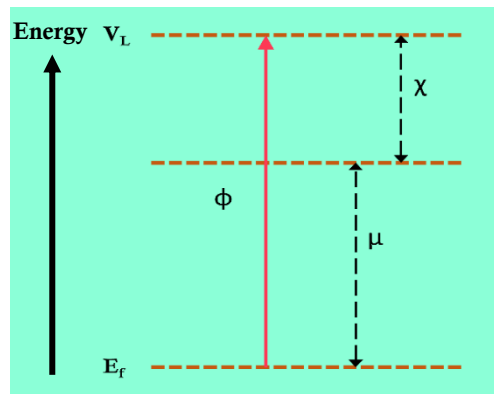


Figure 1.6: Energy level diagram indicating the contribution of the bulk chemical potential (μ) and surface potential (χ) to work function (Φ)

$$\Phi = \mu + \chi$$

Equation 1.3

μ is the amount of energy needed to overcome the interaction with the bulk lattice, which is affected by the position of E_f in the band gap, and therefore the degree of doping. χ is the contribution to the ϕ from the surface dipole. All solids have an electric dipolar layer on the surface, formed as a result of spilling of the electron density into the vacuum. χ is sensitive to the nature of the surface and interactions with adjacent materials. For instance, when electron rich materials are adsorbed onto the surface, the electron density spilling out of the solid will be pushed back due to electrostatic repulsion, reducing the magnitude of χ (Figure 1.7). This is known as the push-back effect.

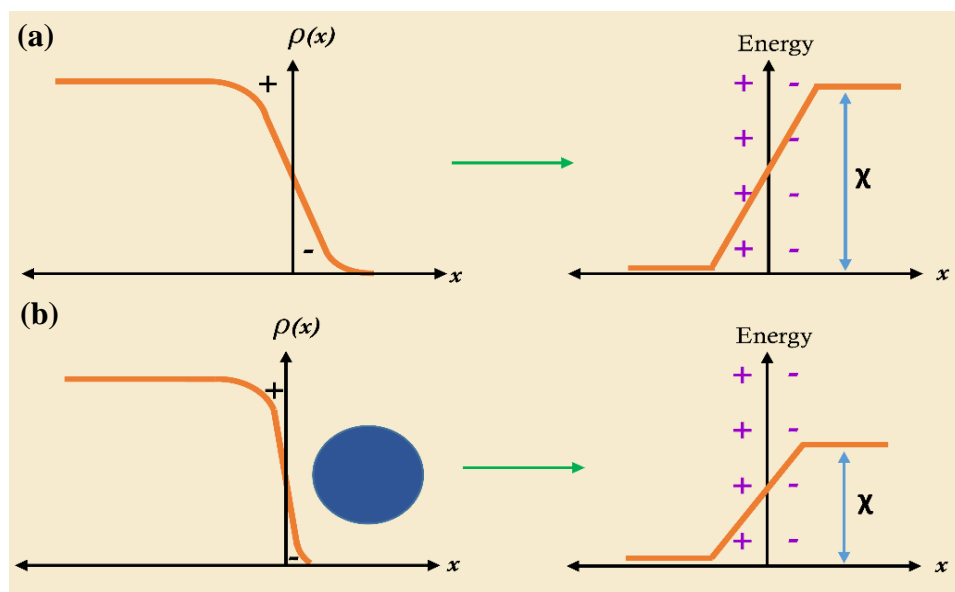


Figure 1.7: Schematic representation of the push-back effect showing the change in electron density distribution as a function of metal surface (a) for a contaminant free metal and (b) when an electron rich material is adsorbed on the surface.

1.7 The Metal – Semiconductor Interface

When a metal is in contact with a semiconductor two types of junctions can be formed depending on the ϕ of the metal and semiconductor;

1. A Schottky contact
2. An Ohmic contact

If the ϕ of the metal (ϕ_M) is greater than that of the semiconductor (ϕ_S), a Schottky barrier is formed at the contacting interface (Figure 1.8).

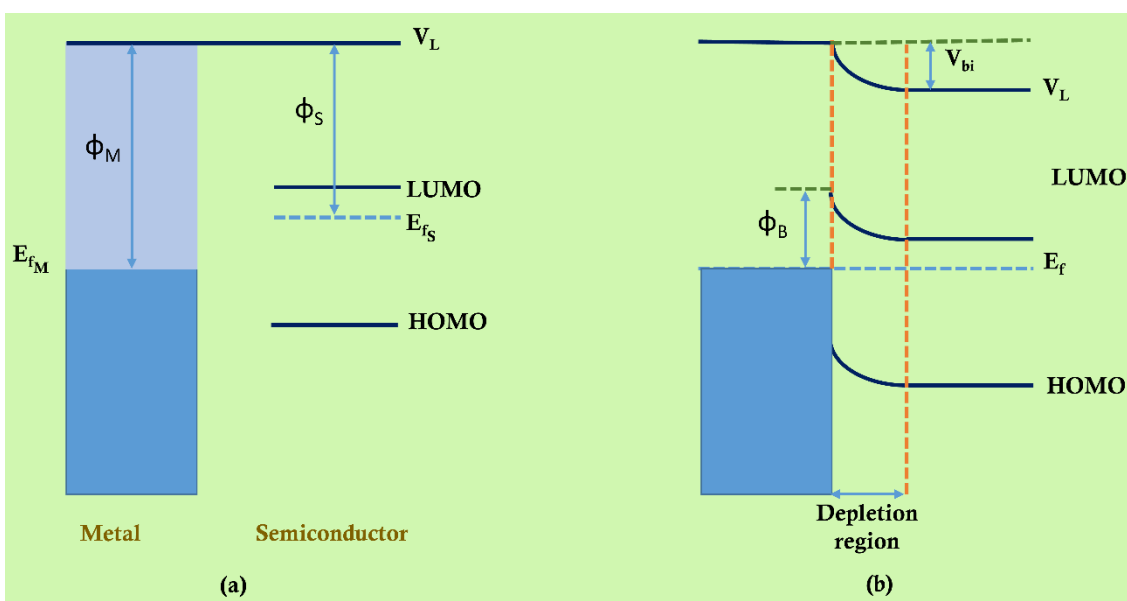


Figure 1.8: Energy level diagram of a metal and semiconductor when (a) separate and (b) when brought into contact with each other where the $\phi_M > \phi_S$

When the metal has a higher ϕ_M compared to the semiconductor, it means that more energy is required to transfer an electron from the E_f to the V_L . When the two are brought into contact, electrons will flow from the semiconductor to the metal. As a result of this electron migration and the associated potential change, band bending occurs in the semiconductor causing the V_L to shift as shown in Figure 1.8(b), resulting in a Schottky barrier of height ϕ_B .^{17,24} The E_f alignment upon contact results in a shift in the V_L generating a built-in potential (V_{bi}) and a region of charge accumulation known as the depletion region.

Conversely when $\phi_M < \phi_S$ (for a heavily doped semiconductor) electrons move in the opposite direction; i.e. from the metal to the semiconductor, generating an Ohmic contact with no rectifying behaviour as shown in Figure 1.9.

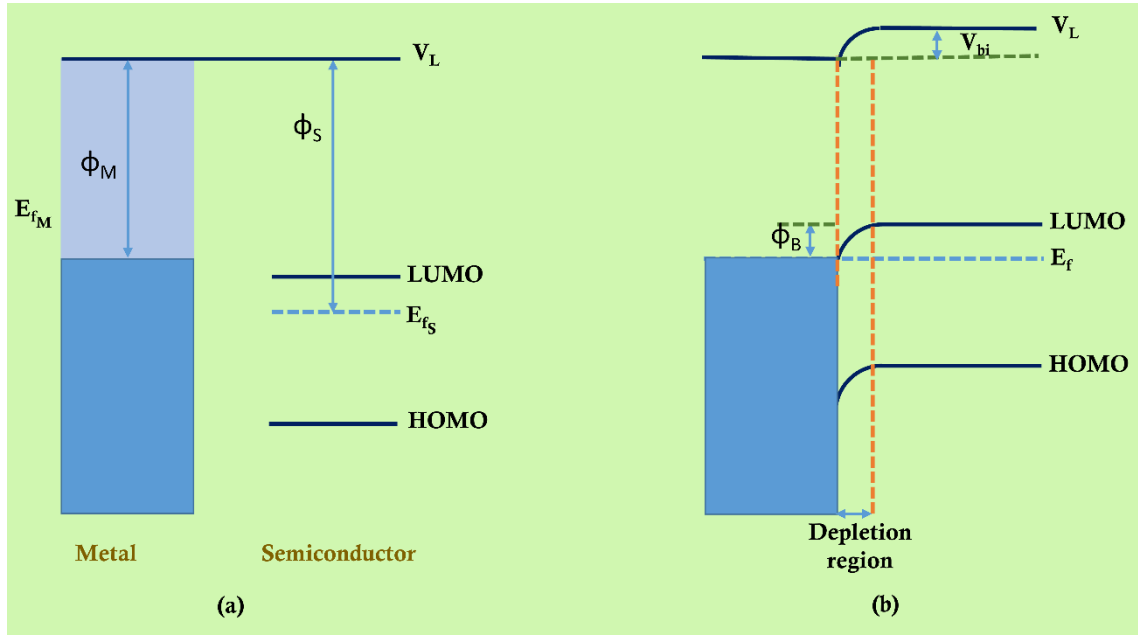


Figure 1.9: Energy level diagram of a metal and heavily doped semiconductor when (a) separate and (b) when brought into contact with each other where the $\Phi_M < \Phi_S$

1.8 Excitons

An exciton is an electrically neutral quasi-particle in which an electron and a hole are bound together by electrostatic Coulombic forces. An exciton is formed when a photon of energy greater or equal than the E_g is absorbed by the semiconductor, promoting an electron to the CB and leaving a hole in the VB. There are two types of excitons defined in terms of the strength of the electron and hole interaction;

1. Mott-Wannier excitons
2. Frenkel excitons

Coulombs law states that the magnitude of the force of electrostatic attraction or repulsion between two point charges (q_1 and q_2) is directly proportional to the product of the charges and inversely proportional to the square of the distance (r) between them.

$$F = \frac{q_1 q_2}{4\pi \epsilon_0 \epsilon_r r^2} \quad \text{Equation 1.4}$$

where ϵ_0 is the vacuum permittivity (or dielectric constant) and ϵ_r is the relative permittivity (or relative dielectric constant).

ϵ_r is a dimensionless quantity that is a measure of the ability of a material to screen the force of interaction between charges by undergoing polarisation.

In the case of highly crystalline inorganic semiconductors, ϵ_r is typically in the range of 10 – 15. Therefore, the force of interaction between electrons and holes is well screened, and so the binding energy between the electron in the CB and hole in the VB, is small; ≤ 25 meV (less than $k_B T$, which is equivalent to the thermal energy of an electron at room temperature). Consequently, at room temperature, photon absorption results in excited electrons and holes that can be very easily separated. This type of weak interaction between an excited electron and hole is known as a Mott-Wannier exciton.^{17,25,26} Mott-Wannier excitons can extend over several lattice sites and so are highly delocalized excitons.

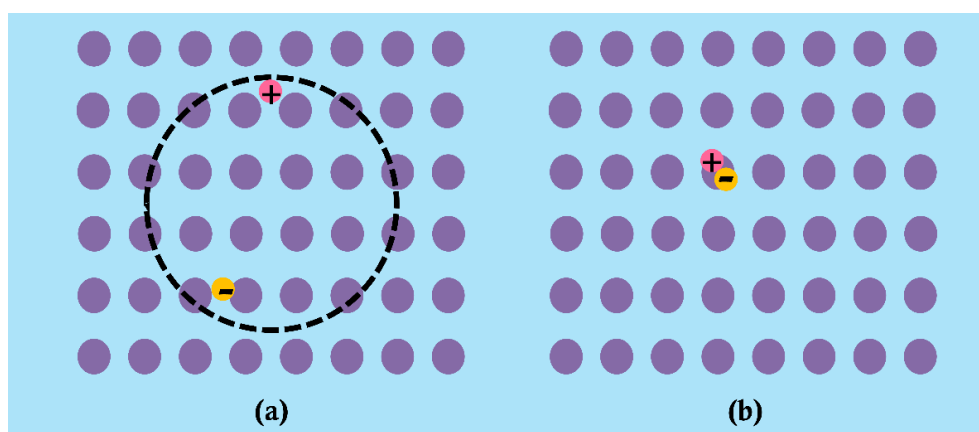


Figure 1.10: Schematic representation of **(a)** Mott-Wannier and **(b)** Frenkel excitons

In the case of organic semiconductors the ϵ_r is very small, typically in the range of 2 - 4 which results in high binding energies between the electron and hole, usually of the order of 0.1-1 eV. Consequently, at room temperature, following excitation the electron in the LUMO and hole in the HOMO of an organic semiconductor are tightly bound giving rise to a Frenkel exciton. As a consequence of small ϵ_r and the localisation of the electron and hole in the potential well of the molecule, Frenkel excitons are tightly bound and relatively small compared to Mott-Wannier excitons. Additionally, because Frenkel excitons have large binding energies, there is a substantial barrier that must be overcome in order to separate them into respective free electrons and holes.^{11,17,18,25,27}

1.9 Working Principle of an OPV

The simplest organic PV device architecture consists of a transparent electrode such as indium tin oxide (ITO) supported on a glass substrate, followed by two layers of organic semiconductor materials; the first having electron donor character and the second with electron acceptor character, followed by a top reflective electrode, typically aluminium (Al) or silver (Ag) (Figure 1.11). Electron donors are materials that generate and transfer

an electron to the acceptor upon illumination. Conversely electron acceptors are materials that are capable of accepting electrons and transferring holes to the donor material.^{28,29} Therefore, the donor type organic semiconductor has a lower ionization potential compared to that of the acceptor, while the electron acceptor has a higher electron affinity compared to that of the donor.

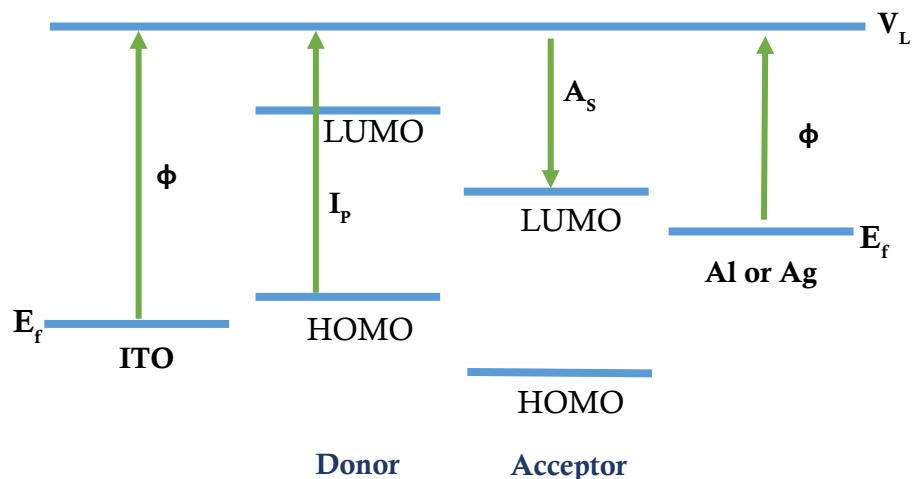


Figure 1.11: A simplified schematic representation of an energy level diagram of a basic OPV device.

The heart of an OPV is therefore a heterojunction between organic molecules with offset frontier orbitals which are responsible for splitting of excitons formed either in the donor or acceptor. The electron donor and acceptor must therefore be carefully chosen so that the abrupt shift in potential energy is just enough to split the excitons. An excessively large energy offset will lead to a reduction in the device voltage as will be discussed later. Usually an energy offset of ~ 0.3 eV is sufficient for splitting of excitons at organic semiconductor junctions.¹⁸ Moreover, excitons in organic semiconductors have relatively low diffusion lengths and therefore careful engineering of the donor and acceptor thickness is essential to ensure exciton separation prior to its relaxation.

Figure 1.12 summarises the four main processes that occur in an OPV:

1. Photon absorption to form excitons;
2. Exciton diffusion and separation at the heterojunction;
3. Charge carrier transport to the electrodes;
4. Charge carrier extraction to the external circuit.

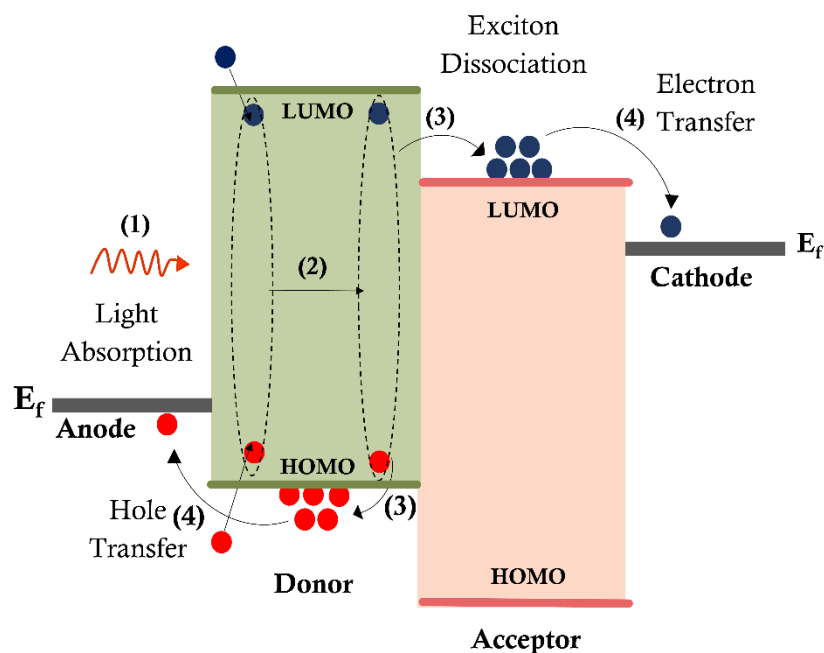


Figure 1.12: Schematic energy level diagram showing the four basic steps in the operation of an OPV device.

Absorption of a photon energy $\geq E_g$ results in the excitation of an electron from the HOMO to the LUMO of the donor/acceptor molecule, (Figure 1.12; step1)). This is followed by thermalisation to release the extra energy followed by formation of an exciton. As discussed in section 1.8, excitons are electrically neutral and therefore not influenced by the built-in electric field across the organic semiconductor layer that arises due to the difference in the ϕ of the electrodes on either end. As a result, excitons diffuse between molecules and may relax back to the ground state, radiatively by emitting light or non-radiatively by liberating the extra energy in the form heat. For efficient operation of an OPV device these excitons must arrive at the heterojunction before the relaxation takes place so that they can contribute to photocurrent generation. Upon diffusion to the heterojunction in the photo-active layer (Figure 1.12; step 2) excitons undergo dissociation to form a hole in the HOMO of the donor and an electron in the LUMO of acceptor (Figure 1.13; step 3). Immediately following separation, the two charge species will be weakly bound, a state that is sometimes referred to as a charge transfer exciton. However, as the interaction is quite weak, the gradient in chemical potential arising due to the charge carrier concentration gradient, together with the static electric field across the device, is sufficient to dissociate the charge carriers forming free electrons and holes. The separated charge carriers are then transported to the corresponding electrodes and extracted to the external circuit under the influence of the electric field (Figure 1.12; step

4). The overall efficiency of the OPV device is dependent on the efficiency of every step of this process.^{11,18,30,31}

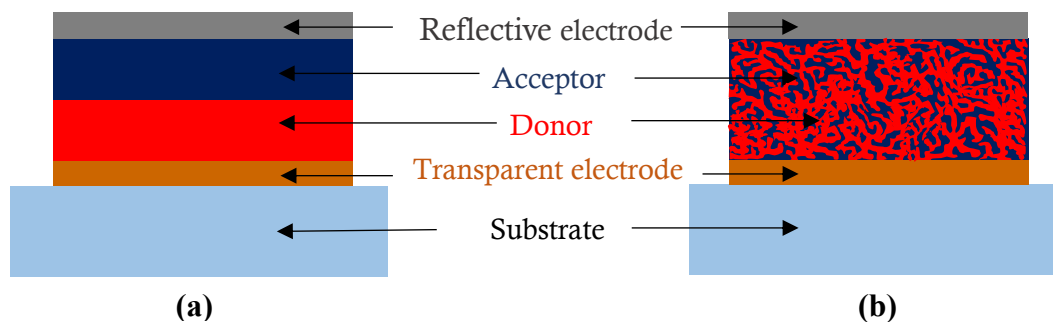


Figure 1.13: A schematic representation of the (a) bilayer and (b) BHJ architectures of the photoactive layer in an OPV with donor (red) and acceptor (blue) phases.

In the early stages of OPV technology donor and acceptor species were deposited as discrete bilayers; the donor adjacent to the hole extracting electrode and the acceptor adjacent to the electron accepting electrode (Figure 1.13 (a)). Frenkel excitons in organic semiconductors exhibit small diffusion lengths (≤ 40 nm) thus, there is a limitation to the maximum thickness of each layer. However, optimal light absorption is obtained only when the photo-active layer is sufficiently thick. Hence an alternative way of depositing the light harvesting layer was sought: Most efficient OPV devices to date are based on a bulk heterojunction (BHJ) architecture in which a complex interpenetrating network of electron donor and electron acceptor type organic semiconductors constitute the photo-active layer^{32,33} (Figure 1.13 (b)). These two components are phase separated on the 10-20 nm scale,^{18,34} which ensures that all excitons are formed within an exciton diffusion length of a dissociating heterojunction. This complex structure also increases the interfacial area available for exciton dissociation relative to the bilayer architecture. As PCE of OPVs is highly dependent on the morphology of this donor-acceptor interface, the size of the donor and acceptor domains must be carefully engineered in order to accommodate the afore-mentioned low exciton diffusion length or exciton bottleneck in organic semiconductors^{35,36} without compromising the absorption of light or electrical resistance for the transport of free carriers out of the device to the external circuit.

1.10 Key Device Performance Parameters

The parameters used to characterise the performance of OPV devices are:

1. Open-circuit voltage (V_{oc});
2. Short circuit current density (J_{sc});

3. Fill factor (FF);
4. Power conversion efficiency (PCE, η).

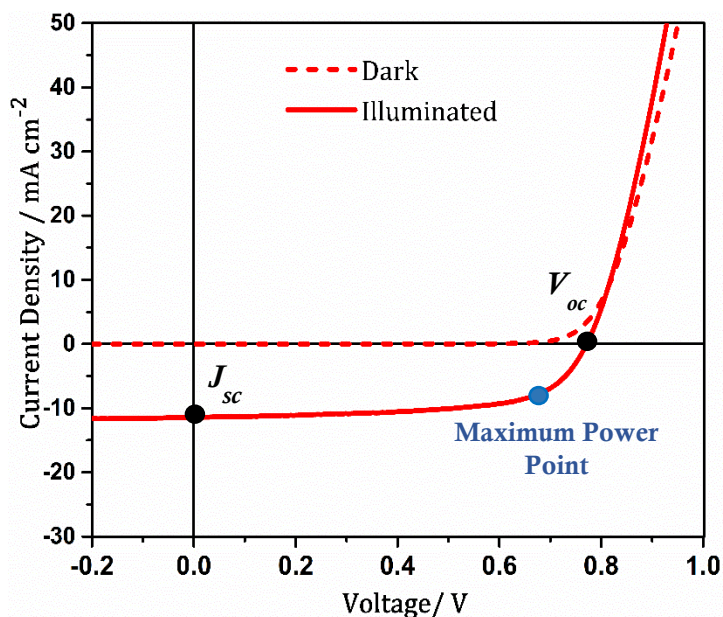


Figure 1.14: Key parameters that can be deduced from a typical JV curve.

J_{sc} is the photocurrent generated by the device under illumination at the short-circuit condition, i.e. when the voltage across the load is zero. It is dependent on the intensity of the incident light, the transparency of the electrode through which light enters the device (the window electrode), the absorption coefficient of the photo-active material (donor and acceptor) and the spectrum of the materials constituting the photo-active layer. The V_{oc} is the maximum voltage that the device can deliver to an external load and it is defined as the voltage under illumination when no current flows across the device. V_{oc} is proportional to the difference between energy levels of the HOMO of the donor and LUMO of the acceptor.^{18,37} Scharber *et al.* proposed an empirical relationship for evaluating V_{oc} by analysing a wide range of material combinations (Equation 1.5).^{37,38} The origin of the 0.3 V correction is postulated to arise due to E_f variations in the donor and acceptor domains as a function of temperature.^{37,39}

$$V_{oc} = \frac{1}{e} (E_{HOMO_{Donor}} - E_{LUMO_{Acceptor}} - 0.3) \quad \text{Equation 1.5}$$

In equation 1.5, $E_{HOMO_{Donor}}$ and $E_{LUMO_{Acceptor}}$ are the HOMO and LUMO energy levels of the donor and acceptor respectively and e is the charge on an electron.

FF is a measure of the ‘squareness’ of the current-voltage characteristic under illumination and is given by the ratio of the maximum power (product of current and voltage at maximum power point) to the product of J_{sc} and V_{oc} (Equation 1.6).

$$FF = \frac{V_{MPP} \times J_{MPP}}{V_{oc} \times J_{sc}} \quad \text{Equation 1.6}$$

where V_{MPP} and J_{MPP} are the voltage and current density at the maximum power point.

The magnitude of the FF is also an indication of the quality of the diode. The FF is determined by the series resistance (R_s) and shunt resistance (R_{SH}) across the device; ideally the R_s is zero and R_{SH} should be infinitely large. Therefore a high FF is achieved when the R_s is low and the device R_{SH} is high.

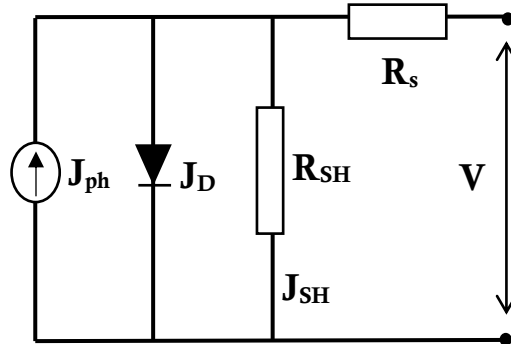


Figure 1.15: Equivalent circuit diagram for a PV device.

The R_s results from resistance to charge carrier transport through the bulk semiconductor, the contact resistance at the metal-semiconductor interface and resistance to current flow from the electrodes to the external circuit.^{14,40,41} The R_{SH} arises from current leakage across the device due to pin holes and/or recombination of charges. Both R_s and R_{SH} can be estimated from the JV curve; R_s is the gradient when the current is zero whilst R_{SH} is the gradient of the JV curve when the current is equal to J_{sc} . Therefore the fourth quadrant of the JV curve, in which the device is generating electricity is important in evaluating the key device parameters that are crucial in determining the PCE of a device.^{8,42}

The PCE is defined as the fraction of incident power converted to electricity by the device and is expressed as follows,

$$PCE = \frac{FF \times J_{sc} \times V_{oc}}{P_{In}} \times 100 \quad \text{Equation 1.7}$$

where P_{In} is the input power under standard 1 sun simulated solar illumination; (100 mW cm^{-2} at AM 1.5G)

The total current density (J) in the circuit (Figure 1.15) under illumination is;

$$J = J_{ph} - J_D - J_{SH} \quad \text{Equation 1.8}$$

where J_{ph} denotes the photo-generated current density, J_D the diode current density and J_{SH} the current density through R_{SH} .

Equation 1.8 in combination with the Shockley diode equation (Equation 1.9) can be used to derive the characteristic equation for a solar cell (Equation 1.10)

Shockley diode equation is given by,

$$J_D = J_0 \left(e^{\frac{V_D}{nV_T}} - 1 \right) \quad \text{Equation 1.9}$$

where J_0 is the reverse bias saturation current density, V_D the voltage across the diode, V_T is the thermal voltage expressed as $k_B T/q$; k_B is the Boltzmann constant, T is the temperature, q is the charge and n is the non-ideality factor.

The characteristic equation for a solar cell can therefore be expressed as,

$$J = J_{ph} - J_0 \left\{ e^{\frac{q(V+JR_S)}{nk_B T}} - 1 \right\} - \frac{V + JR_S}{R_{SH}} \quad \text{Equation 1.10}$$

When R_{SH} is infinite and $J = 0$ (i.e. at the V_{oc} condition) equation 1.10 can be reduced to obtain an expression for V_{oc} as given in equation 1.11;

$$V_{oc} = \frac{nk_B T}{q} \ln \left(\frac{J_{ph}}{J_0} + 1 \right) \quad \text{Equation 1.11}$$

1.11 Materials

1.11.1 Substrate

The substrate is the platform upon which the device is supported and therefore needs to be robust. In the case of a conventional or inverted device architecture, the substrate must be highly transparent so that it does not hinder entry of light into the device, especially in the region where most light harvesting layers absorb: in the wavelength range of $\lambda = 300\text{-}900$ nm. Additionally, the substrate should be relatively smooth so that subsequent layers adhere well forming uniform compact films. Glass is by far the most widely used type of

substrate in OPV research because it is highly transparent, provides a rigid support and exhibits excellent barrier properties towards ingress of oxygen and moisture. However, with the current transition from rigid to flexible OPVs, more plastic substrates are being used because they are compatible with roll-to-roll processing and the resulting flexibility of the device caters for a much broader range of applications.^{11,43–48} Polyethylene terephthalate (PET) and polyethylene naphthalate (PEN) are the commonly used flexible substrates. However, for certain processing steps, the use of plastic substrates can be problematic as they cannot withstand high temperatures (glass transition temperature (T_g) of PET and PEN are $\sim 81\text{ }^\circ\text{C}$ ⁴⁹ and $\sim 120\text{ }^\circ\text{C}$ ⁵⁰ respectively) and are not always compatible with solvents used in OPVs.

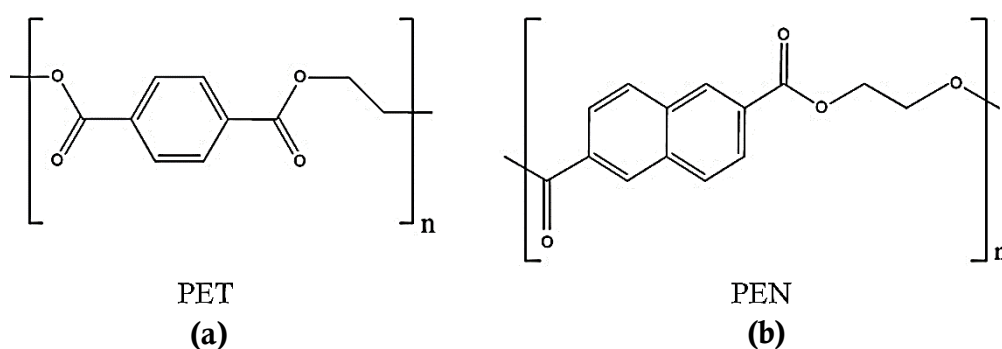


Figure 1.16: Chemical structures of flexible substrates **(a)** PET and **(b)** PEN

In a typical OPV device with a conventional architecture, the transparent window electrode is deposited onto the supporting substrate. As window electrode fabrication forms an important part of the work discussed in this thesis, this will be reviewed later in detail under section 1.13.

1.11.2 Photo-active Material

As already discussed, the photo-active material forms an integral part of the OPV device and is composed of an electron donor material and electron acceptor material. Both donors and acceptors must exhibit high mobility of their respective charge carriers, strong absorption of the solar spectrum, have long exciton diffusion lengths and good solubility in common solvents. These materials can be small molecules or highly conjugated polymeric materials. The structures of the electron donor and electron acceptor materials used in this work are depicted in Figure 1.17.

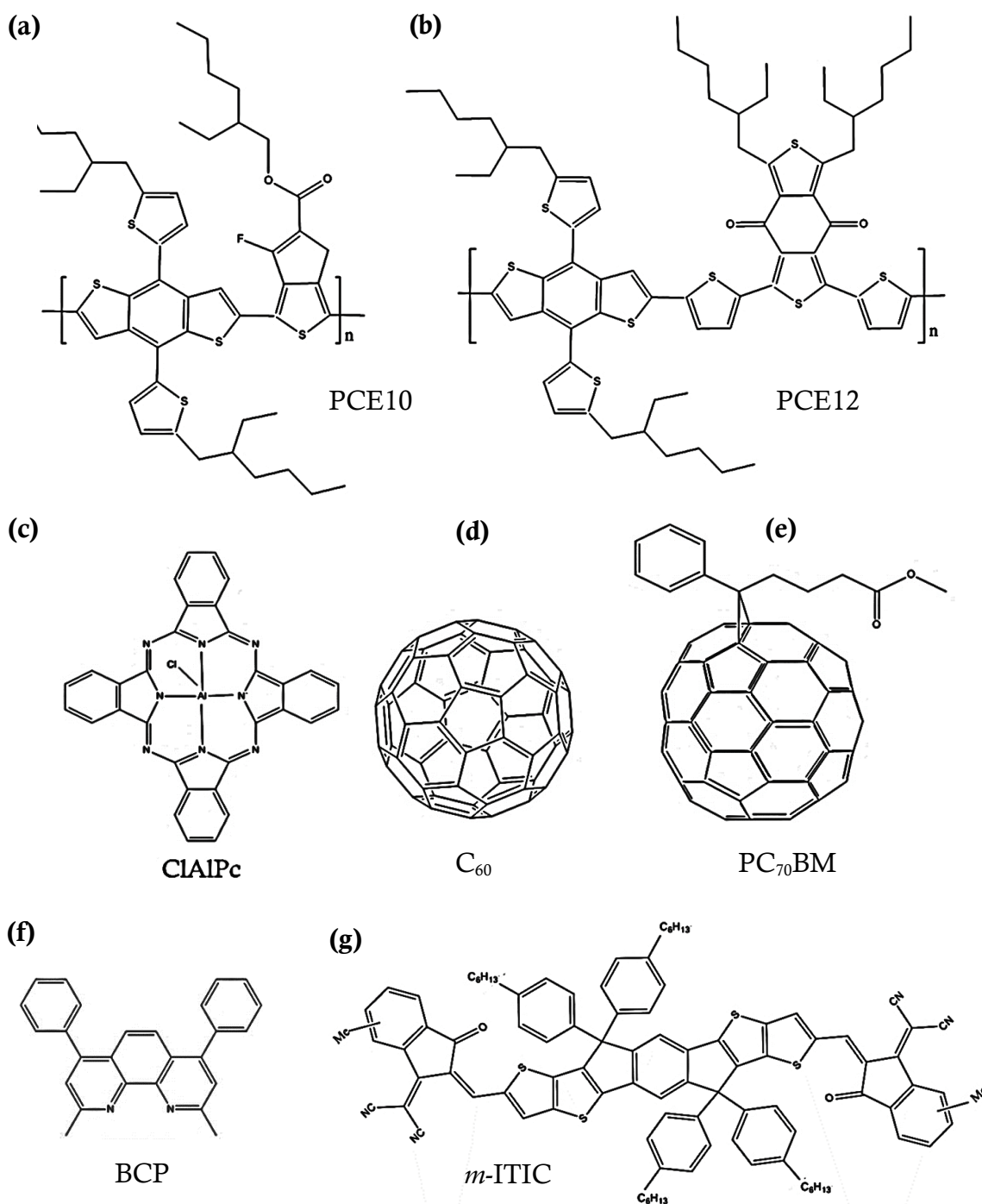


Figure 1.17: Chemical structures of electron donor material; (a) PCE10; (b) PCE12; (c) ClAlPc and electron acceptor material; (d) C₆₀ (e) PC₇₀BM (f) BCP and (g) m-ITIC used in the work reported in this thesis.

These include PCE10 (Poly[4,8-bis(5-(2-ethylhexyl)thiophen-2-yl)benzo[1,2-b;4,5-b']dithiophene-2,6-diyl-alt-(4-(2-ethylhexyl)-3-fluorothiophene-2-carboxylate-2,6-diyl)]), PCE12 (Poly[(2,6-(4,8-bis(5-(2-ethylhexyl)thiophen-2-yl)benzo[1,2-b;4,5-b']dithiophene))-alt-(5,5-(1',3'-di-2-thienyl-5',7'-bis(2-ethylhexyl)benzo[1',2'-c:4',5'-c']dithiophene-4,8-dione))], ClAlPc (Chloro aluminium

phthalocyanine), C₆₀, PC₇₀BM ([6,6]-Phenyl-C₇₁-butyric acid methyl ester) BCP (bathocuproine) and *m*-ITIC (3,9-bis(2-methylene-((3-(1,1-dicyanomethylene)-6/7-methyl)-indanone))-5,5,11,11-tetrakis(4-hexylphenyl)-dithieno[2,3-d':3',3'-d']-s-indaceno[1,2-b:5,6-b']dithiophene).

1.11.3 Charge Transport Layers

High performance OPV devices include two additional layers known as the hole transport layer (HTL) and electron transport layer (ETL) which are collectively described as charge transport layers (CTLs). The HTL is located beside the hole-extracting electrode and ETL beside the electron-extracting electrode and the BHJ is sandwiched between the HTL and ETL. The main function of these layers is to enable selective extraction of only one type of charge carrier (either electrons or holes) by blocking the transport of the other carrier type. This is achieved by ensuring that there is a large barrier to extraction of one carrier type and a small barrier to extraction of the other type as illustrated in Figure 1.18.

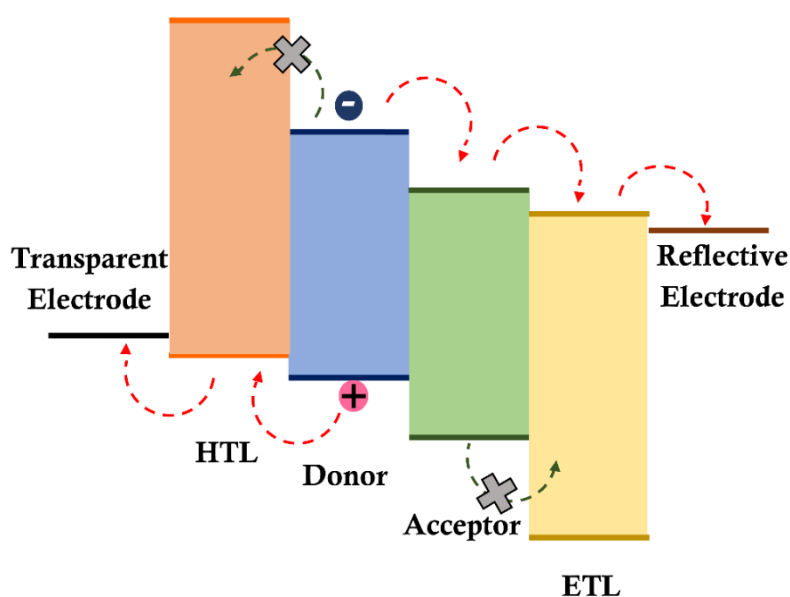


Figure 1.18: Energy level diagram illustrating positioning of CTLs that facilitate selective extraction of a single type of charge carrier.

ETLs have a high electron mobility and enable selective extraction of electrons. Hole transport to the electrode is blocked because the VB edge of the ETL lies at a lower energy compared to the HOMO of the acceptor or donor material (Figure 1.18). Conversely HTLs have a high hole mobility and facilitate only the transport of holes to the electrode by blocking electron transfer because the CB edge of the HTL has a higher energy compared to the LUMO of the donor or acceptor (Figure 1.18). In addition to this primary function, CTLs contribute to improved device performance by preventing unfavourable

interaction between the organic photo-active layer and electrodes such as diffusion or migration of species from the electrode. Very conductive CTLs can also serve as optical spacer layers which is particularly important when the photo-active layer is very thin. CTLs are mostly wide band gap materials and can be metal oxides, polymers or small molecules.

The HTL widely used in this work is MoO₃. Other examples of commonly used HTLs include WO₃ and highly conducting heavily doped poly(3,4-ethylenedioxythiophene) polystyrene sulfonate (PEDOT:PSS). In the case of metal oxides, the properties of the HTL is highly dependent on the stoichiometry of the oxide as charge transport is facilitated by oxygen vacancy defects.⁵¹⁻⁵³ The ETLs used in this work include, BCP, ZnO, polyethylenimine (PEI), ethoxylated polyethylenimine (PEIE) and a thin film of Al (0.8 nm) which oxides to AlO_x.

1.11.4 Reflective Electrode

All high efficiency OPV devices need a reflective metal electrode to redirect the light not absorbed on the first pass through the photo-active layer, back into the device to facilitate reabsorption and subsequent exciton generation. This electrode needs to be a metal with high reflectivity in the wavelength range of operation and is therefore very thick; 50 – 100 nm. Ag and Al are the most widely used reflective electrodes, owing to their very high reflectivity in the wavelength range 300 – 900 nm. Although Ag is more stable towards oxidation in air, Al is preferred due to its relatively low cost. Additionally, Al is more stable under illumination and has a lower probability of diffusing into adjacent organic semiconductor layers because it reacts with oxygen forming aluminium oxide which is stable. However, as discussed in Chapter 5 of this thesis, certain device architectures, prefer Ag over Al.

1.12 Device Architectures

There are three main ways in which the layers constituting a typical OPV device can be arranged.

1. Conventional architecture
2. Inverted architecture
3. Top-illuminated architecture

The type of device architecture used depends on the availability and compatibility of materials as well as the application under consideration. Conventional devices are those that use a transparent electrode to extract holes and a reflective top electrode to extract

electrons. In inverted device architectures the electrical polarity is reversed, such that the window electrode extracts electrons and the top reflective electrode extracts holes. In both conventional and inverted architectures, light enters the device through the transparent electrode which is supported on the substrate. The primary difference in top-illuminated devices is that light enters through a transparent electrode which is located at the top of the device and the substrate electrode serves as the reflective electrode.

As detailed in each results chapter, all three types of devices have been fabricated in the work reported in this thesis.

1.13 Transparent Electrodes

Transparent electrodes, also referred to as window electrodes, permit light into the device. All transparent electrodes used in OPVs must possess a high transparency across the wavelength range 300 – 900 nm together with high electrical conductivity. The electrical conductivity of thin film electrodes is expressed in terms of sheet resistance (R_{sh}) in units of $\Omega \text{ sq}^{-1}$ and high electrical conductivity is needed so that ohmic losses in the plane of the electrode are minimized. However, the problem faced when simultaneously attempting to optimise both these parameters is that the improvement of one invariably leads to a deterioration in the other. This is because high electrical conductivity is usually achieved by having a large density of free electrons, which can also interact with light leading to a reduction in overall transparency due to absorption, reflection and scattering of incident photons. Hence a compromise must inevitably be made between transparency and electrical conductivity. Additionally, the window electrode must have the following properties;

- A suitable ϕ for the extraction of the charge carrier of interest;
- Exhibit stability towards the processing conditions used in OPV fabrication;
- Possess low surface roughness enabling formation of good contacts;
- Compatibility with flexible substrates;
- Be low-cost in terms of both raw materials and fabrication.

The most predominant type of transparent window electrode used for OPVs to date, are doped metal oxides, particularly ITO. These are wide E_g materials and therefore highly transparent ($\geq 80\%$ over the range $\lambda = 300\text{-}900\text{ nm}$) which permits a relatively thick film to be used. The high electrical conductivity in these types of metal oxides is achieved by degenerate n -type doping. The high level of doping and the ability to fabricate relatively thick layers (100-300 nm) contributes to a low R_{sh} , i.e. $10\text{-}15 \Omega \text{ sq}^{-1}$. Therefore, the

electrical conductivity is strongly thickness dependant, with thicker films exhibiting lowest R_{sh} . Owing to the high electrical conductivity and transparency, ITO is the preferred choice of transparent electrode for most OPVs, however, there are notable drawbacks to this type of transparent electrode which has led to the search for alternatives. ITO is a ternary oxide consisting of indium oxide (In_2O_3) with ~10 % tin as the dopant. Indium is a rare earth metal with limited reserves and thus the extensive use of ITO in liquid crystal displays, organic light emitting diodes (OLEDs), touch screens technology and other optoelectronic devices rises concerns about the supply of this material for large area and large scale devices like solar cells. Standard techniques for depositing ITO requires thermal annealing to achieve optimal performance which is an energy intensive process and limits the substrate choice. Additionally, ITO is an inherently brittle material and therefore, matches very poorly with the needs of flexible OPVs.^{11,54-59} Studies have also shown that ITO cracks and therefore degrades readily upon bending through small radii of curvature.⁵⁵ Additionally, indium has been shown to diffuse into the adjacent organic semiconductors leading to degradation in device performance over time.¹¹ Therefore an alternative transparent electrode that is better suited for emerging types of OPV technology is needed.

Alternatives to ITO include other doped oxides such as fluorine doped tin oxide (FTO) and aluminium doped zinc oxide (AZO). In the case of FTO, although it is composed of abundant elements, it has a rough surface making it poorly suited for OPVs⁶⁰ and both AZO and FTO are known to have optical and electrical properties inferior to that of ITO.⁵⁸ The other common alternatives to ITO are carbon nanotube network electrodes^{35,61} and graphene.⁶²⁻⁶⁴ Although carbon nanotubes have good charge mobility, the light absorption and reflection in the visible and IR regions lead to poor transparency. Graphene on the other hand is highly transparent but the R_{sh} of this material is very high.⁴⁶ Furthermore, both carbon nanotubes and graphene exhibit poor adhesion to the underlying substrate, as a result both these materials are inappropriate as stand-alone alternatives to ITO.⁵⁸ The conductive polymer, PEDOT.PSS which is commonly used as a HTL in OPVs, is both highly transparent and electrically conductive and therefore has been used as an alternative transparent electrode. However, a key issue is the hydrophilicity of PEDOT.PSS. The high affinity towards water results in the gradual uptake of water, which is detrimental to OPVs and therefore results in poor long-term stability and performance.⁶⁵ Metal nanowires⁶⁶⁻⁶⁹ and nanogrids⁷⁰ are yet another important class of alternatives to ITO. Ag and Cu are widely used for this application

owing to their very high conductivity. Although metal nanowire electrodes are impressive in terms of transmittance, the R_{sh} is often high.^{71,72} When the density of metal nanowires is high, the R_{sh} is low but high coverage leads to poor transparency. Additionally, the random arrangement of metal nanowires brings about high surface roughness and increased probability of shorting in devices. In the case of metal grids, the spacing between adjacent lines must be large to facilitate higher transmission but this leads to high resistance and high recombination losses.⁷⁰ To overcome this drawback planarising conductive materials are used to increase the conductivity and smoothen the surface which adds to the complexity of the fabrication process.

In the recent years there has been a lot of attention and research interest focused towards the use of thin metal films as window electrodes in OPVs. Metals inherently have a large number of free electrons which makes them highly conductive. However, as stated earlier a careful compromise between electrical conductivity and transmission needs to be struck. Thin metal films (~10 nm) can be fabricated using vacuum deposition techniques with good control and homogeneity. Generally, most attention is given to the coinage metals Au, Ag and Cu. Of these Au is extremely costly and can only realistically be used in laboratory scale investigations. Therefore, Ag is the most predominant choice of metal used in OPVs. However, when the properties of Ag and Cu are considered, Cu has a comparable conductivity to that of Ag at one hundredth of the cost and therefore Cu may be a more viable alternative in the long run. Ag is more transparent compared to Cu in the range of $\lambda = 300-900$ nm because it exhibits the lowest inter-band absorption losses in this region. However all unpatterned thin metal films are not as transparent as ITO and so scalable methods must be implemented to increase the transparency of these thin metal films so they may prove to be more competitive alternatives to ITO. One approach to achieving higher transparency is forming a dielectric/metal/dielectric (DMD) triple layer. Ideally a thin metal film is sandwiched between dielectric materials which are predominantly oxides such as ZnO, WO₃ and MoO₃. These inorganic oxides are wide band gap materials and therefore highly transparent even when relatively thick (30 - 40 nm). The optical and electrical properties of a DMD type electrode is largely dependent on the thickness of individual layers.^{57,73} A thin layer of the metal is preferred but this thickness must be greater than the percolation thickness of the metal to ensure the formation of a homogenous, continuous film and avoid formation of discrete metal islands. Efficient OPV devices have been fabricated using DMD structures as transparent metal films but in most of these studies, sputtering is used to deposit the metal oxide.^{57,74-76} Sputtering is a harsh technique that uses a plasma to ablate the source material directing

it towards the substrate. This can damage the substrate and is also costly compared to vacuum evaporation due to the slowness of the deposition process. Introducing an array of holes into metal films is another effective means of improving the transparency. The objective is to reduce the effective coverage of the metal by patterning techniques so that areas with metal will contribute to electrical conductivity whilst metal free areas enable transmission of light. Generally patterned metals have a higher transparency (provided the pattern has dimensions larger than the wavelength of light) than the unpatterned metal of identical thickness. The electrical conductivity is inevitably reduced due to film discontinuity in the metal and scattering of electrons at the edges of the holes. Therefore, the pattern must be carefully designed to achieve a balance between the two parameters. Additionally, these patterned metal films can be used in conjunction with metal oxides or conductive polymers to reduce the R_{sh} . However, some patterning techniques such as conventional lithography can be quite complex requiring sophisticated equipment and specific conditions, thus inexpensive methods of patterning compatible with thin metal films will be more advantageous and cost effective.

Depositing homogenous films of Cu and Ag directly onto transparent substrates can be problematic due to wetting issues. In such instances surface modification techniques are required to promote good adhesion between the film and the underlying substrate. An effective method of achieving this is using functionalized (amino and mercapto groups) methylsilanes to modify the surface and this method is used throughout the work reported in thesis to fabricate homogenous compact Cu films. The silanes interact strongly with the substrate such as glass, PET and PEN via the Si-O bond and metals are bound by strong S-M or N-M bonds^{77,78} as will be discussed in chapter 2.

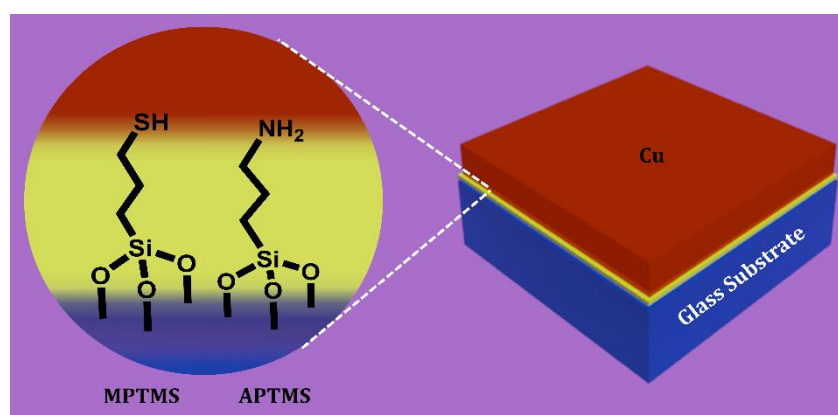


Figure 1.19: Schematic illustration of a Cu film supported on a mixed monolayer consisting of 3-mercaptopropyltrimethoxysilane (MPTMS) and 3-aminopropyltrimethoxysilane (APTMS).

Additionally, metals may need to be passivated to reduce interaction with oxygen, especially in the case of Cu as it is more susceptible to oxidation in ambient air. One very effective approach to achieving this is using a thin Al film. This thin Al layer may also serve as ETL thereby providing dual functionality.^{79–81} A key advantage of optically thin metal films over ITO is that they possess good flexibility owing to the inherent malleability in metals and nature of the metallic bond. Therefore, metal films are suitable for flexible OPVs and provide good mechanical stability against bending and modest physical deformation.

In order to compare all transparent electrodes on a common basis a parameter known as figure-of-merit (FoM) has been introduced. FoM for transparent electrodes is a numerical value that can be used to estimate the performance of a transparent electrode enabling the comparison between different types of electrodes fabricated using various techniques. The most commonly used FoM was proposed by Haacke and so is known as the Haacke FoM: Equation 1.12^{82,83}

$$\text{Haacke FoM} = \frac{T_{avg}^{10}}{R_{sh}} \quad \text{Equation 1.12}$$

The Haacke FoM for a particular electrode can be computed using the average transmission (T_{avg}) and R_{sh} . The larger the magnitude of the FoM, the better the electrode is deemed to be. Throughout this thesis the Haacke FoM has been used to compare the fabricated electrodes with others reported in literature.

1.14 Copper

Cu is an abundant metal in the earth's crust and in nature it may exist in the form of Cu sulphites, carbonates and Cu (I) and Cu (II) oxides. Cu is a d-block element located in the 11th group in the periodic table. Its atomic number is 29 with an electronic configuration of $1s^2 2s^2 2p^6 3s^2 3p^6 3d^{10} 4s^1$. It is a solid at room temperature with a face centered cubic crystalline structure, a melting point of 1085 °C, a boiling point of 2560 °C and an electrical conductivity of $5.96 \times 10^7 \text{ S m}^{-1}$. Cu is extensively used in many applications including for electrical wiring, as a component of alloys in jewellery and in coin manufacture and as part of thermocouples.

1.14.1 Optical Properties of Copper

There have been several studies investigating the band structure of Cu particularly by Krutter,⁸⁴ Fukuchi,⁸⁵ Ehrenreich,⁸⁶ Rudberg⁸⁷ and Burdick⁸⁸ and their investigations are

instrumental in understanding how Cu interacts with light. It was initially postulated that electrons in 4s and 3d bands were separate with no band intermixing⁸⁴ but later it was identified that there is definite mixing of these two bands which gives rise to s-d hybridization in Cu. This is represented in the density of states (DOS) diagram for Cu (Figure 1.20) by the overlapping of the bands arising from 4s and 3d orbitals. Burdrick concluded that these bands should be able to accommodate eleven electrons from each atom arising from the 3d and 4s orbitals.⁸⁸

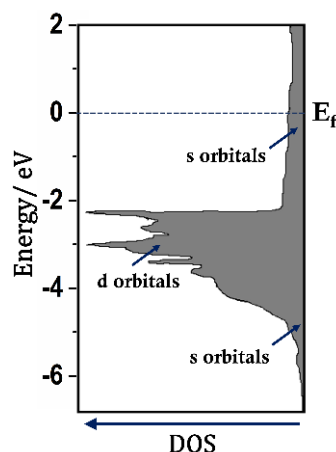


Figure 1.20: Schematic representation of the density of states for Cu adapted from ref.[87,88]. The shaded area indicates available states.

The DOS defines the number of different states of a particular energy level that the electrons are permitted to occupy. As illustrated in Figure 1.20, the 3d band is narrow and shows a high DOS because it can accommodate 10 electrons. The 4s band is broader and can accommodate only one electron, therefore the DOS is small. Figure 1.20 also shows that for Cu, the Fermi surface is located in the 4s band.

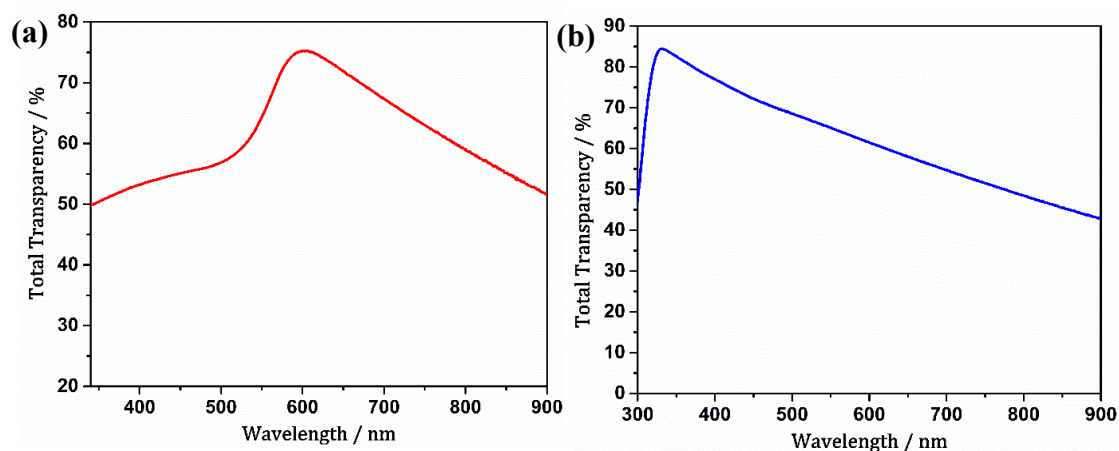


Figure 1.21: Total transmission spectra for 11 nm thick planar (a) Cu and (b) Ag films deposited on glass.

Inter-band transitions can be defined as a transition from the Fermi surface to the next higher empty band or transitions from a lower lying filled band to the Fermi surface.^{86,88} The colour of Cu can be explained in terms of these inter-band transitions.

The transmission spectrum for a thin Cu film has a peak at ~ 600 nm (at ~ 2 eV) (Figure 1.21(a)). A decrease in transmittance at $\lambda \leq 550$ nm can be observed and this is attributed to an inter-band transition from d to s band.^{88,89} To facilitate this transition, absorption of blue-green light takes place resulting in re-emitting the complementary red-orange colour which is perceived as the colour of Cu. Consequently, as Cu absorbs short wavelength visible light, the reflectivity of Cu drops at $\lambda \leq 550$ nm (Figure 1.22).

In the case of Ag, there are no inter-band transitions taking place in the visible region of the EM spectrum because these transitions need much higher energy to promote electrons from a 4d to a 5s band. As a result, inter-band transitions in Ag require absorption of the UV part of the EM spectrum. Therefore, all colours in the visible region are equally re-emitted giving Ag its colour and high reflectivity throughout the entire visible spectrum (Figure 1.22). In Ag, the inter-band transition that promotes electrons from 4d to 5s takes place at ~ 4 eV, resulting in a peak at ~ 325 nm in the transmission spectrum for Ag (Figure 1.21(b)).

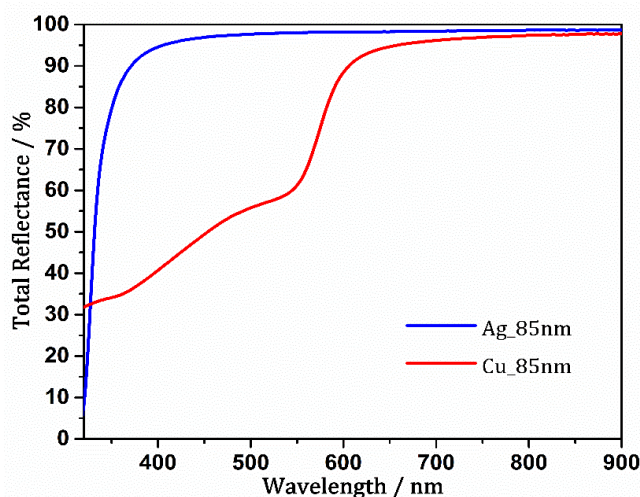


Figure 1.22: Total reflectance of 85 nm thick planar Cu and Ag films deposited on glass.

Considering the behaviour of electrons in metals two types of loss mechanism can be identified. They are the inter-band transition losses and free electron or Drude losses. These losses can be understood by considering the complex dielectric constant (ϵ) of a metal. As described earlier the dielectric constant is a measure of the polarisability of a

material in response to an electric field and therefore the material's ability to screen the force of interaction between charges. Metals have a complex dielectric function in which the real part (ϵ') indicates the strength of the polarisation induced by an external electric field and the imaginary part (ϵ'') denotes the losses encountered when polarising the material.⁸⁹

$$\epsilon(\omega) = \epsilon'(\omega) + i\epsilon''(\omega) \quad \text{Equation 1.13}$$

where ω is the frequency of the applied field.

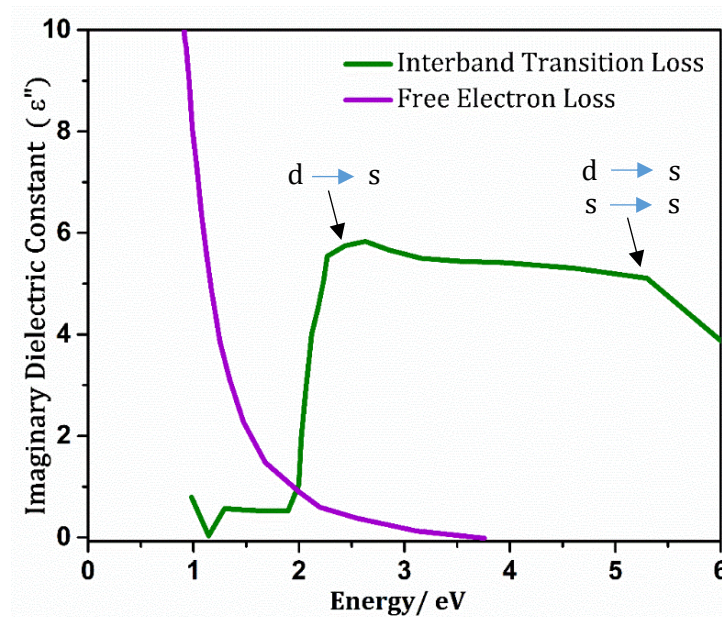


Figure 1.23: Inter-band and free electron losses in Cu adapted from ref. [89]

ϵ'' denotes the total losses comprising of inter-band and free electron losses as shown in Figure 1.23.

The free electron losses are very high at low energies (< 1 eV) and then exponentially reduce, such that at energies > 2 eV, the free electron losses for Cu are negligible. This is because at lower energies electrons behave as a free electron gas and therefore contribute to losses in this region. Conversely, the inter-band transition losses are small until ~ 2 eV and then increase abruptly due to the onset of inter-band transitions. Consequently, for Cu, free electron losses dominate inter-band transition losses at energies ≤ 2 eV whilst inter-band transition losses dominate at energies > 2 eV.

As indicated in the inter-band losses curve for Cu in Figure 1.23, at ~ 2 eV transitions from d to s and at a higher energy, transitions from d to s and s to s bands take place.⁸⁹

1.15 Surface Plasmons

The field of plasmonics deals with the interaction between light and matter and in the area of OPVs this phenomenon has been widely exploited to enhance the photogenerated current via light scattering and near-field enhancement.⁹⁰⁻⁹⁴ Most literature pertaining to the use of plasmonics in OPVs relates to the use of metal nanoparticles such as Au or Ag to achieve increased photocurrent by positioning nanoparticles at different interfaces within a device.^{35,89,94} The positioning of nanoparticles in OPVs and the corresponding potential for photocurrent enhancement is discussed in detail in chapter 6. Another relatively less exploited approach is to use a thin metal film with an array of nanoscale holes or apertures.^{92,95-97} Although the metal structure that gives rise to plasmonics is different in the two cases, there are studies that show that the underlying theory for both cases is quite similar.⁹² Surface plasmon resonances (SPR) are collective oscillations of conduction band electrons at the interface between a metal and a surrounding dielectric medium. This effect is termed as a localized surface plasmon resonance (LSPR) when the SPR is confined to a particular area such as a nanoparticle or nano aperture in a metal film having dimensions smaller than the wavelength of the exciting light. When the SPR gives rise to a wave that propagates freely along the metal - dielectric interface, it is referred to as a surface plasmon polariton (SPP).^{62,89,90} This discussion will be limited to LSPR as this is the type of SPR of most relevance to the research reported in this thesis (Chapter 6).

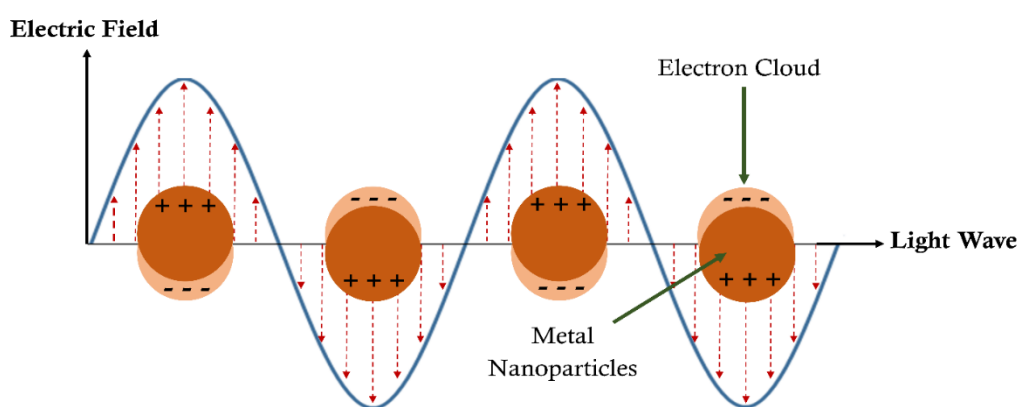


Figure 1.24: Schematic representation of LSPR arising from collective oscillations of conduction band electrons in metal nanoparticles. The lighter shade represents the movement of the electron density.

Metals are electrically conductive because they have a high density of free electrons. When illuminated with EM radiation, these free electrons in the metal can respond to the oscillating electric component of the incident light, for frequencies up to the metal plasma

frequency (ω_p). The metal will respond by redistribution of the charge confined within a metal nanoparticle or nanohole. Thus, the electron density will move to one side leaving the other side positively charged generating a dipole. This dipole gives rise to an electric field that opposes the field of the incident light and acts as a restoring force pushing the electrons back to their equilibrium position.

When the electrons are in the displaced position, if the external field is removed, then the electrons continue to oscillate with a certain frequency. The maximum frequency this restoring oscillation can support is the ω_p of the metal.⁹⁸ Therefore at $\omega > \omega_p$, the metal is unable to respond to the oscillating electric field and light passes unhindered. Conversely at $\omega < \omega_p$, the metal can counteract the oscillating electric field and therefore under this condition planar metal films reflect light.

ω_p is given by

$$\omega_p^2 = \frac{ne^2}{\epsilon_0 m^*} \quad \text{Equation 1.14}$$

where n is the density of conduction electrons, e is the charge on an electron, ϵ_0 is the permittivity of free space and m^* is the effective mass of a conduction electron.

The oscillation of conduction band electrons induced by the incident light corresponds to energy transfer from the light to the nanoparticle, and as energy is always conserved, it follows that, light is attenuated in the process. Hence, the plasmonic effect of metal films can be studied by investigating the optical properties of the metal relative to the incident light; in the absorption spectrum this will be manifested as a peak and in the transmission spectrum this will be depicted as a dip.

However, these plasmonic excitations have a limited lifetime and will eventually decay or undergo damping due to:^{62,89,92}

- i. Intra-band damping – the electrons leave the collective plasmonic oscillation due to scattering;
- ii. Inter-band damping – the electrons leave the surface plasmon oscillation to participate in inter-band transitions;
- iii. Radiative damping – loss of the plasma oscillation in the form of radiation.

As surface plasmons rely on free electrons, key equations can be derived by considering the complex dielectric function (ϵ) of a metal as discussed in section 1.14.1. It follows

that equation 1.13 can be further expanded using the Drude theory to give equation 1.15.^{89,99,100}

$$\varepsilon(\omega) = \varepsilon'(\omega) + i\varepsilon''(\omega) = \varepsilon_{int} - \frac{\omega_p^2}{\omega(\omega + i\Gamma)} \quad \text{Equation 1.15}$$

where ε_{int} is the contribution arising from inter-band transitions which in the case of a perfectly free electron gas, becomes unity.⁸⁹ Γ is the total damping rate.

Therefore, for a perfectly free electron gas,

$$\varepsilon(\omega) = 1 - \frac{\omega_p^2}{\omega(\omega + i\Gamma)} \quad \text{Equation 1.16}$$

It follows that when the ω is lower than the ω_p the complex dielectric function takes a negative value. Consequently for SPRs to be possible the real part of the dielectric constant, ε' should be negative. This is one reason for the extensive use of metals to investigate SPR as metals have an abundance of free electrons that provides the negative ε' which is an essential property for a plasmonic material.^{62,89} Moreover, the use of metals ensures that the ω_p is large and so SPRs can be supported across both the visible and IR parts of the EM spectrum.

SPR requires electrons to behave as a free electron gas and therefore mostly predominant below energies at which inter-band transitions occur. For example, as discussed in section 1.14.1, for Cu inter-band transitions commence at ~ 2 eV and as shown in Figure 1.23, at energies below 2 eV electrons behave like a free electron gas resulting in large free electron losses and at energies greater than 2 eV inter-band transition losses dominate. As SPR is a characteristic related to free conduction band electrons, for Cu, it is predominant at $\omega \leq 2$ eV as beyond this point electrons have sufficient energy to participate in inter-band transitions and as such inter-band transitions will dampen the effects of SPRs. However, when ω is very low the free electron losses increase at an exponential rate (Figure 1.23) and therefore dampening of the SPR can occur via other mechanisms. Hence SPR occur more effectively within a narrow range of wavelengths. For Cu this is in the range of $\lambda = 600$ -800 nm depending on dimensions of the nanoparticle or nanopattern.¹⁰¹ The same has been proven for Au films consisting holes of variable sizes where it was observed that the SPR does not occur beyond 2.4 eV which is the inter-band threshold for Au.⁹² Additionally, several studies have shown that for LSPR in metal nanoparticles, the ω_p is dependent upon the type of metal, size, shape and geometry of the nanoparticle. Similarly, in the case of nano apertures in metal films, investigations

show that the LSPR depends on the size and shape of the nano apertures where as SPP excitation requires periodicity in the aperture pattern with dimensions similar to the SPP wavelength.^{92–94,102–106}

SPRs are distant dependant as it is easier to induce a dipole in the electrons in the metal surface closer to the incident light compared to electrons that are further away from the light source. Therefore, SPRs can be viewed as near-field evanescent waves that decay exponentially with distance. Thus, in the context of applications of SPRs in OPVs it is important that the distance between the point of SPR generation and photoactive layer is optimized so that the near-field enhancements due to light coupling with the nanostructures can be used to generate excitons before the SPR is lost to the surrounding metal due to ohmic losses.^{90,98}

1.16 Polymer Blends

Polymers are molecules composed of many repeating units known as monomers and can range from natural biological polymers such as deoxyribonucleic acid and proteins to synthetic polymers such as polystyrene, polyethylene and nylon. The simplest type of polymer consists of only one type of monomer and is referred to as a homopolymer. The complexity of the polymer increases when many types of monomers are involved and can vary from a simple linear structure to a complex 3-dimensional branched structure. A vast diversity of polymers with different properties are used for a broad range of applications and in the context of OPVs polymers are primarily used as donors and acceptors in BHJ systems as the photoactive material which form a vital part of the device.

Polymer blends consist of two or more polymers which are mixed together to form a new material with different properties to that of the individual components. The simplest case is the mixing of two polymers which is referred to as a binary polymer blend. Principally when two polymers are mixed together there can be two possible outcomes; they will either be completely miscible in one another forming a single phase or immiscible in one another, in which case a phase separation will occur. The behaviour of polymer blends at thermodynamic equilibrium is governed by,¹⁰⁷

- i. The molecular structure of the polymers: linear or branched;
- ii. The composition of the polymer blend;
- iii. The degree of polymerisation which is the number of monomers that make up the polymer chain.

The energy of mixing for a binary homopolymer blend can be estimated using the Flory-Huggins segment-segment interaction parameter denoted by χ_s in equation 1.17,

$$\chi_s = \frac{1}{k_B T} \left[\epsilon_{AB} - \frac{1}{2} (\epsilon_{AA} + \epsilon_{BB}) \right] \quad \text{Equation 1.17}$$

where, ϵ_{ij} represents the contact energy between i and j segments, k_B the boltzmaan constant and T the temperature.

A negative value for χ_s indicates a favourable energy of mixing which means that when A and B segments contact the overall energy of the system is lower than the sum of energy when A and A or B and B segments are in contact. This type of energy of mixing can be obtained when hydrogen bonding is predominant. A positive value for χ_s denotes an increase in energy of mixing when A and B segments are brought into contact compared to when only identical segments are in contact.

The phase behaviour of a linear homopolymer mixture can be summarised by equation 1.18.

$$\frac{\Delta G_m}{k_B T} = \frac{f_A}{N_A} \ln f_A + \frac{(1 - f_A)}{N_B} \ln(1 - f_A) + f_A (1 - f_A) \chi_s \quad \text{Equation 1.18}$$

where ΔG_m is the change in Gibbs free energy upon mixing per segment, f_A refers to the overall volume fraction of component A and N_A is the number of segments per polymer molecule in A.

The first two terms on the right-hand side of equation 1.18 accounts for the entropy upon mixing, ΔS_m . As mixing increases disorder, ΔS_m increased but as larger chains have a limit to the configurations that can be attained compared to smaller chains, increase in N reduces ΔS_m . The last term accounts for the enthalpy of mixing, ΔH_m and may increase or decrease ΔG_m depending on whether χ_s is positive or negative.¹⁰⁷⁻¹⁰⁹

Ideally for a stable homogenous polymer solution to result the ΔG_m should take a negative value. However, this criterion alone is not sufficient to determine the stability of the resulting polymer blend. Upon mixing if a more stable condition, i.e. a lower ΔG_m , can be attained, the polymer blend will further reduce its ΔG_m by undergoing phase separation. In the case of a stable homogenous polymer solution, a plot of ΔG_m vs composition (f) will result in a convex shaped curve with a local minimum.

This can be mathematically expressed as,

$$\frac{\partial^2 \Delta G_m}{\partial f^2} > 0 \quad \text{Equation 1.19}$$

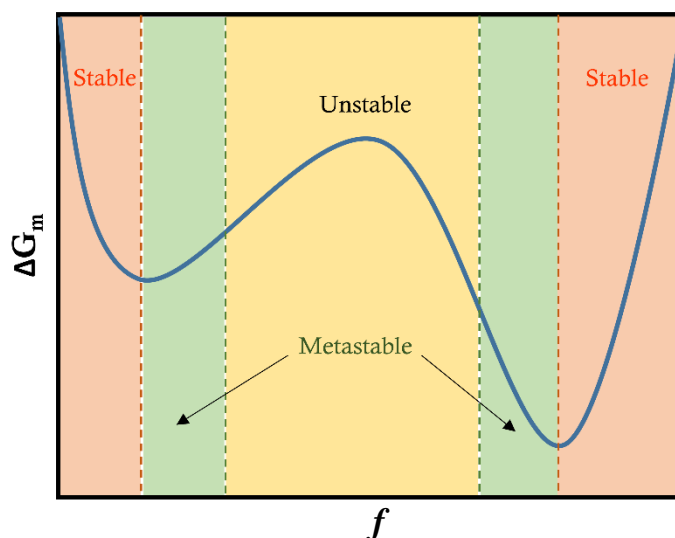


Figure 1.25: A plot of ΔG_m vs composition for a binary homopolymer blend showing stable, unstable and metastable regions.

In general curves of ΔG_m vs f for polymer blends are not simple and can have a combination of minima and maxima (Figure 1.25). Therefore, values derived from this curve are used to plot a corresponding phase diagram for a given combination of polymers. A typical phase diagram for a symmetric binary linear homopolymer blend where $N_A = N_B$ is given in Figure 1.26. Two distinct regions can be identified as a completely miscible single phase and a phase separated region. Within the phase separated region two types of separation can be seen; spinodal decomposition and binodal decomposition.

Binodal decomposition takes place only within the metastable region in phase diagram. The metastable region (green area in Figure 1.25) is mathematically expressed as,

$$\frac{\partial^2 \Delta G_m}{\partial f^2} = 0 \quad \text{Equation 1.20}$$

Under this condition, small droplets of the minor phase in the metastable region begin to form by nucleation and can grow by increasing the size of the droplet. However, once equilibrium (a point on the solid curve in Figure 1.26) has been attained, further growth of droplet size by diffusion is not possible and therefore coalescence takes place increasing the size further.

Thus, binodal decomposition involves nucleation and growth and the free energy barrier towards nucleation must be overcome in order to grow.

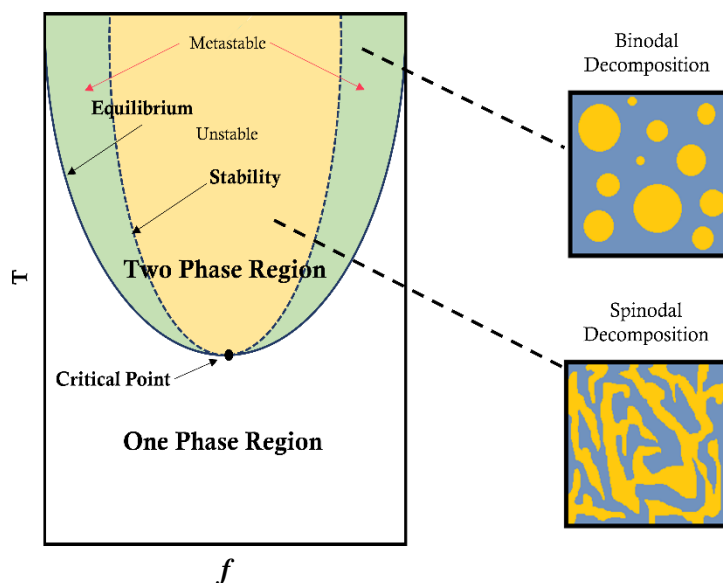


Figure 1.26: Phase diagram for a symmetric binary homopolymer blend and the morphology of binodal and spinodal decomposition taking place at metastable and unstable portions of the two-phase region adapted from ref. [107,109].

Spinodal decomposition takes place when the mixture exists in an unstable region (yellow area in Figure 1.25) which is mathematically expressed in equation 1.21.

$$\frac{\partial^2 \Delta G_m}{\partial f^2} < 0 \quad \text{Equation 1.21}$$

In this region there is no thermodynamic barrier and the mixture spontaneously separates into a bicontinuous morphology as shown in Figure 1.26. However, in both types the coarsening of polymer entities take place in order to minimize interfacial surface tension by reducing the interfacial area.^{107,108} For a given combination of polymers, the phase diagram shown in Figure 1.26 may have a minimum or maximum depending on whether increase in temperature favours miscibility or phase separation.^{107,109}

In the work reported in this thesis, a polymer blend consisting of polystyrene (PS) and poly (methyl methacrylate) (PMMA) has been used to fabricate transparent Cu window electrodes applicable for OPVs. As the objective was to finally fabricate holes in the Cu electrode, a binodal decomposition was preferred over spinodal decomposition for this application. Therefore, the proportions of PS to PMMA were adjusted with guidance from previously reported work in this area^{110,111} to obtain a binodal type phase separation where

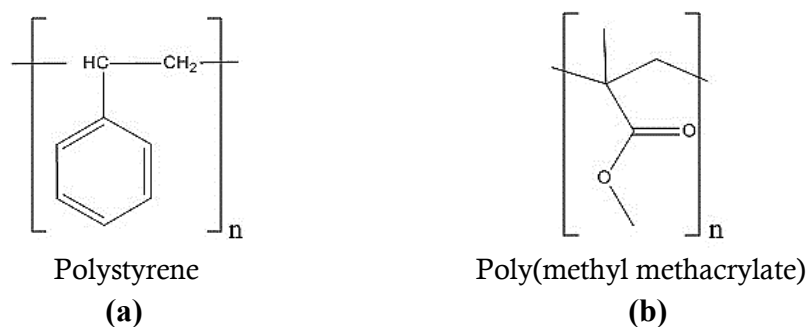


Figure 1.27: Chemical structures of **(a)** PS and **(b)** PMMA used to fabricate apertures in thin Cu films using polymer blend lithography

spherical PS (minor phase) entities were distributed in a PMMA (major phase) matrix. However, achieving the required morphology on Cu proved very challenging and several blend compositions and concentrations were attempted before arriving at the appropriate polymer blend concentration and morphology. As shown in Figure 1.28, the PS:PMMA ratio in the polymer blend plays a critical role in the type of decomposition obtained. The polymer blend preparation and associated electrode fabrication will be discussed in detail in chapter 3.

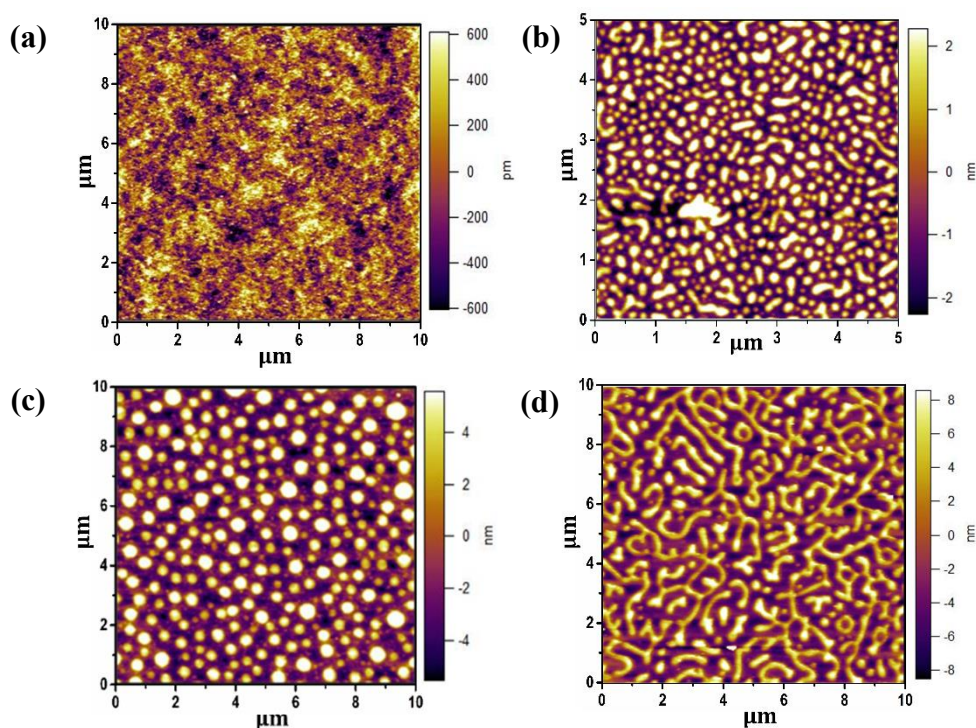


Figure 1.28: Atomic force microscopy images showing the morphology of the PS/PMMA polymer blend spin cast onto a Cu film when the PS:PMMA ratio is **(a)** 1:9; **(b)** 2:8; **(c)** 3:7 and **(d)** 1:1.

1.17 Project Overview

The work presented in this thesis is primarily focused on developing Cu electrodes for OPVs. Over the period of this study (2015 October – 2018 March) and even at present there are only a few reports in which Cu is used as an electrode for OPV devices, and in most instances it is used in the form of Cu wires,^{67–69,71,112–114} DMD type triple layer electrodes^{75,76,115} or in conjunction with other materials such as graphene.⁶³ There are very few reports in which thin Cu films have been used as stand-alone electrodes in OPVs in conjunctions with CTLs that enhance optical and electrical characteristics of the underlying electrode^{79,116} or where the fabrication of such an electrode has been discussed in detail.⁸⁰ Ag is by far the dominant metal choice for transparent metal electrodes because it is more stable towards oxidation and has the lowest inter-band absorption losses in the visible region. However, Ag is a relatively costly metal¹¹⁷ and the transition to a low cost alternative is essential in order to realise the full cost benefit of OPVs over other types of thin film PV. Cu is an abundant metal that can offer comparable conductivity to Ag at one 100th of the cost. Its main drawback is its susceptibility towards oxidation in air, although this can be mitigated by appropriate passivation methods.⁸⁰ The work reported in this thesis directs attention towards the possible applications of Cu as electrodes in OPVs as transparent window electrodes, reflective electrodes, top electrodes for top-illuminated OPVs and plasmon active light-catching electrodes.

1.18 References

- (1) Nerem, R. S.; Beckley, B. D.; Fasullo, J. T.; Hamlington, B. D.; Masters, D.; Mitchum, G. T. Climate-Change–Driven Accelerated Sea-Level Rise Detected in the Altimeter Era. *Proc. Natl. Acad. Sci.* **2018**, *115* (9), 2022–2025.
- (2) Carbon Dioxide | Vital Signs – Climate Change: Vital Signs of the Planet <https://climate.nasa.gov/vital-signs/carbon-dioxide/> (accessed Feb 7, 2019).
- (3) J. Ring, M.; Lindner, D.; F. Cross, E.; E. Schlesinger, M. Causes of the Global Warming Observed since the 19th Century. *Atmos. Clim. Sci.* **2012**, *02* (04), 401–415.
- (4) Oreskes, N. The Scientific Consensus on Climate Change. *Science* (80-.). **2004**, *306* (5702), 1686–1686.
- (5) *Renewables 2018 Global Status Report*; 2018.
- (6) *Renewables 2018 Market Report Series*.
- (7) Grevesse, N.; Sauval, A. J. Standard Solar Composition. *Space Sci. Rev.* **1998**, *85* (1/2), 161–174.
- (8) Garg, H. P.; Prakash, J. *Solar Energy : Fundamentals and Applications*; Tata McGraw-Hill, 2000.
- (9) Scharmer, K.; Greif, J. *The European Solar Radiation Atlas: Fundamentals and Maps*; Les Presses de l'École des Mines, 2000.
- (10) ASTM G173-03(2012). Standard Tables for Reference Solar Spectral Irradiances: Direct Normal and Hemispherical on 37° Tilted Surface. *Astm* **2013**, *03*, 1–21.
- (11) Kippelen, B.; Brédas, J.-L.; Bredas, J.-L. Organic Photovoltaics. *Energ Env. Sci* **2009**, *2* (3), 251–261.
- (12) Yoshikawa, K.; Kawasaki, H.; Yoshida, W.; Irie, T.; Konishi, K.; Nakano, K.; Uto, T.; Adachi, D.; Kanematsu, M.; Uzu, H.; et al. Silicon Heterojunction Solar Cell with Interdigitated Back Contacts for a Photoconversion Efficiency over 26%. *Nat. Energy* **2017**, *2* (5).
- (13) Green, M. A.; Hishikawa, Y.; Dunlop, E. D.; Levi, D. H.; Hohl-Ebinger, J.; Ho-Baillie, A. W. Y. Solar Cell Efficiency Tables (Version 51). *Prog. Photovoltaics*

-
- Res. Appl.* **2018**, 26 (7), 427–436.
- (14) Cuevas, A.; Macdonald, D.; Sinton, R. A. *Practical Handbook of Photovoltaics*; Academic Press, 2012.
- (15) Wenham, S. R.; Green, M. A. Silicon Solar Cells. *Prog. Photovolt Res. Appl.* **1996**, 4 (December 1995), 3–33.
- (16) Luo, G.; Ren, X.; Zhang, S.; Wu, H.; Choy, W. C. H.; He, Z.; Cao, Y. Recent Advances in Organic Photovoltaics: Device Structure and Optical Engineering Optimization on the Nanoscale. *Small* **2016**, 12 (12), 1547–1571.
- (17) Sun Sam-Shajing und Dalton, L. R. *Introduction to Organic Electronic and Optoelectronic Materials and Devices*; CRC Press, 2008.
- (18) Letcher, T. M. (Trevor M. .; Fthenakis, V. M. *A Comprehensive Guide to Solar Energy Systems : With Special Focus on Photovoltaic Systems*; 2018.
- (19) Fan, B.; Zhang, D.; Li, M.; Zhong, W.; Zeng, Z.; Ying, L.; Huang, F.; Cao, Y. Achieving over 16% Efficiency for Single-Junction Organic Solar Cells. *Sci. China Chem.* **2019**.
- (20) Meng, L.; Zhang, Y.; Wan, X.; Li, C.; Zhang, X.; Wang, Y.; Ke, X.; Xiao, Z.; Ding, L.; Xia, R.; et al. Organic and Solution-Processed Tandem Solar Cells with 17.3% Efficiency. *Science (80-.)*. **2018**, 361 (6407), 1094–1098.
- (21) Munn, R. W.; Miniewicz, A.; Kuchta, B. *Electrical and Related Properties of Organic Solids*; Springer Netherlands, 1997.
- (22) Friederich, P.; Meded, V.; Poschlad, A.; Neumann, T.; Rodin, V.; Stehr, V.; Symalla, F.; Danilov, D.; Lüdemann, G.; Fink, R. F.; et al. Molecular Origin of the Charge Carrier Mobility in Small Molecule Organic Semiconductors. *Adv. Funct. Mater.* **2016**, 5757–5763.
- (23) Olivier, Y.; Lemaur, V.; Brédas, J. L.; Cornil, J. Charge Hopping in Organic Semiconductors: Influence of Molecular Parameters on Macroscopic Mobilities in Model One-Dimensional Stacks. *J. Phys. Chem. A* **2006**, 110 (19), 6356–6364.
- (24) Abad, E. *Energy Level Alignment and Electron Transport Through Metal/Organic Contacts*; Springer, 2013.
- (25) Pope, M.; Swenberg, C. E. *Electronic Processes in Organic Crystals*; Oxford
-

- University Press, 1982.
- (26) Mohammad Bagher, A. Comparison of Organic Solar Cells and Inorganic Solar Cells. *Int. J. Renew. Sustain. Energy* **2014**, 3 (3), 53.
- (27) Gledhill, S. E.; Scott, B.; Gregg, B. A. Organic and Nano-Structured Composite Photovoltaics: An Overview. *J. Mater. Res.* **2005**, 20 (12), 3167–3179.
- (28) Rwenyagila, E. R. Review Article A Review of Organic Photovoltaic Energy Source and Its. *Int. J. Photoenergy* **2017**, 2017, 1–12.
- (29) Ierides, I.; Zampetti, A.; Cacialli, F. The Resurgence of Organic Photovoltaics. *Curr. Opin. Green Sustain. Chem.* **2019**, 17, 15–20.
- (30) Hoppe, H.; Sariciftci, N. S. Organic Solar Cells: An Overview. *J. Mater. Res.* **2004**, 19 (7), 1924–1945.
- (31) Wöhrle, D.; Meissner, D.; Wöhrle, B. D.; Meissner, D. Organic Solar Cells. *Adv. Mater.* **1991**, 3 (3), 129–138.
- (32) Vivek, K. A.; Agrawal, G. D. *Organic Solar Cells: Principles, Mechanism and Recent Developments*; 2014.
- (33) Kim, H.; Nam, S.; Jeong, J.; Lee, S.; Seo, J.; Han, H.; Kim, Y. Organic Solar Cells Based on Conjugated Polymers: History and Recent Advances. *Korean J. Chem. Eng.* **2014**, 31 (7), 1095–1104.
- (34) Su, Y. W.; Lan, S. C.; Wei, K. H. Organic Photovoltaics. *Mater. Today* **2012**.
- (35) Abdulrazzaq, O. A.; Saini, V.; Bourdo, S.; Dervishi, E.; Biris, A. S. Organic Solar Cells: A Review of Materials, Limitations, and Possibilities for Improvement. *Part. Sci. Technol.* **2013**, 31 (5), 427–442.
- (36) Yu, J.; Zheng, Y.; Huang, J. Towards High Performance Organic Photovoltaic Cells: A Review of Recent Development in Organic Photovoltaics. *Polymers (Basel)*. **2014**, 6 (9), 2473–2509.
- (37) Elumalai, N. K.; Uddin, A. Open Circuit Voltage of Organic Solar Cells: An in-Depth Review. *Energy Environ. Sci.* **2016**, 9 (2), 391–410.
- (38) Scharber, M. C.; Mühlbacher, D.; Koppe, M.; Denk, P.; Waldauf, C.; Heeger, A. J.; Brabec, C. J. Design Rules for Donors in Bulk-Heterojunction Solar Cells—Towards 10 % Energy-Conversion Efficiency. *Adv. Mater.* **2006**.

-
- (39) Brabec, C. J.; Cravino, A.; Meissner, D.; Sariciftci, N. S.; Fromherz, T.; Sanchez, L. Rispens, M. T.; Hummelen, J. C. Origin of the Open Circuit Voltage of Plastic Solar Cells. *Adv. Funct. Mater.* **2005**, *11* (5), 374–380.
- (40) Servaites, J. D.; Yeganeh, S.; Marks, T. J.; Ratner, M. A. Efficiency Enhancement in Organic Photovoltaic Cells: Consequences of Optimizing Series Resistance. *Adv. Funct. Mater.* **2010**, *20* (1), 97–104.
- (41) Kang, J.-W.; Lee, S.-P. S.; Kim, D.-G.; Lee, S.-P. S.; Lee, G.-H.; Kim, J. H. J.-K.; Park, S.-Y.; Kim, J. H. J.-K.; Kim, H.-K.; Jeong, Y.-S. Reduction of Series Resistance in Organic Photovoltaic Using Low Sheet Resistance of ITO Electrode. *Electrochem. Solid-State Lett.* **2009**, *12* (3), H64.
- (42) Dalton, S.-S. S. L. R. *Introduction to Organic Electronic and Optoelectronic Materials and Devices*; 2008.
- (43) Kaltenbrunner, M.; White, M. S.; Głowacki, E. D.; Sekitani, T.; Someya, T.; Sariciftci, N. S.; Bauer, S. Ultrathin and Lightweight Organic Solar Cells with High Flexibility. *Nat. Commun.* **2012**, *3*, 770.
- (44) Bedeloglu, A.; Demir, A.; Bozkurt, Y.; Sariciftci, N. S. A Photovoltaic Fiber Design for Smart Textiles. *Text. Res. J.* **2010**, *80* (11), 1065–1074.
- (45) Zamarayeva, A. M.; Ostfeld, A. E.; Wang, M.; Duey, J. K.; Deckman, I.; Lechene, B. P.; Davies, G.; Steingart, D. A.; Arias, A. C. Flexible and Stretchable Power Sources for Wearable Electronics. *Sci Adv* **2017**, *3* (6), e1602051.
- (46) Liu, Z.; Li, J.; Yan, F. Package-Free Flexible Organic Solar Cells with Graphene Top Electrodes. *Adv. Mater.* **2013**, *25* (31), 4296–4301.
- (47) Pagliaro, M.; Ciriminna, R.; Palmisano, G. Flexible Solar Cells. *ChemSusChem*. 2008.
- (48) Wong, W. S.; Salleo, A. *Flexible Electronics : Materials and Applications*; Springer, 2008.
- (49) Demirel, B.; Yaraş, A.; Elçiçek, H. Crystallization Behavior of PET Materials. *BAÜ Fen Bil. Enst. Derg. Cilt* **2011**, *13* (1), 26–35.
- (50) Properties of Polyesters [https://polymerdatabase.com/polymer classes/Polyester type.html](https://polymerdatabase.com/polymer%20classes/Polyester%20type.html).
-

-
- (51) White, R. T.; Thibau, E. S.; Lu, Z.-H. Interface Structure of MoO₃ on Organic Semiconductors. *Sci. Rep.* **2016**, *6* (February), 21109.
- (52) Kröger, M.; Hamwi, S.; Meyer, J.; Riedl, T.; Kowalsky, W.; Kahn, A. Role of the Deep-Lying Electronic States of MoO₃ in the Enhancement of Hole-Injection in Organic Thin Films. *Appl. Phys. Lett.* **2009**, *95* (12), 10–13.
- (53) Meyer, J. Electronic Structure of Molybdenum-Oxide Films and Associated Charge Injection Mechanisms in Organic Devices. *J. Photonics Energy* **2011**, *1* (1), 011109.
- (54) O'Connor, B.; Haughn, C.; An, K. H.; Pipe, K. P.; Shtein, M. Transparent and Conductive Electrodes Based on Unpatterned, Thin Metal Films. *Appl. Phys. Lett.* **2008**, *93* (22), 1–4.
- (55) Alzoubi, K.; Hamasha, M. M.; Lu, S.; Sammakia, B. Bending Fatigue Study of Sputtered ITO on Flexible Substrate. *J. Disp. Technol. Ieee* **2011**, *7* (11), 593–600.
- (56) Kaltenbrunner, M.; White, M. S.; Głowacki, E. D.; Sekitani, T.; Someya, T.; Sariciftci, N. S.; Bauer, S.; G, E. D.; Sekitani, T.; Someya, T.; et al. Ultrathin and Lightweight Organic Solar Cells with High Flexibility. *Nat. Commun.* **2012**, *3*, 770.
- (57) Cattin, L.; Bernede, J. C.; Morsli, M.; Bernède, J. C.; Morsli, M. Toward Indium-Free Optoelectronic Devices: Dielectric/Metal/Dielectric Alternative Transparent Conductive Electrode in Organic Photovoltaic Cells. *Phys. Status Solidi Appl. Mater. Sci.* **2013**, *210* (6), 1047–1061.
- (58) Takatori, K.; Nishino, T.; Okamoto, T.; Takei, H.; Ishibashi, K.; Micheletto, R. Indium-Free Organic Thin-Film Solar Cells Using a Plasmonic Electrode. *J. Phys. D. Appl. Phys.* **2016**, *49* (18), 185106.
- (59) Qin, F.; Tong, J.; Ge, R.; Luo, B.; Jiang, F.; Liu, T.; Jiang, Y.; Xu, Z.; Mao, L.; Meng, W.; et al. Indium Tin Oxide (ITO)-Free, Top-Illuminated, Flexible Perovskite Solar Cells. *J. Mater. Chem. A* **2016**, *4* (36), 14017–14024.
- (60) Keller, D. A.; Barad, H.-N.; Rosh-Hodesh, E.; Zaban, A.; Cahen, D. Can Fluorine-Doped Tin Oxide, FTO, Be More like Indium-Doped Tin Oxide, ITO? Reducing FTO Surface Roughness by Introducing Additional SnO₂ Coating. *MRS Commun.* **2018**, *8* (03), 1358–1362.
-

-
- (61) Hecht, D. S.; Hu, L.; Irvin, G. Emerging Transparent Electrodes Based on Thin Films of Carbon Nanotubes, Graphene, and Metallic Nanostructures. *Adv. Mater.* **2011**, *23* (13), 1482–1513.
- (62) Naik, G. V.; Shalaev, V. M.; Boltasseva, A. Alternative Plasmonic Materials: Beyond Gold and Silver. *Adv. Mater.* **2013**, *25* (24), 3264–3294.
- (63) Jeong, G.; Jung, S.; Choi, Y.; Lee, J.; Seo, J.; Kim, D. S.; Park, H. A Highly Robust and Stable Graphene-Encapsulated Cu-Grid Hybrid Transparent Electrode Demonstrating Superior Performance in Organic Solar Cells. *J. Mater. Chem. A* **2018**, *6* (48), 24805–24813.
- (64) De Arco, L. G.; Zhang, Y.; Schlenker, C. W.; Ryu, K.; Thompson, M. E.; Zhou, C. Continuous, Highly Flexible, and Transparent Graphene Films by Chemical Vapor Deposition for Organic Photovoltaics. *ACS Nano* **2010**, *4* (5), 2865–2873.
- (65) Aleksandrova, M.; Kurtev, N.; Videkov, V.; Tzanova, S.; Schintke, S. Material Alternative to ITO for Transparent Conductive Electrode in Flexible Display and Photovoltaic Devices. *Microelectron. Eng.* **2015**, *145*, 112–116.
- (66) Lee, J. Y.; Connor, S. T.; Cui, Y.; Peumans, P. Semitransparent Organic Photovoltaic Cells with Laminated Top Electrode. *Nano Lett.* **2010**, *10* (4), 1276–1279.
- (67) Rathmell, A. R.; Bergin, S. M.; Hua, Y. L.; Li, Z. Y.; Wiley, B. J. The Growth Mechanism of Copper Nanowires and Their Properties in Flexible, Transparent Conducting Films. *Adv. Mater.* **2010**, *22* (32), 3558–3563.
- (68) Guo, H.; Lin, N.; Chen, Y.; Wang, Z.; Xie, Q.; Zheng, T.; Gao, N.; Li, S.; Kang, J.; Cai, D.; et al. Copper Nanowires as Fully Transparent Conductive Electrodes. *Sci. Rep.* **2013**, *3*.
- (69) Wang, X.; Wang, R.; Zhai, H.; Shen, X.; Wang, T.; Shi, L.; Yu, R.; Sun, J. Room-Temperature Surface Modification of Cu Nanowires and Their Applications in Transparent Electrodes, SERS-Based Sensors, and Organic Solar Cells. *ACS Appl. Mater. Interfaces* **2016**, *8* (42), 28831–28837.
- (70) Hu, L.; Wu, H.; Cui, Y. Metal Nanogrids, Nanowires, and Nanofibers for Transparent Electrodes. *MRS Bull.* **2011**, *36* (10), 760–765.
- (71) Chen, J.; Zhou, W.; Chen, J.; Fan, Y.; Zhang, Z.; Huang, Z.; Feng, X.; Mi, B.;
-

- Ma, Y.; Huang, W. Solution-Processed Copper Nanowire Flexible Transparent Electrodes with PEDOT:PSS as Binder, Protector and Oxide-Layer Scavenger for Polymer Solar Cells. *Nano Res.* **2015**, *8* (3), 1017–1025.
- (72) Kim, A.; Lee, H.; Kwon, H.-C.; Jung, H. S.; Park, N.-G.; Jeong, S.; Moon, J. Fully Solution-Processed Transparent Electrodes Based on Silver Nanowire Composites for Perovskite Solar Cells. *Nanoscale* **2016**, *8* (12), 6308–6316.
- (73) Han, S.; Lim, S.; Kim, H.; Cho, H.; Yoo, S. Realization of Efficient Semitransparent Organic Photovoltaic Cells with Metallic Top Electrodes: Utilizing the Tunable Absorption Asymmetry. *IEEE J. Sel. Top. Quantum Electron.* **2010**, *16* (6), 1656–1664.
- (74) Ham, J.; Dong, W. J.; Park, J. Y.; Yoo, C. J.; Lee, I.; Lee, J. L. A Challenge beyond Bottom Cells: Top-Illuminated Flexible Organic Solar Cells with Nanostructured Dielectric/Metal/Polymer (DMP) Films. *Adv. Mater.* **2015**, *27* (27), 4027–4033.
- (75) Zhao, G.; Song, M.; Chung, H. S.; Kim, S. M.; Lee, S. G.; Bae, J. S.; Bae, T. S.; Kim, D.; Lee, G. H.; Han, S. Z.; et al. Optical Transmittance Enhancement of Flexible Copper Film Electrodes with a Wetting Layer for Organic Solar Cells. *ACS Appl. Mater. Interfaces* **2017**, *9* (44), 38695–38705.
- (76) Zhao, G.; Wang, W.; Bae, T. S.; Lee, S. G.; Mun, C. W.; Lee, S.; Yu, H.; Lee, G. H.; Song, M.; Yun, J. Stable Ultrathin Partially Oxidized Copper Film Electrode for Highly Efficient Flexible Solar Cells. *Nat. Commun.* **2015**, *6*, 8830.
- (77) Stec, H. M.; Hatton, R. A. Widely Applicable Coinage Metal Window Electrodes on Flexible Polyester Substrates Applied to Organic Photovoltaics. *ACS Appl. Mater. Interfaces* **2012**, *4* (11), 6013–6020.
- (78) Stec, H. M.; Williams, R. J.; Jones, T. S.; Hatton, R. A. Ultrathin Transparent Au Electrodes for Organic Photovoltaics Fabricated Using a Mixed Mono-Molecular Nucleation Layer. *Adv. Funct. Mater.* **2011**, *21* (9), 1709–1716.
- (79) Hutter, O. S.; Stec, H. M.; Hatton, R. A. An Indium-Free Low Work Function Window Electrode for Organic Photovoltaics Which Improves with in-Situ Oxidation. *Adv. Mater.* **2013**, *25* (2), 284–288.
- (80) Bellchambers, P.; Lee, J.; Varagnolo, S.; Amari, H.; Walker, M.; Hatton, R. A. Elucidating the Exceptional Passivation Effect of 0.8 Nm Evaporated Aluminium

- on Transparent Copper Films. *Front. Mater.* **2018**, *5*:71.
- (81) Pereira, H. J.; Hatton, R. A. Copper Substrate Electrode for Efficient Top-Illuminated Organic Photovoltaics. *ACS Appl. Mater. Interfaces* **2018**, acsami.8b18453.
- (82) Haacke, G. New Figure of Merit for Transparent Conductors. *J. Appl. Phys.* **1976**, *47* (9), 4086–4089.
- (83) Haacke, G. Transparent Conducting Coatings. *Annu. Rev. Mater. Sci.* **1977**, *7* (1), 73–94.
- (84) Krutter, H. M. Energy Bands in Copper. *Phys. Rev.* **1935**, *48* (8), 664–671.
- (85) Fukuchi, M. The Energy Band Structure of the Metallic Copper. *Prog. Theor. Phys.* **1956**, *16* (3), 222–230.
- (86) Ehrenreich, H.; Philipp, H. R. Optical Properties of Ag and Cu. *Phys. Rev.* **1962**, *128* (4), 1622–1629.
- (87) Rudberg, E.; Slater, J. C. Theory of Inelastic Scattering of Electrons from Solids. *Phys. Rev.* **1936**, *50* (2), 150–158.
- (88) Burdick, G. A. Energy Band Structure of Copper. *Phys. Rev.* **1963**, *129* (1), 138–150.
- (89) West, P. R.; Ishii, S.; Naik, G. V.; Emani, N. K.; Shalaev, V. M.; Boltasseva, A. Searching for Better Plasmonic Materials. *Laser Photonics Rev.* **2010**, *4* (6), 795–808.
- (90) Tang, Z.; Tress, W.; Inganäs, O. Light Trapping in Thin Film Organic Solar Cells. *Materials Today*. 2014, pp 389–396.
- (91) Morfa, A. J.; Iii, T. H. R.; Johnson, J. C.; Van De Lagemaat, J. Plasmons in Solar Energy Conversion. *Phys. E* **2009**, 3–5.
- (92) Schwind, M.; Kasemo, B.; Zorić, I. Localized and Propagating Plasmons in Metal Films with Nanoholes. *Nano Lett.* **2013**, *13* (4), 1743–1750.
- (93) Atwater, H. A. The Promise of Plasmonics A Technology That Squeezes Electromagnetic Waves into Minuscule Structures May Yield a New Generation of Superfast Computer Chips and Ultrasensitive Molecular Detectors. *Sci. Am.* **2009**, 2007–2010.

-
- (94) Atwater, H. A.; Polman, A. Plasmonics for Improved Photovoltaic Devices. *Nat. Mater.* **2010**, *9* (10), 865–865.
- (95) Stec, H. M.; Hatton, R. A. Plasmon-Active Nano-Aperture Window Electrodes for Organic Photovoltaics. *Adv. Energy Mater.* **2013**, *3* (2), 193–199.
- (96) Reilly, T.; van de Lagemaat, J.; Tenent, R. C.; Morfa, A. J.; Rowlen, K. L. Surface-Plasmon Enhanced Transparent Electrodes in Organic Photovoltaics. *Appl. Phys. Lett.* **2008**, *92* (24), 243304.
- (97) Stelling, C.; Singh, C. R.; Karg, M.; König, T. A. F.; Thelakkat, M.; Retsch, M. Plasmonic Nanomeshes: Their Ambivalent Role as Transparent Electrodes in Organic Solar Cells. *Sci. Rep.* **2017**, *7* (February), 42530.
- (98) Garcia, M. A. Surface Plasmons in Metallic Nanoparticles: Fundamentals and Applications. *J. Phys. D. Appl. Phys.* **2012**, *45* (38), 389501.
- (99) Jang, Y. H.; Jang, Y. J.; Kim, S.; Quan, L. N.; Chung, K.; Kim, D. H. Plasmonic Solar Cells: From Rational Design to Mechanism Overview. *Chem. Rev.* **2016**, *acs.chemrev.6b00302*.
- (100) Uddin, A.; Yang, X. Surface Plasmonic Effects on Organic Solar Cells. *J. Nanosci Nanotechnol* **2014**, *14* (2), 1099–1119.
- (101) Chan, G. H.; Zhao, J.; Hicks, E. M.; Schatz, G. C.; Van Duyne, R. P. Plasmonic Properties of Copper Nanoparticles Fabricated by Nanosphere Lithography. *Nano Lett.* **2007**, *7* (7), 1947–1952.
- (102) Park, T. H.; Mirin, N.; Lassiter, J. B.; Nehl, C. L.; Halas, N. J.; Nordlander, P. Optical Properties of a Nanosized Hole in a Thin Metallic Film. *ACS Nano* **2008**, *2* (1), 25–32.
- (103) Green, M. A.; Pillai, S. Harnessing Plasmonics for Solar Cells. *Nat. Photonics* **2012**, *6* (3), 130–132.
- (104) Ferry, V. E.; Munday, J. N.; Atwater, H. A. Design Considerations for Plasmonic Photovoltaics. *Adv. Mater.* **2010**, *22* (43), 4794–4808.
- (105) Catchpole, K.; Polman, A.; Müller, J.; Rech, B.; Springer, J.; Vanecek, M. *Plasmonic Solar Cells References and Links*; 2008.
- (106) Wu, J. L.; Chen, F. C.; Hsiao, Y. S.; Chien, F. C.; Chen, P.; Kuo, C. H.; Huang,
-

- M. H.; Hsu, C. S. Surface Plasmonic Effects of Metallic Nanoparticles on the Performance of Polymer Bulk Heterojunction Solar Cells. *ACS Nano* **2011**.
- (107) Bates, F. S. Polymer- Polymer Phase Behavior. *Sci. Reports* **1990**, *251* (1986), 898–904.
- (108) Kammer, H. W. Phase Behavior of Polymer Blends. *J. Macromol. Sci. Part A - Chem.* **1990**, *27* (13–14), 1713–1732.
- (109) Robeson, L. M. Fundamentals of Polymer Blends. In *Polymer Blends*; 2007; pp 11–64.
- (110) Huang, C.; Förste, A.; Walheim, S.; Schimmel, T. Polymer Blend Lithography for Metal Films: Large-Area Patterning with over 1 Billion Holes/Inch 2. *Beilstein J. Nanotechnol.* **2015**, *6*, 1205–1211.
- (111) Huang, C.; Moosmann, M.; Jin, J.; Heiler, T.; Walheim, S.; Schimmel, T. Polymer Blend Lithography: A Versatile Method to Fabricate Nanopatterned Self-Assembled Monolayers. *Beilstein J. Nanotechnol.* **2012**, *3* (1), 620–628.
- (112) Nam, V.; Lee, D. Copper Nanowires and Their Applications for Flexible, Transparent Conducting Films: A Review. *Nanomaterials* **2016**.
- (113) Rathmell, A. R.; Wiley, B. J. The Synthesis and Coating of Long, Thin Copper Nanowires to Make Flexible, Transparent Conducting Films on Plastic Substrates. *Adv. Mater.* **2011**, *23* (41), 4798–4803.
- (114) Song, J.; Li, J.; Xu, J.; Zeng, H. Superstable Transparent Conductive Cu@Cu₄Ni Nanowire Elastomer Composites against Oxidation, Bending, Stretching, and Twisting for Flexible and Stretchable Optoelectronics. *Nano Lett.* **2014**.
- (115) Tyler, M. S.; Hutter, O. S.; Walker, D. M.; Hatton, D. R. A. A Silver-Free, Reflective Substrate Electrode for Electron Extraction in Top-Illuminated Organic Photovoltaics. *ChemPhysChem* **2015**, *16* (6), 1203–1209.
- (116) Hutter, O. S.; Hatton, R. A. A Hybrid Copper:Tungsten Suboxide Window Electrode for Organic Photovoltaics. *Adv. Mater.* **2015**, *27* (2), 326–331.
- (117) Søndergaard, R. R.; Espinosa, N.; Jørgensen, M.; Krebs, F. C. Efficient Decommissioning and Recycling of Polymer Solar Cells: Justification for Use of Silver. *Energy Environ. Sci.* **2014**, *7* (3), 1006–1012.

Chapter 2

Experimental Techniques

This chapter gives a detailed overview of the experimental techniques, methods and instruments used for the research work reported in this thesis together with a brief outline of the theory behind each method. Specific details of each method are given in the experimental section of each chapter.

2.1 Substrate Cleaning

All substrates, including ITO coated glass slides (glass substrates with an 8 mm wide ITO strip were purchased from Thin Film Devices Inc. with an ITO stated thickness of 145 nm \pm 10 nm and a sheet resistance of 15 Ω sq⁻¹ \pm 3 Ω sq⁻¹), glass (1.2 mm thick Academy microscope slides) and plastic (PET, Mitsubishi, Hostaphan GN 125 4600A) substrates were cleaned using the following protocol prior to all types of analysis and OPV device fabrication. Glass and plastic substrates were cut to the required size, 13 \times 13 mm for OPV device fabrication, 18 \times 18 mm for electrode characterisation and 26 \times 26 mm for sheet resistance and transparency measurements, before cleaning.

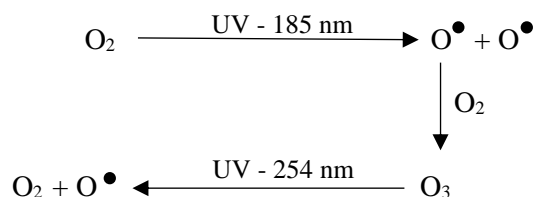
1. Rinsing with de-ionized water followed by ultrasonic agitation in a diluted aqueous solution of surfactant (Hellmanex III) for 20 minutes and then drying in a stream of nitrogen.
2. Ultrasonic agitation in de-ionized water for 20 minutes following by drying under a stream of nitrogen.
3. Ultrasonic agitation in acetone for 20 minutes following by drying under a stream of nitrogen.
4. Ultrasonic agitation in iso-propanol (IPA) for 20 minutes following by drying under a stream of nitrogen.

Ultra-sonic agitation was performed using a Fisherbrand FB11002 ultrasonic bath at 100% power.

2.2 UV Ozone Treatment

UV ozone treatment was performed on substrate surfaces following substrate cleaning, prior to deposition of metals or semiconductors primarily to remove any residual solvents and physisorbed organic material. This treatment also serves to increase the wetting

properties of the surface by increasing the surface energy of the substrate. The setup consists of an UV lamp irradiating at two wavelengths: 185 nm and 254 nm. The shorter UV radiation facilitates the dissociation of molecular oxygen into oxygen free radicals and these reactive oxygen species interact with molecular oxygen yielding ozone.¹ The ozone formed in this manner absorbs UV radiation of 254 nm and breaks down back to an oxygen free radical and molecular oxygen.



Scheme 2.1: Reactions that lead to formation and degradation of ozone when illuminated with a UV lamp that irradiates radiation corresponding to 185 nm and 254 nm

As UV photons are high energy photons (UV A – UV C = 3.1 – 12.4 eV), this energy is sufficient to decompose organic contaminants present on the surface of the sample via several chain scission reactions. The resulting reactive species interact with atomic oxygen radicals (which have a very strong oxidizing capacity) generated by either the formation or decomposition of ozone, resulting in the production of CO₂, H₂O, N₂, O₂ and other short chain organic compounds which can easily be desorbed into the gas phase giving an organic contaminant free substrate surface.



Figure 2.1: The Novascan PSD-UVT UV/O₃ system

UV/O₃ treatment was carried out using a Novascan PSD-UVT (185 nm and 254 nm, 20 mW cm⁻²) UV surface decontamination system. Glass, PET and ITO slides were UV/O₃ treated for 15 minutes with UV illumination followed by a further 5 minutes with the

lamp off during which period the O_3 level gradually decreases. The remaining O_3 was finally extracted using a rotary pump.

2.3 Monolayer Deposition

All glass and plastic substrates were derivatised with a methoxysilane monolayer prior to evaporation of the metal electrodes. This is an important step because the molecular monolayer promotes adhesion between the substrate and the condensing metal, enabling the formation of a compact, smooth and uniform metal film even at a very low metal thickness. The silanes used for this purpose are 3-mercaptopropyltrimethoxysilane (MPTMS) and 3-aminopropyltrimethoxysilane (APTMS) which contain a thiol and primary amine functional group respectively.

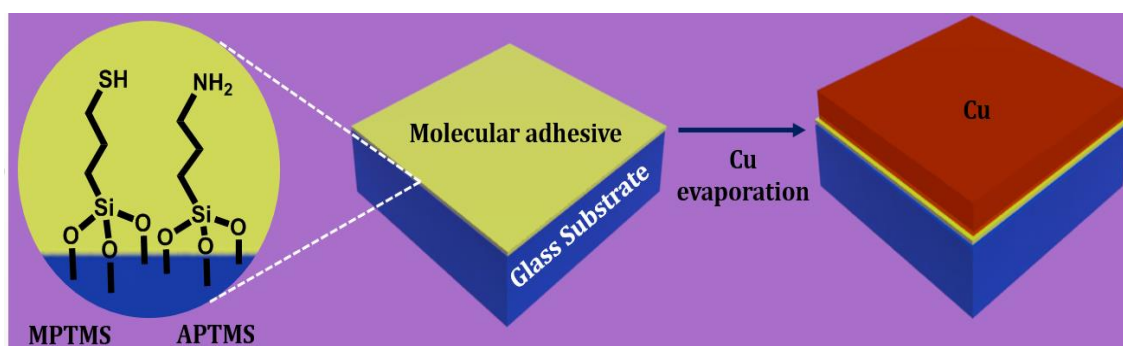


Figure 2.2: Schematic showing the derivatisation of the glass surface with a MPTMS and APTMS monolayer

When substrates undergo a UV/ O_3 treatment the surface will be decorated with hydroxyl moieties making the surface more hydrophilic. Subsequently, when the substrates are exposed to these methoxysilanes, hydrolysis and condensation reactions result in the formation of a strong silane bond with glass. Consequently, the thiol and primary amine ends which become exposed at the surface can form a bond with the deposited metal giving rise to a compact metal film. This method of surface derivatization using a mixed monolayer deposited from the vapor phase was first developed by the Hatton group for Au,² and later extended to other metals such as Cu and Ag.³ It was found that although the bond Cu makes with thiol is much stronger than that with the amine group, APTMS is important as it catalyses the reaction between methoxysilanes and hydroxy moieties at the glass surface forming a dense monolayer within a short period than when MPTMS is used on its own. Stec *et al.* have shown this method to give an APTMS: MPTMS composition of 3.4: 1 and a monolayer thickness of ~ 0.8 nm.² Thus, this monolayer provides a high density of sites for metal nucleation, promoting continuous growth of

smaller crystallites.^{2,3} For this work a mixed monolayer comprising of MPTMS and APTMS (97% Sigma Aldrich) was used for monolayer formation when the metal being deposited was Cu and in the case of Ag, MPTMS was used on its own. Equal parts of the two silanes were transferred to a small uncapped vial, together with freshly UV/O₃ treated substrates into a desiccator and left under reduced pressure (~5 mbar) for at least 4 hours for complete monolayer formation and then transferred to the evaporator for deposition of the metal.

2.4 Thermal Evaporation

Thermal evaporation is a simple physical vapour deposition technique used to evaporate metals and small molecule semiconductors and condense them onto a substrate, enabling the fabrication of thin films typically in the range of a few angstroms to several microns in thickness. The setup consists of a chamber which is maintained under high vacuum so that the mean free path of the material under evaporation, (i.e. the distance the atom or molecule travels before it collides with another particle) is much greater than the distance between the source and the substrate, to facilitate minimum disruption to the evaporating atoms/molecules. Materials to be evaporated in the form of pellets or powders are placed in appropriate boats or crucibles composed of refractive metals such as tungsten or molybdenum and gradually heated to their melting point by passing a current through the boat. As a result of this heating the material melts and then eventually evaporates towards the rotating substrates located in the upper part of the chamber. On reaching the substrates the evaporated material condenses and forms a film. The amount of heat supplied needs to be controlled in order to maintain a particular rate of evaporation so that the material evaporates gradually facilitating the formation of a uniform film.⁴

For the work reported in this thesis, a MBraun bell-jar evaporator co-located in a N₂ filled glove box (MBraun MB 20G LMF) was used. The lifting and lowering of the bell-jar is performed using an electro-pneumatic mechanism. The evaporation unit consists of two organic sources and two metal thermal sources located in the bottom of the chamber and a rotary substrate holder positioned in the upper part of the evaporation unit. The rotary substrate holder and all sources are equipped with shutters. The working pressure of this system is $\leq 1 \times 10^{-6}$ mbar and this high vacuum is achieved using a rotary pump which reduces the pressure to about 1×10^{-2} mbar followed by a turbo pump which further brings down the pressure to $\leq 1 \times 10^{-6}$ mbar. The rate of evaporation and thickness of the deposited material was monitored using a quartz crystal microbalance (QCM) mounted on either side of the rotating substrate. The QCM measures the rate of evaporation by

computing the change in frequency of oscillation induced by condensation of material on the crystal. The change in oscillation frequency of the crystal resulting from its change in mass can be converted to film thickness when physical properties such as density of the material being deposited is known.

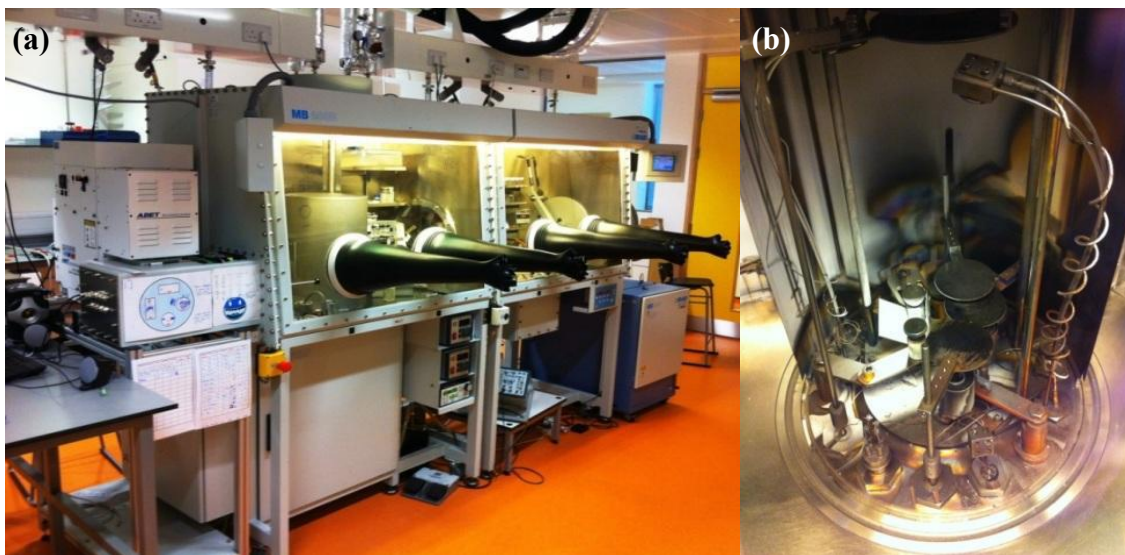


Figure 2.3: (a) The MBraun MB 20G LMF Glovebox with solar simulator (far left) and (b) the interior view of the CreaPhys organic molecular evaporator (right) used in this work.

However, as the QCM is not exactly aligned with the substrate, to ensure that the measurement is correct, the QCM is calibrated by depositing a known thickness of the material and comparing this with the actual value obtained by making a measurement using the AFM. The actual and measured values are then used to calculate a tooling factor which accounts for the QCM position. The material density and tooling factor pertaining to each material are entered into a monitoring unit (Thin film thickness SQM 160) which then displays the rate and thickness of the material being deposited during an evaporation.

$$\text{Tooling Factor} = \frac{\text{Actual thickness of the deposited film}}{\text{Thickness indicated by the QCM}} \times \text{Initial tooling factor}$$

Equation 2.1

2.4.1 Evaporation of metals

Metal films were evaporated onto glass or plastic substrates of the required dimensions, derivatised with a molecular monolayer to facilitate adhesion. Evaporation was done using one of the two thermal sources and the metals (Cu, Ag and Al) in the form of pellets (K J Lesker, 99.99%) were placed in a tungsten dimple boat positioned between two Cu feedthroughs, and gradually heated until the required rate was achieved. Details of rates

and the thickness of each metal deposited are given in the method section of each chapter. Inorganic oxides such as MoO_3 were also evaporated using a thermal source however in this case a boron nitride crucible placed within a heat shielded crucible heater was used, for more uniform heating.

2.4.2 Evaporation of inorganic oxides and organic semiconductors

Organic semiconductors such as ClAlPc, C_{60} and BCP were evaporated using an organic source with boron nitride crucibles. The crucibles were placed inside a resistive heating coil and the heating temperature was set and monitored using a Creaphys controller unit. The typical rates and thicknesses used are given in the method section of each chapter.

For each evaporation, appropriate stainless steel masks/substrate holders were used to deposit material on different substrate sizes depending on the characterisation technique and to control the area exposed to a deposited material on a given substrate size, especially in the case of a solar cell.

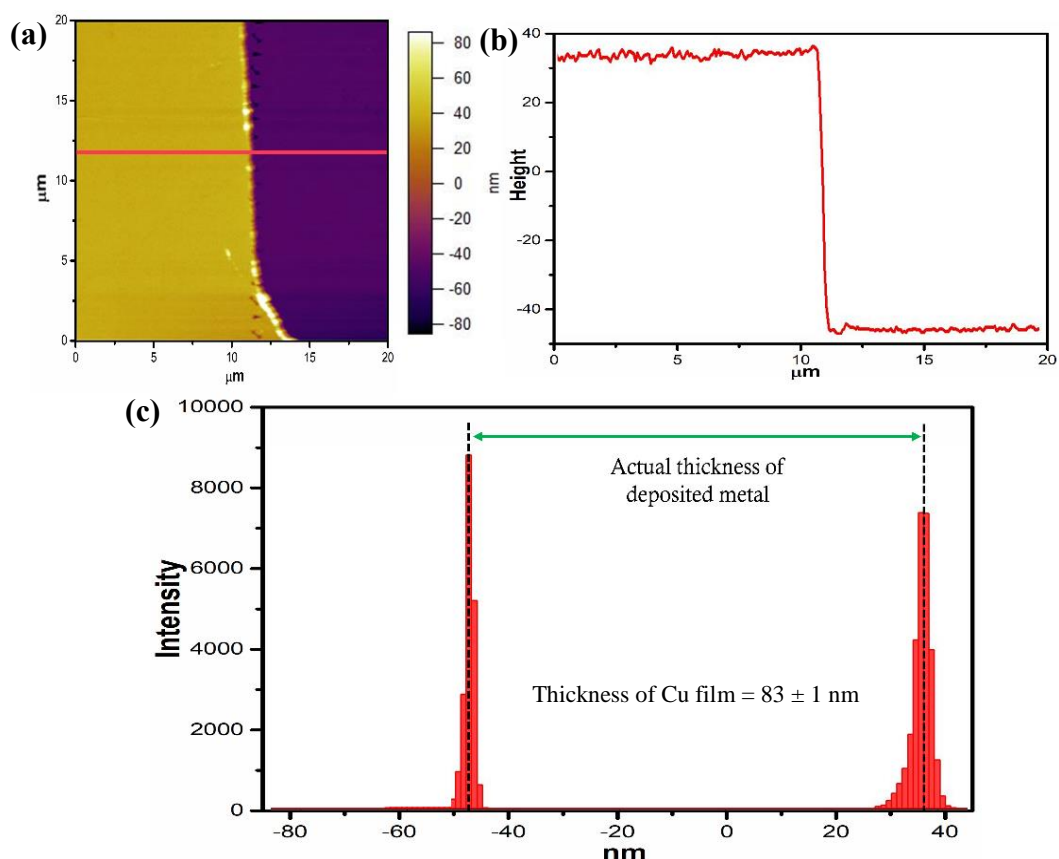


Figure 2.4: (a) AFM image of a scored Cu film deposited on glass; (b) a cross section of the image along the line shown in (a) and (c) histogram showing how the actual thickness is computed.

| Material | General Thickness / nm | Function |
|------------------|------------------------|-----------------------|
| Cu | 11 | Transparent Electrode |
| | 85 | Reflective Electrode |
| Ag | 9 - 11 | Transparent Electrode |
| | 85 | Reflective Electrode |
| Al | 0.8 | ETL/Passivation layer |
| | 100 | Reflective Electrode |
| MoO _x | 5 - 10 | HTL |
| CIAIPc | 20 | Electron Donor |
| BCP | 5 | ETL |
| C ₆₀ | 40 | Electron Acceptor |

Table2.1: General thicknesses and function of evaporated material used in this thesis.

2.5 Spin Coating

This technique is used to deposit thin layers of solution processable materials onto flat substrates with thickness in the range of 5 – 500 nm.⁵ The material dispersed in a suitable solvent medium is deposited onto a substrate and is spread evenly by the centrifugal force of the rotating substrate, thereby forming a uniform thin film. There are two methods of depositing the solution onto the substrate,

1. Static dispensing or drop casting in which the solution is deposited on to a stationary substrate and then spun
2. Dynamic dispensing or spin casting in which the solution is deposited on to a spinning substrate

The sample is held in position using a vacuum chuck and the solution is deposited using one of the above methods. Rotation facilitates even spread of the film as the centrifugal force together with the surface tension of the liquid pulls the solution towards the substrate boundary forming an even covering. Typically variation in thickness across a 3×3 cm sample is ~ ± 5 %. The solvents generally used for spin coating are volatile and therefore spinning at high speeds results in the formation of a dry film. However, in most cases further drying or annealing on a hot-plate may be required to completely remove the solvent or cure the material giving rise to an evenly deposited solid layer of the desired material. The spin speed and concentration of the solution can be used to control the

thickness of the resulting film; higher spin speeds and low concentrations give thinner films.^{5,6}

For the work presented herein, spin coating was performed using a SUSS MicroTec Delta 6RC spin coater for samples spun in the glovebox. For spin coating outside the glovebox a Chemat-Technologies KW-4A spin coater was used.

2.6 Sheet Resistance Measurements

Sheet resistance (R_{sh}) is a measure of the lateral resistance of thin films of uniform thickness, usually composed of conducting or semiconducting materials. In this work the van der Pauw four probe method was used to measure the R_{sh} of metal films. This method was proposed by Leo J. van der Pauw in 1958 and is commonly used to measure the resistivity of irregularly shaped samples.⁷ In order to use this method with minimum errors the following conditions need to be fulfilled;

1. The sample should be solid, flat, homogeneous and uniform in thickness with no isolated holes
2. Contacts need to be placed at the edges of the sample
3. The area of an individual contact should be at least an order of magnitude smaller than the area of the entire sample
4. Sample thickness should be less than the width and length

R_{sh} measurements reported in this thesis were performed using 26×26 mm samples and good contact between the sample and probes were established by depositing a very small amount of conductive silver paint on the four edges. A Keithley 2400 source measurement unit was used to apply a voltage (V) of 5 mV to two contacts on one side whilst the resulting current (I) was measured by placing two leads on the opposite side. Van der Pauw formula states that for an arbitrary shaped sample the R_{sh} can be determined using resistance measurements made along the vertical ($R_{vertical}$) and horizontal ($R_{horizontal}$) edges and accordingly,

$$e^{-\frac{\pi R_{vertical}}{R_{sh}}} + e^{-\frac{\pi R_{horizontal}}{R_{sh}}} = 1 \quad \text{Equation 2.2}$$

However, in this case as the sample is a square,

$$R_{vertical} = R_{horizontal} = R \quad \text{Equation 2.3}$$

Therefore, the van der Pauw equation can be simplified in the following manner;

$$e^{\frac{-\pi R}{R_{sh}}} + e^{\frac{-\pi R}{R_{sh}}} = 1$$

$$R_{sh} = \frac{\pi R}{\ln 2}$$

$$R_{sh} = \frac{\pi}{\ln 2} \left(\frac{V}{I} \right) \quad \text{Equation 2.4}$$

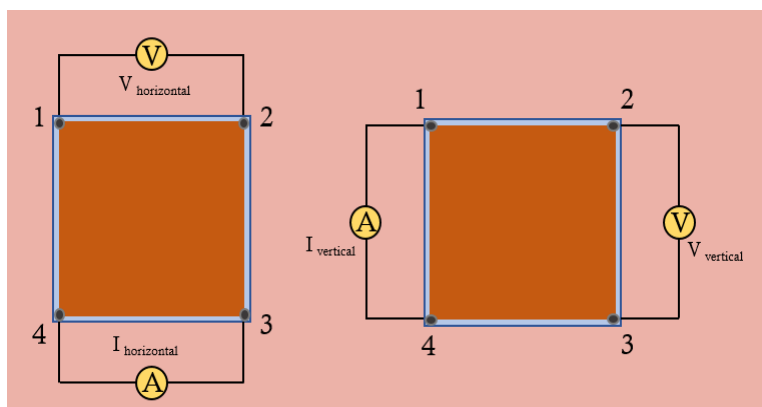


Figure 2.5: Schematic depicting the measurement of sheet resistance using Van der Pauw method

Two measurements were performed on each sample and an average value was input into equation 2.4 to obtain the R_{sh} of a particular sample. For a particular type of electrode / metal film at least 9 such individual samples were measured and the average of all these measurements were quoted as the R_{sh} .

2.7 Atomic Force Microscopy

Atomic Force Microscopy (AFM), which was invented by Binnig, Quate and Gerber in 1985, is a type of scanning probe microscope that is extensively used to obtain quantitative data on different types of surfaces including metals, semiconductors and insulating substances. Unlike scanning tunnelling microscopy, which can only image conducting or semi-conducting substances, the AFM can be used to image almost any type of surface providing information about topology, potential, conductivity and resistance.⁸ The AFM consists of a cantilever with a sharp pyramidal shaped tip made of silicon or silicon nitride. The tip is 3-6 μm tall and has a radius of 15-40 nm. This tip is used to scan over the surface and when the tip approaches the surface, the attractive and repulsive forces between the tip and the sample induce deflection of the cantilever in accordance with Hooke's law. The forces between the tip and the sample are maintained at a low and constant level by a feedback mechanism and the resulting alterations in the

deflection of the cantilever are detected by the positional changes in a laser beam that reflects off the top surface of the cantilever. The changes in deflection manifested by the reflected beam are monitored by a position sensitive photodiode which enables the generation of a topographic map of the surface.⁸⁻¹⁰

The AFM can be used in three main modes¹¹

1. Contact Mode

This is a static mode where the tip contacts the sample and is dragged along the surface of the sample. The deflection of the tip is monitored and maintained at a constant level by applying a voltage to the piezo on which the sample is mounted. This results in lowering or raising of the sample thereby changing the distance between the tip to the sample to maintain the deflection of the cantilever. As the tip contacts the sample there is a higher possibility of damaging both the tip and sample.

2. Non-Contact Mode

The cantilever does not directly contact the sample but is oscillated above the sample surface. The amplitude, phase and frequency of this oscillation is monitored and used to compute the force between the tip and the sample. The inevitable liquid meniscus on top of the surface may interfere with scanning, there by imaging the true surface may prove to be difficult in certain situations.

3. Tapping Mode or Intermittent Contact Mode

This method was used in all the work described here in and provides a technique for obtaining high resolution images of surface topology. The cantilever is vibrated close to or at its resonant frequency using a piezoelectric crystal at a high amplitude, when it is away from the surface and then brought down to the surface where it lightly touches the sample. Therefore, the tip alternately taps the surface and lifts off and this motion affects the amplitude of oscillation. When the tip approaches a bump there is less room for oscillation thus amplitude decreases and when at a depression in the surface, the opposite takes place increasing the amplitude of oscillation. The amplitude of oscillation is kept constant by changing the distance between the tip and the sample by varying the voltage applied to the piezo and this information is used to generate an image of the surface under study.

In this work, tapping mode was used to obtain surface topologies, film thicknesses and roughness of various substrates and deposited materials and was performed using an Asylum Research MFP3D instrument (located within a Faraday cage). The tips used for the analysis were purchased from Olympus (OMCL-AC240TS-R3, resonant frequency 70 kHz and spring constant 2 N m^{-1}). Analysis was done using an Asylum Research AFM software and WxSM software.

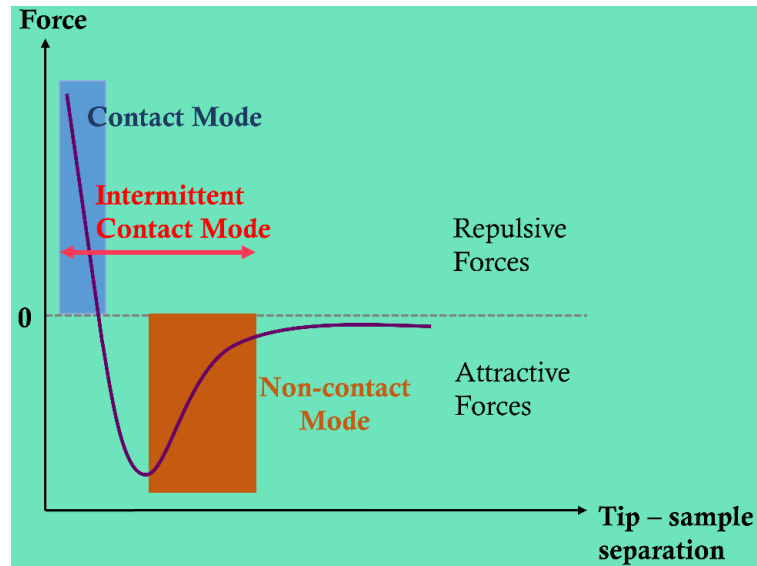


Figure 2.6: Force-distance curve showing the regimes under which different modes are used, adapted from ref. [11].

2.8 Conductive Atomic Force Microscopy

Conductive Atomic Force Microscopy (C-AFM) which was first developed by John O'Shea and co-workers in 1993, enables the scanning of the topography of the sample and the measurement of the electric current at the point of contact simultaneously. This is usually operated in contact mode where the tip is scanned over the substrate surface under a constant voltage and the resulting current measured.¹² In order to perform C-AFM,

- The probe tip needs to be conductive
- A voltage needs to be applied between the sample holder and the tip
- An electric-current amplifier is required to quantify the electric conductivity

The current produced as a result of the applied voltage follows the relationship,

$$I = JA_{eff} \quad \text{Equation 2.5}$$

where I is the total current flowing through the tip and sample holder, J is the current density and A_{eff} is the effective area through which flow of electrons occurs.

C-AFM studies reported in this thesis, were performed using an Asylum Research MFP3D instrument (located within a Faraday cage) under contact mode and the samples were fixed to the sample holder using silver paint. The tips used for C-AFM were diamond coated silicon tips (HQ:NSC14/Hard/Al BS, resonant frequency 160kHz and spring constant 5 N m^{-1}) purchased from Mikromasch. The resulting morphology and current maps were analysed using an Asylum Research AFM software.

2.9 Scanning Electron Microscope

The scanning electron microscope (SEM) is a tool used to study the surface of a sample using a high energy focused electron beam, which interacts with the sample generating various signals which can be used to deduce the nature of the sample. These signals are used to create a 2D image of the surface displaying the topography including all spatial variations. A magnification of 50 – 2,000,000 times and a very high spatial resolution of 1- 20 nm can be achieved using a SEM. The samples must be under vacuum when the analysis is conducted because a high energy electron beam is used. Samples must also be sufficiently conductive to avoid charging enabling the generation a clear image.^{13,14} An electron gun is used to generate an electron beam which passes through a series of lenses so that the beam spot is reduced to a few nanometres. When this high energy beam strikes the sample surface, a number of outputs originate due to electron – sample interactions and can be used to obtain information about the sample. These include,

- Low energy secondary electrons which are used to generate the SEM image
- High energy back scattered electrons which provide information on the chemical composition of the sample which is expressed by a variation in contrast
- Diffracted back scattered electrons which enable the determination of crystal structures and orientations in minerals
- Characteristic X-rays which can be used for elemental analysis

In this work SEM imaging was performed using ZEISS Gemini 500 to study the morphology of planar and nano-aperture Cu electrodes. ZEISS Supra SP55 equipped with a heating stage was used to evaluate the temperature at which aperture formation commences in Cu electrodes supported on plastic substrates.

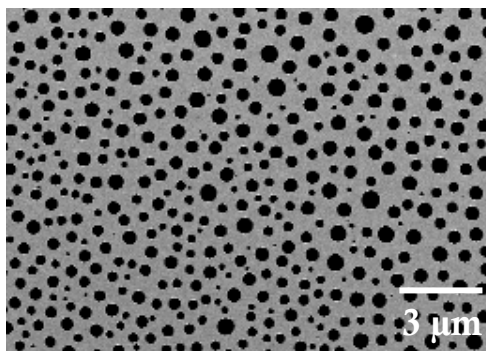


Figure 2.7: SEM image of an 11nm thick Cu film with holes fabricated using polymer blend lithography

2.10 Energy Dispersive X-ray Spectroscopy

Energy Dispersive X-ray Spectroscopy (EDXS) is a useful analytical technique that enables the identification of chemical species present in a sample. This is done by bombarding the sample with high energy electrons and analysing the X-rays emitted by the sample from the resulting interaction with the electron beam. When the beam strikes the surface of the sample, inner electrons will be ejected and outer electrons may move into the vacancies. As outer electrons are of a much high energy, the difference in energy between the two electrons is emitted in the form of X-rays which are characteristic for different elements providing a means of identifying the chemical elements present in the sample. A high energy electron beam is used in SEM and therefore can be used for EDXS provided it is integrated with an appropriate detector to identify the emitted X-rays. As many elements can have overlapping X-ray peaks, care must be taken when using this method to draw conclusions and the accuracy, sensitivity and spatial resolution of EDXS is greatly dependent on the penetration depth of the beam, composition and density of the sample.¹⁵

For this work, EDXS spectra were recorded using an Oxford Instruments Si-Li detector unit on the SEM (ZEISS Gemini 500) instrument, at an accelerating voltage of 17- 25 keV.

2.11 Integrating Sphere

An integrating sphere also known as an Ulbricht sphere is an optical component that can be used to spatially integrate radiant light. It is used for a variety of photometric, radiometric and optical measurements. In this work it was used in conjunction with a UV/Vis/NIR spectrophotometer to measure total (specular and diffuse) and diffuse, transmittance and reflectance of metal films and polymers used as photoactive materials

in OPV devices. The integrating sphere consists of a hollow spherical cavity with its interior surface covered with a uniform diffuse white reflective coating, ports for entry and exit of light and a detector to determine the radiant light. The coating is of prime importance and both reflectivity of the coating as well as its durability in the environment in which is operated need to be considered. The type of coating used depends on the wavelength range of operation and barium sulphate is used for the visible region but can be stretched for use in UV and NIR regions. Diffused gold coatings are used for operation in NIR to mid IR regions.^{16,17}

In quantifying the radiation, the integrating sphere considers the following,

- i. Light introduced into the integrating sphere
- ii. Reflectance of the sphere wall
- iii. Surface area of the sphere
- iv. Multiple surface reflections light undergoes
- v. Losses arising from port openings

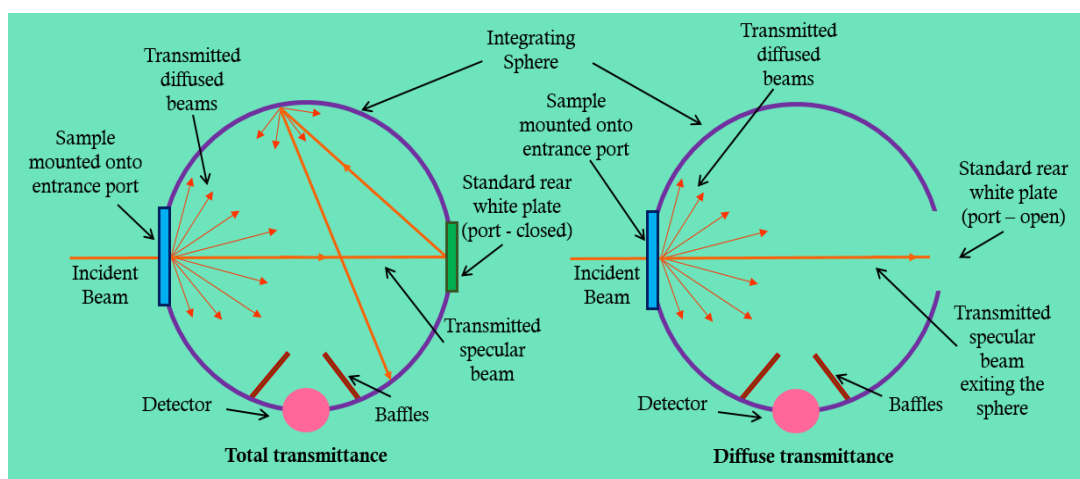


Figure 2.8: Cross sectional view of the integrating sphere showing the setup for total and diffuse transmittance

The light that enters the integrating sphere, will be nearly perfectly diffused by initial reflection. A fraction of this light then arrives on another point on the surface and will again be diffused on striking the interior surface of the sphere. This process will occur multiple times causing the individual beams to reach the same intensity. When the photodetector that is housed inside the sphere is struck by one of these beams it can measure the total flux.

The total flux (L) incident over the entire sphere surface is given by,

$$L = \frac{Y}{\pi A_s} \frac{P}{1 - P(1 - f)} \quad \text{Equation 2.6}$$

Radiance of the Sphere
diffused sphere multiplier

where Y is the light introduced into the sphere, A_s is the area of the sphere, P is the reflectance of the sphere wall and f is fraction of the port area. The second part of the equation which is the sphere multiplier accounts for increase in radiance due to multiple reflections.¹⁷

When measuring the transmittance using the integrating sphere, the sample is mounted on the sample port located in the sphere wall and depending on whether total or diffused transmittance is being measured the port at the rear of the instrument is left closed or open respectively (Figure 2.8).^{16,18}

In the case of reflectance measurements, samples are mounted on the rear port and the specular light port is closed for total reflectance measurements and opened for diffused reflectance measurements. It is also important to note that the integrating sphere is equipped with baffles to prevent direct entry of light from a source port to the detector prior to undergoing reflection by the interior of the sphere wall.^{16,18}

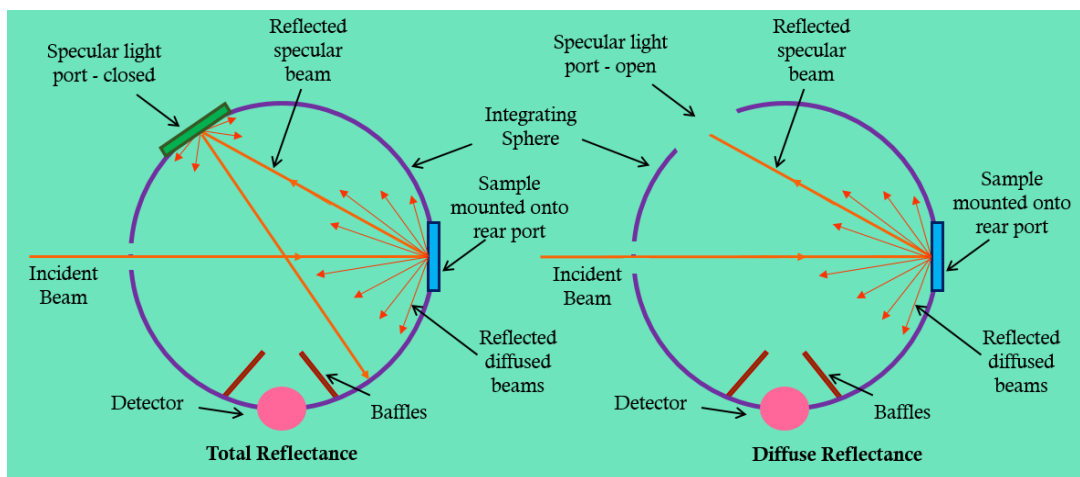


Figure 2.9: Cross sectional view of the integrating sphere showing the setup for total and diffuse reflectance

In this work total and diffuse transmittance and reflectance measurements were conducted using a 150 mm Spectralon Integrating Sphere coupled to PerkinElmer LAMBDA high performance UV/vis spectrophotometer over a wavelength range of 300- 900 nm.

2.12 Kelvin Probe

A Kelvin probe was used in this work to determine the work function (ϕ) of materials used to fabricate OPV devices, but this non-destructive measurement technique is also useful in corrosion studies, surface analysis, catalytic studies and to investigate the band bending and doping in semiconductors. As discussed in the introduction, the ϕ has two components; a bulk chemical potential contribution and surface potential contribution. Although the former is independent of the nature of the surface, the latter is strongly affected by the surface environment, hence Kelvin probe measurements are not just useful in determining the magnitude of the ϕ , but useful for probing the surface properties.

Sir William Thompson, later known as Lord Kelvin observed that Cu and Zn plates mounted on insulating shafts developed a charge when they were electrically connected and moved apart. This setup was then further modified by William Zisman who introduced a vibrating reference surface. In principle, when two materials with different ϕ s are close enough to one another, their vacuum levels will be aligned as shown below in Figure 2.10. When electrical contact is established between these materials, electrons will flow from the material with a lower ϕ to that with a higher ϕ so that the two materials become charged positively and negatively respectively. This generates an electric potential and the electron transfer takes place until this generated electric potential is compensated; in other words, until E_f alignment is attained. In this state, the potential offset between the two materials is known as the contact potential difference (CPD). The CPD when multiplied by the charge on an electron is equal to the difference in ϕ between the two materials.

A Kelvin probe consists of a gold probe which is brought close to the surface of the sample and oscillated. The gold probe is electrically connected to the sample and so this oscillation generates an AC current in the wire connecting them which is monitored using an oscilloscope. A gradual counter potential (V_c) is then applied until the observed AC current approaches zero at which point V_c is equal in magnitude but opposite in polarity to the CPD.¹⁹ The relationship between the CPD and separation of the probe and sample can be understood in terms of the equation for a parallel plate capacitor:

$$C = \frac{Q}{V} = \frac{\epsilon_r \epsilon_0 A}{d} \quad \text{Equation 2.7}$$

$$\therefore V = \frac{Qd}{\epsilon_r \epsilon_0 A} \quad \text{Equation 2.8}$$

where C is the capacitance, Q is the charge, V is the potential/CPD, ϵ_r is the relative permittivity of dielectric between the two material, ϵ_0 is the permittivity of free space, A is the area of overlap and d is the separation between the two materials. As d increases, C decreases and as Q remains constant, V increases, thus oscillation of the probe to and fro generates a current.²⁰

This method only enables the determination of CPD between the probe and the sample. To obtain the ϕ of the sample, it needs to be calibrated against a reference material of known ϕ . Highly oriented pyrolytic graphite (HOPG) is used as the reference material because it is a chemically inert material. HOPG has a ϕ of 4.475 eV. In this work, prior to measuring the ϕ of the sample a calibration was done using a freshly cleaved HOPG sample in order to establish a reference point. The Kelvin probe is housed in a Faraday cage located inside the glove box to minimize stray capacitance. The samples used for Kelvin probe measurements were deposited on glass/plastic and the substrate was ground using a Cu pin and screwed down to the movable sample holder located at the base of the Faraday cage.

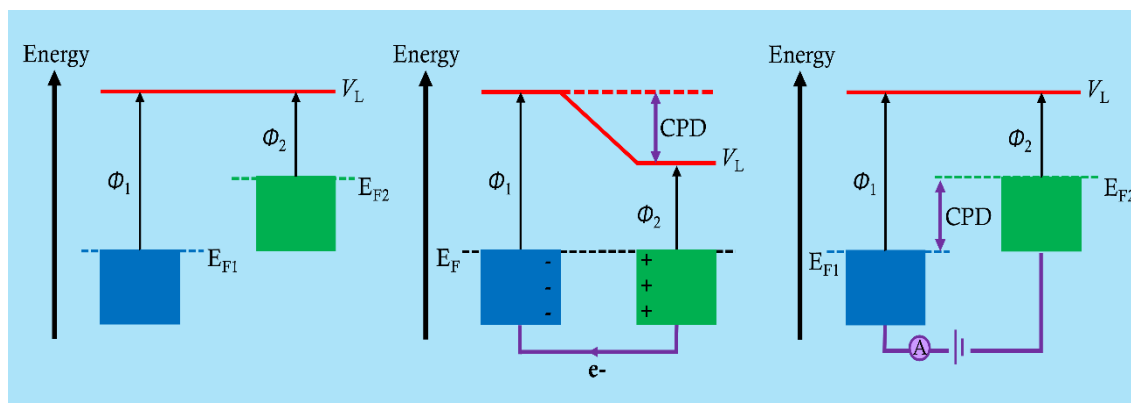


Figure 2.10: Working principle behind Kelvin probe measurements

2.13 Tube Furnace

A tube furnace is widely used in synthesis and purification of materials and is capable of electrically heating materials in a controlled manner. However, for the work reported in this thesis, a tube furnace was used to anneal Cu films on PET substrates in an oxygen free environment to prevent formation of copper oxides.

The setup consists of a long glass tube surrounded by heating coils securely embedded in a thermally insulating material. The Cu films were mounted on a glass slide and placed in the central position of the tube. The tube was securely placed within the heater and

clasped into position and evacuated to a pressure of 10^{-5} mbar using a rotary pump followed by a turbo pump. Once this pressure was reached the heater was switched on and the required final temperature, duration and ramp was set on the furnace controls. On reaching and stabilizing at the set temperature annealing starts automatically and continues until the set duration is completed.

A Carbolite horizontal split-hinge tube furnace (HST 12/300) was used to conduct annealing experiments reported in this thesis.



Figure 2.11: The Carbolite horizontal split-hinge tube furnace (HST 12/300)

2.14 X – Ray Diffraction

X-Ray Diffraction (XRD) is a non-destructive analytical technique used to evaluate the atomic or molecular structure of a crystal. The technique uses Bragg's reflections to determine unit cell dimensions and perform phase identification. Bragg's law states that when a crystal is bombarded with X-rays, the intensity of the scattered beam will be a maximum, when the angle of incidence is equal to the angle of scattering and the path difference between two scattered waves from two different planes in the crystal is an integral multiple of the wavelength of the incident X-rays.

$$n\lambda = 2d\sin\theta \quad \text{Equation 2.9}$$

where d is the spacing between crystal planes, λ is the wavelength of X-rays incident at an angle θ and n is an integer giving the order of diffraction.

The instrument uses a cathode ray tube to generate X-rays. The cathode ray tube consists of a filament which is heated to produce electrons and these electrons are then accelerated towards a target, usually Cu, using a high voltage. When electrons with adequate energy strike the target, inner shell electrons can be dislodged and outer shell electrons move in

to fill the vacancies. As a result of the difference in binding energy associated with the energy levels of the two electrons, the additional energy is emitted in the form of X-rays. For the experimental work reported in this thesis, Cu was used as the target material and following the filtering, monochromatic X-rays of $\text{CuK}_{\alpha 1}$ and $\text{CuK}_{\alpha 2}$ are produced. As these two have very similar λ s a weighted average of the two is used; $\text{CuK}_{\alpha} = 1.5418 \text{ \AA}$. These X-rays are then collimated and directed to the sample. The sample is rotated through an angle θ while the detector which collects the diffracted X-rays rotates at an angle 2θ permitting the detection of the diffracted beam at every orientation of the crystal. When the Bragg condition is satisfied, constructive interference occurs giving rise to a peak. The detector records the angle and the intensity of the diffracted beam and a spectrum of 2θ angle vs counts/intensities is produced.^{21,22} The resulting spectrum can be compared with those available in public databases providing a means of identifying the crystal structure.

XRD measurements reported herein, were carried out using a Siemens D5000 X-ray diffractometer operated in grazing angle. The scans were run for 14 h (for better peak resolution) and the samples were mounted inside a purged graphite dome under a continuous flow of N_2 to avoid formation of copper oxides during prolonged scans. The XRD peaks were assigned using the Mercury software and the CDS National Chemical Database.

2.15 X-ray Photoelectron Spectroscopy

X-ray Photoelectron Spectroscopy (XPS) which is often known as electron *spectroscopy* for chemical analysis (ESCA) is a surface analytical technique used to determine the elemental composition of the sample. Spectra are obtained by irradiating the surface with a beam of soft X-rays (200 – 2000 eV) which results in the ejection of core electrons from the surface of the sample. The kinetic energy of these electrons as well as the number of electrons are detected. Analysis is conducted in ultra-high vacuum as the detectors used in XPS analysis need to be operated under low pressure conditions. The resulting information is used to generate a photo electron spectrum showing the intensity of electrons and the corresponding kinetic energies, which enable the identification of elements present on the surface of the sample as atoms emit electrons at characteristic energies.

XPS is a surface sensitive technique because, whilst X-rays penetrate deeply into the sample, photo-ejected electrons can only escape from a depth of a few nanometres. Consequently, for most materials $\geq 95\%$ of the signal comes from the top 1-10 nm.²³

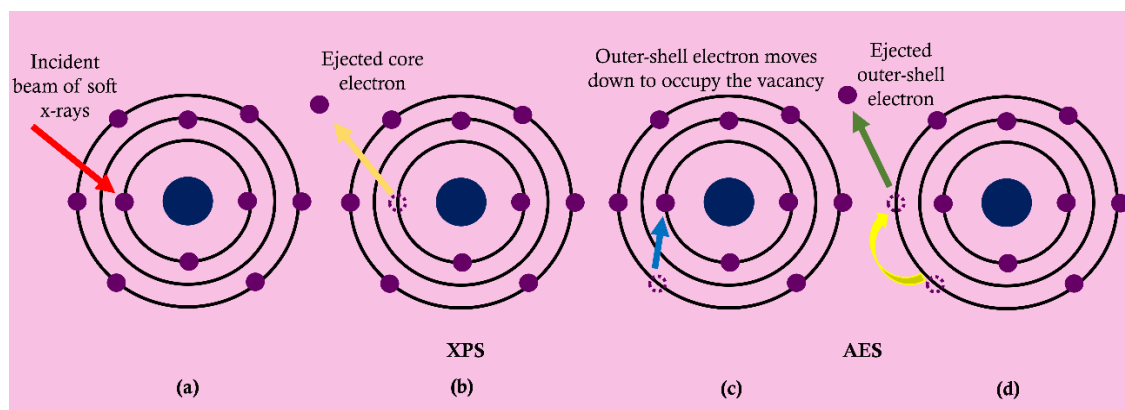


Figure 2.12: A schematic representing the photoelectric effect used in XPS and AES; (a) incident x-ray beams (b) eject an electron generating a vacancy; (c) higher energy outer electrons move to occupy this vacancy resulting in (d) transfer of energy to another bound electron which is then ejected as an Auger electron.

XPS also provides information on the empirical formula, chemical state and electronic state of the elements. As the kinetic energy of ejected electrons depend on photon energy, ϕ and binding energy, this also provides useful details on the chemical environment and the orbital from which the electron was emitted. The former is very useful and can be regarded as the major strength in XPS as shifts in the characteristic binding energy of an electron for a specific element provides information on the bonding environment and formal oxidation state.

Additionally, angle dependent studies can be performed in XPS enabling control over penetration depth providing an opportunity to investigate and compare chemical composition at various thicknesses from the top surface of the sample.^{23,24} The binding energy (B.E) is determined from the known photon energy, the kinetic energy (K.E) of the emitted electrons measured at the detector and the ϕ of the detector (Figure 2.13).

In the work reported in this thesis, XPS was performed on thin Cu electrodes using a Kratos Axis Ultra DLD spectrometer and XPS peak fitting was carried out using the CasaXPS software.

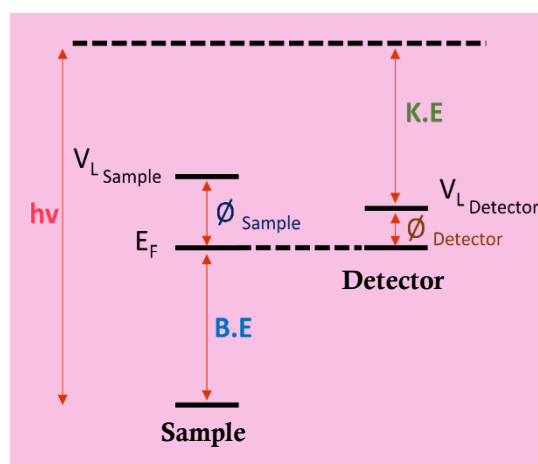


Figure 2.13: An energy level diagram illustrating how the binding energy is calculated using the kinetic energy of electrons reaching the detector

2.16 OPV Fabrication

The OPV devices reported in this thesis have one of the following architectures;

- Conventional architecture
- Inverted architecture
- Top-illuminated devices

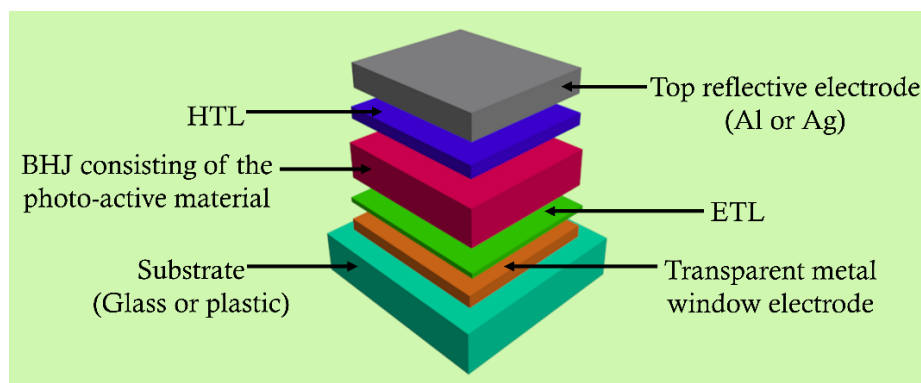


Figure 2.14: Basic architecture of an inverted device

However, as the work presented predominantly use an inverted architecture, the general steps followed in fabricating such an OPV device is outlined below.

- Substrate cleaning with solvents followed by UV/O₃ cleaning
- Molecular monolayer deposition
- Deposition of the transparent metal window electrode
- Deposition of ETLs by evaporation or spin coating followed by annealing if necessary

5. Deposition of the photo-active layer by spin-coating followed by annealing or drying under vacuum for completion of film formation
6. HTL deposition by evaporation or spin coating followed by annealing
7. Deposition of top reflective electrode through a shadow mask forming six individual devices on a given slide each having an area of 6 mm^2

Further details on materials, processing conditions, evaporation rates, thicknesses used for different layers and important information pertaining to individual steps are outlined in the experimental section of each chapter.

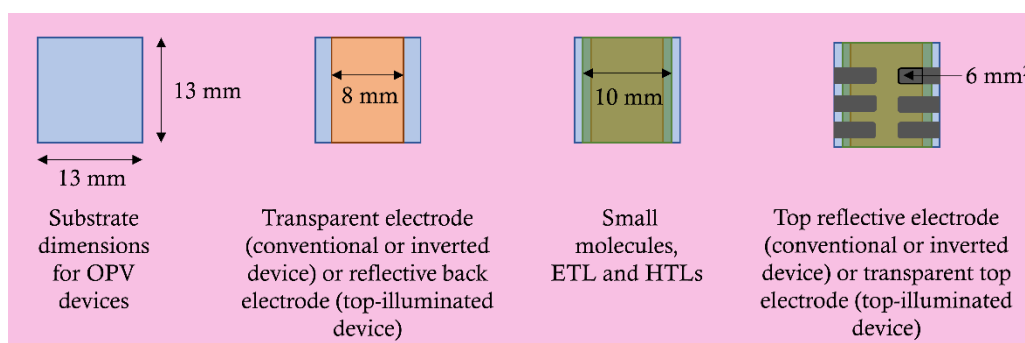


Figure 2.15: Dimensions of various masks used for evaporation of different layers in an OPV device

2.17 OPV Device Testing

The performance of OPV devices was evaluated using JV measurements in the dark and under 1 sun simulated solar illumination. The setup consists of a solar simulator (ABET technologies Sun 2000) housed in a glove box enabling measurements to be performed in a N_2 atmosphere. The solar simulator uses a xenon short arc lamp as the light source together with AM 1.5 filters to provide AM 1.5G solar illumination at 100 mW cm^{-2} (1 sun) which is the standard global spectrum for testing flat plate PV modules.²⁵ Characterization under standard conditions enables comparison of PV devices with different architectures reported by different manufacturers and research laboratories worldwide.

The fabricated OPV device was mounted on a bespoke device holder, with 6 probes for the six separate devices on the slide (Figure 2.15) and one probe to contact with the bottom common electrode. Silver paint was placed on the edges of each electrode to ensure good electrical connection with the probes. To ensure that current density is computed accurately, measurements were performed with masks which accurately defined the device area exposed to light. For device characteristics reported in this thesis,

the device performance was measured using a mask having a pixel area of 0.013 cm². A Keithley 2400 source measurement unit was used to sweep a voltage of -1 V to 1 V across the device in 0.01 increments at a rate of 0.1 Vs⁻¹. A Labview program was used to change the Keithley settings and analyse the output *JV* curve. The J_{sc} , V_{oc} , FF and % PCE values were automatically calculated from the software.

All *JV* measurements were performed in the dark and under illumination and prior to each measurement the light source was calibrated using a silicon diode (PV measurements Inc.) to ensure the lamp intensity was correct. Typically for a particular type of device, a batch consisting of 9 slides were fabricated with each having 6 individual devices. This gives a total of 54 individual devices/pixels per batch.

2.18 Quantum Efficiency

The quantum efficiency of a PV device which is also referred to as the incident photon to converted electron (IPCE) ratio is a measure of how efficiently photons striking a PV device are converted to electrons in the external circuit.²⁶ Quantum efficiency can be reported as,

1. External Quantum Efficiency (EQE)
2. Internal Quantum Efficiency (IQE)

The EQE takes into account all of the light striking the PV device and therefore is dependent on how much light reaches the photo-active layer, the efficiency of exciton dissociation and the efficiency of charge carrier extraction. As the energy of the impinging photon changes with wavelength, EQE is usually measured over a range of wavelengths in which the photo-active material absorbs, typically extending from about 300 nm to 850 nm. The integrated measurement gives the total current (J_{sc}) generated when the device is exposed to solar radiation.

$$EQE(\lambda) = \frac{\text{No. of charge carriers collected}}{\text{No. of photons incident on the device}} = \frac{J_{sc}(\lambda)}{qN(\lambda)} \quad \text{Equation 2.10}$$

$$J_{sc} = \frac{q\lambda}{hc} \int_{300}^{850} P_{AM1.5G}(\lambda) EQE(\lambda) \cdot d(\lambda) \quad \text{Equation 2.11}$$

where $N(\lambda)$ is the incident photon flux density at given wavelength, q is the electronic charge, h is Planck's constant, c is the speed of light and $P_{AM1.5G}$ is the solar spectral light intensity.

EQE should ideally be 1 across all wavelengths, however due to losses arising from insufficient material thickness for complete light absorption, reflection at the glass surface and recombination, it is not possible to generate an electron for every incident photon and therefore EQE is always less than unity.

The IQE is the efficiency with which photons that are absorbed by the photo-active material are converted to electrons in the external circuit. Therefore, IQE is always larger than EQE for a particular device.

$$IQI = \frac{\text{No. of charge carriers collected}}{\text{No. of photons absorbed by the device}}$$

$$\therefore IQI = \frac{EQE}{(1 - \text{Reflection})} \quad \text{Equation 2.12}$$

For this work, only EQE measurements were performed using a white light xenon arc lamp as the light source (Sciencetech SF150) which was directed to a monochromator to separate the light into different λ s. A series of optics including, focusing and splitting lenses were used to separate the monochromatic light beam into two parts out of which one was directed to a stationary rear photo-diode and the other to a front photo-diode²⁷ (818UV, Newport). The front photo-diode is used for calibration of the light beam prior to probing the sample. When obtaining the EQE the front diode is replaced with the device under study. The monochromatic light beam is chopped at 180 Hz to enable a lock-in-amplifier (Stanford Research Systems SR 830) to remove any background light and enhance the signal. The current generated in the device was measured as a function of λ , using a current-voltage amplifier (Femto DHPCA-100) and the resulting EQE was recorded and analysed using a custom Labview interface.

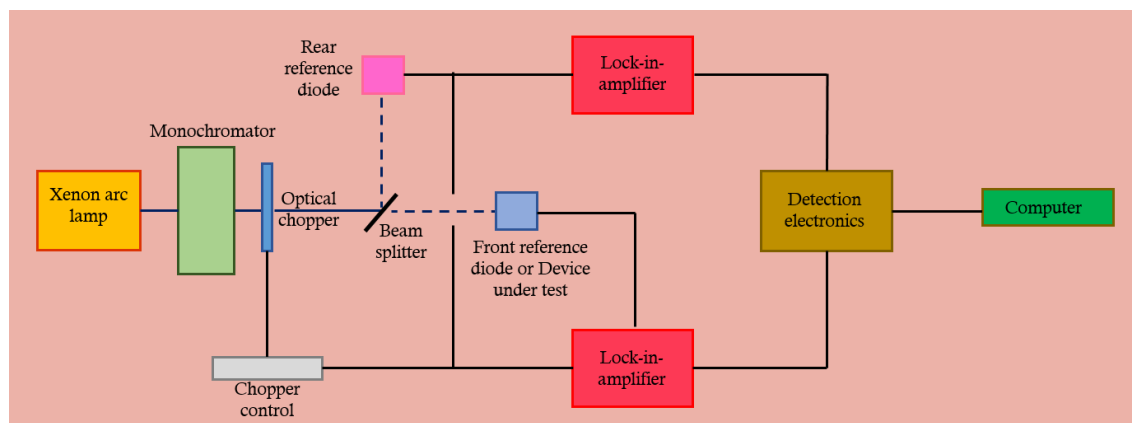


Figure 2.16: Block diagram of the setup of an EQE showing the key components

2.19 Optical Simulations

2.19.1 Essential MacLeod (Version 9.7)

Simulations of transmittance, reflectance, absorbance and electric field distribution within a device were performed using the program Essential MacLeod V9.7 by Thin Film Center Inc. The software requires refractive indices (n) and extinction coefficients (k) of materials to model the above properties. The values of common materials such as Ag, Cu and Au were already in-built into the software but for specialist materials such as HTLs, ETLs and BHJ polymer materials, the n and k values over the required λ range were obtained from literature. This simulation software assumes the films to be slab-like and homogenous.²⁸

2.19.2 COMSOL Multiphysics 5.2a

This finite-element modelling software was used to perform simulations for Cu films with irregularly shaped apertures (chapter 6) and to evaluate the electric field distribution in the vicinity of apertures. COMSOL Multiphysics 5.2a uses Maxwell's equations to perform the simulations and has a series of different modules. For the work reported in this thesis the RF module designed for EM wave simulations was used. A representative 3 dimensional model of the electrode/device is first setup and subsequently the model parameters, constants (such as n and k values) for each material, physics configurations, boundary conditions, ports and meshing are defined to perform the simulation.²⁹

2.20 References

- (1) Vig, J. R.; Bus, J. W. L. UV/Ozone Cleaning of Surfaces. *IEEE Trans. Parts, Hybrids, Packag.* **1976**, *12* (4), 365–370.
- (2) Stec, H. M.; Williams, R. J.; Jones, T. S.; Hatton, R. A. Ultrathin Transparent Au Electrodes for Organic Photovoltaics Fabricated Using a Mixed Mono-Molecular Nucleation Layer. *Adv. Funct. Mater.* **2011**, *21* (9), 1709–1716.
- (3) Stec, H. M.; Hatton, R. A. Widely Applicable Coinage Metal Window Electrodes on Flexible Polyester Substrates Applied to Organic Photovoltaics. *ACS Appl. Mater. Interfaces* **2012**, *4* (11), 6013–6020.
- (4) M. Mattox, D. *The Foundation of Vacuum Coating Technology*; Noyes Publications, 2003.
- (5) Taylor, J. F. Spin Coating: An Overview. *Met. Finish.* **2001**, *99* (1), 16–21.
- (6) Sahu, N.; Parija, B.; Panigrahi, S. Fundamental Understanding and Modeling of Spin Coating Process: A Review. *Indian J. Phys.* **2009**, *83* (4), 493–502.
- (7) Lim, S. H. N.; McKenzie, D. R.; Bilek, M. M. M. Van Der Pauw Method for Measuring Resistivity of a Plane Sample with Distant Boundaries. *Rev. Sci. Instrum.* **2009**, *80* (7).
- (8) Binnig, G.; Quate, C. F.; Gerber, C. C. N.-P. Atomic Force Microscope. *Phys. Rev. Lett.* **1986**, *56* (9), 930–933.
- (9) Amer, N. M.; Meyer, G. *Atomic Force Microscopy*. 1992.
- (10) Rugar, D.; Hansma, P. Atomic Force Microscopy. *Phys. Today* **1990**, *43*, 23–30.
- (11) Giessibl, F. J. Advances in Atomic Force Microscopy. *Rev. Mod. Phys.* **2003**, *75* (3), 949–983.
- (12) Ionescu-Zanetti, C.; Mechler, A. Applications of Conductive Atomic Force Microscopy. *Eur. Microsc. Anal.* **2005**, *19* (1), 9–11.
- (13) Goldstein, J. *Scanning Electron Microscopy and Microanalysis*; 2003.
- (14) Reimer, L. *Scanning Electron Microscopy : Physics of Image Formation and Microanalysis*; Springer, 1998.
- (15) Russ, J. C. *Fundamentals of Energy Dispersive X-Ray Analysis: Butterworths Monographs in Materials*; Elsevier Science, 2013.

-
- (16) Taylor, J. L. Integrating Sphere Functionality : The Scatter Transmission Measurement. **2013**, 1–6.
 - (17) Rosa, E. B.; Taylor, A. H. Theory, Construction, and Use of the Photometric Integrating Sphere. *J. Franklin Inst.* **1923**, *195* (1), 107–109.
 - (18) Hanssen, L. Integrating-Sphere System and Method for Absolute Measurement of Transmittance, Reflectance, and Absorptance of Specular Samples. *Appl. Opt.* **2001**, *40* (19), 3196–3204.
 - (19) Nonnenmacher, M.; O’Boyle, M. P.; Wickramasinghe, H. K. Kelvin Probe Force Microscopy. *Appl. Phys. Lett.* **1991**, *58* (25), 2921–2923.
 - (20) Melitz, W.; Shen, J.; Kummel, A. C.; Lee, S. Kelvin Probe Force Microscopy and Its Application. *Surf. Sci. Rep.* **2011**, *66* (1), 1–27.
 - (21) Cullity, B. D. (Bernard D. *Elements of X-Ray Diffraction*; Addison-Wesley Publishing Company, Inc, 1978.
 - (22) Klug, H. P. (Harold P.; Alexander, L. E. (Leroy E. *X-Ray Diffraction Procedures for Polycrystalline and Amorphous Materials*.
 - (23) Briggs, D. (David); Grant, J. T.; SurfaceSpectra Limited. *Surface Analysis by Auger and X-Ray Photoelectron Spectroscopy*; IM Publications, 2003.
 - (24) Van Grieken, R. E.; Markowicz, a a. *Handbook of X-Ray Spectrometry*; 2002; Vol. 64.
 - (25) ASTM G173-03(2012). Standard Tables for Reference Solar Spectral Irradiances: Direct Normal and Hemispherical on 37° Tilted Surface. *Astm* **2013**, *03*, 1–21.
 - (26) Cuevas, A.; Macdonald, D.; Sinton, R. A. *Practical Handbook of Photovoltaics*; Academic Press, 2012.
 - (27) Brenner, T. J. K.; Vaynzof, Y.; Li, Z.; Kabra, D.; Friend, R. H.; McNeill, C. R. White-Light Bias External Quantum Efficiency Measurements of Standard and Inverted P3HT:PCBM Photovoltaic Cells. *J. Phys. D. Appl. Phys.* **2012**, *45* (41).
 - (28) Essential, T.; Version, M. Macleod Medium. **2015**, *23* (2), 1–8.
 - (29) COMSOL. Introduction to COMSOL Multiphysics. **2015**, 184.

Chapter 3

Fabrication of Copper Window Electrodes with $\sim 10^8$ Apertures cm^{-2}

The work presented in this chapter has been published in:

H. J. Pereira, J. Reed, J. Lee, S. Varagnolo, G. D. R. Dabera, R. A. Hatton, Fabrication of Copper Window Electrodes with $\sim 10^8$ Apertures cm^{-2} for Organic Photovoltaics, *Advanced Functional Materials*, 2018, 28,1802893.

3.1 Background

As discussed in the introductory chapter, transparent conductive oxides (TCO) form an integral part of many optoelectronic devices including PVs, organic light emitting diodes (OLEDs), liquid-crystal displays and touchscreens. To date ITO is the predominantly used TCO, however due to its high material cost, brittle nature and the limited resource of indium which is a rare earth metal, there is a constant search for viable alternatives. As a result, optically thin metal films with a thickness of < 10 nm are attracting growing attention as window electrodes for a variety of emerging applications¹⁻³ including thin film PVs⁴⁻⁶ and displays,^{7,8} because they are compatible with flexible substrates⁹⁻¹⁵ and can be deposited using simple vacuum evaporation. Roll-to-roll vacuum evaporation is attractive as a method for metal electrode deposition for organic optoelectronics^{3,11} because it is a proven industrial process for the manufacture of low cost food packaging and insulation foils based on very thin metal films, offering excellent control over metal thickness and uniformity. To date, Ag has been the metal of choice for window electrode applications^{9,16} because it offers the highest electrical conductivity and lowest optical losses¹⁷ over the visible and NIR spectrum. To maximise transparency the thin Ag film is typically sandwiched between two wide bandgap inorganic oxides or organic semiconductor layers to form a triple layer electrode architecture.¹⁸⁻²⁰ However, Cu is much more abundant and cheaper and therefore the most attractive from all the coinage metals for low-cost applications. Hence, for price-sensitive applications such as OPVs Cu is an attractive alternative to Ag because it offers comparable electrical conductivity¹⁷ at one hundredth of the cost.^{21,22} At the time this work was reported there were three reports of high performance OPVs, using a Cu based window electrode that exhibits performance close to that achieved using an ITO electrode: Hutter *et al.*²³ used an 8 nm

thick thermally evaporated Cu film and a WO_3 over layer which serves both as an anti-reflecting layer and HTL. Zhao *et al.*^{24,25} have demonstrated a high performance window electrode based on a partially oxidised Cu film sandwiched between ZnO layers, which proved to be remarkably stable towards air oxidation. However, in the latter case both the metal and oxide metal layers were deposited by the process of sputtering,^{24,25} the slowness and complexity of which partially offsets the benefit of using a low-cost metal. A different approach for the passivation of optically thin Cu film electrodes, that is compatible with vacuum evaporation, is the use of a sub-1 nm Al over layer which also serves to reduce the electrode ϕ so that it can be used as the electron-extracting electrode in OPVs.^{26,27}

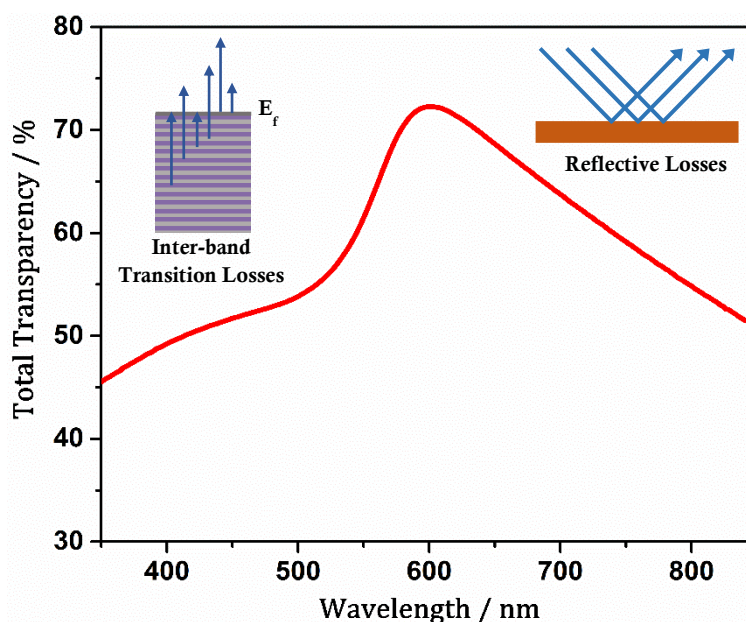


Figure 3.1: Total transparency spectrum of an 11 nm thick Cu film on glass showing the reflective losses at $\lambda > 550$ nm and inter-band transition losses at $\lambda < 550$ nm

For window electrode applications the primary disadvantage of Cu as compared to Ag is its lower far-field transparency for wavelengths below ~ 550 nm, which stems from inter-band absorptions^{28,29} that do not occur in Ag. For wavelengths above ~ 550 nm the transparency is reduced due to reflection (Figure 3.1) similar to the case of Ag. Ebner *et al.*³⁰ and Zhao *et al.*²⁵ have shown that absorption losses in optically thin Cu films can be reduced to an acceptable level by reducing the thickness of the Cu film, with a thickness of 6.5 nm proving to be most effective. Whilst losses due to reflection can be suppressed using a wide bandgap semi-conducting layer of specific thickness, there is a compromise to be struck between the optimal thickness to suppress reflection and the thickness needed for optimal electronic functionality.

In this chapter, a different approach to simultaneously reducing inter-band absorption losses in optically thin Cu films for wavelengths below ~ 550 nm and dramatically suppressing reflection for wavelengths above ~ 550 nm is demonstrated, which is based on incorporating into the metal film ~ 100 million circular apertures per cm^2 with a mean diameter of ~ 500 nm. The size of the apertures is selected to be large enough to ensure that short wavelength light can pass through unhindered, whilst being small enough to ensure that, in the context of an OPV, photo-generated free charge carriers formed in the light harvesting semiconductor adjacent to apertures in the metal electrode can still be extracted by the electrode without the need for a highly conducting charge extracting layer such as heavily doped PEDOT:PSS to span the gaps in the electrode, as is the case for metal nanowire and metal grid electrodes.^{31,32} This approach to metal window electrode design is applicable to thicker metal films than the optimal thickness of 6.5 nm reported previously,²⁵ which is likely to prove more practical to deposit over large areas. Conventional lithographic techniques for fabricating arrays of apertures of this size over large areas are prohibitively costly. One potentially low-cost approach is to use micron-sized polymer nanoparticles as a shadow mask, deposited directly from a colloidal solution, which has been widely used^{31,33–35}, or formed by polymer blend lithography^{36,37} followed by mask and metal lift-off. The work of Huang *et al.*^[35] demonstrates the use of polymer blend lithography as a mask to pattern metal films. Inspired by the latter, the electrode fabrication process reported herein is based on a simplified method of forming a dense array of apertures in metal films based on polymer blend lithography that has the advantage that it does not require a metal lift-off step. It is shown that these electrodes can be easily combined with a widely used, solution processed, electron transport semiconductor that also serves as an anti-reflecting layer, to realise window electrodes suitable for use in OPVs. The advantage of this approach to Cu window electrode fabrication is the technological simplicity that results from the use of metal deposition by simple vacuum evaporation combined with a mask that self-organises from a single solution, instead of having to synthesise the mask prior to deposition onto the substrate to be etched, as is the case for conventional microsphere lithography. Also, all the solution-based steps use widely available low-cost chemicals, based on earth-abundant elements, and there is no requirement to control humidity or need for post-deposition annealing of the polymer blend. When this electrode is used in conjunction with the solution processed wide bandgap *n*-type semiconductor ZnO, which is very widely used as an ETL in OPVs, a dramatic ~ 66 % reduction in electrode R_{sh} occurs due to low

temperature diffusion of Cu into the adjacent ZnO layer, which greatly increases its performance as a transparent electrode for OPVs.

3.2 Experimental Methods

Experimental details specific to the work presented in this chapter are as follows;

3.2.1 Substrate cleaning

Glass substrates of the required dimension and ITO coated glass substrates were cleaned as described in section 2.1 and 2.2.

3.2.2 Mixed monolayer deposition

For glass substrates, a mixed monolayer was deposited prior to evaporation of Cu by exposing the substrates to vapours of MPTMS and APTMS at 50 mbar for 4 hours immediately after UV/O₃ treatment.

3.2.3 Deposition of Cu

Cu was deposited by thermal evaporation of Cu pellets placed in a tungsten boat at a rate of 2.2 – 2.5 Å s⁻¹ to give the required thickness.

3.2.4 Fabrication of apertures using polymer blend lithography

A polymer blend consisting of PS (M_w = 280 000) and PMMA (M_w = 50 000) in the weight ratio of 3:7 having a concentration of 15 mg ml⁻¹ was prepared in 2-butanone (Methyl ethyl ketone (MEK)). The blend was deposited on Cu by spin coating at 2500 rpm for 60 seconds. The PS entities were selectively removed by rinsing the films in cyclohexane followed by UV/O₃ treatment for 15 minutes. A dilute solution of ammonium persulphate (0.002 mol dm⁻³) was used to etch Cu through the PMMA mask to fabricate holes by immersing the substrates in the etchant for 15 - 20 seconds followed by washing with deionized water and drying with a stream of N₂. The PMMA template was finally removed by ultrasonic agitation in toluene and then in glacial acetic acid. (For the selective removal of the 62 nm thick ZnO layer from a ZnO (62 nm) / Cu (11 nm) film, the sample was etched with glacial acetic acid for ~1 min.)

3.2.5 Morphology and distribution of apertures

AFM imaging was performed using an Asylum Research MFP – 3D operated in tapping mode to study the morphology of the Cu films. The size distribution of apertures was evaluated using WXS software. C-AFM was performed on nano-aperture Cu films with ZnO using the same instrument in contact mode by applying a constant voltage between the tip and the sample holder and the resulting morphology and current maps were

analyzed using the Asylum Research AFM software. SEM imaging was performed using ZEISS Gemini 500 with an accelerating voltage of typically 0.3-0.6 kV to evaluate the distribution and coverage of apertures. EDXS spectra were recorded using an Oxford Instruments Si-Li detector unit on the SEM instrument, at an accelerating voltage of 17 keV.

3.2.6 Optical transparency and reflectance measurements

Far-field transmittance and reflectance of metal films on glass were measured over the wavelength range of 350 – 850 nm using a 150 mm Spectralon® Integrating Sphere coupled to a PerkinElmer® LAMBDA™ high performance UV/Vis spectrometer. Measurements were performed with reference to the substrate.

3.2.7 X-ray Diffraction Measurements

XRD measurements were carried out using a Siemens D5000 X-ray diffractometer operated in grazing angle using Cu ($K\alpha$) radiation with a wavelength of 1.542 Å. The scans were run for 14 h (for better peak resolution) and the samples (on glass) were mounted inside a purged graphite dome under a continuous flow of N_2 to avoid formation of Cu oxides during prolonged scans. The XRD peaks were assigned using the Mercury software and the CDS National Chemical Database.

3.2.8 X-ray Photoelectron Spectroscopy measurements

XPS measurements were performed using a Kratos Axis Ultra DLD spectrometer. The samples were illuminated using X-rays from a monochromated Al $K\alpha$ source ($h\nu=1486.6$ eV) and detected at a take-off angle of 90° . The resolution, binding energy referencing, and transmission function of the analyser were determined using a clean polycrystalline Ag foil. XPS peak fitting was carried out using the CasaXPS software. The peaks were corrected with respect to C 1s at 284.7 eV due to the use of neutraliser to avoid charging.

3.2.9 Fabrication of OPV devices

A ZnO ink (5.6% w/v) in IPA was purchased from Infinity PV and a diluted solution (0.5 – 1.4 % w/v) was spun at 1000 rpm for 60 seconds followed by annealing at 180°C for 15 minutes to fabricate the ETL. The enhanced device performance obtained by incorporating an ultra-thin layer of poly(ethyleneimine) (PEI) has already been reported.^{38,39} Therefore, a thin layer of PEI was spun on top of ZnO as a capping layer³⁸, following the annealing process to maximize device performance. PCE10 and PC₇₀BM were mixed in 2:3 mass ratio to make a 35 mg ml^{-1} solution in chlorobenzene (97%) and 1,8-diiodooctane (3%) and deposited by spin coating from a static start at 3000 rpm for

120 seconds to form the photo-active layer. These slides were left inside the evaporator overnight and MoO₃ (10 nm at 0.1- 0.2 Å s⁻¹) was deposited as the HTL followed by Ag (80 nm at 1.0-1.2 Å s⁻¹) as the reflective top electrode. Notably, whilst the molybdenum oxide layer is deposited from a powder of MoO₃, it is known that during vacuum evaporation, partial reduction to MoO_{3- α} occurs, where α is < 0.3 (therefore labelled as MoO _{x}). Ag was deposited through a shadow mask to give an electrode area of 0.06 cm².

3.2.10 Characterization of OPV devices

Current density-voltage (*JV*) testing was performed as described in section 2.17 and the OPV devices were measured through a mask having a pixel area of 0.013 cm². EQE measurements were done as described in section 2.18 in the wavelength range of 300 – 850 nm.

3.3 Results and Discussion

Figure 3.2 depicts the process of electrode fabrication developed in this study. Cu films were thermally evaporated onto glass substrates modified with a mixed molecular monolayer of MPTMS and APTMS. It has been previously shown that this class of adhesion layer can be applied to both glass and plastic substrates to realise robust Cu films without contributing to light absorption.^{31,40} A blend of the immiscible polymers, PS and PMMA in 2-butanone was spin cast directly onto the Cu film (Figure 3.2, step 1), where upon spontaneous phase separation into well-defined isolated spherical PS domains in a PMMA matrix occurs. Crucially the PS domains protrude from the PMMA surface and extend through most, or all, of the film thickness.

Whilst spontaneous phase separation of PS/PMMA is well known, achieving the desired PS domain size distribution and density on Cu using previously reported protocols proved very difficult and hundreds of hours of effort went into development of a blend composition and reproducible method that was well suited for this particular study.

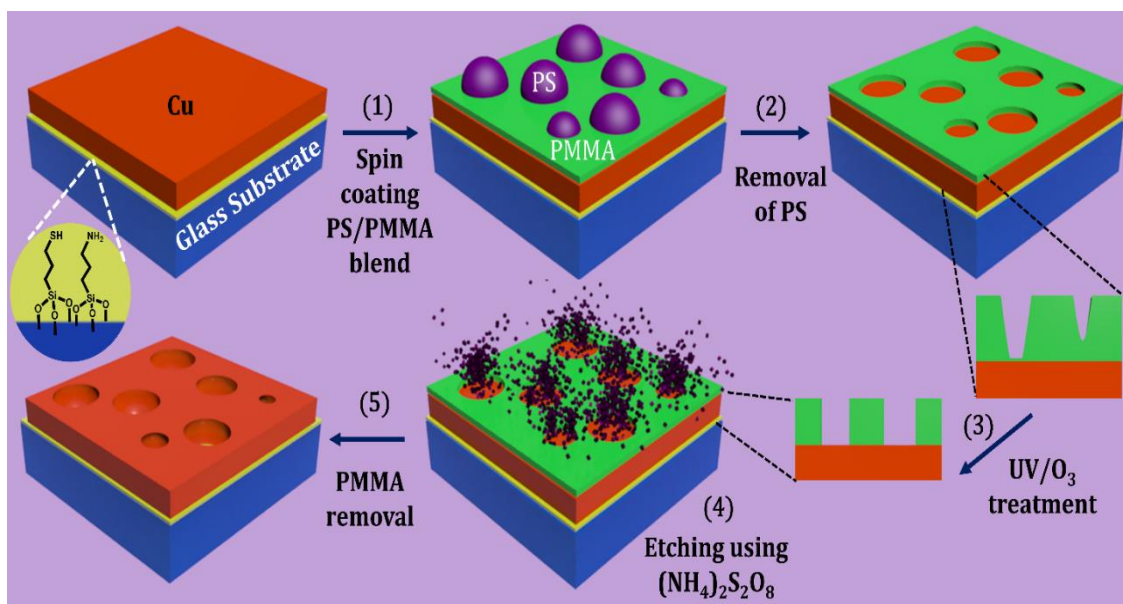


Figure 3.2: Schematic of electrode fabrication process.

Selective removal of PS using cyclohexane (Figure 3.2, step 2) leaves behind a layer of PMMA with circular holes, which serves as a mask to etch copper. (Figure 3.3 (b))

To date literature reports pertaining to phase separation in PS/PMMA blends have emphasised that the size of the PS domains in the PMMA matrix can be controlled by varying the polymer molecular mass combination,³⁶ or weight ratio,^{37,41,42} or the humidity of the atmosphere in which the film is deposited³⁶, or with post-deposition annealing⁴².

The deposition protocol described herein, is distinct from these earlier works in that the molecular mass and weight ratio of the two polymers is held constant and the PS domain size is controlled only by adjustment of the overall concentration of the polymer blend solution: A higher concentration yields larger PS domains suitable for transparent electrodes, whilst low concentrations give very small island sizes that couple strongly with incident light (Figure 3.4). Crucially this process does not require post-deposition annealing or control over humidity, and so is more amenable to up-scaling

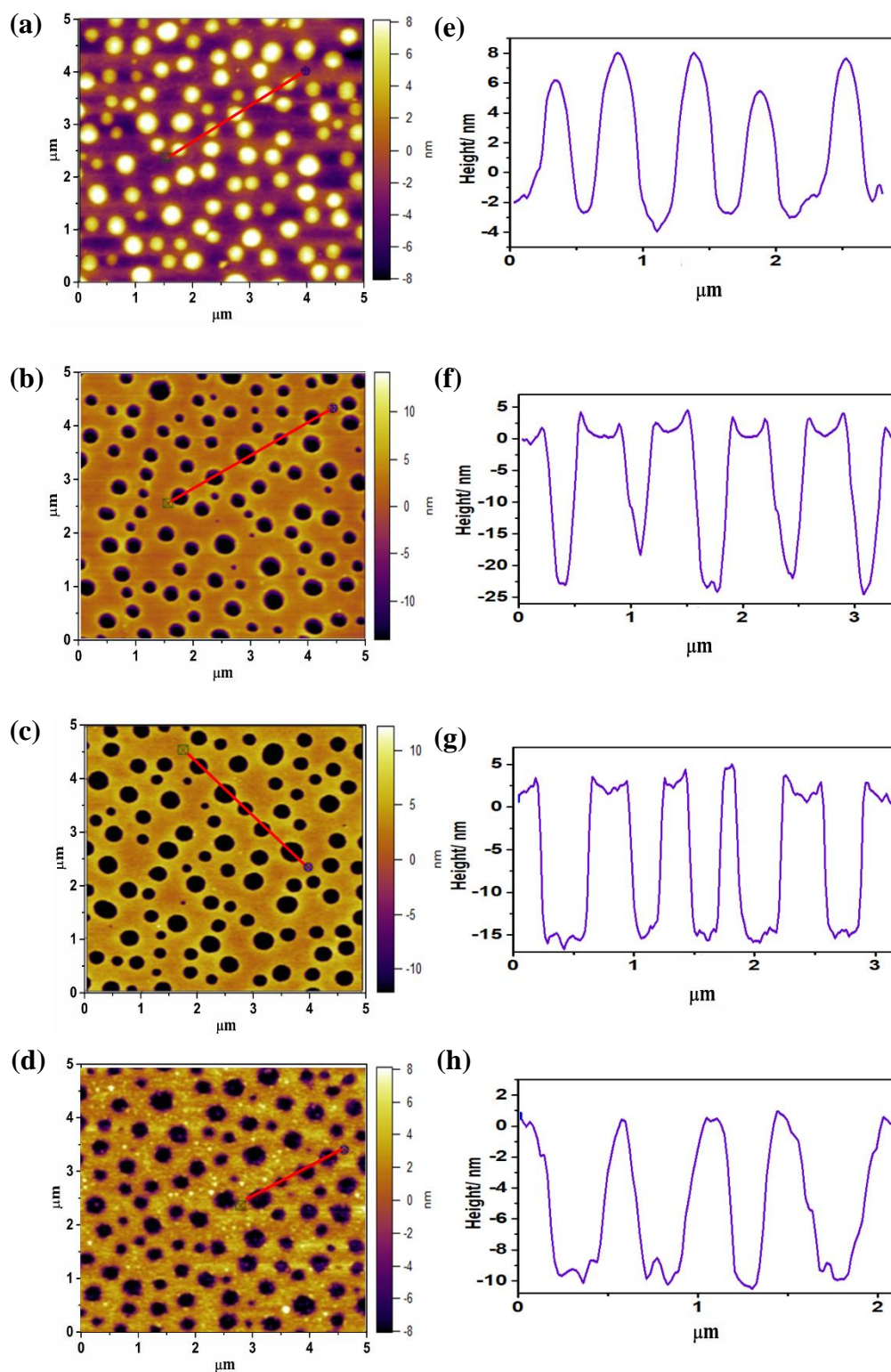


Figure 3.3: AFM images showing the morphology of **(a)** the PS/PMMA polymer blend (7.5 mg ml^{-1}) spin cast onto a Cu film showing spherical PS islands dispersed in a PMMA matrix; **(b)** holes formed in the PMMA layer by selective removal of PS using cyclohexane; **(c)** UV/O₃ treated PMMA film on Cu; **(d)** etched Cu film showing circular apertures; **(e) – (h)** are representative AFM cross-sections taken from **(a) – (d)** respectively along the lines shown; **(g)** shows that the holes in the PMMA layer extend to an equal depth after UV/O₃ treatment.

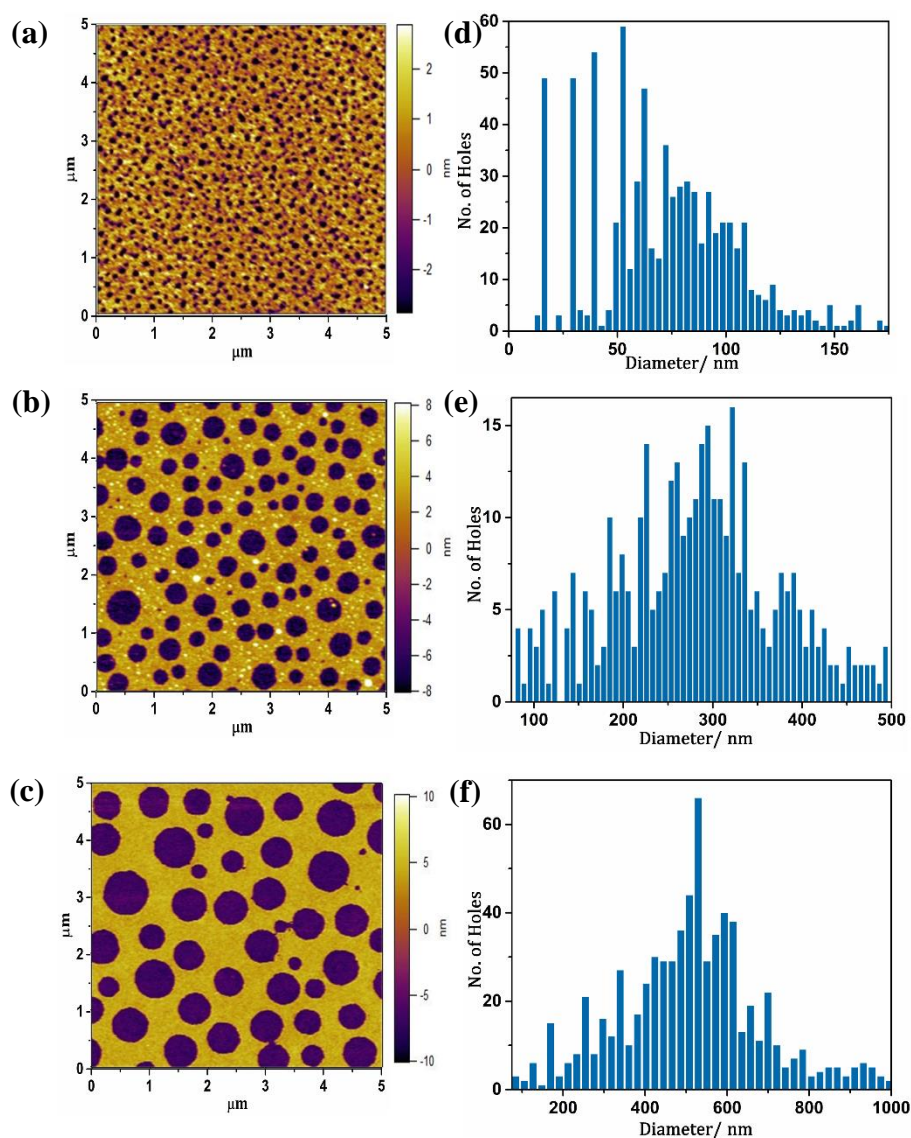


Figure 3.4: AFM images of Cu electrodes (11 nm) etched using polymer blend solutions having concentrations **(a)** 2.9 mg ml^{-1} ; **(b)** 7.5 mg ml^{-1} ; **(c)** 15 mg ml^{-1} respectively; **(d)** size distribution of **(a)**; **(e)** size distribution for **(b)** computed for a $10 \times 10 \mu\text{m}^2$ AFM image and **(f)** size distribution for **(c)** computed for a $20 \times 20 \mu\text{m}^2$ AFM image.

An important step in the electrode fabrication process is the brief UV/O₃ treatment to remove PMMA at the bottom of the holes formed by PS removal (Figure 3.2, step 3). PMMA is uniformly etched under exposure to UV radiation^{43,44} and so this treatment ensures the holes in the PMMA film extend all the way through to the underlying Cu film, as evidenced by the cross-sections of AFM images (Figure 3.3(g) and Figure 3.5), forming a clear pathway for the etchant to travel to the surface of metal film. This step is necessary to achieve a high density and uniform distribution of holes in the Cu film,

without which a significant proportion of holes formed by removal of PS do not extend down to the underlying Cu (Figure 3.3(f)).

Etching of the Cu film through the PMMA mask (Figure 3.2, step 4) is achieved by dipping the substrate for 15-20 seconds into the low-cost etchant ammonium persulphate ((NH₄)₂S₂O₈, APS), which is a common oxidizing and bleaching agent. The etching process is very rapid because the metal thickness is very low, although it can be further speeded up by increasing the concentration of the etchant. In the presence of water, APS undergoes decomposition as shown in equation 3.1.^{45,46}



A further reaction may occur where oxidation of some of the ammonia forms nitrate ions as shown in equation 3.2.



Therefore, the ability of APS to act as an etching agent arises due to the reaction between metallic Cu and resulting acids which may be further intensified by the presence of free oxygen.^{45,46}

The PMMA mask is removed by ultra-sonic agitation in toluene, followed by glacial acetic acid. Glacial acetic acid simultaneously dissolves residual PMMA and any oxide layer at the surface of the Cu film that may have formed if the etching processing is performed in air. Glacial acetic acid is known to preferentially remove Cu oxides (Equation 3.3 and 3.4) from the surface of Cu leaving the metal surface residue free^{29,47}.



Notably, for PMMA layers that are ≤ 25 nm thick, acetic acid treatment alone is sufficient⁴⁷ to completely remove the PMMA layer. Together the process illustrated in Figure 3.2 enables the fabrication of Cu electrodes with a random distribution of ~ 100 million circular apertures cm^{-2} , the average size of which can be altered by changing the concentration of the polymer blend, which enables control within the diameter range 50 to 1000 nm (Figure 3.4).

For OPV device applications the R_{sh} of the window electrode is a key determinant of device performance and in practice cannot exceed $20 \Omega \text{ sq}^{-1}$ without incurring unacceptable electrical losses.^{48–50} To determine the thickness needed to achieve the highest far-field transparency, whilst retaining a R_{sh} below $20 \Omega \text{ sq}^{-1}$, different thicknesses of copper films ranging from 9 to 17 nm were used to fabricate electrodes with the same aperture size distribution shown in Figure 3.5(a).

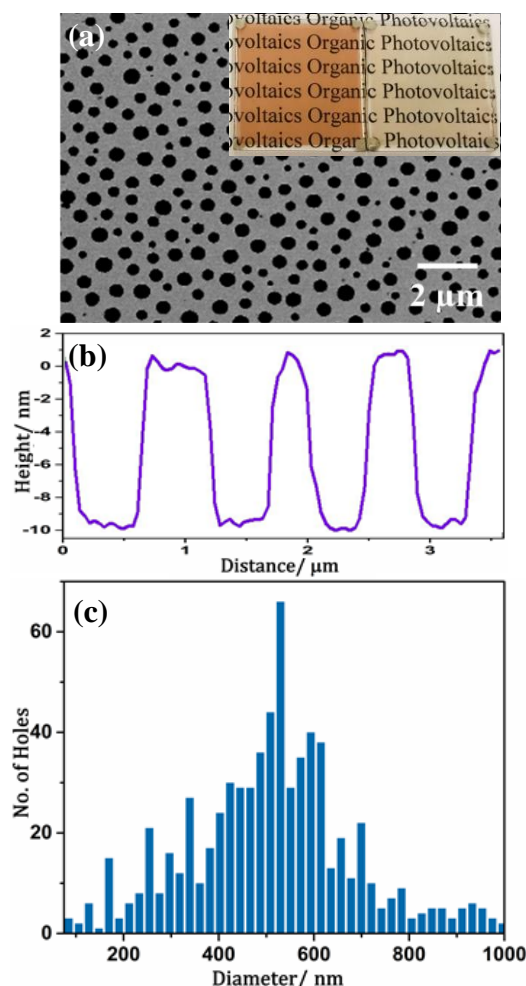


Figure 3.5: (a) SEM showing the morphology of 11 nm thick Cu films with apertures; *Inset:* A photograph of an 11 nm thick Cu electrode with (right) and without (left) apertures; (b) cross-section taken from an AFM image of the same sample as in (a) showing the depth of the apertures; and (c) histogram showing the size distribution of apertures computed for a $20 \times 20 \mu\text{m}^2$ AFM image.

The total transmittance and reflectance (i.e. specular and diffuse combined) is shown in Figure 3.6 for films with and without apertures. As expected, the transmittance is highest for the thinnest film and the reflectance is greatest for the thickest film. The transmittance is increased by $\geq 20\%$ in absolute terms when apertures are introduced into the film, across the wavelength range of 400–850 nm. For wavelengths below ~ 550 nm the

transmittance is increased by 20-25 % for all metal thicknesses, which can be rationalised primarily in terms of a reduction in absorption, since the aperture density and size distribution shown in Figure 3.5(a) corresponds to removal of one quarter (24 ± 1 %) of the metal electrode.

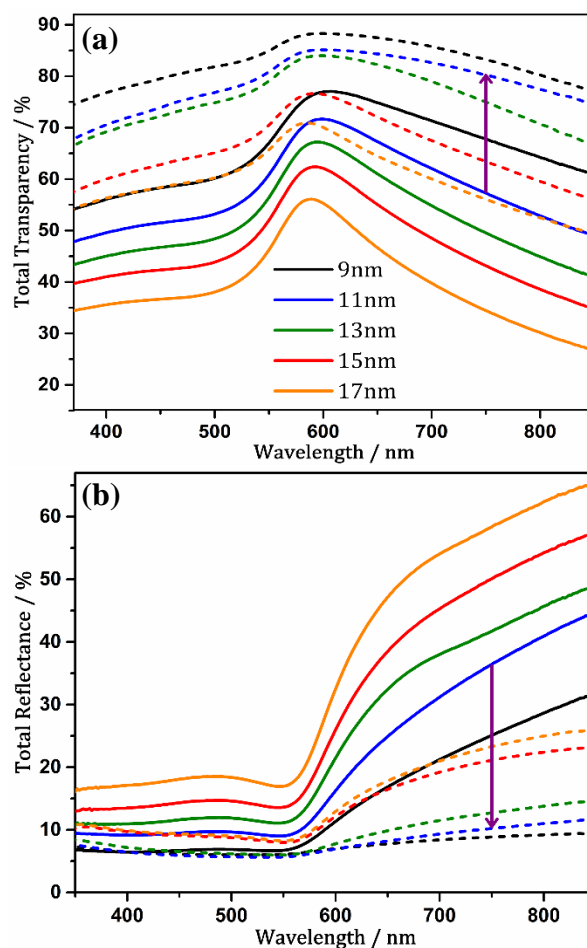


Figure 3.6: (a) Total far-field transparency and; (b) reflectance of different thicknesses of Cu films (referenced to glass) with (broken lines) and without (solid lines) apertures.

For wavelengths above ~ 550 nm, it is evident that the total reflectance is dramatically reduced upon incorporation of apertures, although this does not entirely translate into a commensurate increase in transparency. For example, for an 11 nm thick film the reflectance at 850 nm is reduced from $\sim 45\%$ to $\sim 12\%$, a decrease of 33%, whilst the transparency increases from 50% to 75%; an increase of only 25%. The $\sim 8\%$ difference is attributed to parasitic absorption due to surface plasmon excitation in the Cu electrode^{14,51,52} which, as shown in the subsequent section, can be largely mitigated by appropriate selection of the adjacent CTL.

The data in Figure 3.6 show that the highest transparency is achieved using the thinnest Cu film. However, since R_{sh} increases with decreasing film thickness, as shown in Figure 3.7(a), a compromise must be struck between these properties for optimal performance as a window electrode in OPVs.⁵³ It is evident from Figure 3.7(a) that incorporation of apertures increases the R_{sh} for all metal thicknesses, consistent with scattering of electrons at the aperture edges.³¹ The R_{sh} of films with apertures is only below $20 \Omega \text{ sq}^{-1}$ for a metal thickness above 14 nm. However, for application in OPVs the window electrode is invariably buried beneath a wide bandgap CTL such as ZnO^{54,55} or PEDOT:PSS⁵⁴, both of which require annealing at low temperature (100-200°C) for optimal performance.

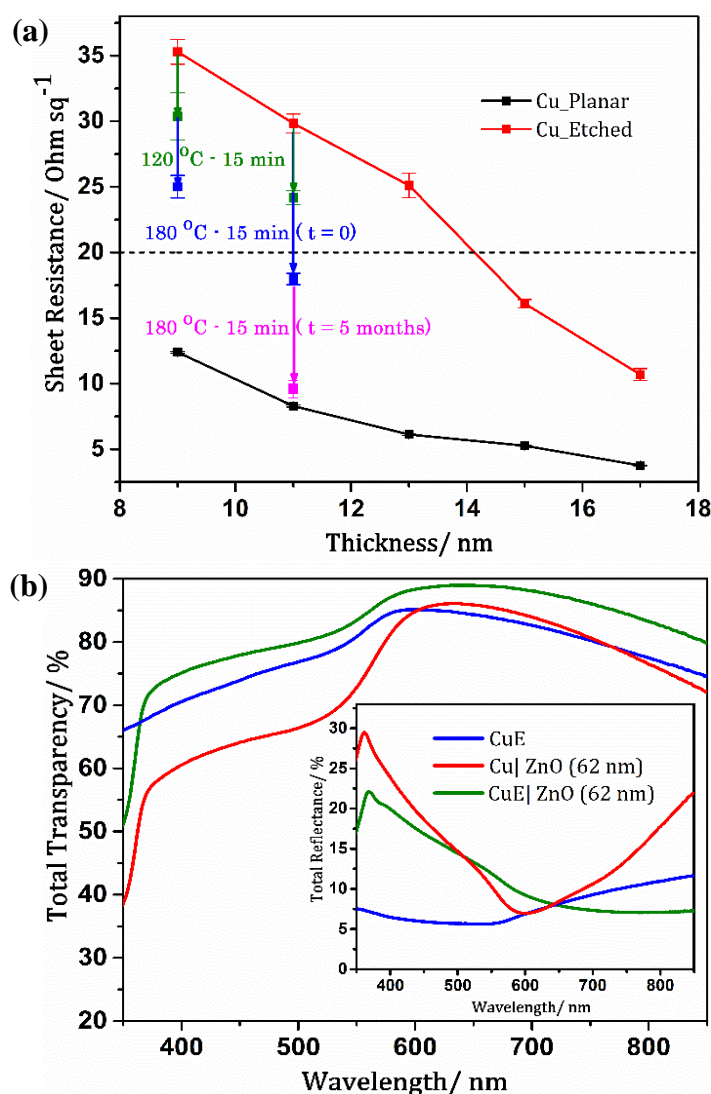


Figure 3.7: (a) R_{sh} as a function of thickness for electrodes of different thicknesses with (red) and without (black) apertures, and the change in R_{sh} when 11 nm thick Cu films are annealed at 120 °C and 180 °C following deposition of a 62 nm ZnO over layer ($t = 0$ and $t = 5$ months); (b) Total far-field transparency (referenced to glass) and; *inset*: total reflectance for 11 nm Cu films with apertures (CuE) and Cu films with a 62 nm ZnO over layer with and without apertures.

In this study a solution processable ZnO ETL was used, which can be processed using a variety of deposition methods including screen printing and doctor blading. The ZnO annealing step was initially performed at 120 °C which, for an 11 nm thick Cu film with apertures, resulted in a notable reduction in the R_{sh} of the electrode from $29.8 \pm 0.7 \Omega \text{ sq}^{-1}$ to $24.2 \pm 0.7 \Omega \text{ sq}^{-1}$. Increasing the annealing temperature to 180 °C resulted in a larger reduction in R_{sh} to $17.9 \pm 0.4 \Omega \text{ sq}^{-1}$.

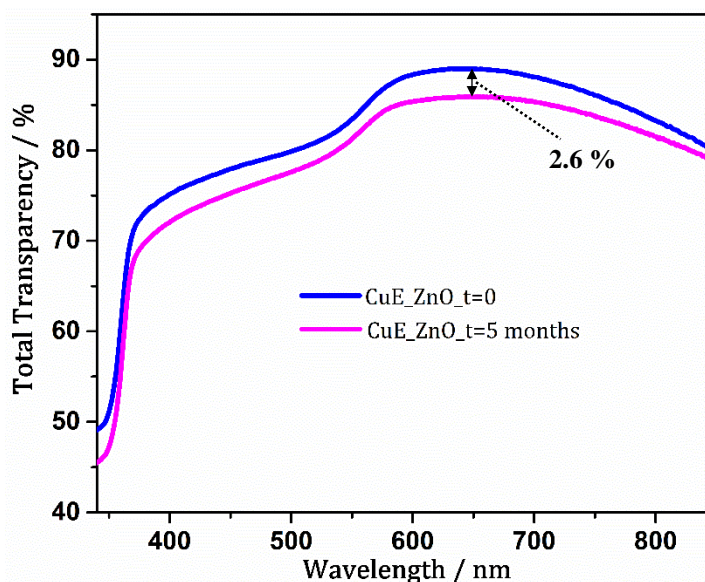


Figure 3.8: Total far-field transparency of nano-aperture Cu electrodes (11nm) with ZnO (62 nm) annealed at 180 °C for 15 mins at $t = 0$ and $t = 5$ months.

Remarkably, the R_{sh} continued to decrease upon long term storage in a glove box, reaching $\sim 9.6 \Omega \text{ sq}^{-1}$ after 5 months of storage. Over the same period there is a small reduction in the far-field transparency of $\sim 2.6 \%$ across the visible spectrum (Figure 3.8), although in terms of the electrode Haacke FoM^{56,57}, which is widely used to compare the performance^{8,18,24} of window electrode materials, the benefit of the large reduction in R_{sh} far outweighs the detrimental effect of the small reduction in transparency: The FoM increases from $0.0099 \Omega^{-1}$ to $0.0135 \Omega^{-1}$.

At the time of this study, for a Cu based window electrode, this FoM had only been exceeded by electrodes with a more complex triple layer; oxide-metal-oxide structure, fabricated by sputter deposition: Table 3.1.

| Group | Substrate | Electrode Architecture | Average Transparency (T_{avg}) | R_{sh} ($\Omega \text{ sq}^{-1}$) | $\frac{T_{avg}^{10}}{R_{sh}}$ (Ω^{-1}) |
|--|------------------|---|---------------------------------------|--|--|
| Zhao <i>et al.</i> ^{24,25} | PET | ZnO/Cu (9.5nm)/ZnO | 79.47 | 9.49 | 0.0106 |
| | | ZnO/Cu (6.5nm) on Cu(O)/ZnO | 85.84 | 11.12 | 0.0195 |
| | | ZnO/Cu (9.5nm) on Cu(O)/ZnO | 83.54 | 6.26 | 0.0264 |
| | | ZnO/Cu (7 nm) (O = 5%) /ZnO | 85 | 13 | 0.0151 |
| | | ZnO/Cu (8 nm) (O = 5%) /ZnO | 83 | 9 | 0.0172 |
| Wang <i>et al.</i> ⁵⁸ | Glass or Polymer | Ag nanoparticle coated CuNWs | 89.1 | 47 | 0.0067 |
| Sachse <i>et al.</i> ⁵⁹ | Glass | CuNWs | 88 | 24 | 0.0116 |
| Rathmell <i>et al.</i> ²¹⁶⁰ | Glass | CuNWs | 65 | 15 | 0.0009 |
| | Plastic | CuNWs | 85 | 30 | 0.0066 |
| Ebner <i>et al.</i> ³⁰ | Glass | TiOx/Cu (10 nm)/AZO | 80 | 6.5 | 0.0165 |
| | | TiOx/Cu (7.5 nm)/AZO | 74 | 17 | 0.0029 |
| Song <i>et al.</i> ⁶¹ | Glass or PET | CuNW films | 80 | 26.2 | 0.0041 |
| | | CuNW elastomers | 80 | 58.6 | 0.0018 |
| Current Study | Glass | Cu(11nm) nano-aperture | 79.1 | 29.8 | 0.0032 |
| | | Cu(11nm) nano-aperture/ZnO (t=0) | 84.1 | 17.9 | 0.0099 |
| | | Cu(11nm) nano-aperture/ZnO (t=5 months) | 81.5 | 9.6 | 0.0135 |

Table 3.1: Comparison of optical and electrical characteristics of different types of Cu electrodes reported. T_{avg} is the average far-field transparency between $\lambda = 400 - 800 \text{ nm}$.

XRD analysis; Figure 3.9, reveals that this ~66 % total reduction in R_{sh} cannot be attributed to a change in crystallinity of the Cu film¹⁴ since the intensity of the reflections from Cu crystal planes does not change, consistent with the very high surface melting temperature of Cu (>400 °C)^{38,62}. An alternative explanation is that the intrinsic conductivity of the ZnO film is increased when annealed at the higher temperature of 180 °C and/or the conductivity is increased due to doping of the ZnO by Cu that diffuses from the underlying Cu film. To test this hypothesis C-AFM analysis was performed on nano-aperture Cu electrodes covered with a 62 nm thick ZnO over layer annealed at 120 °C and 180 °C. It is evident from the C-AFM images and the corresponding cross-sections given in Figure 3.10, that the current drop across the aperture when annealed at 120 °C is very abrupt and distinct (indicated by green arrows), and so the boundary of the aperture in the underlying Cu layer is well-defined.

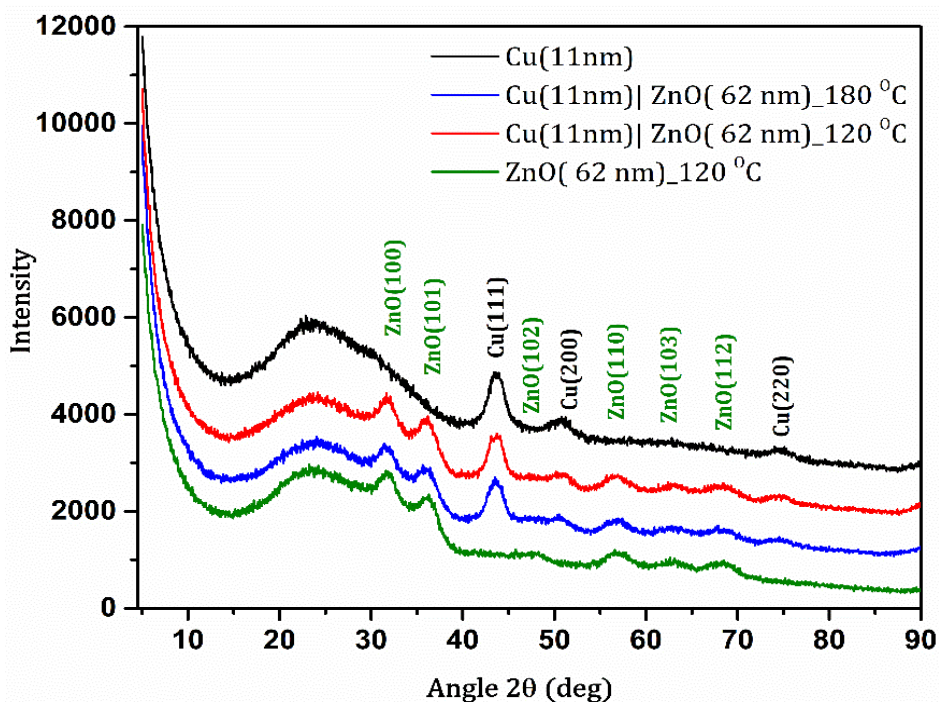


Figure 3.9: XRD pattern of Cu, ZnO annealed at 120 °C, Cu/ZnO annealed at 120 °C and 180 °C. All films were deposited on glass and XRD patterns have been offset along the y-axis for clarity. The XRD patterns for Cu and ZnO have been compared with the standards ICSD-43493 and ICSD-67454 respectively to assign peak positions.

Conversely, the electrode annealed at a higher temperature of 180 °C shows a more gradual drop in current as the probe moves over the site of an aperture in the underlying Cu film and has a minimum at the centre of the aperture, so the boundaries of the apertures appear more diffuse in the current map. These spatially resolved electrical measurements are compelling evidence for an increase in the conductivity of ZnO in the plane of the oxide close to the metal film, which is consistent with the reduction in measured R_{sh} . Notably, the applied voltage for the electrode annealed at 180 °C is twice that needed to achieve the same current as compared to the film annealed at 120 °C (8V vs 4V), which seems to contradict the conclusion that the conductivity of the ZnO layer is increased in the sample annealed at 180 °C. It is however important to note that C-AFM measures the conductance normal to the plane of the film surface, and so it is sensitive to variations in the conductivity of the uppermost surface of the oxide as compared to the bulk, which may have become more resistive due to a higher barrier to charge extraction/injection and transport at higher annealing temperature.⁶³ Whilst solid state diffusion of Cu into the ZnO layer would be expected to be accelerated by thermal annealing, diffusion of Cu into oxides at very low temperature is also known,^{23,64,65} and so electrical doping of the ZnO layer by Cu offers an explanation for the reduction in electrode R_{sh} upon annealing.

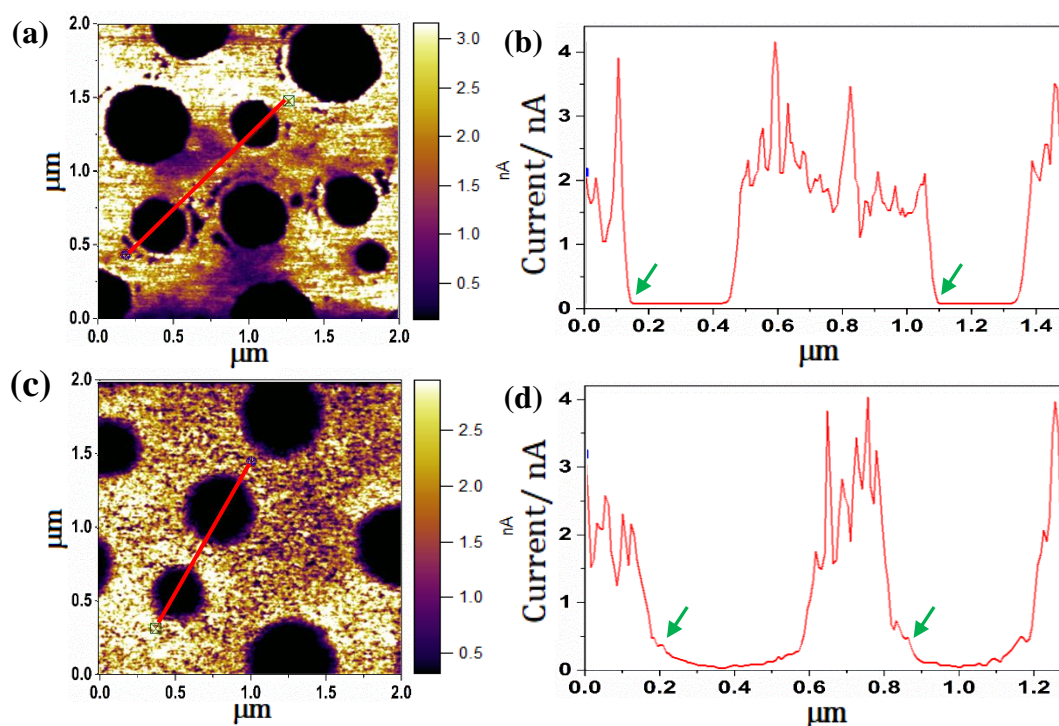


Figure 3.10: C-AFM images showing the current profiles obtained by applying a bias of 4V and 8V respectively for Cu nanohole electrodes with 62 nm ZnO annealed at (a) 120 °C and (c) 180 °C; (b) and (d) correspond to the cross sections of (a) and (c) respectively along the lines shown.

Direct evidence for Cu diffusion from the underlying Cu film into the ZnO layer is provided by XPS analysis of a Cu electrode buried beneath a 62 nm thick ZnO layer, annealed at 120 °C and 180 °C: Figure 3.11 and Table 3.2. The escape depth of Cu 2p photo-electrons is limited to < 10 nm and so, the presence of clearly defined Cu 2p peaks in the spectrum for the film annealed at 180 °C, confirms that Cu has diffused through the entire thickness of the ZnO layer and the process is thermally accelerated. Based on this XPS analysis, the elemental composition at the ZnO surface is estimated to be < 1% Cu.

| Element | O | C | Cu | Zn |
|--------------------------------|------|------|------|------|
| Annealing Temperature - 120 °C | | | | |
| Percentage | 48.7 | 30.2 | 0 | 21.1 |
| Annealing Temperature - 180 °C | | | | |
| Percentage | 45.8 | 37.3 | 0.86 | 16.0 |

Table 3.2: Elemental composition from XPS spectra of nano-aperture Cu films (on glass) with ZnO annealed at 120 °C and 180 °C.

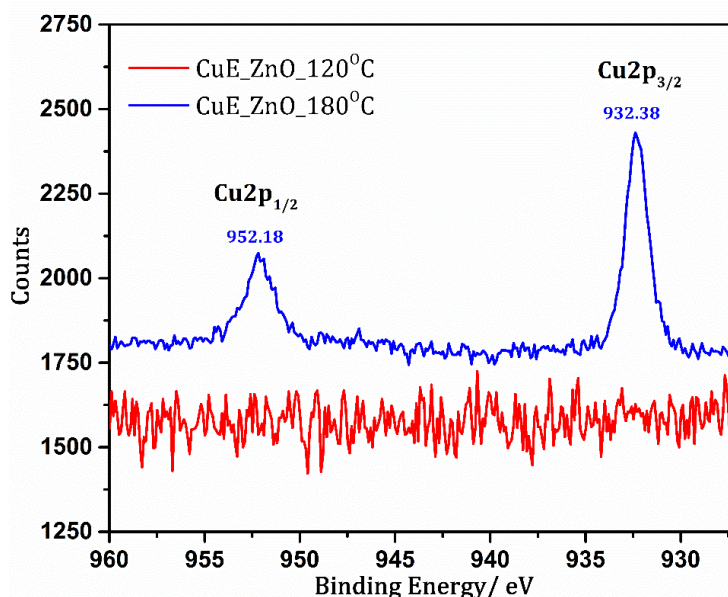


Figure 3.11: XPS spectra of nano-aperture Cu films with ZnO annealed at 120 °C and 180 °C showing the presence of Cu by the characteristic Cu 2p_{1/2} and Cu 2p_{3/2} peaks in the latter.

Evidence for Cu doping of the ZnO film at the sites above apertures in the Cu film is provided using spatially resolved EDXS: Figure 3.12 and Table 3.3, although, unlike XPS, EDXS probes the elemental composition of the entire ZnO thickness. It is clear from the composition derived from the EDXS analysis (Table 3.3) that the proportion of Cu in ZnO regions adjacent to the underlying Cu is very much higher than 1%, which evidences very extensive Cu diffusion into the ZnO over layer. The large difference between the Cu concentration derived from XPS and EDXS measurements provides compelling evidence that the Cu concentration in the ZnO film normal to the plane of the film is not homogenous but concentrated in the region nearest the Cu film. This gradient in Cu concentration offers a plausible explanation for the apparent reduction in conductivity of the ZnO film measured using C-AFM, since the conductivity of Cu doped ZnO is known to depend strongly on concentration of Cu.^{66,67}

ZnO is known to exhibit *n*-type conductivity^{68,69} and it has been shown that at low concentrations (< 1 %) Cu dopants act as deep acceptors, which reduce the *n*-type character by acting as a compensating center.⁷⁰ Conversely at higher concentrations of > 3% the conductivity is increased due to accumulation of metallic Cu at the grain boundaries, which reduces the contact resistance between the ZnO crystallites.⁶⁶ The high concentration of Cu dopant nearest the Cu film could therefore give rise to the observed reduction in the electrode R_{sh} . At the same time, the low concentration of Cu dopant at the uppermost surface of the 62 nm ZnO film would reduce the *n*-type character of the

oxide thus increasing the barrier to electron injection into the conduction band, which would manifest as an apparent reduction in the conductivity normal to the plane of oxide film as evidenced from C-AFM measurements.

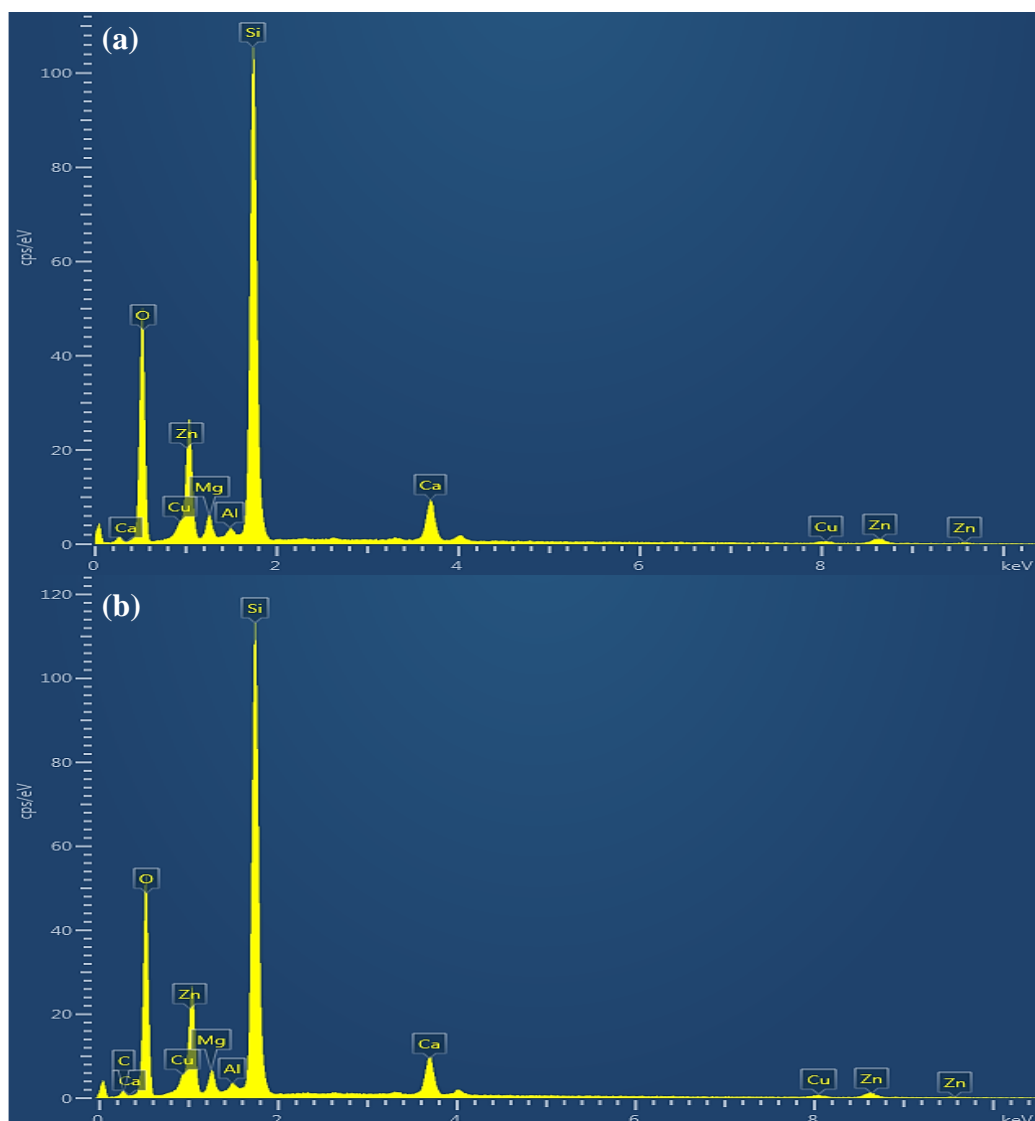


Figure 3.12: Representative EDXS spectra of nano-aperture Cu films with ZnO (on glass) annealed at 180 °C showing the distribution of elements (a) inside a hole and (b) in a continuous area.

To confirm that an increase in the conductivity of the ZnO over layer is the reason for the reduction in the large electrode R_{sh} , the ZnO layer on 5 month old electrodes with a R_{sh} of $9 \Omega \text{ sq}^{-1}$ was selectively removed by etching with acetic acid: Figure 3.13.^[27,41]

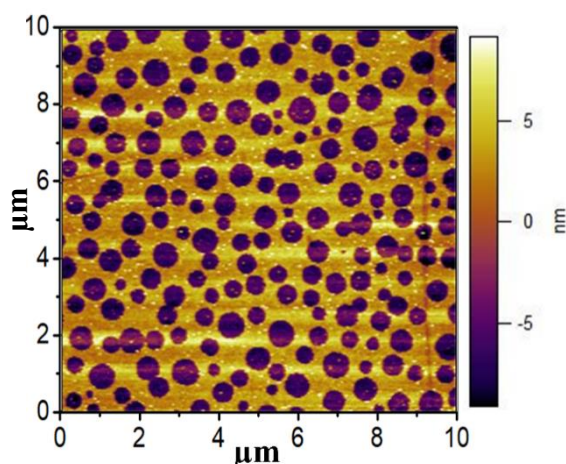


Figure 3.13: AFM image of a Cu electrode (11 nm) which has been stored in the glove box for 5 months prior to removal of the ZnO over layer using glacial acetic acid. The presence of apertures is evidence that the ZnO has been completely removed.

After this treatment the R_{sh} increases to $\sim 40 \Omega \text{ sq}^{-1}$, which confirms that the doped ZnO over layer is the reason for the reduction in R_{sh} . Notably, $\sim 40 \Omega \text{ sq}^{-1}$ is $\sim 10 \Omega \text{ sq}^{-1}$ higher than that of freshly etched Cu electrodes; $29.8 \pm 0.7 \Omega \text{ sq}^{-1}$. Such an increase is not however unexpected since: (i) The Cu that has diffused into the ZnO layer (and is thus removed upon etching) has reduced the thickness of the metal film; (ii) At the interface between the Cu film and the ZnO over layer, it is plausible that the Cu has been partially oxidised, forming a thin Cu oxide interlayer which would be readily etched by acetic acid^[27,41], and so this would also reduce the Cu metal thickness.

| Sample | O | Mg | Al | Si | Ca | Cu | Zn |
|-----------------|------|-----|-----|------|-----|-----|-----|
| Inside Hole | 49.1 | 2.6 | 0.6 | 35.9 | 4.9 | 1.4 | 5.4 |
| Continuous Area | 43.9 | 2.5 | 0.5 | 38.2 | 5.8 | 3.7 | 5.4 |

Table 3.3: Representative elemental composition from EDXS spectra of nano-aperture Cu films with ZnO (on glass) annealed at 180 °C showing the distribution of elements (a) inside a hole and (b) in a continuous area.

A Cu film thickness of 11 nm was chosen to demonstrate utility of this electrode as the window electrode in an OPV device. In OPVs the ZnO layer serves primarily as a charge extraction layer although, like other wide band gap charge extraction materials, can also serve as an anti-reflecting layer when used in conjunction with metal film window electrodes: Figure 3.14 shows how the transparency of an 11 nm Cu film (without

apertures) is improved as a function of ZnO layer thickness (20 – 96 nm). The average transparency of the Cu electrode (400 – 800 nm) with apertures is increased from 75.9% to 84.1% using the optimised ZnO thickness of ~ 62 nm (Figure 3.7(b)), which is comparable to that achieved using thinner Cu films without apertures reported previously (Table 3.1).^{23–25,30} Importantly, the inclusion of ZnO does not complicate the process of electrode fabrication, since wide band gap charge extraction layers are an essential component of high performance OPVs regardless of the choice of electrodes.

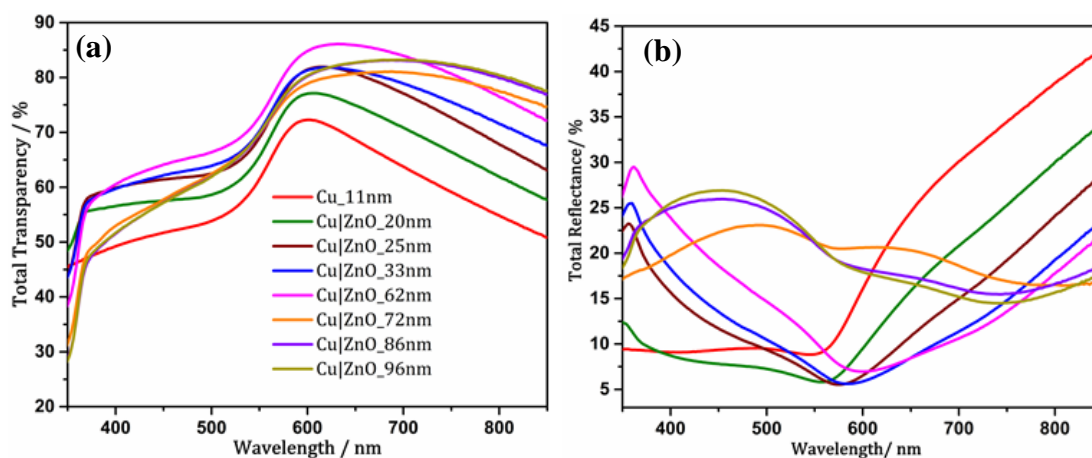


Figure 3.14: (a) Total far-field transparency and (b) reflectance of different thicknesses of ZnO spin cast on 11 nm thick planar Cu films.

To demonstrate these electrodes as window electrodes in OPVs, devices were fabricated with the architecture; Cu (11 nm)/ZnO (β nm)/ PEI (2 nm) / PCE10 – PC₇₀BM (160 nm) / MoO_x (10 nm) / Ag (80 nm), where $\beta = 20 - 62$ nm. Whilst the highest electrode transmittance was achieved using a ZnO thickness of 62 nm, the efficiency of an OPV device depends on a complex interplay of optical and electrical factors,^{38,39,71,72} and so devices with different thicknesses of ZnO ranging from 20 - 62 nm were tested: Table 3.4 and Figure 3.15(a). The device PCE is maximised when the thickness of ZnO is 33 nm. Champion devices achieved a PCE of 4.9% and 6.8% for devices using an 11 nm thick Cu electrode without and with apertures respectively. The large difference in PCE results from a ~35% improvement in J_{sc} in devices using the electrode with apertures as shown in Figure 3.15 (b), which is consistent with more light entering the device. Crucially, there is no significant difference in V_{oc} or device FF , which is consistent with the expectation that the apertures in the Cu film electrode are sufficiently small not to require the use of a highly conducting polymer to span the apertures.

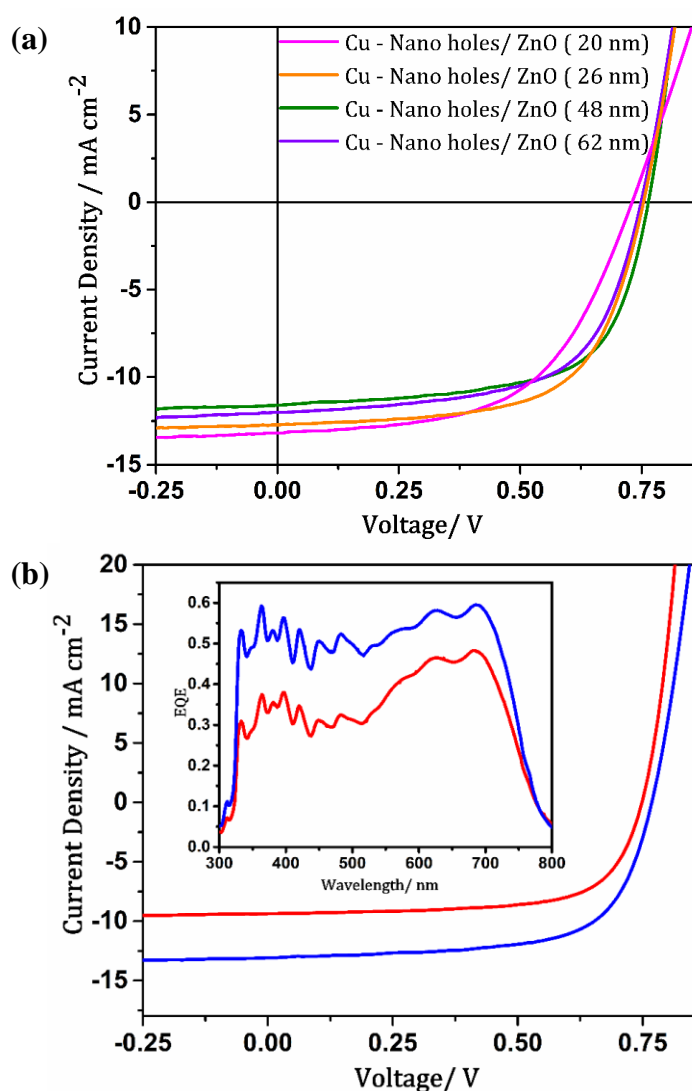


Figure 3.15: (a) Representative current density – voltage characteristics under one sun simulated solar illumination (100 mW cm^{-2} ; AM 1.5G) for devices with the architecture: Cu (11nm) with nano holes / ZnO (β nm) / PEI (2 nm) / PCE10 – PC₇₀BM (160 nm) / MoO_x (10 nm) / Ag (80 nm) for different thicknesses of ZnO; **(b)** Representative current density-voltage and; **Inset:** EQE data recorded under same conditions for devices with the architecture: Cu (11nm) with (blue) and without (red) apertures / ZnO (33 nm) / PEI (2 nm) / PCE10 – PC₇₀BM (160 nm) / MoO_x (10 nm) / Ag (80 nm). The integrated EQE for the red and blue curves shown are 9.17 mA cm^{-2} and 12.30 mA cm^{-2} respectively which is within 3.7 % of the measured J_{sc} .

| Sample | J_{sc} /mA cm ⁻² | V_{oc} / V | FF | R_s /Ω cm ² | R_{shunt} /Ω cm ² | PCE/ % |
|---|----------------------------------|---------------------|---------------------|-----------------------------|-----------------------------------|---------------------|
| Cu – Planar / ZnO (33 nm) <i>Champion</i> | 9.58 ± 0.18 9.73 | 0.74 ± 0.01 0.74 | 0.68 ± 0.01 0.68 | 6.0 ± 0.5 | 1420 ± 65 | 4.77 ± 0.12 4.93 |
| Cu - Nano holes/ ZnO (20 nm) <i>Champion</i> | 13.17 ± 0.15 13.37 | 0.73 ± 0.01 0.75 | 0.58 ± 0.03 0.60 | 14.1 ± 0.7 | 662 ± 55 | 5.66 ± 0.30 6.00 |
| Cu - Nano holes/ ZnO (26 nm) <i>Champion</i> | 12.78 ± 0.27 12.76 | 0.76 ± 0.01 0.76 | 0.64 ± 0.02 0.66 | 8.1 ± 0.5 | 772 ± 47 | 6.18 ± 0.14 6.44 |
| Cu - Nano holes/ ZnO (33 nm) <i>Champion</i> | 12.90 ± 0.46 13.51 | 0.76 ± 0.01 0.76 | 0.66 ± 0.01 0.67 | 6.1 ± 0.3 | 820 ± 52 | 6.47 ± 0.27 6.80 |
| Cu - Nano holes/ ZnO (48 nm) <i>Champion</i> | 11.64 ± 0.17 11.87 | 0.76 ± 0.01 0.76 | 0.64 ± 0.02 0.66 | 7.9 ± 0.7 | 680 ± 63 | 5.64 ± 0.16 5.90 |
| Cu - Nano holes/ ZnO (62 nm) <i>Champion</i> | 11.98 ± 0.08 12.00 | 0.75 ± 0.01 0.75 | 0.61 ± 0.01 0.62 | 8.7 ± 0.5 | 666 ± 36 | 5.47 ± 0.06 5.57 |
| ITO/ ZnO (62 nm) <i>Champion</i> | 16.14 ± 0.13 16.40 | 0.72 ± 0.01 0.72 | 0.69 ± 0.01 0.69 | 7.3 ± 0.6 | 722 ± 38 | 8.04 ± 0.03 8.15 |

Table 3.4: Summary of current density - voltage characteristics of devices with the architecture; Cu (11nm)/ ZnO (β nm)/ PEI (2 nm) / PCE10 – PC₇₀BM (160 nm) / MoO_x (10 nm) / Ag (80 nm) where β = 20 - 62 nm tested under 1 sun simulated solar illumination. The error bars represent ± 1 standard deviation determined from the performance of 20 - 30 devices with identical architecture.

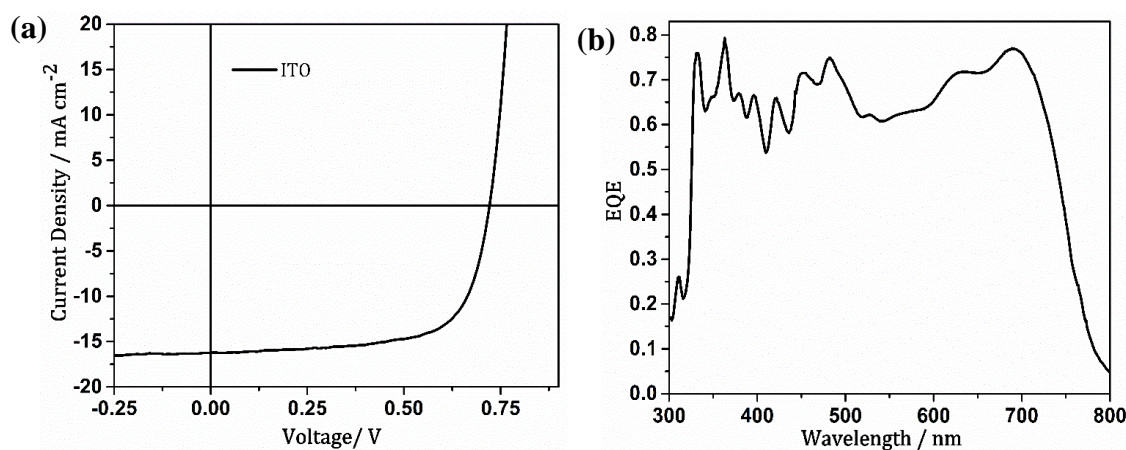


Figure 3.16: (a) Representative current density – voltage characteristics and (b) EQE recorded under one sun simulated solar illumination (100 mW cm^{-2} ; AM 1.5G) for devices with the architecture: ITO /ZnO (33 nm)/ PEI (2 nm) / PCE10 – PC₇₀BM (160 nm) /MoO_x (10 nm)/ Ag (80 nm).

3.4 Conclusion

In summary, this chapter describes a novel approach to simultaneously reducing inter-band absorption losses in optically thin Cu films for wavelengths below $\sim 550 \text{ nm}$ and dramatically suppressing reflection for wavelengths above $\sim 550 \text{ nm}$, which is based on incorporation of ~ 100 million circular apertures per cm^2 into the Cu film with a mean aperture diameter of $\sim 500 \text{ nm}$. Additionally, this work describes a method for the realisation of such an electrode that could be applied to other thin metal films. The advantage of this method is that the metal is deposited by simple vacuum evaporation and all subsequent steps are solution-based processes using widely available low-cost chemicals based on earth abundant elements, without the need to control humidity or for post-deposition annealing.

Remarkably, when this electrode is constrained beneath a solution processed ZnO layer, widely used as an ETL in OPVs, brief thermal annealing at only $180 \text{ }^\circ\text{C}$ dramatically improves the electrode conductivity due to spontaneous diffusion of Cu into the ZnO over layer which is particularly important for improving the conductivity across those regions above apertures in the Cu film, which ensures that the device FF is not degraded as compared to that achieved using an electrode without apertures in the Cu film. Notably, in the current study, the Cu electrodes are supported on glass for ease of handling. However, it has been previously demonstrated that unpatterned optically thin Cu films of the same thickness have identical properties on glass and plastic substrates when using the metal deposition protocol used in the current work.³⁶ Since the approach reported herein, for the formation of apertures in Cu films is compatible with plastic substrates,

there is no barrier to translating this approach to plastic substrates for the realisation of flexible OPVs.

3.5 References

- (1) Lam Po Tang, S. Recent Developments in Flexible Wearable Electronics for Monitoring Applications. *Trans. Inst. Meas. Control* **2007**, 29 (2007), 283–300.
- (2) Yang, Z.; Deng, J.; Sun, X.; Li, H.; Peng, H. Stretchable, Wearable Dye-Sensitized Solar Cells. *Adv. Mater.* **2014**.
- (3) Yun, J. Ultrathin Metal Films for Transparent Electrodes of Flexible Optoelectronic Devices. *Advanced Functional Materials*. 2017.
- (4) Wang, Q.; Xie, Y.; Soltani-Kordshuli, F.; Eslamian, M. Progress in Emerging Solution-Processed Thin Film Solar Cells - Part I: Polymer Solar Cells. *Renewable and Sustainable Energy Reviews*. 2016.
- (5) Kippelen, B.; Brédas, J.-L.; Bredas, J.-L. Organic Photovoltaics. *Energ Env. Sci* **2009**, 2 (3), 251–261.
- (6) Tang, Z.; Tress, W.; Inganäs, O. Light Trapping in Thin Film Organic Solar Cells. *Materials Today*. 2014, pp 389–396.
- (7) Lee, J.; Lee, P.; Lee, H.; Lee, D.; Lee, S. S.; Ko, S. H. Very Long Ag Nanowire Synthesis and Its Application in a Highly Transparent, Conductive and Flexible Metal Electrode Touch Panel. *Nanoscale* **2012**, 4 (20), 6408.
- (8) Madaria, A. R.; Kumar, A.; Zhou, C. Large Scale, Highly Conductive and Patterned Transparent Films of Silver Nanowires on Arbitrary Substrates and Their Application in Touch Screens. *Nanotechnology* **2011**, 22 (24).
- (9) Zou, J.; Li, C. Z.; Chang, C. Y.; Yip, H. L.; Jen, A. K. Y. Interfacial Engineering of Ultrathin Metal Film Transparent Electrode for Flexible Organic Photovoltaic Cells. *Adv. Mater.* **2014**, 26 (22), 3618–3623.
- (10) Kaltenbrunner, M.; White, M. S.; Głowacki, E. D.; Sekitani, T.; Someya, T.; Sariciftci, N. S.; Bauer, S. Ultrathin and Lightweight Organic Solar Cells with High Flexibility. *Nat. Commun.* **2012**, 3, 770.
- (11) Ghosh, D. S. Basics of Ultrathin Metal Films and Their Use as Transparent Electrodes. In *Springer*; Springer, Heidelberg, 2013; pp 11–32.
- (12) Pagliaro, M.; Ciriminna, R.; Palmisano, G. Flexible Solar Cells. *ChemSusChem*. 2008.

-
- (13) Wong, W. S.; Salleo, A. *Flexible Electronics : Materials and Applications*; Springer, 2008.
- (14) Pereira, H. J.; Hutter, O. S.; Dabera, G. D. M. R.; Rochford, L. A.; Hatton, R. A. Copper Light-Catching Electrodes for Organic Photovoltaics. *Sustain. Energy Fuels* **2017**, *1* (4), 859–865.
- (15) Dharmasena, R. D. I. G.; Jayawardena, K. D. G. I.; Mills, C. A.; Deane, J. H. B.; Anguita, J. V.; Dorey, R. A.; Silva, S. R. P. Triboelectric Nanogenerators: Providing a Fundamental Framework. *Energy Environ. Sci.* **2017**, *10* (8), 1801–1811.
- (16) Kim, A.; Won, Y.; Woo, K.; Kim, C. H.; Moon, J. Highly Transparent Low Resistance ZnO / Ag Nanowire / ZnO Composite Electrode for Thin Film Solar Cells. *ACS Nano* **2013**, *7* (2), 1081–1091.
- (17) West, P. R.; Ishii, S.; Naik, G. V.; Emani, N. K.; ShalaeV, V. M.; Boltasseva, A. Searching for Better Plasmonic Materials. *Laser Photonics Rev.* **2010**, *4* (6), 795–808.
- (18) Peres, L.; Bou, A.; Barakel, D.; Torchio, P. ZnS|Ag|TiO₂ Multilayer Electrodes with Broadband Transparency for Thin Film Solar Cells. *RSC Adv.* **2016**, *6* (66), 61057–61063.
- (19) Schubert, S.; Meiss, J.; Müller-Meskamp, L.; Leo, K. Improvement of Transparent Metal Top Electrodes for Organic Solar Cells by Introducing a High Surface Energy Seed Layer. *Adv. Energy Mater.* **2013**, *3* (4), 438–443.
- (20) Han, S.; Lim, S.; Kim, H.; Cho, H.; Yoo, S. Realization of Efficient Semitransparent Organic Photovoltaic Cells with Metallic Top Electrodes: Utilizing the Tunable Absorption Asymmetry. *IEEE J. Sel. Top. Quantum Electron.* **2010**, *16* (6), 1656–1664.
- (21) Rathmell, A. R.; Bergin, S. M.; Hua, Y. L.; Li, Z. Y.; Wiley, B. J. The Growth Mechanism of Copper Nanowires and Their Properties in Flexible, Transparent Conducting Films. *Adv. Mater.* **2010**, *22* (32), 3558–3563.
- (22) U.S. Geological Survey. *Mineral Commodity Summaries*; 2016.
- (23) Hutter, O. S.; Hatton, R. A. A Hybrid Copper:Tungsten Suboxide Window Electrode for Organic Photovoltaics. *Adv. Mater.* **2015**, *27* (2), 326–331.
-

-
- (24) Zhao, G.; Wang, W.; Bae, T. S.; Lee, S. G.; Mun, C. W.; Lee, S.; Yu, H.; Lee, G. H.; Song, M.; Yun, J. Stable Ultrathin Partially Oxidized Copper Film Electrode for Highly Efficient Flexible Solar Cells. *Nat. Commun.* **2015**, *6*, 8830.
- (25) Zhao, G.; Song, M.; Chung, H. S.; Kim, S. M.; Lee, S. G.; Bae, J. S.; Bae, T. S.; Kim, D.; Lee, G. H.; Han, S. Z.; et al. Optical Transmittance Enhancement of Flexible Copper Film Electrodes with a Wetting Layer for Organic Solar Cells. *ACS Appl. Mater. Interfaces* **2017**, *9* (44), 38695–38705.
- (26) Hutter, O. S.; Stec, H. M.; Hatton, R. A. An Indium-Free Low Work Function Window Electrode for Organic Photovoltaics Which Improves with in-Situ Oxidation. *Adv. Mater.* **2013**, *25* (2), 284–288.
- (27) Bellchambers, P.; Lee, J.; Varagnolo, S.; Amari, H.; Walker, M.; Hatton, R. A. Elucidating the Exceptional Passivation Effect of 0.8 Nm Evaporated Aluminium on Transparent Copper Films. *Front. Mater.* **2018**, *5*:71.
- (28) Gong, C.; Leite, M. S. Noble Metal Alloys for Plasmonics. *ACS Photonics* **2016**, *3* (4), 507–513.
- (29) Chan, G. H.; Zhao, J.; Hicks, E. M.; Schatz, G. C.; Van Duyne, R. P. Plasmonic Properties of Copper Nanoparticles Fabricated by Nanosphere Lithography. *Nano Lett.* **2007**, *7* (7), 1947–1952.
- (30) Ebner, D.; Bauch, M.; Dimopoulos, T. High Performance and Low Cost Transparent Electrodes Based on Ultrathin Cu Layer. *Opt. Express* **2017**, *25* (8), A240.
- (31) Stec, H. M.; Williams, R. J.; Jones, T. S.; Hatton, R. A. Ultrathin Transparent Au Electrodes for Organic Photovoltaics Fabricated Using a Mixed Mono-Molecular Nucleation Layer. *Adv. Funct. Mater.* **2011**, *21* (9), 1709–1716.
- (32) Lim, J. E.; Lee, S. M.; Kim, S. S.; Kim, T. W.; Koo, H. W.; Kim, H. K. Brush-Paintable and Highly Stretchable Ag Nanowire and PEDOT:PSS Hybrid Electrodes. *Sci. Rep.* **2017**, *7* (1), 1–12.
- (33) Kwon, N.; Kim, K.; Sung, S.; Yi, I.; Chung, I. Highly Conductive and Transparent Ag Honeycomb Mesh Fabricated Using a Monolayer of Polystyrene Spheres. *Nanotechnology* **2013**.
- (34) Gao, T.; Wang, B.; Ding, B.; Lee, J. K.; Leu, P. W. Uniform and Ordered Copper
-

- Nanomeshes by Microsphere Lithography for Transparent Electrodes. *Nano Lett.* **2014**, No. 14, 2105–2110.
- (35) Colson, P.; Henrist, C.; Cloots, R. Review Article Nanosphere Lithography : A Powerful Method for the Controlled Manufacturing of Nanomaterials. *J. Nanomater.* **2013**, 2013.
- (36) Huang, C.; Moosmann, M.; Jin, J.; Heiler, T.; Walheim, S.; Schimmel, T. Polymer Blend Lithography: A Versatile Method to Fabricate Nanopatterned Self-Assembled Monolayers. *Beilstein J. Nanotechnol.* **2012**, 3 (1), 620–628.
- (37) Huang, C.; Förste, A.; Walheim, S.; Schimmel, T. Polymer Blend Lithography for Metal Films: Large-Area Patterning with over 1 Billion Holes/Inch 2. *Beilstein J. Nanotechnol.* **2015**, 6, 1205–1211.
- (38) Woo, S.; Hyun Kim, W.; Kim, H.; Yi, Y.; Lyu, H. K.; Kim, Y. 8.9% Single-Stack Inverted Polymer Solar Cells with Electron-Rich Polymer Nanolayer-Modified Inorganic Electron-Collecting Buffer Layers. *Adv. Energy Mater.* **2014**.
- (39) Kim, H.; Nam, S.; Jeong, J.; Lee, S.; Seo, J.; Han, H.; Kim, Y. Organic Solar Cells Based on Conjugated Polymers: History and Recent Advances. *Korean J. Chem. Eng.* **2014**, 31 (7), 1095–1104.
- (40) Stec, H. M.; Hatton, R. A. Widely Applicable Coinage Metal Window Electrodes on Flexible Polyester Substrates Applied to Organic Photovoltaics. *ACS Appl. Mater. Interfaces* **2012**, 4 (11), 6013–6020.
- (41) Prosycevas, I.; Tamulevicius, S.; Guobiene, A. The Surface Properties of PS/PMMA Blends Nanostructured Polymeric Layers. *Thin Solid Films* **2004**, 453–454, 304–311.
- (42) Ahn, D. U.; Wang, Z.; Campbell, I. P.; Stoykovich, M. P.; Ding, Y. Morphological Evolution of Thin PS/PMMA Films: Effects of Surface Energy and Blend Composition. *Polym. (United Kingdom)* **2012**, 53 (19), 4187–4194.
- (43) Eve, S.; Mohr, J. Study of the Surface Modification of the PMMA by UV-Radiation. *Procedia Eng.* **2009**, 1 (1), 237–240.
- (44) Wochnowski, C.; Eldin, M. A. S.; Metev, S. UV-Laser-Assisted Degradation of Poly(Methyl Methacrylate). *Polym. Degrad. Stab.* **2005**, 89 (2), 252–264.
- (45) Turrentine, J. W. Action of Ammonium Persulphate on Metals. *J. Phys. Chem.*

- 2005**, *11* (8), 623–631.
- (46) Rawdon, H. S. Use of Ammonium Persulphate for Revealing the Macrostructure of Iron and Steel. *Sci. Pap. Bur. Stand.* **2013**, *16* (li), 715.
- (47) Chavez, K. L.; Hess, D. W. Removal of Resist Materials Using Acetic Acid. *J. Electrochem. Soc.* **2003**, *150* (4), G284.
- (48) Choi, S.; Potscavage, W. J.; Kippelen, B. Area-Scaling of Organic Solar Cells. *J. Appl. Phys.* **2009**, *106* (5).
- (49) Kang, J.-W.; Lee, S.-P. S.; Kim, D.-G.; Lee, S.-P. S.; Lee, G.-H.; Kim, J. H. J.-K.; Park, S.-Y.; Kim, J. H. J.-K.; Kim, H.-K.; Jeong, Y.-S. Reduction of Series Resistance in Organic Photovoltaic Using Low Sheet Resistance of ITO Electrode. *Electrochem. Solid-State Lett.* **2009**, *12* (3), H64.
- (50) Jin, H.; Pivrikas, A.; Lee, K. H.; Aljada, M.; Hambsch, M.; Burn, P. L.; Meredith, P. Factors Influencing the Efficiency of Current Collection in Large Area, Monolithic Organic Solar Cells. *Adv. Energy Mater.* **2012**, *2* (11), 1338–1342.
- (51) Schwind, M.; Kasemo, B.; Zorić, I. Localized and Propagating Plasmons in Metal Films with Nanoholes. *Nano Lett.* **2013**, *13* (4), 1743–1750.
- (52) Park, T. H.; Mirin, N.; Lassiter, J. B.; Nehl, C. L.; Halas, N. J.; Nordlander, P. Optical Properties of a Nanosized Hole in a Thin Metallic Film. *ACS Nano* **2008**, *2* (1), 25–32.
- (53) O'Connor, B.; Haughn, C.; An, K. H.; Pipe, K. P.; Shtein, M. Transparent and Conductive Electrodes Based on Unpatterned, Thin Metal Films. *Appl. Phys. Lett.* **2008**, *93* (22), 1–4.
- (54) Lu, L.; Zheng, T.; Wu, Q.; Schneider, A. M.; Zhao, D.; Yu, L. Recent Advances in Bulk Heterojunction Polymer Solar Cells. *Chem. Rev.* **2015**, *115* (23), 12666–12731.
- (55) Xiao, B.; Wu, H.; Cao, Y. Solution-Processed Cathode Interfacial Layer Materials for High-Efficiency Polymer Solar Cells. *Mater. Today* **2015**, *18* (7), 385–394.
- (56) Haacke, G. New Figure of Merit for Transparent Conductors. *J. Appl. Phys.* **1976**, *47* (9), 4086–4089.

- (57) Haacke, G. Transparent Conducting Coatings. *Annu. Rev. Mater. Sci.* **1977**, *7* (1), 73–94.
- (58) Wang, X.; Wang, R.; Zhai, H.; Shen, X.; Wang, T.; Shi, L.; Yu, R.; Sun, J. Room-Temperature Surface Modification of Cu Nanowires and Their Applications in Transparent Electrodes, SERS-Based Sensors, and Organic Solar Cells. *ACS Appl. Mater. Interfaces* **2016**, *8* (42), 28831–28837.
- (59) Sachse, C.; Weiß, N.; Gaponik, N.; Müller-Meskamp, L.; Eychmüller, A.; Leo, K. ITO-Free, Small-Molecule Organic Solar Cells on Spray-Coated Copper-Nanowire-Based Transparent Electrodes. *Adv. Energy Mater.* **2014**, *4* (2), 1–6.
- (60) Rathmell, A. R.; Wiley, B. J. The Synthesis and Coating of Long, Thin Copper Nanowires to Make Flexible, Transparent Conducting Films on Plastic Substrates. *Adv. Mater.* **2011**, *23* (41), 4798–4803.
- (61) Song, J.; Li, J.; Xu, J.; Zeng, H. Superstable Transparent Conductive Cu@Cu₄Ni Nanowire Elastomer Composites against Oxidation, Bending, Stretching, and Twisting for Flexible and Stretchable Optoelectronics. *Nano Lett.* **2014**.
- (62) Krasnikov, G. Y.; Bokarev, V. P. Surface Melting of Crystals and the Sintering of Powders. *J. Surf. Investig. X-ray, Synchrotron Neutron Tech.* **2015**, *9* (5), 1116–1119.
- (63) Krzywiecki, M.; Grządziel, L.; Sarfraz, A.; Iqbal, D.; Szwajca, A.; Erbe, A. Zinc Oxide as a Defect-Dominated Material in Thin Films for Photovoltaic Applications – Experimental Determination of Defect Levels, Quantification of Composition, and Construction of Band Diagram. *Phys. Chem. Chem. Phys.* **2015**, *17* (15), 10004–10013.
- (64) Greiner, M. T.; Chai, L.; Helander, M. G.; Tang, W. M.; Lu, Z. H. Metal/Metal-Oxide Interfaces: How Metal Contacts Affect the Work Function and Band Structure of MoO₃. *Adv. Funct. Mater.* **2013**, *23* (2), 215–226.
- (65) Nguyen, D.-T.; Vedraïne, S.; Cattin, L.; Torchio, P.; Morsli, M.; Flory, F.; Bernède, J. C. Effect of the Thickness of the MoO₃ Layers on Optical Properties of MoO₃/Ag/MoO₃ Multilayer Structures. *J. Appl. Phys.* **2012**, *112* (May 2016), 063505.
- (66) Samarasekera, P.; Wijesinghe, U.; Jayaweera, E. N. N. Impedance and Electrical Properties of Cu Doped ZnO Thin Films. *GESJ Phys.* **2015**, *1* (13), 3–9.

-
- (67) Yusof, A. S.; Hassan, Z.; Zainal, N. Fabrication and Characterization of Copper Doped Zinc Oxide by Using Co-Sputtering Technique. *Mater. Res. Bull.* **2018**.
- (68) Janotti, A.; Van De Walle, C. G. Fundamentals of Zinc Oxide as a Semiconductor. *Reports Prog. Phys.* **2009**, 72 (12).
- (69) Tang, K.; Gu, S.-L.; Ye, J.-D.; Zhu, S.-M.; Zhang, R.; Zheng, Y.-D. Recent Progress of the Native Defects and P-Type Doping of Zinc Oxide. *Chinese Phys. B* **2017**, 26 (4), 047702.
- (70) Muller, G. Optical and Electrical Spectroscopy of Zinc Oxide Crystals Simultaneously Doped with Copper and Donors. *Phys. Status Solidi* **1976**, 76 (2), 525–532.
- (71) He, Z.; Wu, H.; Cao, Y. Recent Advances in Polymer Solar Cells: Realization of High Device Performance by Incorporating Water/Alcohol-Soluble Conjugated Polymers as Electrode Buffer Layer. *Adv. Mater.* **2014**, 26 (7), 1006–1024.
- (72) Karabacak, T.; Deluca, J. S.; Wang, P. I.; Ten Eyck, G. A.; Ye, D.; Wang, G. C.; Lu, T. M. Low Temperature Melting of Copper Nanorod Arrays. *J. Appl. Phys.* **2006**.

Chapter 4

High Figure-of-merit Transparent Copper Window Electrodes for Organic Photovoltaics

A manuscript derived from the work presented in this chapter has been submitted:

H. J. Pereira, R. A. Hatton, High Figure-of-merit Transparent Copper Window Electrodes for Organic Photovoltaics, *Front. Mater.*

4.1 Background

The low-cost associated with processing organic semiconductors by printing, together with low processing temperature and colour tuneability make OPVs attractive for a diverse range of applications.^{1,2} The flexibility and light weight of OPVs supported on flexible plastic substrates also enables integration into wearable electronics, roofing, automobile and building related applications where conventional rigid PVs are not suitable³⁻⁷, as well as enabling compact storage for transportation. All OPVs require a transparent electrode with low R_{sh} , which is often expressed in terms of the Haacke FoM which quantifies the trade-off between transmission and R_{sh} . A higher magnitude for the Haacke FoM is preferred and indicates an effective electrode with high transparency and good conductivity.⁸⁻¹⁰ In addition to requiring a high FoM, flexible OPVs require a transparent electrode that does not degrade when bent, both for application purposes and for compatibility with roll-to-roll processing. Whilst ITO and FTO are predominantly used in research scale OPVs due to their high FoM, they are unsuitable for flexible OPVs because of the inherent brittleness of these oxide films¹¹⁻¹³, which cause their R_{sh} to degrade quite readily upon modest physical deformation.¹¹⁻¹⁶ Consequently, flexible OPVs reported to date use a transparent electrode composed of carbon nanotubes,¹⁷ metal nanowires,^{14,18,19} graphene,^{16,20} metal nanogrids^{11,19} or optically thin (6-12 nm) films of Au, Ag or Cu.^{12,19} As already discussed, of the metals Ag is by far the dominant choice owing to its relatively slow oxidation under ambient conditions and its very low optical losses in the visible and IR regions.^{21,22} However, Ag is a costly precious metal and so Cu is attractive as an alternative because it offers a conductivity comparable to that of Ag at one hundredth of the cost.^{22,23} Unfortunately, parasitic absorption in Cu due to inter-band absorption losses mean that optically thin Cu films are not as transparent as Ag films of the same thickness.²²⁻²⁵ To address this problem a new approach was described in

chapter 3 based on incorporating a random distribution of ~100 million holes of the order of 500 nm per cm² which simultaneously reduces absorption losses whilst suppressing reflective losses.²⁴

In this chapter, the work presented in chapter 3 is advanced by showing that; (i) the method of electrode fabrication can be translated to the technologically important transparent plastic substrate, PET, with only slight adaptation, and that the Haacke FoM can be increased substantially above that previously reported on glass substrates by increasing the aperture density; (ii) it is possible to fabricate the polymer mask by dip coating, which, unlike spin coating, is a scalable deposition method compatible with roll-to-roll processing; (iii) these electrodes outperform ITO coated plastic as the transparent electrode in flexible OPVs.

4.2 Experimental Methods

Experimental details specific to the work presented in this chapter are as follows;

4.2.1 Substrate cleaning

Substrate slides of the required dimension were cut from a roll of PET and cleaned as described in section 2.1 and 2.2. Notably both sides of the PET sheet were not identical in surface roughness and so AFM imaging was performed in tapping mode using an Asylum Research MFP – 3D AFM to determine the smooth side onto which all surface treatment was done prior to deposition of Cu.

4.2.2 Mixed Monolayer deposition

A mixed monolayer was deposited prior to evaporation of Cu by exposing the substrates to vapours of MPTMS and APTMS, at 50 mbar for 4 hours immediately after UV/O₃ treatment.

4.2.3 Deposition of Cu

Cu was deposited by thermal evaporation of Cu pellets at a rate of 2.2 – 2.5 Å s⁻¹ to give the required thickness.

4.2.4 Fabrication of apertures using polymer blend lithography

A polymer blend consisting of PS (M_w = 280 000) and PMMA (M_w = 50 000) in the weight ratio of 3:7 having a concentration of 15 mg ml⁻¹ was prepared in 2-butanone (MEK). The blend was deposited on Cu by spin coating at 2500 rpm for 60 seconds or by dip coating, using an automated setup, at a dipping rate of 2 mm s⁻¹ and a dwell time of 2 seconds. The PS entities were selectively removed by rinsing the films in

cyclohexane. The films were then UV/O₃ treated for 15 minutes. A dilute solution of ammonium persulphate (0.002 mol dm⁻³) was used to etch Cu through the PMMA mask to fabricate holes by immersing the substrates in the etchant for 15-20 seconds followed by washing with deionized water and drying with a stream of N₂. The PMMA template was finally removed by ultrasonic agitation in toluene and then very briefly in glacial acetic acid to remove any residual PMMA and Cu oxides on the surface of the electrode.

4.2.5 Morphology and distribution of apertures

AFM imaging was performed using an Asylum Research MFP – 3D operated in tapping mode to study the morphology of the Cu films. The size distribution of apertures was evaluated using WXS_M software. SEM imaging was performed using ZEISS Gemini 500 with an accelerating voltage of typically 0.1 - 0.4 kV to evaluate the distribution and coverage of apertures.

4.2.6 Optical transparency and reflectance measurements

Far-field transmittance and reflectance of metal films supported on PET were measured over the wavelength range of 350 – 850 nm using 150 mm Spectralon® Integrating Sphere coupled to a PerkinElmer® LAMBDA™ high performance UV/Vis spectrometer. Measurements were performed with reference to the substrate.

4.2.7 Fabrication of flexible OPV devices

A ZnO ink (5.6% w/v) in IPA was purchased from Infinity PV and a diluted solution was spun at 1000 rpm for 60 seconds followed by annealing at 145 °C for 15 minutes to fabricate the ETL. PCE12 and *m*-ITIC were mixed in 1:1 mass ratio to make a 20 mg ml⁻¹ solution in chlorobenzene (99%) and 1,8-diiodooctane (1%) and was deposited by spin coating from a static start at 1900 rpm for 60 seconds to form the photo-active layer having a thickness of ~100 nm. These slides were left inside the evaporator overnight and MoO_x (10 nm at 0.1- 0.2 Å s⁻¹) was deposited as the HTL followed by Ag (85 nm at 1.0- 1.2 Å s⁻¹) as the top reflective electrode. Ag was deposited through a shadow mask to give an electrode area of 0.06 cm².

4.2.8 Characterization of OPV devices

Current density-voltage (*JV*) testing was performed as described in section 2.17 and the OPV devices were measured through a mask having a pixel area of 0.013 cm². EQE measurements were done as described in section 2.18.

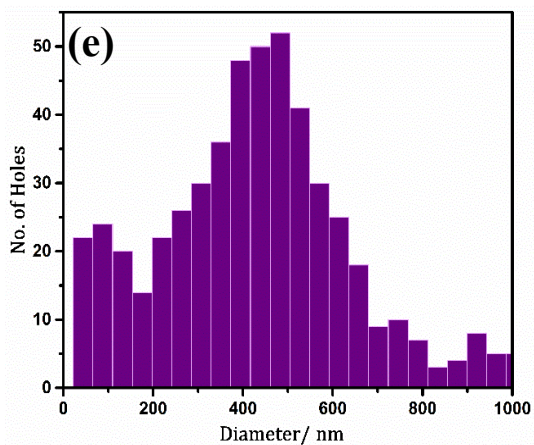
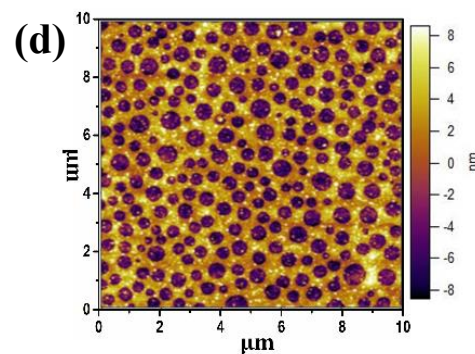
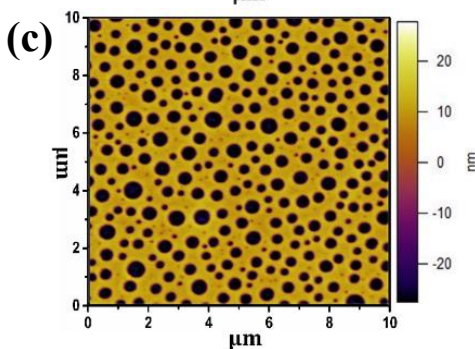
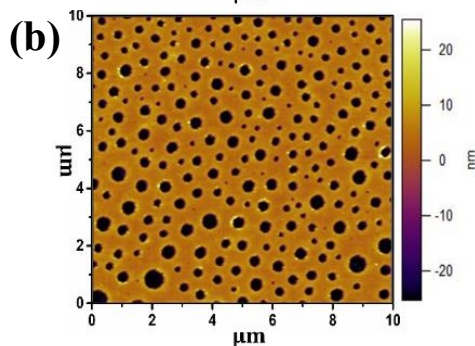
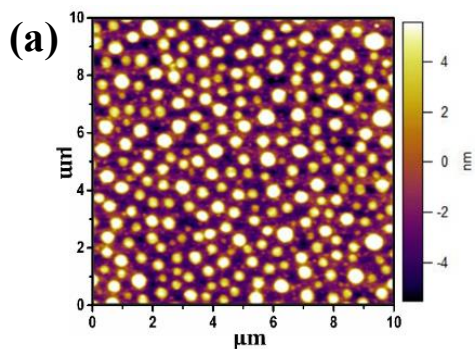
4.3 Results and Discussion

Optically thin Cu films with a thickness of 11 nm were thermally evaporated onto PET substrates modified with a mixed molecular nucleation layer of MPTMS and APTMS.^{15,26} In the first instance, a 15 mg ml⁻¹ PS/PMMA blend with the ratio 3:7 in MEK was spin coated onto these 11 nm Cu films on PET. The PS phase was then selectively removed using cyclohexane, followed by a UV/O₃ treatment to open out the base of the holes in the PMMA, and finally rapid etching and removal of the PMMA mask, similar to the protocol designed for glass substrates²⁴ as discussed in chapter 3 (Figure 4.1(a) – (d)).

Spin coating is not compatible with roll-to-roll processing and large area fabrication of electrodes, and so the possibility of dip-coating the polymer blend was also tested. It is evident from the AFM images in Figure 4.1 (f) - (i), that the polymer blend mask can be deposited by dip-coating. Using a dipping rate of 2 mm s⁻¹ and a dwell time of 2 seconds, a very similar aperture size distribution to that obtained by spin coating was achieved even though the solvent evaporation rates for spin coating and dip coating are very different,²⁷ which demonstrates the robustness of this method for mask formation and scope for increasing the dipping speed. The primary difference between the spin cast and dip coated films is in the density of apertures (Figure 4.1(e) and (j)) in the Cu film: Electrodes fabricated by spin casting the resist layer have a total aperture area of 29 ± 1 % vs 25 ± 1 % for electrodes fabricated using a dip coated resist layer. It is anticipated that by fine tuning of the dip coating deposition parameters it will be possible to achieve the same result using the two different methods. For convenience, all of the OPV devices fabricated as part of this study were fabricated by spin coating the polymer blend.

The AFM images in Figure 4.1 show that the distribution of aperture sizes using both methods is very similar, consistent with a previously reported observation that the aperture size is primarily determined by the solution concentration.

Spin Coating



Dip Coating

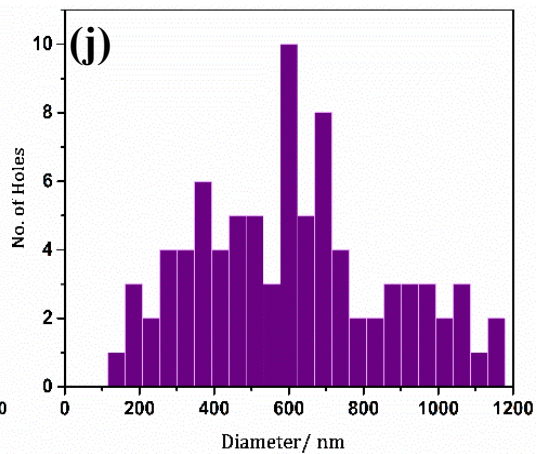
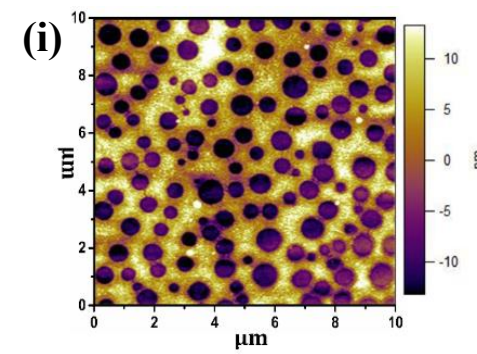
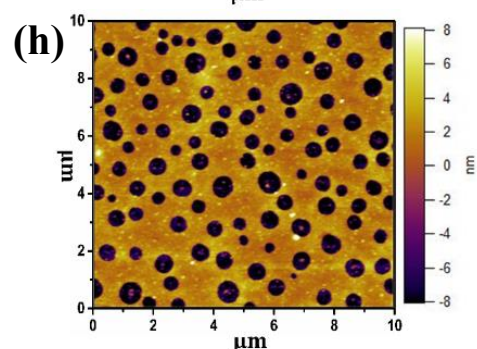
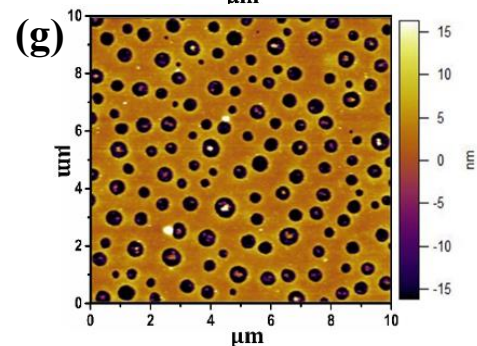
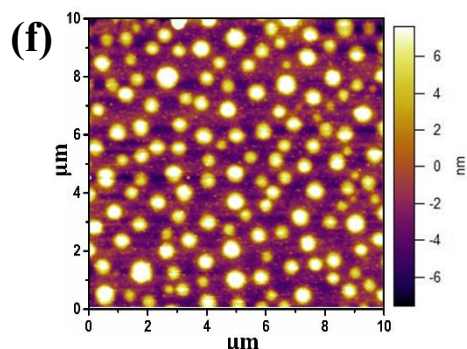


Figure 4.1: AFM images showing the morphology of: **(a)** the PS/PMMA polymer blend (15 mg ml^{-1}) spin cast onto a Cu film vacuum evaporated on PET substrates showing spherical PS islands dispersed in a PMMA matrix; **(b)** following the selective removal of PS using cyclohexane the peaks are transformed into holes; **(c)** the resulting PMMA film is UV/O₃ treated to remove residual polymers within the holes and to ensure the holes extends the entire depth right down to the surface of the metal; **(d)** etched Cu film showing circular apertures; **(f) – (i)** are representative AFM images showing the morphology of the film when the same steps are repeated following the deposition of the polymer blend by dip coating; histogram showing the size distribution of apertures computed for a $10 \times 10 \mu\text{m}^2$ AFM image of the etched Cu electrode when the PMMA mask is deposited by **(e)** spin coating and **(j)** dip coating of the polymer blend.

It is evident from the SEM image and cross-sectional AFM image (Figure 4.2) that the edges of the apertures taper in towards the centre, which was not observed to occur on glass substrates. However, the AFM image also shows that the hole in the film is 2-5 nm deeper than the combined thickness of the metal film and the APTMS/MPTMS adhesion layer. The tapered edge in the film is therefore attributed to sagging of the surrounding metal into the hole in PET that forms as a result of etching of the PET substrate during the acetic acid wash used to remove residual PMMA and surface Cu oxides. Consequently, when fabricating electrodes on PET substrates, the acetic acid rinse time must be very brief.

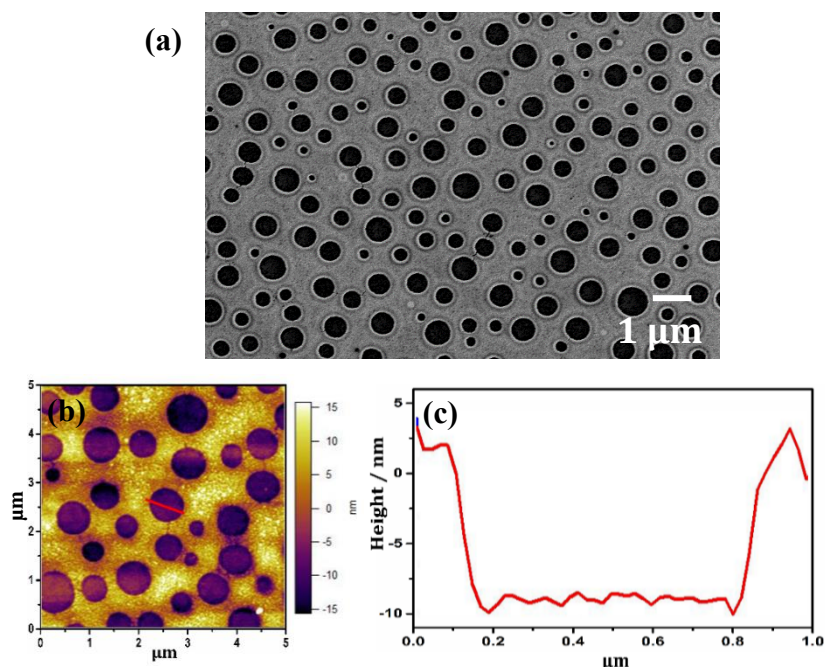


Figure 4.2: **(a)** SEM image showing the morphology of 11 nm thick Cu films with apertures; and **(b)** AFM image and **(c)** cross section of the aperture along the line in **(b)** showing the depth of the hole is larger than the metal thickness (11 nm) indicating the etching of the PET substrate when the acetic acid wash is prolonged. .

The Cu electrodes with apertures have an average far-field transparency (T_{avg}) of 75.9% over the wavelength range of 400 - 800 nm (Figure 4.3(a)) with an 18.8% average increase in the total transmittance over this wavelength as compared to an unpatterned electrode of similar thickness. The reduction in reflectance upon introduction of apertures is very large, particularly for $\lambda \geq 620$ nm where the reduction as compared to planar Cu film is $> 30\%$ (Figure 4.3 (b)). The transmittance of these flexible window electrodes is further increased to an impressive 86.4% (400 - 800 nm) upon deposition of a ~ 62 nm thick ZnO over layer (Figure 4.3(a)) from solution at low temperature.

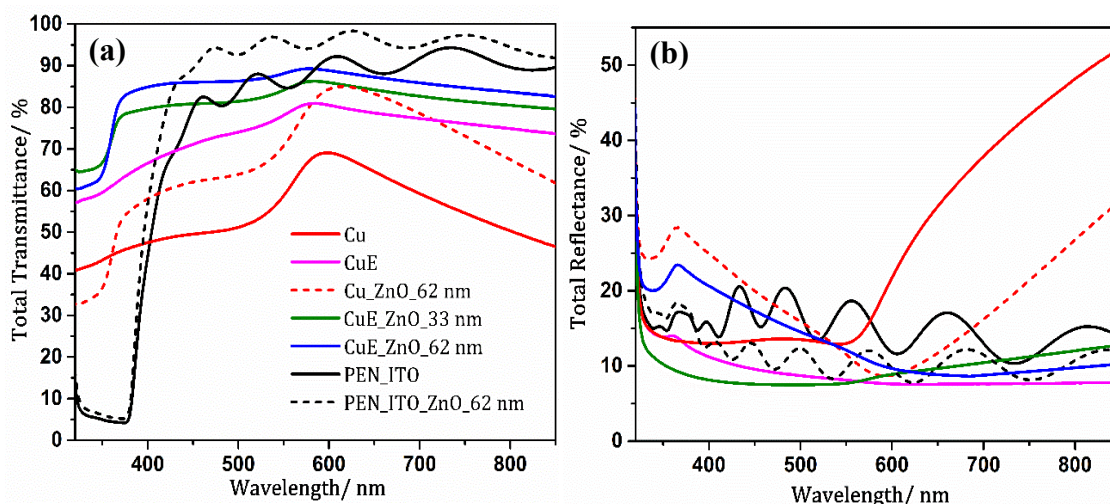


Figure 4.3: (a) Total far-field transparency and (b) total reflectance of 11 nm Cu films before and after the introduction of nano-apertures (CuE), and ITO coated PEN substrates with and without ZnO (referenced to glass).

Importantly the ZnO not only contributes to an increase in transmittance but also serves as an ETL and spans the apertures substantially reducing the electrode R_{sh} . The introduction of apertures increases the R_{sh} from $8.4 \pm 0.5 \Omega \text{ sq}^{-1}$ to $29.9 \pm 1.2 \Omega \text{ sq}^{-1}$ because the apertures disrupt the flow of electrons in the plane of the electrode by scattering. However, after deposition of a ZnO over layer, which includes annealing at 145°C , the R_{sh} drops to $21.9 \pm 1.1 \Omega \text{ sq}^{-1}$, and continues to fall upon storage, such that after 4 months, the R_{sh} is reduced to $11.3 \pm 1.5 \Omega \text{ sq}^{-1}$. This improvement in R_{sh} with time has previously been shown for these Cu electrodes supported on glass (chapter 3), and is due to diffusion of Cu into the ZnO where it accumulates in the grain boundaries contributing to an increase in the conductivity.²⁴ In this case the ZnO annealing temperature was reduced from 180°C to 145°C to avoid thermal distortion of the PET substrate. This was also accompanied with a very small reduction in the overall transmittance to $T_{\text{avg}} = 84.6\%$ (400 - 800 nm) (Figure 4.4). However, the Haacke FoM is increased from $0.0107 \Omega^{-1}$ to $0.0166 \Omega^{-1}$ after 4 months of storage in the glove box, which

is much higher than previously achieved on glass ; i.e. $0.0099 \Omega^{-1}$ and $0.0135 \Omega^{-1}$ at time = 0 and 5 months respectively.²⁴

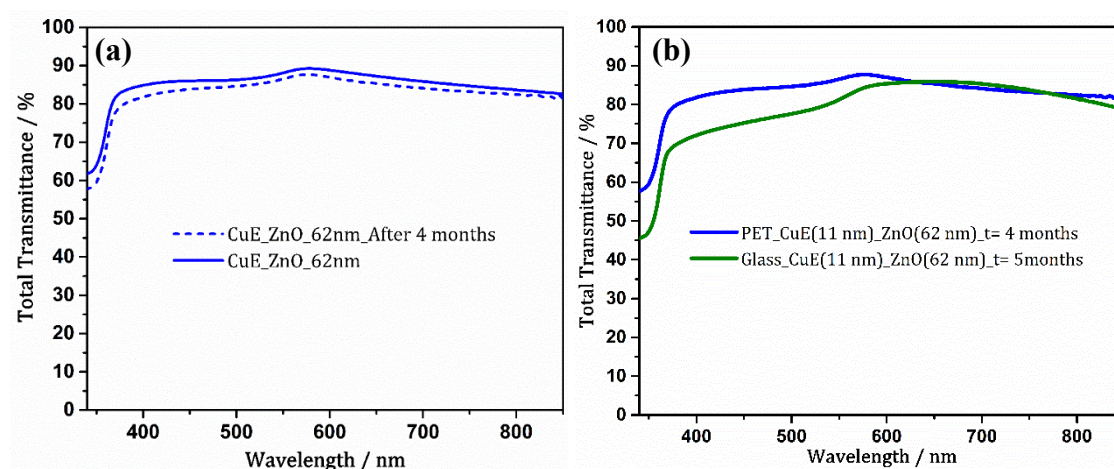


Figure 4.4: (a) Total far-field transparency of an 11 nm thick flexible CuE electrode with a ZnO (62 nm) over layer immediately after fabrication and following storage in a glove box for a period of 4 months and (b) comparison of the total far-field transparency of an 11 nm thick CuE electrode with a ZnO (62 nm) over layer supported on PET and glass after storage in a glove box for a period of 4 months and 5 months respectively.

An essential characteristic of flexible electrodes is the ability to sustain physical deformation without significant deterioration in R_{sh} . In order to evaluate how these Cu on PET electrodes behave upon deformation, a bending test was performed in which the electrode was bent repeatedly (100 times) through a 4 mm radius of curvature. Electrodes were bent inwards (compressed) and outwards (stretched) in separate experiments.

It is evident from the data in Figure 4.5 that there is negligible change in R_{sh} for Cu electrodes with and without apertures. In contrast the R_{sh} of the ITO on PEN deteriorate rapidly upon repeated bending. These differences in robustness can be rationalised in terms of metal thickness and the nature of the bonds in a metal as compared to ITO. The metal thickness in these electrodes (11 nm) is at least an order of magnitude thinner than the thickness of ITO and so the stress in the Cu film upon bending is proportionally lower. This together with the flexibility of metallic bonds between metal atoms enable moderate deformation without damaging the electrode. Additionally, unlike the directional covalent bonds in ITO, metallic bonds are flexible, enabling moderate elastic deformation.¹³

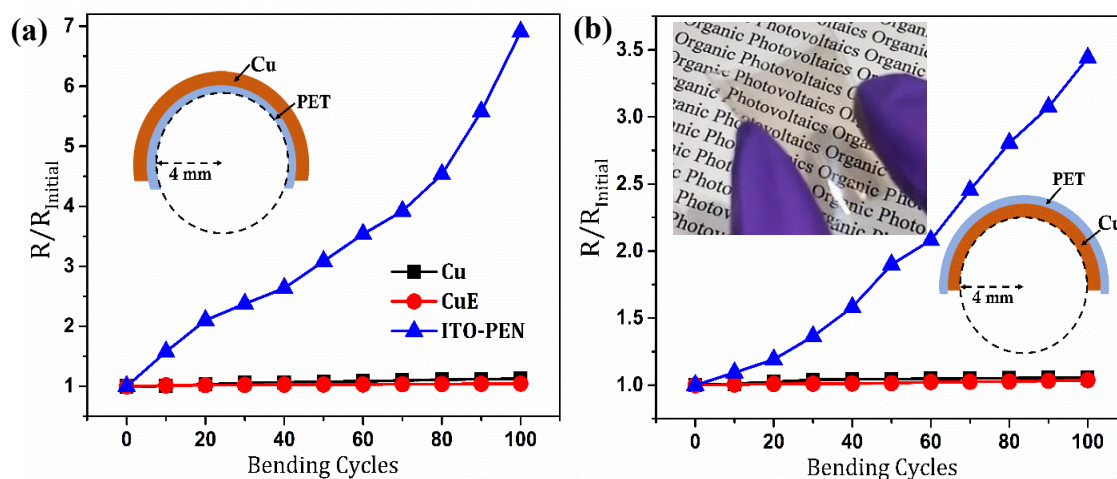


Figure 4.5: Change in R_{sh} when Cu, CuE electrodes supported on PET and ITO coated PEN electrodes are subjected to repeated bending in the (a) outward (stretched) and (b) inward (compressed) directions. *Inset:* A photograph of a flexible CuE electrode with a ZnO (~62 nm) over layer.

In order to test the applicability of these electrodes in flexible solution processed OPVs, devices were fabricated using PCE12 and *m*-ITIC as the donor and acceptor respectively in BHJ OPV devices with the architecture; transparent electrode /ZnO (β nm)/ PCE12 – *m*-ITIC (100 nm) /MoO_x (10 nm) / Ag (85 nm), where $\beta = 25$ -62 nm.

Whilst the maximum far-field transparency was achieved when the ZnO thickness was ~62 nm (Figure 4.3(a)) this was not the optimal thickness for OPV devices. When the ZnO thickness was varied, the best device performance was achieved for a ZnO thickness of ~33 nm (Table 4.1 and Figure 4.6(a)). Transfer matrix optical simulations of the entire device, with the extinction coefficient (k) for the BHJ set to zero, confirm that more light is coupled into the device when the ZnO thickness is 33 nm than when it is 62 nm: Figure 4.6(b) and (c)). Using this optimal ZnO thickness a champion PCE of 8.68 % (8.25 ± 0.32 %) was achieved, which is the highest efficiency reported to date for an OPV device using a Cu based window electrode.²⁸

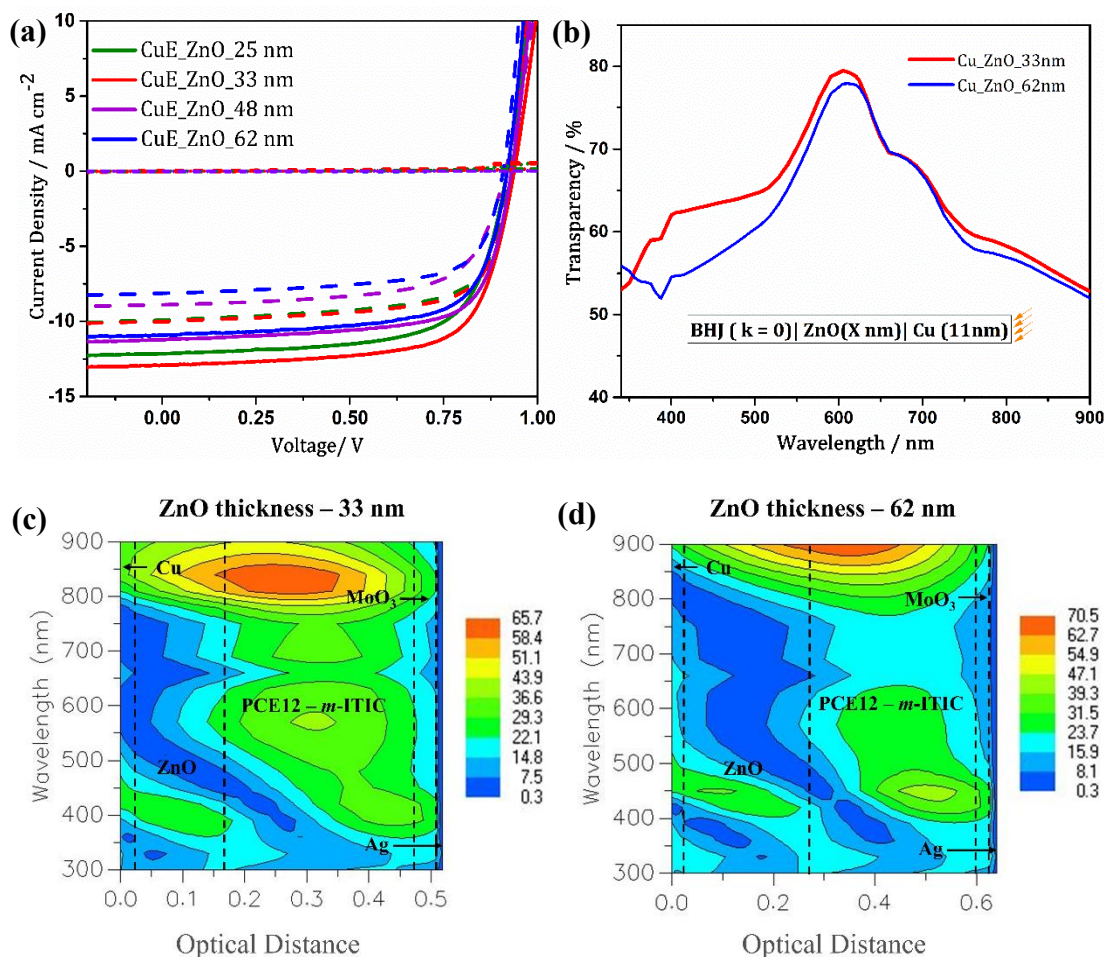


Figure 4.6: (a) Representative current density – voltage characteristics recorded under one sun simulated solar illumination (100 mW cm^{-2} ; AM 1.5G) for devices with the architecture: Cu (11nm) with (solid lines) and without (broken lines) nano-apertures / ZnO (β nm) / PCE12 – m-ITIC / MoO_x (10 nm) / Ag (85 nm); (b) Transfer-matrix simulation of the transmittance for an 11 nm thick unpatterned Cu electrode in an inverted OPV device with the architecture: Cu (11nm) / ZnO (β nm) / PCE12 – m-ITIC ($k = 0$) showing the amount of light entering the device; Simulated optical field variation for devices at different wavelengths with $k = 0$ for the BHJ when the thickness of ZnO is (c) 33 nm and (d) 62 nm for devices with the architecture: Cu (11 nm) / ZnO (β nm) / PCE12 – m-ITIC (100 nm) / MoO_x (10 nm) / Ag (85 nm).

It is evident from the EQE data in Figure 4.7(c) that the improvement in J_{sc} as compared to the electrode without apertures correlates with the increase in electrode transparency; being most enhanced for shorter wavelengths. Notably the dark current characteristics of both Cu and CuE electrodes exhibit suppressed forward current injection when compared to that under illumination. This significant change in J_{sc} at $V > V_{oc}$ in the dark, is associated with ZnO^{29,30} and will be discussed in chapter 5.

| Sample | ZnO Thickness /nm | Quantity | $J_{sc} \pm 1 SD$ / mA cm^{-2} | $V_{oc} \pm 1 SD$ / V | $FF \pm 1 SD$ | $PCE \pm 1 SD$ / % |
|-------------|-------------------|-----------------|---|-----------------------|-----------------|--------------------|
| Cu | 62 | Average | 8.28 ± 0.22 | 0.91 ± 0.01 | 0.69 ± 0.02 | 5.21 ± 0.22 |
| | | <i>Champion</i> | 8.66 | 0.92 | 0.70 | 5.61 |
| CuE | | Average | 11.19 ± 0.52 | 0.92 ± 0.02 | 0.68 ± 0.02 | 7.00 ± 0.51 |
| | | <i>Champion</i> | 11.90 | 0.94 | 0.70 | 7.85 |
| Cu | 48 | Average | 8.87 ± 0.24 | 0.91 ± 0.01 | 0.67 ± 0.01 | 5.39 ± 0.12 |
| | | <i>Champion</i> | 8.85 | 0.91 | 0.69 | 5.52 |
| CuE | | Average | 11.32 ± 0.55 | 0.93 ± 0.01 | 0.70 ± 0.01 | 7.32 ± 0.37 |
| | | <i>Champion</i> | 11.98 | 0.93 | 0.70 | 7.86 |
| Cu | 33 | Average | 10.16 ± 0.24 | 0.91 ± 0.02 | 0.66 ± 0.04 | 6.16 ± 0.27 |
| | | <i>Champion</i> | 10.07 | 0.93 | 0.70 | 6.52 |
| CuE | | Average | 12.67 ± 0.33 | 0.93 ± 0.01 | 0.70 ± 0.01 | 8.25 ± 0.32 |
| | | <i>Champion</i> | 13.19 | 0.94 | 0.70 | 8.68 |
| Cu | 25 | Average | 10.08 ± 0.57 | 0.91 ± 0.02 | 0.65 ± 0.02 | 5.97 ± 0.37 |
| | | <i>Champion</i> | 10.50 | 0.92 | 0.67 | 6.47 |
| CuE | | Average | 12.10 ± 0.62 | 0.91 ± 0.02 | 0.67 ± 0.03 | 7.43 ± 0.22 |
| | | <i>Champion</i> | 12.20 | 0.92 | 0.70 | 7.87 |
| ITO (PEN) | 33 | Average | 14.54 ± 0.23 | 0.85 ± 0.04 | 0.45 ± 0.02 | 5.60 ± 0.32 |
| | | <i>Champion</i> | 14.73 | 0.87 | 0.47 | 5.98 |
| ITO (Glass) | | Average | 15.51 ± 0.21 | 0.93 ± 0.01 | 0.70 ± 0.01 | 10.05 ± 0.19 |
| | | <i>Champion</i> | 15.73 | 0.94 | 0.70 | 10.32 |

Table 4.1: Summary of current density - voltage characteristics of devices with the architecture; Cu or CuE (11nm) or ITO on PEN/ ZnO (β nm) / PCE12 – m-ITIC (100 nm) / MoO_x (10 nm)/ Ag (85 nm) where β = 25-62 nm tested under 1 sun simulated solar illumination (100 mW cm^{-2} ; AM 1.5G). The error bars represent ± 1 standard deviation determined from the performance of 20-30 devices with identical architecture.

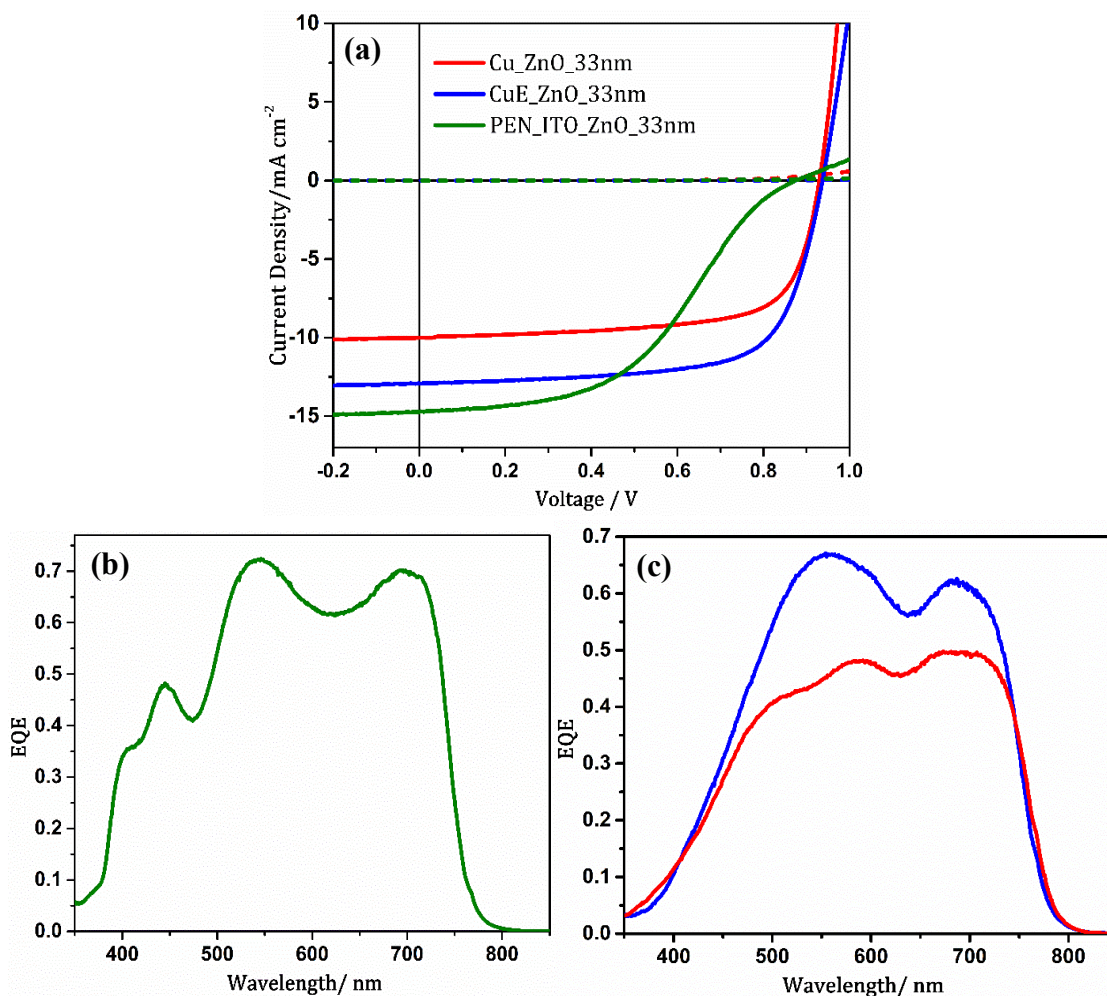


Figure 4.7: (a) Representative current density – voltage characteristics recorded under one sun simulated solar illumination (100 mW cm^{-2} ; AM 1.5G) for devices with the architecture: Transparent electrode / ZnO (33 nm) / PCE12 – *m*-ITIC (100 nm) / MoO_x (10 nm) / Ag (85 nm) and EQE recorded under same conditions for identical devices when the transparent electrode is (b) ITO coated PEN and (c) Cu (red) or CuE (blue).

To directly compare the performance of the Cu electrode on PET against commercial ITO coated plastic substrates, OPV devices were fabricated using ITO coated PEN as the transparent electrode. It is clear from Figure 4.7(a) and Table 4.1 that devices using the ITO electrode exhibit a higher J_{sc} ($14.5 \pm 0.2 \text{ mA cm}^{-2}$) than those using the Cu electrode ($12.8 \pm 0.25 \text{ mA cm}^{-2}$), but both the V_{oc} and FF are much lower in the former. The larger J_{sc} correlates with the higher far-field transmittance of ITO (Figure 4.3(a)) although this does not translate to a higher PCE because the FF is significantly degraded due to a s-shaped kink, which also erodes the V_{oc} . A s-shaped kink in the JV characteristic is typical of accumulation of one charge carrier type at an interface in the device.³⁰ Given that both OPVs are identical except in the choice of the transparent electrode, the interface in question must be that between the ITO and ZnO. Alternatively the s-shape kink may result from a local deterioration in the ITO conductivity due to deformation of the ITO layer by

the spring loaded pins connecting each device to the external circuit. The origin of the s-shaped kink in the JV characteristic is the subject of ongoing investigation, although the poor performance of inverted OPVs using ITO supported on PEN as the substrate electrode serves to highlight the inadequacy of this transparent substrate electrode for flexible OPVs. Thus, although identical devices on ITO coated glass exhibited a PCE over 10% (10.05 ± 0.19 %; Table 4.1 and Figure 4.8) in accordance with values reported for this particular BHJ, the PCE of the flexible ITO based devices were limited to 5.57 ± 0.36 %.

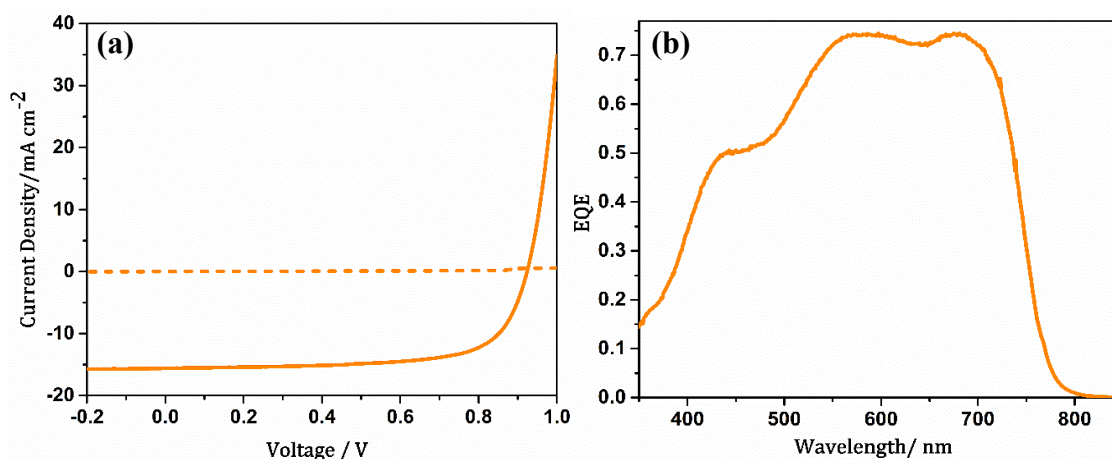


Figure 4.8: (a) Representative current density – voltage characteristics and (b) EQE recorded under one sun simulated solar illumination (100 mW cm^{-2} ; AM 1.5G) for devices with the architecture: ITO on glass / ZnO (33 nm) / PCE12 – m-ITIC / MoO_x (10 nm)/ Ag (85 nm).

4.4 Conclusion

In summary this chapter reports the fabrication of highly transparent flexible Cu window electrodes applicable to flexible OPVs. The fabrication process based on incorporation of over hundred million holes having a diameter of about 500 nm per cm² which was initially reported for optically thin Cu films on glass (chapter 3) has been successfully transferred to Cu on PET substrates resulting in a flexible electrode having a T_{avg} of 84.6 % (400 – 800 nm) with a R_{sh} of $11.3 \pm 1.5 \Omega \text{ sq}^{-1}$. This electrode enabled the fabrication of flexible OPV devices having a champion PCE of 8.68%, which is the highest reported PCE to date for a Cu based window electrode. The possibility of depositing the polymer mask used to fabricate the dense array of apertures by dip coating is demonstrated. Dip coating is a scalable deposition method compatible with roll-to-roll processing and bodes well for practical application of this type of electrode. Therefore, this approach which utilises simple self-organization of a polymer blend at ambient conditions and uses low toxic

solvents will be a powerful approach in fabrication of transparent flexible metal window electrodes for next-generation photovoltaics and related applications. It is also quite evident that the absorption edge for this BHJ system lies at $\lambda \sim 750$ nm, although a significant improvement in transparency is taking place at $\lambda > 750$ nm. Thus, if a ternary BHJ with multiple donor or multiple acceptor is employed a broader absorption of the solar spectrum (up to $\lambda \geq 1000$ nm) will lead to a higher J_{sc} contributing to an improved PCE³¹⁻³³ enabling the full potential of this electrode to be exploited.

4.5 References

- (1) Kippelen, B.; Brédas, J.-L.; Bredas, J.-L. Organic Photovoltaics. *Energ Env. Sci* **2009**, 2 (3), 251–261.
- (2) Ierides, I.; Zampetti, A.; Cacialli, F. The Resurgence of Organic Photovoltaics. *Curr. Opin. Green Sustain. Chem.* **2019**, 17, 15–20.
- (3) Dennler, G.; Sariciftci, N. S. Flexible Conjugated Polymer Based Plastic Solar Cells: From Basics to Applications. . *Proc. IEEE* **2005**, 93 (8), 1429–1439.
- (4) Mohammad Bagher, A. Comparison of Organic Solar Cells and Inorganic Solar Cells. *Int. J. Renew. Sustain. Energy* **2014**, 3 (3), 53.
- (5) Brabec, C. J. Organic Photovoltaics: Technology and Market. *Sol. Energy Mater. Sol. Cells* **2004**, 83 (2–3), 273–292.
- (6) Stoppa, M.; Chiolerio, A. Wearable Electronics and Smart Textiles: A Critical Review. *Sensors (Switzerland)* **2014**, 14 (7), 11957–11992.
- (7) Zamarayeva, A. M.; Ostfeld, A. E.; Wang, M.; Duey, J. K.; Deckman, I.; Lechene, B. P.; Davies, G.; Steingart, D. A.; Arias, A. C. Flexible and Stretchable Power Sources for Wearable Electronics. *Sci Adv* **2017**, 3 (6), e1602051.
- (8) Haacke, G. New Figure of Merit for Transparent Conductors. *J. Appl. Phys.* **1976**, 47 (9), 4086–4089.
- (9) Haacke, G. Transparent Conducting Coatings. *Annu. Rev. Mater. Sci.* **1977**, 7 (1), 73–94.
- (10) Garner, S. M. *Flexible Glass : Enabling Thin, Lightweight, and Flexible Electronics*; 2017.
- (11) Galagan, Y.; J.m. Rubingh, J. E.; Andriessen, R.; Fan, C. C.; W.m. Blom, P.; Veenstra, S. C.; Kroon, J. M. ITO-Free Flexible Organic Solar Cells with Printed Current Collecting Grids. *Sol. Energy Mater. Sol. Cells* **2011**, 95 (5), 1339–1343.
- (12) Zou, J.; Li, C. Z.; Chang, C. Y.; Yip, H. L.; Jen, A. K. Y. Interfacial Engineering of Ultrathin Metal Film Transparent Electrode for Flexible Organic Photovoltaic Cells. *Adv. Mater.* **2014**, 26 (22), 3618–3623.
- (13) Alzoubi, K.; Hamasha, M. M.; Lu, S.; Sammakia, B. Bending Fatigue Study of

- Sputtered ITO on Flexible Substrate. *J. Disp. Technol. Ieee* **2011**, 7 (11), 593–600.
- (14) Rathmell, A. R.; Wiley, B. J. The Synthesis and Coating of Long, Thin Copper Nanowires to Make Flexible, Transparent Conducting Films on Plastic Substrates. *Adv. Mater.* **2011**, 23 (41), 4798–4803.
- (15) Stec, H. M.; Hatton, R. A. Widely Applicable Coinage Metal Window Electrodes on Flexible Polyester Substrates Applied to Organic Photovoltaics. *ACS Appl. Mater. Interfaces* **2012**, 4 (11), 6013–6020.
- (16) De Arco, L. G.; Zhang, Y.; Schlenker, C. W.; Ryu, K.; Thompson, M. E.; Zhou, C. Continuous, Highly Flexible, and Transparent Graphene Films by Chemical Vapor Deposition for Organic Photovoltaics. *ACS Nano* **2010**, 4 (5), 2865–2873.
- (17) Yu, L.; Shearer, C.; Shapter, J. Recent Development of Carbon Nanotube Transparent Conductive Films. *Chem. Rev.* **2016**, 116 (22), 13413–13453.
- (18) Lee, J.; Lee, P.; Lee, H.; Lee, D.; Lee, S. S.; Ko, S. H. Very Long Ag Nanowire Synthesis and Its Application in a Highly Transparent, Conductive and Flexible Metal Electrode Touch Panel. *Nanoscale* **2012**, 4 (20), 6408.
- (19) Hu, L.; Wu, H.; Cui, Y. Metal Nanogrids, Nanowires, and Nanofibers for Transparent Electrodes. *MRS Bull.* **2011**, 36 (10), 760–765.
- (20) Park, H.; Chang, S.; Zhou, X.; Kong, J.; Palacios, T.; Gradecak, S. Flexible Graphene Electrode-Based Organic Photovoltaics with Record-High Efficiency. *ECS Trans.* **2015**, 69 (14), 77–82.
- (21) Naik, G. V.; Shalaev, V. M.; Boltasseva, A. Alternative Plasmonic Materials: Beyond Gold and Silver. *Adv. Mater.* **2013**, 25 (24), 3264–3294.
- (22) West, P. R.; Ishii, S.; Naik, G. V.; Emani, N. K.; Shalaev, V. M.; Boltasseva, A. Searching for Better Plasmonic Materials. *Laser Photonics Rev.* **2010**, 4 (6), 795–808.
- (23) Pereira, H. J.; Hutter, O. S.; Dabera, G. D. M. R.; Rochford, L. A.; Hatton, R. A. Copper Light-Catching Electrodes for Organic Photovoltaics. *Sustain. Energy Fuels* **2017**, 1 (4), 859–865.
- (24) Pereira, H. J.; Reed, J.; Lee, J.; Varagnolo, S.; Dabera, G. D. R.; Hatton, R. A. Fabrication of Copper Window Electrodes with $\approx 10^8$ Apertures cm^{-2} for

- Organic Photovoltaics. *Adv. Funct. Mater.* **2018**, 28 (36), 1802893.
- (25) Burdick, G. A. Energy Band Structure of Copper. *Phys. Rev.* **1963**, 129 (1), 138–150.
- (26) Stec, H. M.; Williams, R. J.; Jones, T. S.; Hatton, R. A. Ultrathin Transparent Au Electrodes for Organic Photovoltaics Fabricated Using a Mixed Mono-Molecular Nucleation Layer. *Adv. Funct. Mater.* **2011**, 21 (9), 1709–1716.
- (27) Scriven, L. E. Dip Coating and Spin Coating. *MRS Proc.* **1988**, 121, 717–729.
- (28) Jeong, G.; Jung, S.; Choi, Y.; Lee, J.; Seo, J.; Kim, D. S.; Park, H. A Highly Robust and Stable Graphene-Encapsulated Cu-Grid Hybrid Transparent Electrode Demonstrating Superior Performance in Organic Solar Cells. *J. Mater. Chem. A* **2018**, 6 (48), 24805–24813.
- (29) Manor, A.; Katz, E. A.; Tromholt, T.; Krebs, F. C. Enhancing Functionality of ZnO Hole Blocking Layer in Organic Photovoltaics. *Sol. Energy Mater. Sol. Cells* **2012**, 98, 491–493.
- (30) Pereira, H. J.; Hatton, R. A. Copper Substrate Electrode for Efficient Top-Illuminated Organic Photovoltaics. *ACS Appl. Mater. Interfaces* **2018**, acsami.8b18453.
- (31) Huang, W.; Cheng, P.; Yang, Y. M.; Li, G.; Yang, Y. High-Performance Organic Bulk-Heterojunction Solar Cells Based on Multiple-Donor or Multiple-Acceptor Components. *Adv. Mater.* **2018**, 30 (8), 1–24.
- (32) Xiao, Z.; Jia, X.; Ding, L. Ternary Organic Solar Cells Offer 14% Power Conversion Efficiency. *Sci. Bull.* **2017**, 1562 (2016), 2016–2019.
- (33) An, Q.; Zhang, F.; Zhang, J.; Tang, W.; Deng, Z.; Hu, B. Versatile Ternary Organic Solar Cells: A Critical Review. *Energy Environ. Sci.* **2016**, 9 (2), 281–322.

Chapter 5

Copper Substrate Electrode for Efficient Top-illuminated Organic Photovoltaics

The work presented in this chapter has been published in:

H. J. Pereira, R. A. Hatton, Copper Substrate Electrodes for Efficient Top-illuminated Organic Photovoltaics, *ACS Applied Materials and Interfaces*, 2019, 11(1) pp 43-48, DOI: 10.1021/acsami.8b18453

5.1 Background

OPV devices have recently achieved a record PCE of 17.3%¹ using solution processed BHJ light harvesting layers and so have reached the efficiency needed for a broad range of emerging applications.²⁻⁴ Key advantages of OPVs over other thin film PVs, is their compatibility with high-speed roll-to-roll processing and that rare or toxic elements can be completely avoided, which minimises materials cost⁵ and ensures environmental sustainability. Many different OPV device architectures have been developed falling into the categories of conventional, inverted, top-illuminated, semi-transparent and multi-junction, each offering advantages for particular applications or fabrication methods. For OPVs based on a single BHJ layer, conventional wisdom dictates that the PCE is maximised when one of the electrodes is highly reflective across the full range of wavelengths over which the BHJ absorbs, because the thickness of the BHJ in most efficient single junction OPVs reported to date is only 100-150 nm, which is insufficient to absorb all of the incident light across all wavelengths on the first pass through the BHJ layer. This constraint on the thickness of the light harvesting layer stems from the low and mismatched charge carrier mobility in the donor and acceptor phases comprising the BHJ.⁶⁻⁸ However, in recent years there has been a concerted effort towards developing solution processed OPVs with high performance using a much thicker BHJ of up to 400 nm,⁹⁻¹¹ because it is now clear that the high defect density associated with much thinner BHJ layers, together with the difficulty in achieving a uniform layer thickness over large areas using low cost printing methods when the BHJ is very thin, are serious obstacles to scaling up for potential applications.^{8,12-15} Whilst there are relatively few BHJs suitable for thick-junction OPVs, this paradigm is beginning to shift since it is now understood that if the charge carrier mobility in the donor and acceptor phases are sufficiently high

and well matched it is possible to increase the junction thickness^{8,14} to ~400 nm without incurring an unacceptable increase in device series resistance.^{8-11,14} At the same time, for many applications the top-illuminated device architecture, in which the substrate electrode is the opaque electrode and light enters the device through the transparent top electrode,¹⁶ is particularly attractive for a wide range of applications including in automotive¹⁷ and buildings integration^{17,18} applications. Using an opaque bottom electrode has the advantage that it enables much more flexibility towards the choice of substrate by removing the need to use conducting oxide coated glass or plastic.¹⁹ Whilst there have been continuous developments in the materials used for top-illuminated OPVs with regard to device engineering²⁰⁻²³, the substrate electrode used is invariably Ag because it is highly reflective in the wavelength range of 350 – 900 nm and offers good stability towards oxidation in air.^{20,22,24} However, using a Ag layer that is sufficiently thick to be opaque (> 80 nm) as the reflective electrode seriously erodes the cost advantage of OPVs,²⁵ since Ag is a high cost metal. Consequently, there is a need to identify a viable much lower cost alternative to Ag for this important emerging application space. Cu is an attractive replacement for Ag in this context because it is less than 1% of the cost of Ag with comparable electrical conductivity.^{26,27} However to date there are no reports of using Cu as the reflective substrate electrode in top-illuminated OPVs because the reflectance of Cu for wavelengths < 600 nm is less than 60% of that of Ag due to absorptive losses associated with inter-band transitions,^{26,28} which renders it unsuitable for OPVs with a light harvesting layer ≤ 150 nm. Additionally, Cu is more susceptible to air oxidation than Ag, limiting the extent to which Cu electrodes can be manipulated in air prior to device fabrication, and arguably also limiting the long-term device stability, since slow air ingress into the device is inevitable. Addressing the latter issue, it has recently been shown that Cu can be passivated towards oxidation in air without electrical isolation or significantly altering the optical properties, rendering it as stable as Ag.²⁹

This chapter shows that Cu can be used in place of Ag as the reflective substrate electrode in high performance top-illuminated OPVs, without compromising device PCE when the photo-active layer is thick enough to absorb majority of the incident photons with energies above the optical band gap, on first pass through the photo-active layer. Since Cu is approximately one hundredth of the cost of Ag, its use as a drop-in replacement for Ag in thick film OPVs will help to significantly reduce the bill of materials for OPV manufacture.

5.2 Experimental Methods

Experimental details specific to the work presented in this chapter are as follows;

5.2.1 Substrate cleaning

Glass substrates of the required dimension were cut and cleaned as described in section 2.1 and 2.2.

5.2.2 Mixed monolayer deposition

A mixed monolayer was deposited prior to evaporation of Cu by exposing the substrates to vapours of MPTMS and APTMS at 50 mbar for 4 hours immediately after UV/O₃ treatment. For Ag electrodes monolayer deposition was done using only MPTMS.

5.2.3 Deposition of Cu and Ag

Cu was deposited by thermal evaporation of Cu pellets at a rate of 2.2 – 2.5 Å s⁻¹ and Ag by thermal evaporation of Ag pellets at a rate of 1.0 – 1.5 Å s⁻¹ to give the required thickness.

5.2.4 Optical transparency and reflectance measurements

Far-field transmittance and reflectance of metal films on glass were measured over the wavelength range of 350 – 850 nm using a 150 mm Spectralon® Integrating Sphere coupled to PerkinElmer® LAMBDA™ high performance UV/Vis spectrometer. Measurements were performed with reference to the air.

5.2.5 Fabrication of OPV devices

A ZnO ink (5.6% w/v) in IPA was purchased from Infinity PV and a diluted solution (0.5% w/v) was spun at 1000 rpm for 60 seconds followed by annealing at 180 °C for 15 minutes to fabricate the ETL. For devices that used Al as the ETL, a thin layer of Al (0.8 nm) was deposited by thermal evaporation. For these devices both the metal (Cu or Ag) and Al were evaporated under the same vacuum. PCE10 and PC₇₀BM were mixed in 2:3 mass ratio to make a 35 mg ml⁻¹ solution in dichlorobenzene (97%) and 1,8-diiodooctane (3%) and deposited by spin coating from a static start at 3000 rpm for 120 seconds to form a photo-active layer having a thickness of 100 nm. For thicker BHJs a solution having a higher concentration of 50 mg ml⁻¹ was used and was spun at 2500 rpm and 1500 rpm to obtain a thickness of 300 nm and 400 nm respectively. These slides were left inside the evaporator overnight and MoO_x (10 nm at 0.1-0.2 Å s⁻¹) was deposited as the HTL followed by Ag (11 nm at 1.0-1.2 Å s⁻¹) as the top transparent electrode. Ag was deposited through a shadow mask to give an electrode area of 0.06 cm².

5.2.6 Characterization of OPV devices

Current density-voltage (JV) testing was performed as described in section 2.17 and EQE measurements were done as described in section 2.18 in the wavelength range of 300 – 850 nm.

5.3 Results and Discussion

Optically thick metal films were deposited onto glass substrates modified with a monolayer of MPTMS for Ag, and a mixed monolayer of MPTMS and APTMS for Cu. These molecular adhesive layers ensure that the metal films are smooth and compact by nucleating slab-like film growth at a very low thickness, which helps to ensure that parasitic losses due to surface plasmon excitation²⁸ are minimised.³⁰ A PCE10/PC₇₀BM BHJ was employed as the photo-active material for this study because PCE10 and PC₇₀BM have well-matched electron and hole mobility enabling a study of BHJ thickness of up to 400 nm.³¹

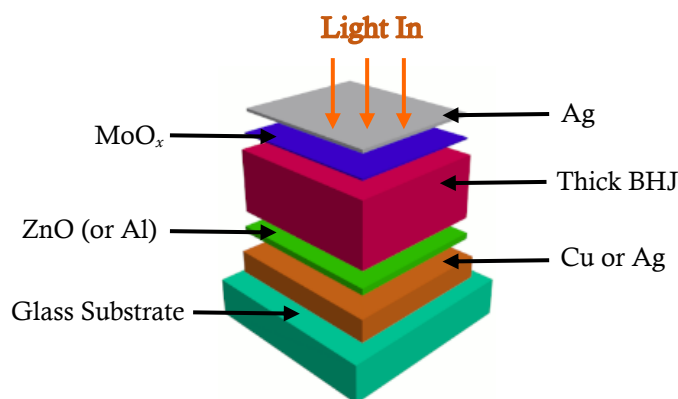


Figure 5.1: Schematic showing the top-illuminated device architecture.

In the first instance inverted OPVs (Figure 5.1) were fabricated using the previously reported optimal thickness for PCE10/PC₇₀BM heterojunctions of ~100 nm.³² In such a thin BHJ the light distribution across the photoactive layer is strongly determined by the interference between the incoming light and that reflected from the back electrode, and charge carriers are generated within the bulk of the photo-active layer regardless of the incident photon energy.¹² It is evident from Figure 5.2 that the reflectance of the Cu electrode is much lower than that of Ag for wavelengths ≤ 600 nm, falling to less than 60% for wavelengths below 550 nm, which would be expected to result in a significantly reduced J_{sc} compared to identical devices using Ag as the reflective substrate electrode. However, it is important to recognize that the solar photon flux³³ drops away steeply for

wavelengths < 500 nm (Figure 5.2), which moderates the adverse impact of the lower reflectivity of Cu in this region.

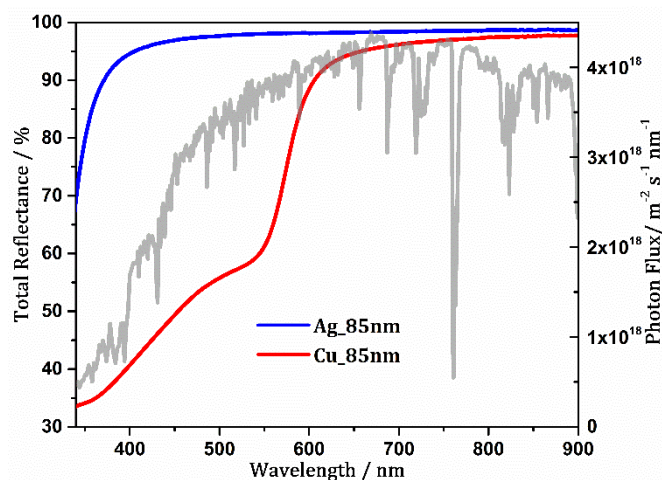


Figure 5.2: Total reflectance of 85 nm thick Ag and Cu electrodes deposited by vacuum evaporation on glass substrates derivatized with a silane molecular adhesive layer together with the AM 1.5G solar photon flux spectrum overlaid in the background.

It is however apparent from the JV characteristics given in Figure 5.3(a), that the change in J_{sc} when Cu is used in place of Ag is relatively small and there is no significant change in V_{oc} or device FF . The EQE for devices using Cu as the substrate electrode (Figure 5.3 (b)) is lower than for devices using Ag for wavelengths < 600 nm but converges for wavelengths ≥ 650 nm, and in both cases the EQE is highest for wavelengths > 600 nm, which is qualitatively consistent with the difference in the reflectance of the Cu and Ag substrate electrodes weighted by the solar photon flux.

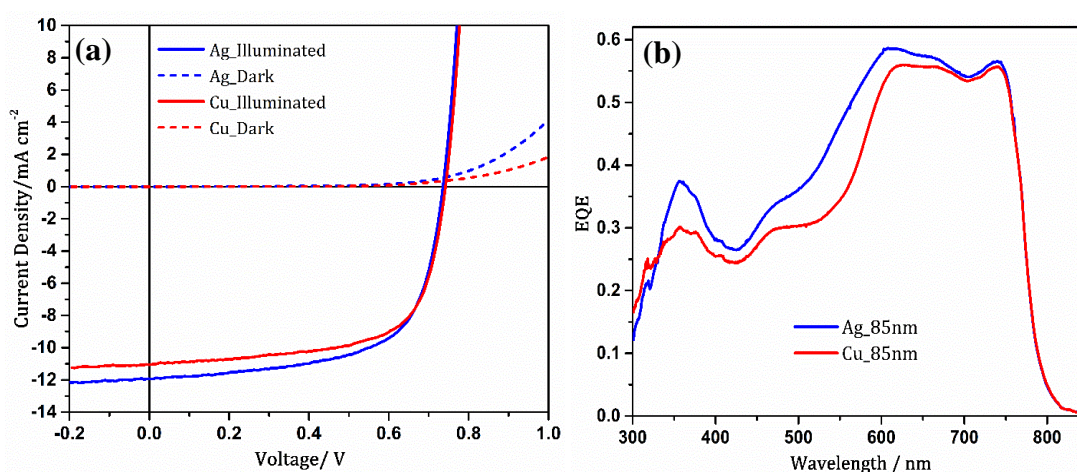


Figure 5.3: Representative (a) current density - voltage (JV) characteristics and (b) EQE measured under one sun simulated solar illumination (100 mW cm^{-2} ; AM 1.5G) for devices with the architecture: Cu or Ag (85nm) / ZnO (25 nm) / PCE10 – PC₇₀BM (100 nm) / MoO_x (10 nm) / Ag (11 nm).

Simulations of the optical field distribution using transfer matrix model with extinction coefficient, $k = 0$ for the BHJ (Figure 5.4(a) & (b)), show that there is a cavity resonance condition at $\lambda \sim 700$ nm, and so photons with wavelength at and near to this value make a disproportionate contribution to J_{sc} as is evident from the EQE. Consequently, because of this strong optical interference effect, the average PCE when Cu is used as the substrate electrode is only fractionally lower than when Ag is used (5.56% and 5.79% respectively (Table 5.1)).

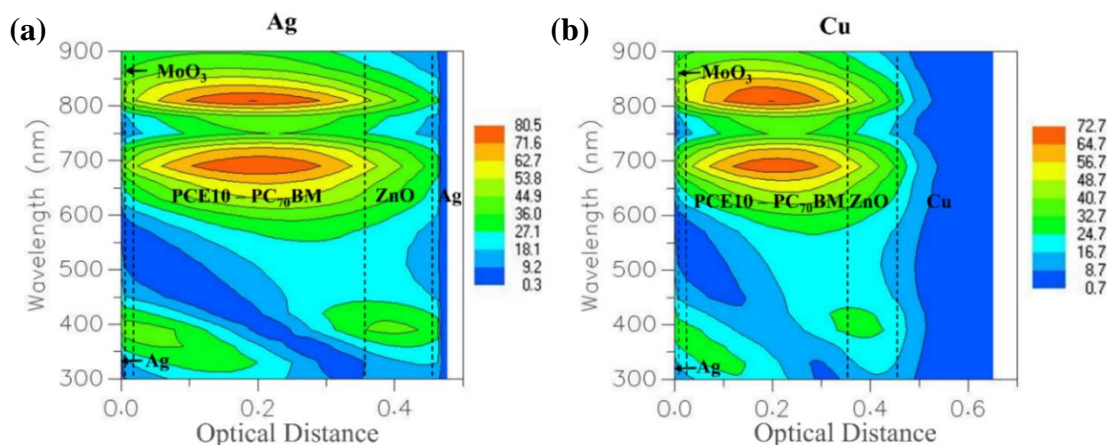


Figure 5.4: Simulated optical field variation for devices at different wavelengths with $k = 0$ for the BHJ when (a) Ag and (b) Cu are used as back electrodes for devices with the architecture: Cu or Ag (85nm) / ZnO (25 nm) / PCE10 – PC₇₀BM (100 nm) / MoO_x (10 nm) / Ag (11 nm).

| Bottom Electrode | Active Layer Thickness/ nm | $J_{sc} \pm 1SD$ / mA cm ⁻² | $V_{oc} \pm 1SD$ / V | $FF \pm 1SD$ | %PCE $\pm 1SD$ |
|------------------|----------------------------|--|----------------------|-----------------|-----------------|
| Cu | 100 | 11.06 \pm 0.24 | 0.76 \pm 0.02 | 0.66 \pm 0.01 | 5.56 \pm 0.23 |
| | 300 | 10.62 \pm 0.11 | 0.74 \pm 0.01 | 0.60 \pm 0.01 | 4.68 \pm 0.18 |
| | 400 | 10.68 \pm 0.21 | 0.74 \pm 0.01 | 0.54 \pm 0.01 | 4.32 \pm 0.16 |
| Ag | 100 | 11.97 \pm 0.44 | 0.75 \pm 0.02 | 0.64 \pm 0.01 | 5.79 \pm 0.32 |
| | 300 | 10.53 \pm 0.07 | 0.74 \pm 0.01 | 0.59 \pm 0.01 | 4.61 \pm 0.10 |
| | 400 | 10.84 \pm 0.22 | 0.74 \pm 0.01 | 0.52 \pm 0.01 | 4.18 \pm 0.15 |

Table 5.1: Summary of current density - voltage characteristics of devices with the architecture; Cu or Ag (85nm) / ZnO (25 nm) / PCE10 – PC₇₀BM (Z nm) / MoO_x (10 nm) / Ag (11 nm); where Z = 100 - 400 nm, tested under 1 sun simulated solar illumination (100 mW cm⁻²; AM 1.5G). The error bars represent ± 1 standard deviation ($\pm 1SD$) determined from the performance of 20 - 30 devices with identical architecture.

Interestingly, when devices with a similar BHJ thickness were fabricated with a thin layer of Al (0.8 nm) as the ETL in place of ZnO, a clear difference in the efficiency of charge extraction was observed as shown in the EQE given in Figure 5.5(b). It is evident that

although the performance is similar at $\lambda > 600$ nm, the devices with a Ag reflective electrode extract charges more efficiently in the wavelength range of $\lambda \sim 450 - 600$ nm, contributing to a larger J_{sc} of 12.36 ± 0.35 mA cm⁻² in comparison to an identical device with a Cu electrode (Figure 5.5(b)). As evidenced by the optical simulation data given in Figure 5.5(c) & (d), the underlying reason for this observation is clearly a shift in the position of the cavity resonance to a lower wavelength ($\lambda < 550$ nm) where the reflectance of Cu drops rapidly compared to that of Ag. Hence, at this wavelength range Cu is unable to compete with the superior charge extraction of Ag, resulting in a lower J_{sc} of 11.22 ± 0.33 mA cm⁻². However in terms of overall device performance, the gap between the PCE of devices based on Ag and Cu electrodes is still small, considering the reflectance of Cu at shorter wavelengths, and the only contribution to this difference stems from the J_{sc} as V_{oc} and FF are similar for both sets of devices. Therefore in the context of thin BHJs, the performance gap between devices that use Cu and Ag reflective substrate electrodes is dependent on the optical field distribution within the device.

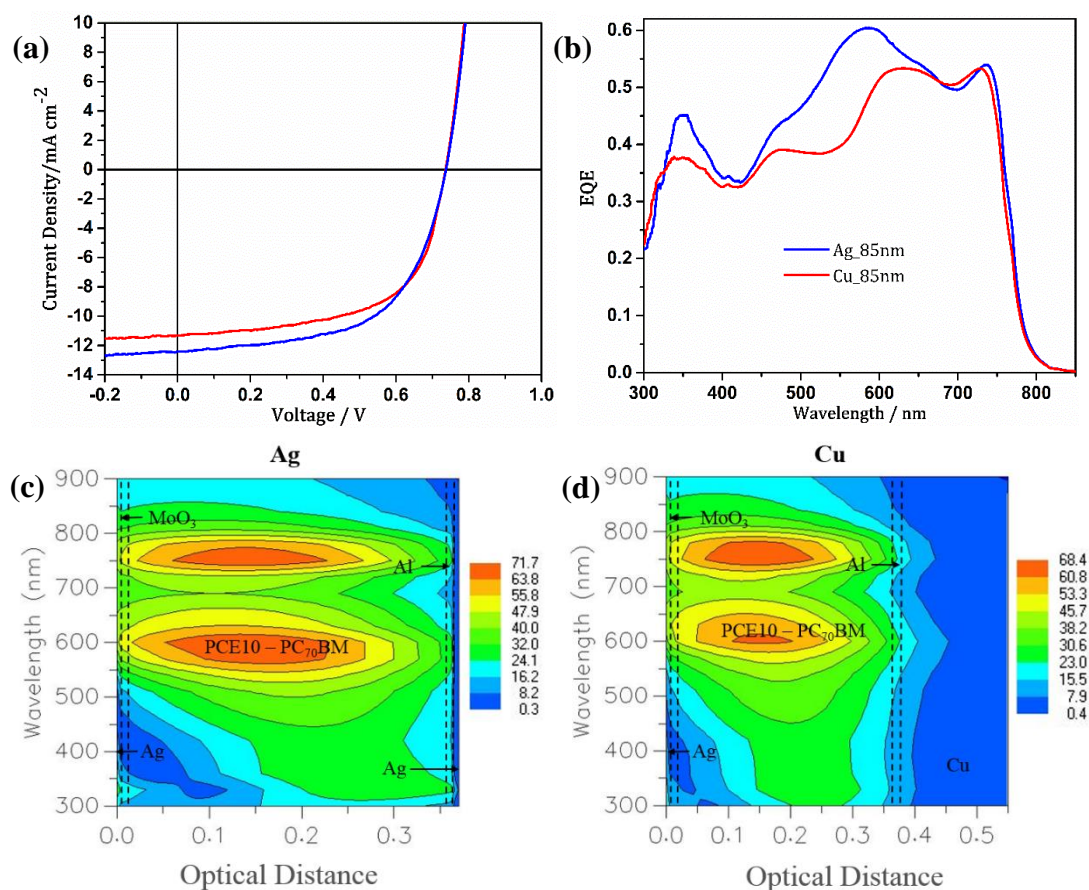


Figure 5.5: Representative (a) current density - voltage (JV) characteristics and (b) EQE measured under one sun simulated solar illumination (100 mW cm⁻²; AM 1.5G) for devices with the architecture: Cu or Ag (85nm) / Al (0.8 nm) / PCE10 - PC₇₀BM (100 nm) / MoO_x (10 nm) / Ag (11 nm). Simulated optical field variation for OPV devices at different wavelengths with $k = 0$ for the BHJ when (c) Ag and (d) Cu are used as reflective substrate electrodes.

Devices that use ZnO as the ETL exhibited slightly better overall performance and therefore subsequent experiments were based on devices with this architecture. It was shown in chapter 3 that spontaneous diffusion of Cu to ZnO occurs upon annealing at 180 °C for 15 mins³⁴ and this was also shown to be accompanied by an increase in total reflectance at shorter wavelengths for optically thin Cu electrodes. Thus in order to study the effects of annealing these thick metal films, total reflectance was measured after annealing the samples at 180 °C for 15 mins and 45 mins. The annealing time was extended to 45 mins with the intention of facilitating further diffusion as the migration of Cu into ZnO was observed to increase overtime. However, as shown in Figure 5.6, the incorporation of ZnO slightly reduces the total reflectance at $\lambda < 430$ nm for Ag and at $\lambda < 570$ nm for thick Cu films and there is no apparent change arising from annealing time as metal films annealed for 15 mins and 45 mins show identical reduction (curves are one over the other). Interestingly, these positions correspond with the wavelengths at which inter-band transition losses begin to rise in the two metals; at $\lambda < 450$ nm for Ag and $\lambda < 600$ nm for Cu.²⁶ As the diffusion of Cu into ZnO progresses, ZnO becomes more metallic in character with more free electrons than its pure counterpart and the parasitic absorption losses associated with these electrons may contribute towards a reduction in total reflectance. As a similar explanation can be given for Ag, it is possible that annealing Ag films under same conditions causes Ag to diffuse into ZnO. A small degree of this reduction in reflectance may also be due to absorption of ZnO (Figure 5.6(b)) but it is limited to very short wavelengths ($\lambda < 370$ nm).

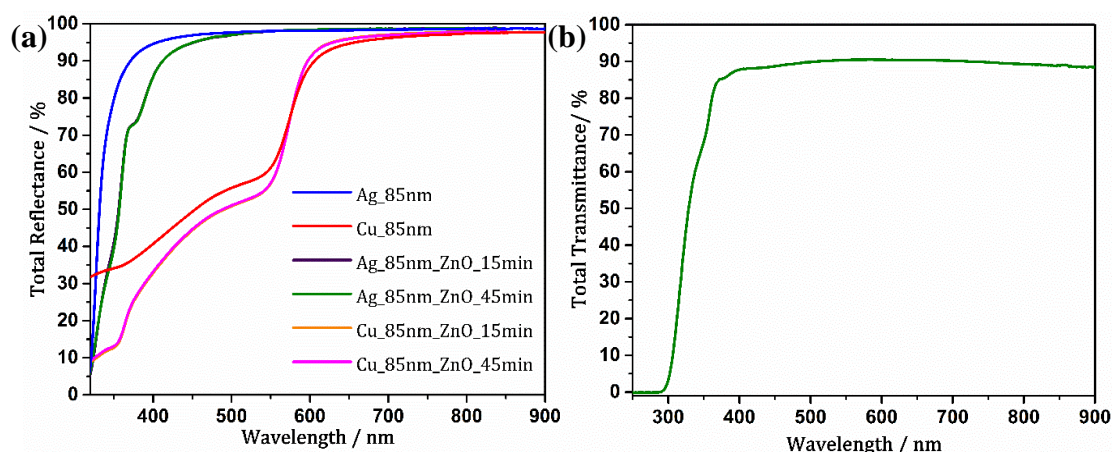


Figure 5.6: (a) Total Reflectance of thick Cu and Ag films (85 nm) before and after deposition of ZnO followed by annealing at 180 °C for 15 mins and 45 mins; and (b) total transmittance of ZnO (25 nm) deposited on glass.

For these devices, the thickness of the photo-active layer was ~ 100 nm and so over the wavelength range of 400 – 700 nm nearly 50% of the incident light is not absorbed on the first pass through the BHJ layer: Figure 5.7(a). Consequently, the absorption of this residual light strongly depends on the efficient reflectance from the bottom substrate electrode, which directs the unabsorbed light back through the photo-active layer. Increasing the thickness of the photo-active layer increases the total amount of light absorbed on the first pass through the BHJ and when the thickness is increased to 400 nm the average absorbed light between 400 - 700 nm is increased to $\sim 80\%$.

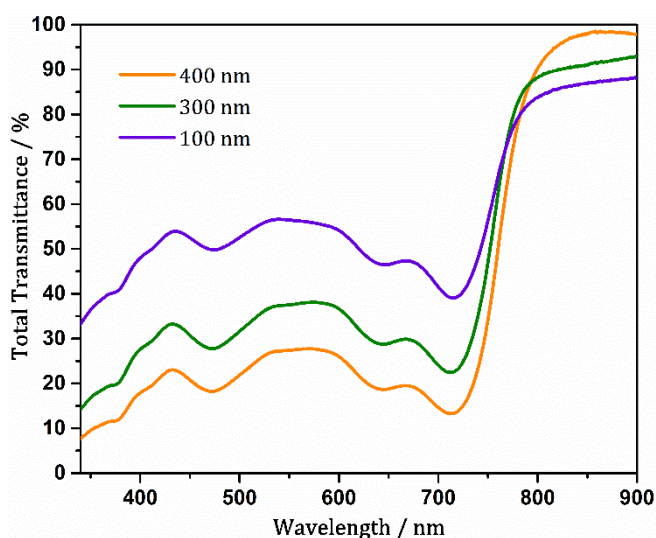


Figure 5.7: Total transmittance of PCE10 – PC₇₀BM BHJ at different film thicknesses.

Simulations of the optical intensity with $k = 0$ for the BHJ, show that for these thicker layers there are several cavity resonant modes occurring at wavelengths ~ 450 nm, ~ 680 nm and ~ 820 nm for a 300 nm thick BHJ and at ~ 425 nm, ~ 575 nm and ~ 750 nm for the 400 nm thick BHJ (Figure 5.8). However, in the limit where all of the incident light is absorbed on the first pass through the BHJ only the cavity resonance effect at the optical edge is of importance for photocurrent generation, since for shorter wavelengths there is a Beer-Lambert like optical field distribution.

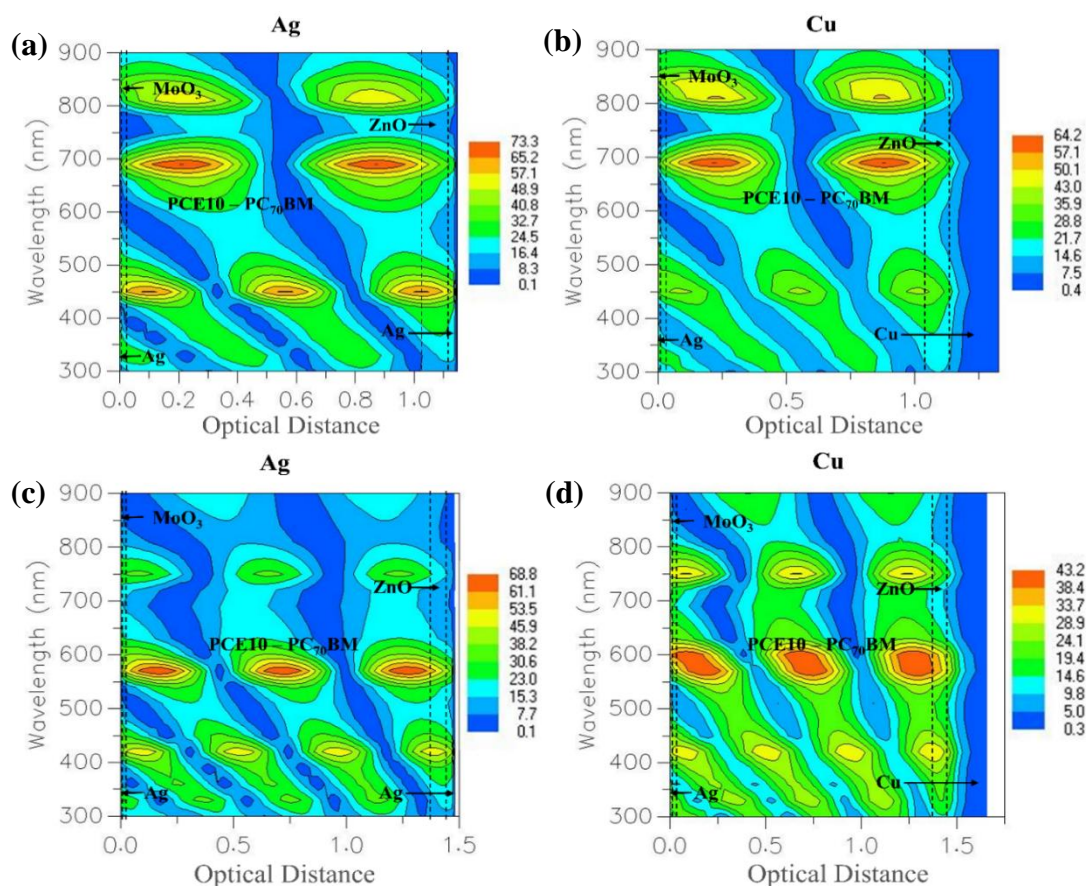


Figure 5.8: (a) Transfer matrix simulation of the optical field in OPV devices with the structure: reflective substrate electrode / ZnO (25 nm) / PCE10 – PC₇₀BM (Z nm) / MoO_x (10 nm) / Ag (11 nm). When Z = 300 nm and the reflective substrate electrode is 85 nm of (a) Ag or (b) Cu and when Z = 400 nm and the reflective substrate electrode is 85 nm of (c) Ag or (d) Cu.

It is evident from Figure 5.9 that with increasing BHJ layer thickness, the J_{sc} and shape of the EQE spectrum when Ag and Cu are used as substrate electrodes converge, such that they are essentially identical when the BHJ is 400 nm in thickness. Increasing the thickness from 300 nm to 400 nm also shifts the cavity resonance so that it is more closely matched to the absorption edge: Figure 5.8, which is a significant advantage since it helps to extend the light harvesting capability of the device by a further ~50 nm as evidenced by Figure 5.9(c) & (d).

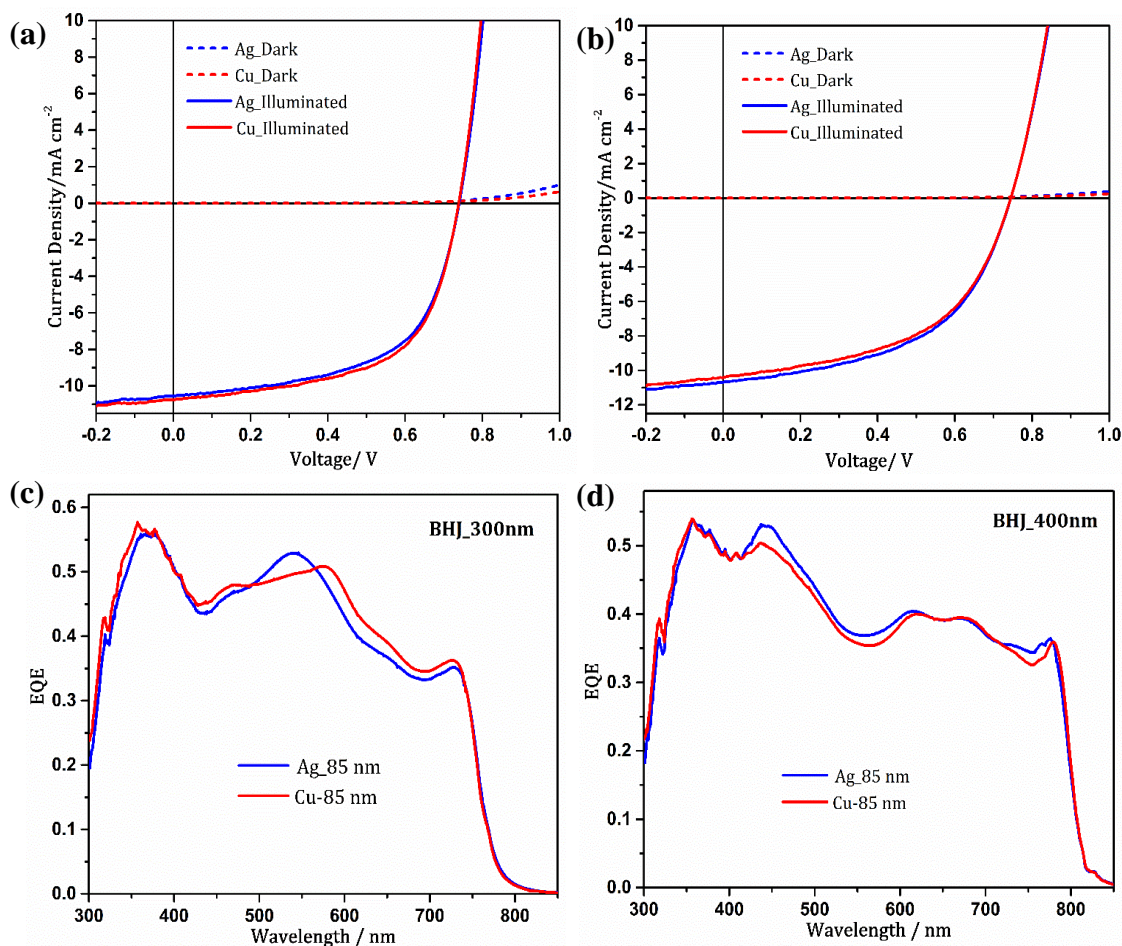


Figure 5.9: Representative current density – voltage characteristics for devices with the architecture: Cu or Ag (85 nm) / ZnO (25 nm) / PCE10 – PC₇₀BM (Z nm) / MoO_x (10 nm) / Ag (11 nm) measured under one sun simulated solar illumination (100 mW cm⁻²; AM 1.5G) where (a) Z = 300 nm and (b) Z = 400 nm; (c) and (d) are representative EQE for devices given in (a) and (b) respectively.

Notably, in Figures 5.3 and 5.9 the onset of forward current injection in the dark is greatly suppressed as compared to that under illumination, which is atypical for OPVs. The large disparity in current density in the dark and light for $V > V_{oc}$ disappears after a few minutes of constant illumination, although is restored when the device is kept in the dark for an extended period: Figure 5.10(a). When the ZnO layer is substituted with a very thin (0.8 nm) Al layer²⁹ (which also enables efficient extraction of electrons as shown in Figure 5.5) this anomaly in the dark current characteristic does not occur; Figure 5.10(b), indicating that it is associated with the use of a ZnO ETL. This behaviour has previously been reported for OPVs using a ZnO electron extraction layer and is attributed to UV light induced O₂ desorption from ZnO, followed by its re-adsorption in the dark.³⁵

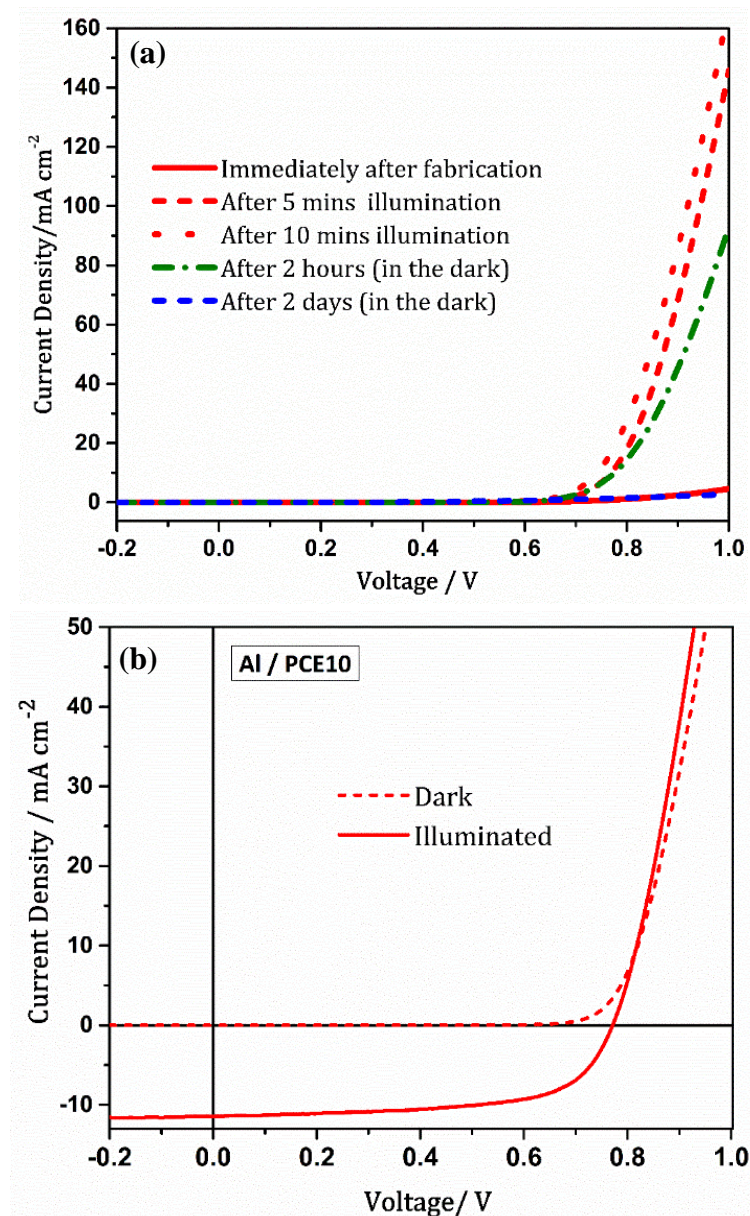


Figure 5.10: (a) Representative dark current density – voltage (JV) characteristics for top-illuminated OPV devices with the architecture: Cu (85 nm) / ZnO (25 nm) / PCE10 – PC₇₀BM (100 nm) / MoO_x (10 nm) / Ag(11 nm) measured after different periods of exposure under one sun simulated solar illumination and (b) representative JV characteristics for top-illuminated OPV devices with the architecture: Cu (85 nm) / Al (0.8 nm) / PCE10 – PC₇₀BM (100 nm) / MoO_x (10 nm) / Ag (11 nm) measured under same conditions (100 mW cm⁻²; AM 1.5G).

Notably, the PCE of model top-illuminated devices used in this study is lower than that achievable using ITO coated glass as the transparent electrode, because the semi-transparent top Ag (11 nm) electrode reflects ~ 36% of the incident light before it can enter the BHJ layer (Figure 5.11(a) and (b)). It is expected that optimisation of the transparency of the top electrode, either by using a thinner Ag top-electrode and/or Ag grid in conjunction with an anti-reflecting layer, would reduce the reflectance to < 10%, such that substantially more light could be coupled into the device.

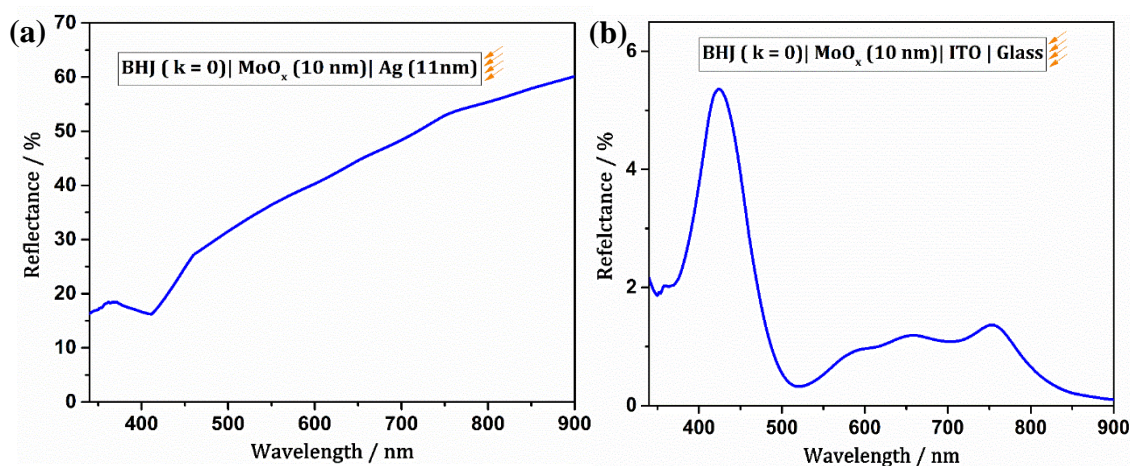


Figure 5.11: Transfer matrix simulation of the reflectance **(a)** from the top 11 nm Ag electrode in a top-illuminated OPV with the architecture: Ag (85nm) / ZnO (25 nm) / PCE10 – PC₇₀BM (300 nm) / MoO_x (10 nm) / Ag (11 nm). The average reflectance in the range of $\lambda = 400 - 850$ nm is 36.8% and **(b)** from the ITO glass electrode in an OPV with the architecture: Ag (85nm) / ZnO (25 nm) / PCE10 – PC₇₀BM (300 nm) / MoO_x (10 nm) / ITO glass. The average reflectance in the range of $\lambda = 400 - 850$ nm is 2.0%

5.4 Conclusion

In summary this chapter shows that optically thick Cu films can be used as a drop-in replacement for reflective Ag electrodes in efficient top-illuminated OPV devices without sacrificing device efficiency, when the photo-active layer is thick enough to absorb most of the incident light on the first pass through the BHJ layer, since Cu is as reflective as Ag where it matters most for high performance BHJ OPV devices; i.e. at the band edge ($\lambda > 700$ nm). Given the inevitable transition to BHJs with a thickness of ≥ 300 nm in the coming years, using Cu in place of Ag will ensure that the bill of materials for the reflective substrate electrode is a small part of the total device cost.

5.5 References

- (1) Meng, L.; Zhang, Y.; Wan, X.; Li, C.; Zhang, X.; Wang, Y.; Ke, X.; Xiao, Z.; Ding, L.; Xia, R.; et al. Organic and Solution-Processed Tandem Solar Cells with 17.3% Efficiency. *Science (80-.)*. **2018**, *361* (6407), 1094–1098.
- (2) Wong, W. S.; Salleo, A. *Flexible Electronics : Materials and Applications*; Springer, 2008.
- (3) Lam Po Tang, S. Recent Developments in Flexible Wearable Electronics for Monitoring Applications. *Trans. Inst. Meas. Control* **2007**, *29* (2007), 283–300.
- (4) Zamarayeva, A. M.; Ostfeld, A. E.; Wang, M.; Duey, J. K.; Deckman, I.; Lechene, B. P.; Davies, G.; Steingart, D. A.; Arias, A. C. Flexible and Stretchable Power Sources for Wearable Electronics. *Sci Adv* **2017**, *3* (6), e1602051.
- (5) Wöhrle, D.; Meissner, D.; Wöhrle, B. D.; Meissner, D. Organic Solar Cells. *Adv. Mater.* **1991**, *3* (3), 129–138.
- (6) Chen, L.-M.; Xu, Z.; Hong, Z.; Yang, Y. Interface Investigation and Engineering – Achieving High Performance Polymer Photovoltaic Devices. *J. Mater. Chem.* **2010**, *20* (13), 2575–2598.
- (7) Liao, H. H.; Chen, L. M.; Xu, Z.; Li, G.; Yang, Y. Highly Efficient Inverted Polymer Solar Cell by Low Temperature Annealing of Cs₂CO₃ Interlayer. *Appl. Phys. Lett.* **2008**, *92* (17), 1–4.
- (8) Armin, A.; Hambsch, M.; Wolfers, P.; Jin, H.; Li, J.; Shi, Z.; Burn, P. L.; Meredith, P. Efficient, Large Area, and Thick Junction Polymer Solar Cells with Balanced Mobilities and Low Defect Densities. *Adv. Energy Mater.* **2015**, *5* (3), 1401221.
- (9) Sun, C.; Pan, F.; Bin, H.; Zhang, J.; Xue, L.; Qiu, B.; Wei, Z.; Zhang, Z. G.; Li, Y. A Low Cost and High Performance Polymer Donor Material for Polymer Solar Cells. *Nat. Commun.* **2018**, *9* (1), 1–10.
- (10) Liu, X.; Ye, L.; Zhao, W.; Zhang, S.; Li, S.; Su, G. M.; Wang, C.; Ade, H.; Hou, J. Morphology Control Enables Thickness-Insensitive Efficient Nonfullerene Polymer Solar Cells. *Mater. Chem. Front.* **2017**, *1*, 2057–2064.
- (11) Zhang, G.; Zhang, K.; Yin, Q.; Jiang, X. F.; Wang, Z.; Xin, J.; Ma, W.; Yan, H.;

- Huang, F.; Cao, Y. High-Performance Ternary Organic Solar Cell Enabled by a Thick Active Layer Containing a Liquid Crystalline Small Molecule Donor. *J. Am. Chem. Soc.* **2017**, *139* (6), 2387–2395.
- (12) Armin, A.; Yazmaciyan, A.; Hambsch, M.; Li, J.; Burn, P. L.; Meredith, P. Electro-Optics of Conventional and Inverted Thick Junction Organic Solar Cells. *ACS Photonics* **2015**, *2* (12), 1745–1754.
- (13) Zang, Y.; Xin, Q.; Zhao, J.; Lin, J. Effect of Active Layer Thickness on the Performance of Polymer Solar Cells Based on a Highly Efficient Donor Material of PTB7-Th. *J. Phys. Chem. C* **2018**, *122* (29), 16532–16539.
- (14) Moulé, A. J.; Bonekamp, J. B.; Meerholz, K. The Effect of Active Layer Thickness and Composition on the Performance of Bulk-Heterojunction Solar Cells. *J. Appl. Phys.* **2006**, *100* (9), 94503.
- (15) Yang, J.; Vak, D.; Clark, N.; Subbiah, J.; Wong, W. W. H.; Jones, D. J.; Watkins, S. E.; Wilson, G. Organic Photovoltaic Modules Fabricated by an Industrial Gravure Printing Proofer. *Sol. Energy Mater. Sol. Cells* **2013**, *109*, 47–55.
- (16) Jiang, Y.; Luo, B.; Jiang, F.; Jiang, F.; Fuentes-Hernandez, C.; Liu, T.; Mao, L.; Xiong, S.; Li, Z.; Wang, T.; et al. Efficient Colorful Perovskite Solar Cells Using a Top Polymer Electrode Simultaneously as Spectrally Selective Antireflection Coating. *Nano Lett.* **2016**, *16* (12), 7829–7835.
- (17) Granqvist, C. G. Transparent Conductors as Solar Energy Materials: A Panoramic Review. *Sol. Energy Mater. Sol. Cells* **2007**, *91* (17), 1529–1598.
- (18) Miyazaki, T.; Akisawa, A.; Kashiwagi, T. Energy Savings of Office Buildings by the Use of Semi-Transparent Solar Cells for Windows. *Renew. Energy* **2005**.
- (19) Qin, F.; Tong, J.; Ge, R.; Luo, B.; Jiang, F.; Liu, T.; Jiang, Y.; Xu, Z.; Mao, L.; Meng, W.; et al. Indium Tin Oxide (ITO)-Free, Top-Illuminated, Flexible Perovskite Solar Cells. *J. Mater. Chem. A* **2016**, *4* (36), 14017–14024.
- (20) Lin, H. W.; Chiu, S. W.; Lin, L. Y.; Hung, Z. Y.; Chen, Y. H.; Lin, F.; Wong, K. T. Device Engineering for Highly Efficient Top-Illuminated Organic Solar Cells with Microcavity Structures. *Adv. Mater.* **2012**, *24* (17), 2269–2272.
- (21) An, C. J.; Cho, C.; Choi, J. K.; Park, J. M.; Jin, M. L.; Lee, J. Y.; Jung, H. T. Highly Efficient Top-Illuminated Flexible Polymer Solar Cells with a

- Nanopatterned 3D Microresonant Cavity. *Small* **2014**, *10* (7), 1278–1283.
- (22) Huang, J.; Li, C. Z.; Chueh, C. C.; Liu, S. Q.; Yu, J. S.; Jen, A. K. Y. 10.4% Power Conversion Efficiency of ITO-Free Organic Photovoltaics Through Enhanced Light Trapping Configuration. *Adv. Energy Mater.* **2015**, *5* (15), 4–9.
- (23) Zhang, C.; Zhao, D.; Gu, D.; Kim, H.; Ling, T.; Wu, Y. K. R.; Guo, L. J. An Ultrathin, Smooth, and Low-Loss Al-Doped Ag Film and Its Application as a Transparent Electrode in Organic Photovoltaics. *Adv. Mater.* **2014**.
- (24) Ham, J.; Dong, W. J.; Park, J. Y.; Yoo, C. J.; Lee, I.; Lee, J. L. A Challenge beyond Bottom Cells: Top-Illuminated Flexible Organic Solar Cells with Nanostructured Dielectric/Metal/Polymer (DMP) Films. *Adv. Mater.* **2015**, *27* (27), 4027–4033.
- (25) Søndergaard, R. R.; Espinosa, N.; Jørgensen, M.; Krebs, F. C. Efficient Decommissioning and Recycling of Polymer Solar Cells: Justification for Use of Silver. *Energy Environ. Sci.* **2014**, *7* (3), 1006–1012.
- (26) West, P. R.; Ishii, S.; Naik, G. V.; Emani, N. K.; Shalaev, V. M.; Boltasseva, A. Searching for Better Plasmonic Materials. *Laser Photonics Rev.* **2010**, *4* (6), 795–808.
- (27) Rathmell, A. R.; Bergin, S. M.; Hua, Y. L.; Li, Z. Y.; Wiley, B. J. The Growth Mechanism of Copper Nanowires and Their Properties in Flexible, Transparent Conducting Films. *Adv. Mater.* **2010**, *22* (32), 3558–3563.
- (28) Pereira, H. J.; Hutter, O. S.; Dabera, G. D. M. R.; Rochford, L. A.; Hatton, R. A. Copper Light-Catching Electrodes for Organic Photovoltaics. *Sustain. Energy Fuels* **2017**, *1* (4), 859–865.
- (29) Bellchambers, P.; Lee, J.; Varagnolo, S.; Amari, H.; Walker, M.; Hatton, R. A. Elucidating the Exceptional Passivation Effect of 0.8 nm Evaporated Aluminium on Transparent Copper Films. *Front. Mater.* **2018**, *5*:71.
- (30) Stec, H. M.; Hatton, R. A. Plasmon-Active Nano-Aperture Window Electrodes for Organic Photovoltaics. *Adv. Energy Mater.* **2013**, *3* (2), 193–199.
- (31) Deshmukh, K. D.; Prasad, S. K. K.; Chandrasekaran, N.; Liu, A. C. Y.; Gann, E.; Thomsen, L.; Kabra, D.; Hodgkiss, J. M.; McNeill, C. R. Critical Role of Pendant Group Substitution on the Performance of Efficient All-Polymer Solar

-
- Cells. *Chem. Mater.* **2017**, 29 (2), 804–816.
- (32) Liao, S. H.; Jhuo, H. J.; Yeh, P. N.; Cheng, Y. S.; Li, Y. L.; Lee, Y. H.; Sharma, S.; Chen, S. A. Single Junction Inverted Polymer Solar Cell Reaching Power Conversion Efficiency 10.31% by Employing Dual-Doped Zinc Oxide Nano-Film as Cathode Interlayer. *Sci. Rep.* **2014**, 4, 4–10.
- (33) ASTM G173-03(2012). Standard Tables for Reference Solar Spectral Irradiances: Direct Normal and Hemispherical on 37° Tilted Surface. *Astm* **2013**, 3, 1–21.
- (34) Pereira, H. J.; Reed, J.; Lee, J.; Varagnolo, S.; Dabera, G. D. R.; Hatton, R. A. Fabrication of Copper Window Electrodes with $\approx 10^8$ Apertures cm^{-2} for Organic Photovoltaics. *Adv. Funct. Mater.* **2018**, 28 (36), 1802893.
- (35) Manor, A.; Katz, E. A.; Tromholt, T.; Krebs, F. C. Enhancing Functionality of ZnO Hole Blocking Layer in Organic Photovoltaics. *Sol. Energy Mater. Sol. Cells* **2012**, 98, 491–493.

Chapter 6

Copper Light-catching Electrodes

The work presented in this chapter has been published in:

H. J. Pereira, O. S. Hutter, G. D. M. R. Dabera, L. A. Rochford, R. A. Hatton, Copper Light-catching Electrodes for Organic Photovoltaics, *Sustainable Energy & Fuels* 2017, *1*, 859.

6.1 Background

The thickness of the photo-active layer is limited by the low charge carrier mobility in organic semiconductors used in OPVs and therefore it is seldom possible to ensure that the entire useful portion of the incident solar spectrum between $\lambda = 350 - 900$ nm is absorbed. As a consequence, light trapping strategies need to be implemented to increase the effective optical path length of light within a device without increasing the thickness of the photo-active material.² Over the past decade several ways to circumvent this thickness limitation arising from the low charge carrier mobility have been proposed based on using of Au and Ag nanoparticles to increase the photon-to-electron conversion efficiency by increasing light absorption in the photo-active layer.¹

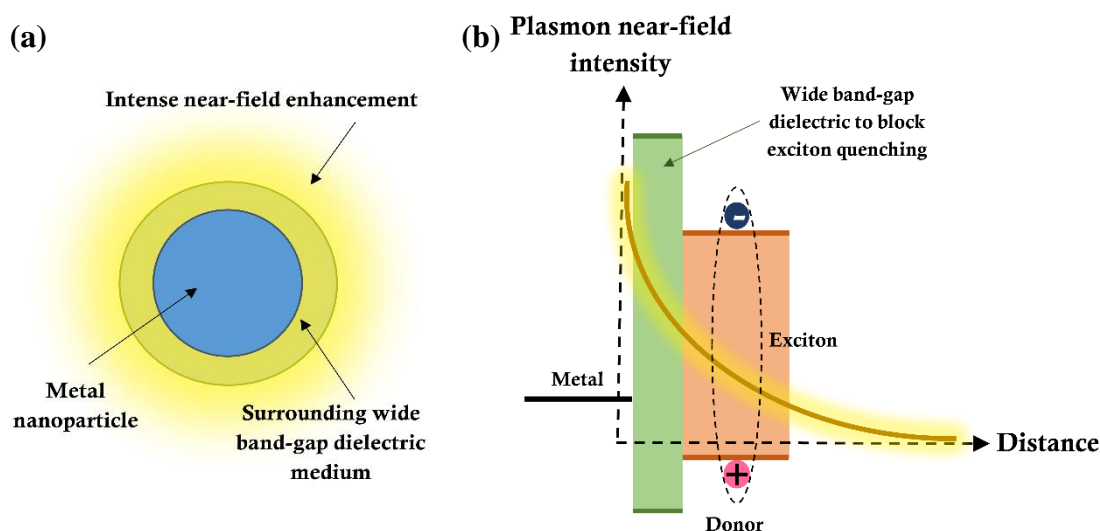


Figure 6.1: (a) Schematic representation of the near-field enhancement at the metal nanoparticle – dielectric interface and (b) the distance dependent exponential decay of the optical field intensity indicating the need for the photo-active layer to be as close to the metal as possible to generate excitons prior to plasmon relaxation.

Noble metal nanoparticles couple strongly with visible light as a result of excitation of LSPRs,² which are collective oscillations of the conduction band electrons confined to the interface between the metal and the surrounding dielectric medium, that occur when the particle dimensions are much smaller than the wavelength of the incident light.³ The very large absorption cross-section of noble metal nanoparticles⁴ combined with the possibility of engineering the nanoparticle size and geometry to tune the LSPR frequency, offers the possibility for them to be used in OPVs to enhance light absorption across a broad range of wavelengths via two different mechanisms: (i) by efficient scattering of the incident light into the far-field, thereby increasing the path length through the photo-active layer⁵; and/or (ii) by confining and concentrating the incident light as an intense near-field evanescent wave at the nanoparticle-dielectric interface (i.e. LSPR excitations),^{3,6} (Figure 6.1(a)) where the near-field enhancement decays exponentially into the surrounding dielectric over a range of several tens of nanometres.⁶ The latter approach requires that the light harvesting organic semiconductor is as close to the nanoparticle as possible (Figure 6.1(b)), although not so close that the competing process of exciton quenching by the metal becomes significant.^{6,7} In practice the optimal separation is of the order of 3-5 nm.^{6,7} Due to the very large absorption coefficient in organic semiconductors used to harvest light in OPVs it is possible that this trapped light can be harnessed directly to excite electron transitions from HOMO to the LUMO in the adjacent organic semiconductor, before the surface plasmonic excitations dissipate their energy as heat due to ohmic losses in the metal.⁸

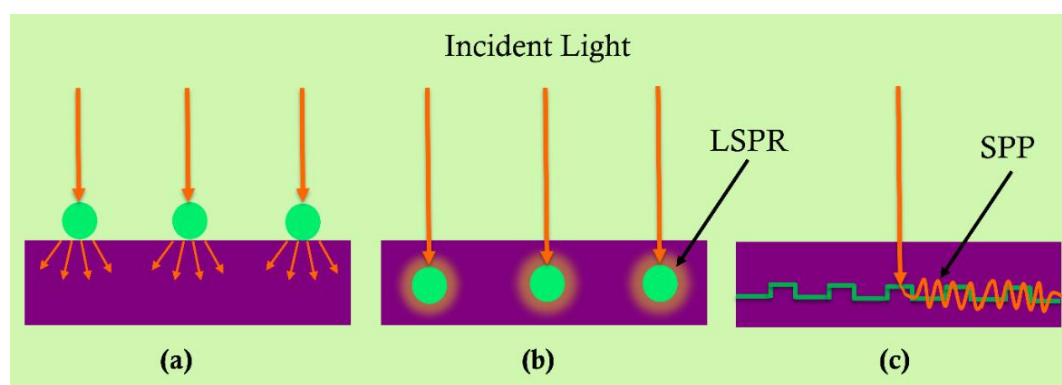


Figure 6.2: (a) Plasmon assisted forward light scattering by metal nanoparticles on the front surface of the PV device; (b) light concentration by metal nanoparticles in the vicinity of the photo-active layer; (c) and light trapping using propagating surface plasmons by a corrugated metal electrode.

Plasmonic structures can be integrated into PVs in different ways¹⁰ as depicted in Figure 6.2. Metal nanoparticles on the surface of devices can be used as light scattering elements to increase the path length of incident light in the absorbing semiconductor thin film. The

efficiency of forward light scattering by metal nanoparticles is highly dependent on the size, shape and permittivity of the surrounding dielectric medium.^{3,9–12} Thus, depending on the requirements these parameters need to be carefully optimised⁹ in order to exploit the full potential of this phenomenon in OPVs. An alternate approach to trap light is the use of plasmons localised on nanoparticles to concentrate light. This approach exploits the strong local field enhancement at the surface of metal nanoparticles embedded in the semiconductor. In this approach the nanoparticles behave as sub-wavelength antennas that store the incident light in the form of LSPRs.¹⁰ Embedding plasmon-active metal nanoparticles near the photo-active layer allows light being trapped at the metal/dielectric interface to contribute to exciton generation in the adjacent organic semiconductor.² Unfortunately, the dimensions of Au and Ag nanoparticles needed for efficient scattering and concentration of light is of the order of several tens of nanometres⁵ and so integration into OPV device architectures over large areas presents a significant challenge for scale-up.¹

An alternative scalable approach that has received relatively little attention to date, but is well matched to OPV device architectures, is to trap the incident light⁹ as surface plasmonic excitations at the surface of a noble metal electrode having a random array of sub-optical wavelength apertures.^{3,13–15} Since metal electrodes are a vital component of all OPV device designs, this approach can be easily integrated into the device architecture. Similar to metal nanoparticles, nano-holes in a noble metal film have large absorption cross-sections enabling strong coupling with plane wave incident light,^{15,16} whilst having the advantage of being confined to the plane of the electrode. Consequently, unlike metal nanoparticles, nano-apertures in a metal film electrode do not risk compromising the shunt resistance of a device with a very thin light harvesting layer, such as in an OPV. Unlike metal nanoparticles, periodic arrays of metal nano-holes can support both propagating and localised plasmonic-excitations, which are strongly coupled.^{9,15,10} This approach to light trapping in OPVs was first proposed by Reilly *et al.* who used a 30 nm thick Ag electrode with a random distribution of circular apertures of the same radius formed by micro-sphere lithography.¹⁷ Stec *et al.*¹⁴ advanced that work in three important ways: (i) by developing a scalable method for the formation of a dense array of random apertures over large areas based on annealing optically thin (~10 nm) Ag films; (ii) by demonstrating that Au could be used in place of Ag; (Figure 6.3) and (iii) by showing that OPV devices using random nano-hole electrodes could actually outperform conventional ITO glass window electrodes in OPVs. Importantly the

apertures formed by thermal annealing have a broad distribution of shapes and sizes which ensures a broad-band plasmonic response, which is well-matched to OPV applications.¹⁵

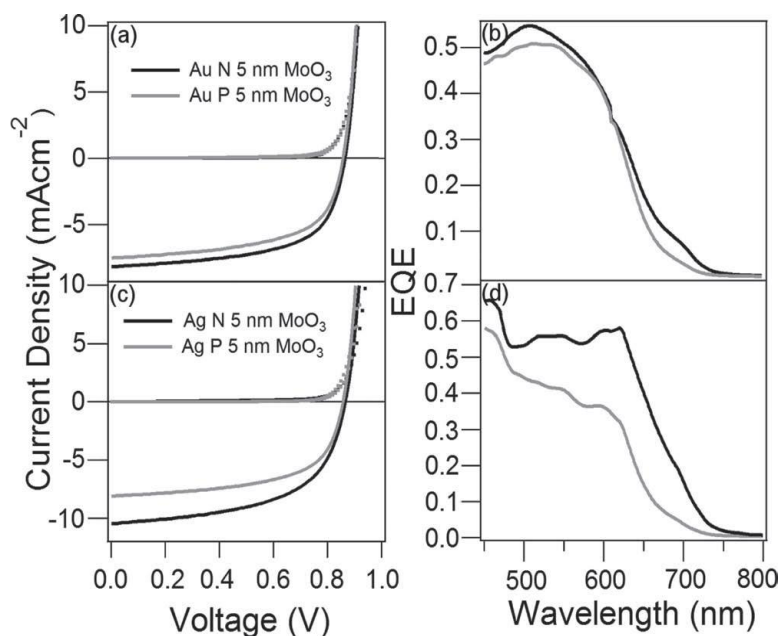


Figure 6.3: JV characteristics and associated EQE for devices that employ Au (8.4 nm) and Ag (11 nm) electrodes with (N) and without (P) nano-holes demonstrating superior performance of the plasmon-active nano-hole electrodes compared to the planar electrodes of identical thickness. Reprinted with permission from Stec et al.^[14] Copyright © 2013, John Wiley and Sons.

However, whilst Ag and Au are the preferred metals for this application, because of their high conductivity and relatively low optical losses,⁸ the use of such high cost metals inevitably erodes the cost advantage of OPVs over other types of thin film PVs, and so there is a need to identify lower cost alternatives to these metals as explained in the introduction. Cu is attractive as an alternative to Ag owing to its abundance, high electrical conductivity and because it is $\sim 100^{\text{th}}$ of the cost of Ag¹⁸. What is not widely appreciated is that the optical losses in Cu due to inter-band transitions and free electrons are comparable to that of Au, so it can also support intense SPRs in the visible region similar to Au.^{19,20} Cu has not received much attention as a plasmon-active material for PVs due to its susceptibility to oxidation in air, which results in the formation of a surface oxide that damps surface plasmonic excitations.^{19,20} However, in recent years there has been considerable progress in the development of ultra-thin surface passivation layers for Cu which offer a means of addressing this problem,^{21–23} and so nano-structured Cu may yet prove useful for light trapping and concentration in OPVs.

This chapter discusses the *proof-of-principle* that Cu electrodes with a random array of sub-optical wavelength apertures can be used to catch incident light and efficiently transfer that energy to an adjacent organic semiconductor in a model OPV device. This energy transfer process is demonstrated using model small molecule and polymer OPV devices (based on ClAlPc : C₆₀ and PCE10 : PC₇₀BM heterojunctions respectively) in conjunction with a nano-hole Cu electrode formed by thermal annealing an optically thin Cu film supported on PET.

6.2 Experimental Methods

Experimental details specific to the work presented in this chapter are as follows;

6.2.1 Substrate cleaning

Substrate slides of the required dimension were cut from a roll of PET and cleaned as described in section 2.1 and 2.2. Notably both sides of the PET sheet were not identical in surface roughness and so AFM imaging was performed in tapping mode using an Asylum Research MFP – 3D AFM to determine the smooth side onto which all surface treatment was done prior to deposition of Cu.

6.2.2 Deposition of Cu

Cu was deposited by thermal evaporation of Cu pellets at a rate of 2.2 – 2.5 Å s⁻¹ to give a thickness of 11 nm.

6.2.3 Fabrication of apertures

Cu films were annealed in a tube furnace at 175 °C at a pressure of $\leq 5 \times 10^{-4}$ mbar for 10 minutes. SEM imaging was performed using ZEISS Supra SP55 with an accelerating voltage of typically 5-7 kV to evaluate the distribution and coverage of apertures. The coverage of apertures was evaluated using WXS software.

6.2.4 Optical transparency measurements

Far-field transmittance of metal films on PET was measured over the wavelength range 300 – 900 nm using a 150 mm Spectralon® Integrating Sphere coupled to a PerkinElmer® LAMBDA™ high performance UV/Vis spectrometer. The incident beam passed through the plastic substrate first and measurements were done with reference to the substrate.

6.2.5 Fabrication of OPV devices

ClAlPc was purified by thermal gradient sublimation prior to deposition. All other chemicals were used without further purification. MoO_x (5 nm at 0.1-0.2 Å s⁻¹) was deposited on annealed Cu thin films using thermal evaporation. For fabrication of devices

with a bilayer architecture ClAlPc (20 nm) and C₆₀ (40 nm) were deposited by thermal evaporation at a rate of 0.9 – 1.2 Å s⁻¹ and 0.3 – 0.4 Å s⁻¹ respectively. For devices with a BHJ architecture, PCE10 and PC₇₀BM were mixed in 2:3 mass ratio to make a 35 mg ml⁻¹ solution in chlorobenzene (97%) and 1,8-diiodooctane (3%) and deposited by spin coating from a static start at 4000 rpm for 120 s, followed by a methanol treatment at 4000 rpm for 30 s. These slides were then allowed to dry under vacuum overnight. BCP (5 nm at 0.3-0.5 Å s⁻¹) as the ETL and Al (80 nm at 1.0-1.3 Å s⁻¹) as the reflective electrode were deposited by thermal evaporation. Al was deposited through a shadow mask to give an electrode area of 0.06 cm².

6.2.6 Characterisation of OPV devices

Current density-voltage (*JV*) testing was performed as described in section 2.17 and EQE measurements were done as described in section 2.18 in the wavelength range of 300 – 850 nm.

6.3 Results and Discussion

Cu films with a thickness of 11 nm were deposited onto the transparent plastic substrate PET by thermal evaporation, forming films with a R_{sh} of ~11 Ω sq⁻¹.

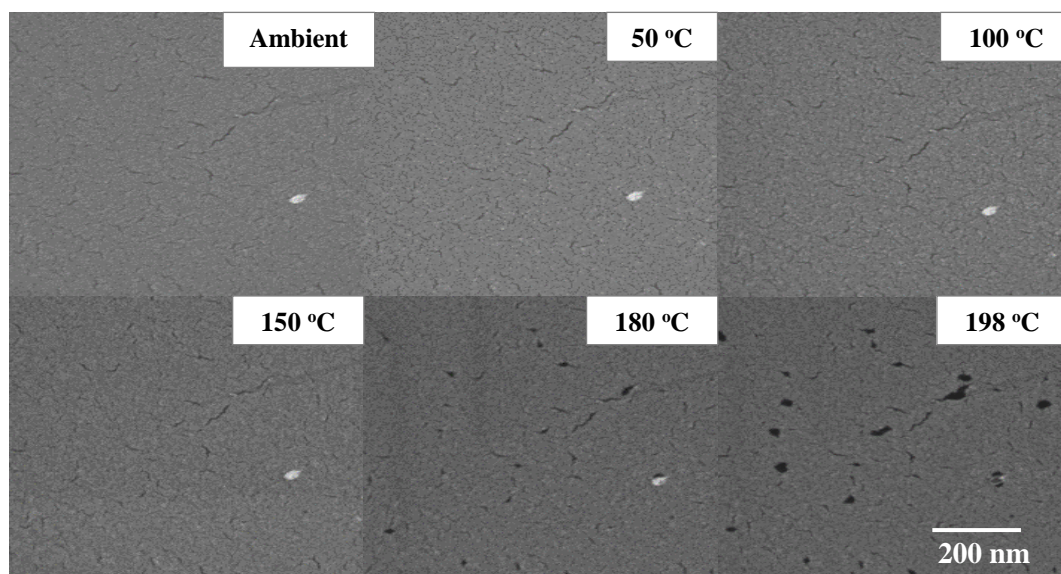


Figure 6.4: SEM images of 11 nm thick Cu films on PET upon annealing from 50 °C to 198 °C using an SEM with a built-in heating stage showing aperture formation

Thermal annealing of these films under high vacuum results in the formation of a random array of irregularly shaped sub-optical wavelength apertures, the number density and size being determined by the annealing time and temperature. The optimal annealing

conditions were determined by observing aperture formation as a function of annealing temperature using a heated stage mounted inside a SEM (Figure 6.4).

When the electrodes were annealed in vacuum (5×10^{-4} mbar) at 175 °C for 10 minutes, a dense random array of apertures with dimensions in the size range 50-100 nm and area coverage of $\sim 10\%$ were formed (Figure 6.5(b)). Thermal annealing was accompanied by an increase in R_{sh} of the films to $\sim 27 \Omega \text{ sq}^{-1}$ which can be attributed to the combined effects of the inclusion of apertures and increase in film surface roughness (from 1.5 ± 0.5 nm for a planar Cu film to 5.2 ± 1.7 nm for an annealed Cu film), both of which increase the scattering of electrons as they move in the plane of the metal film under the influence of the applied bias. Importantly, this increase in R_{sh} is not sufficient to significantly change the series resistance of the OPV devices fabricated as part of this study because the devices have a small area of 0.06 cm^2 .

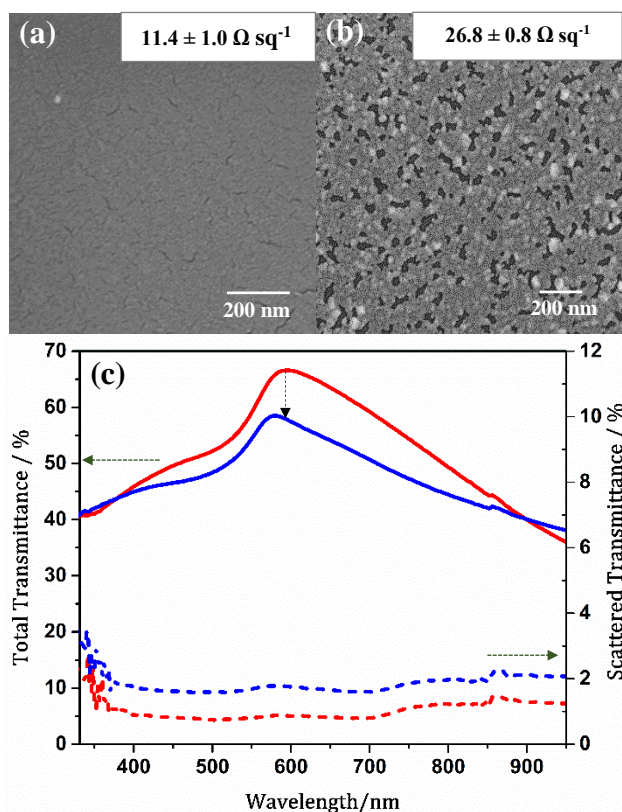


Figure 6.5: SEM showing the morphology of Cu films (11 nm) (a) before and (b) after annealing; and (c) Optical transparency (solid lines) and far-field scattering (dashed lines) measurements of 11 nm Cu films with (blue) and without (red) nano-apertures.

The incorporation of apertures into the Cu film results in a large reduction in the far-field transparency across a broad wavelength range between $\lambda = 450$ -850 nm, with the largest absolute reduction of 10% for wavelengths in the range of $\lambda = 590$ -700 nm. Light scattering measurements performed using an integrating sphere (Figure 6.5(c)) confirmed

that this reduction in transparency is not the result of far-field light scattering, which is consistent with the small size of the apertures compared to the wavelength of the incident light. Since the apertures are not of uniform size or uniformly distributed and the largest reduction in transparency occurs for wavelengths in the range of $\lambda = 590\text{-}700\text{ nm}$ and peaks at $\sim 625\text{ nm}$, the reduction in transparency for wavelength $> 600\text{ nm}$ is attributed (primarily) to light absorption arising from excitation of SPRs at the site of apertures in the Cu film, since this wavelength range coincides with that over which Cu can support surface plasmon resonant excitations and the optical losses due to inter-band transitions and free electron losses are at their lowest.⁸

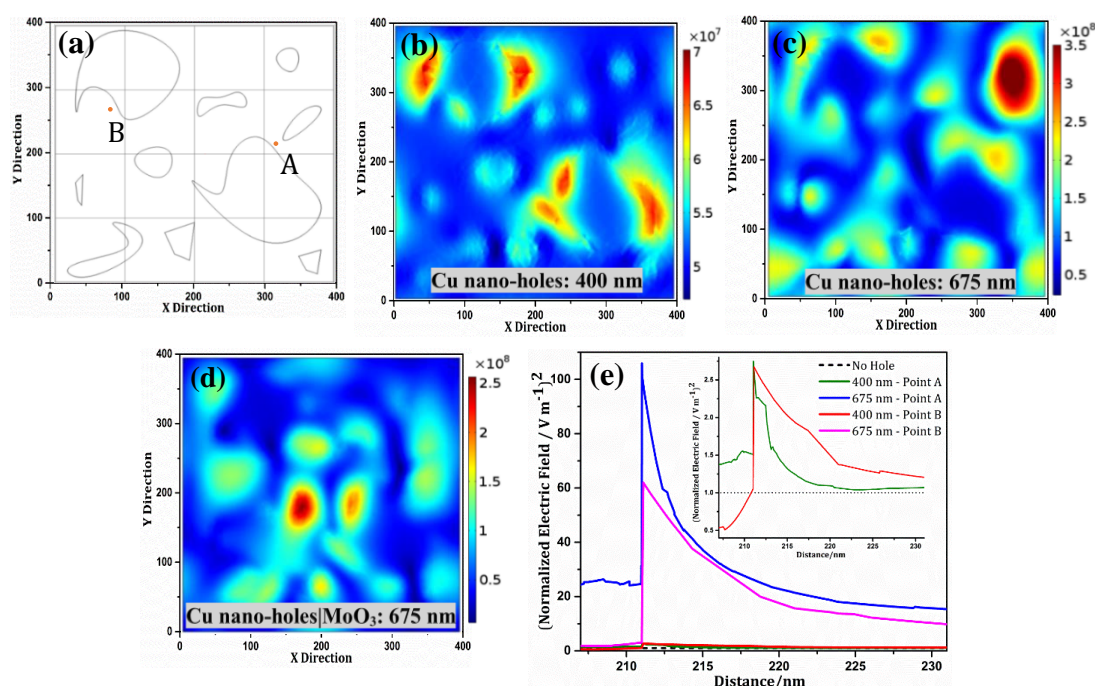


Figure 6.6: Finite-element modelling of the near field 15 nm above the surface of an 11 nm thick Cu nano-hole electrode supported on PET, with a random arrangement of different shaped apertures (representative of that achieved experimentally) as shown in (a); optical field for (b) $\lambda = 400\text{ nm}$ and (c) $\lambda = 675\text{ nm}$ for plane polarised incident light; (d) Optical field 15 nm above the metal electrode for plane polarised incident light of $\lambda = 675\text{ nm}$, simulated for PET (200 nm) / Cu (11 nm) / MoO_x (5 nm) / CIAPc (20 nm); (e) Normalized field strength as a function of distance from the surface of the Cu nano-hole electrode for PET (200 nm) / Cu (11 nm) at points A and B (indicated in (a)) for plane polarised incident light.

Finite-element modelling of the near-field intensity in Cu films with and without apertures of the size and shapes formed by annealing Cu films corroborate the conclusion that light is trapped at the surface as a near-field evanescent wave. The simulations also show that the intensity distribution across the electrode surface is highly heterogeneous, consistent with the complex interaction between plasmonic excitations associated with different features on the electrode surface (Figure 6.6). In principle these regions of

intense near-field radiation can be used to excite electronic transitions from the HOMO to the LUMO in the organic semiconductor before the surface plasmons dissipate their energy as heat due to ohmic losses in the metal.²⁴

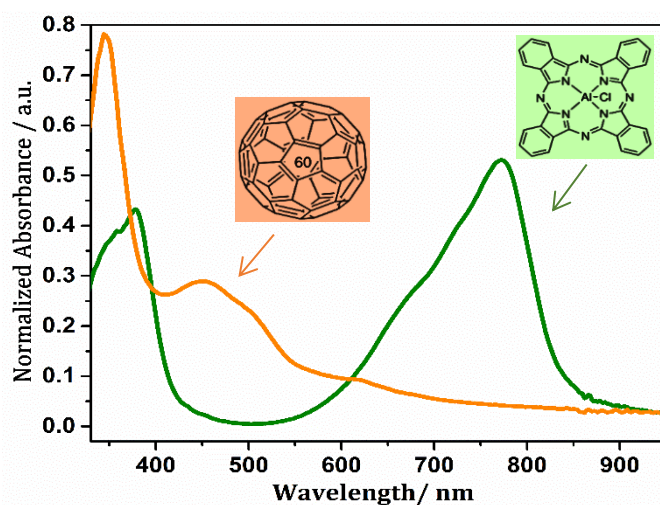


Figure 6.7: Absorption spectra of ClAlPc (20 nm) and C₆₀ (40 nm) films - the same thickness used in the model OPV devices fabricated as part of this study.

To explore this possibility, model OPVs based on a bilayer heterojunction of small molecule donor ClAlPc and acceptor C₆₀ were fabricated using Cu electrodes with and without a random array of apertures (Figures 6.5(a) & (b)). This simple device architecture and the thickness of the organic semiconductor layers were specifically selected as a model structure to test the aforementioned hypothesis: ClAlPc was used because its intense Q-band^{25,26} is located between 600 – 850 nm (Figure 6.7) which coincides with the range over which surface plasmon resonant excitations are most intense in the Cu nano-hole electrode. MoO_x was used as the hole-extraction layer because it is well-known to facilitate efficient extraction of holes from most donor type organic semiconductors for thicknesses in the range 3-20 nm and its thickness can be accurately controlled by thermal evaporation.^{27,28,29} Additionally, the results of the finite-element modelling given in Figure 6.6 (d) and (e) show that a 5 nm thick MoO_x layer is sufficiently thin for there to be significant spatial overlap between the ClAlPc layer and the near-field evanescent wave extending from the electrode surface, since the range of the trapped light extends to several tens of nanometres from the electrode surface.

The device *JV* characteristics in the dark and under 1 sun simulated solar illumination are shown in Figure 6.8 and Table 6.1. It is evident that the J_{sc} is comparable for devices using Cu electrodes with and without nano-holes, despite the lower far-field transparency of the Cu nano-hole electrode, particularly over the wavelength range between $\lambda = 600 -$

800 nm which coincides with the range over which CIAIPc most strongly absorbs (Figure 6.7). This finding is consistent with the hypothesis that the light trapped as surface plasmonic excitations in the Cu nano-hole electrode (which results in the reduced transparency for $\lambda > 575$ nm in the nano-hole electrode) is to a large extent coupled into the adjacent CIAIPc layer, since in the bilayer device architecture, CIAIPc is the only layer within range of the evanescent wave extending from the surface of the nano-hole electrode (Figure 6.6(d) & (e)).

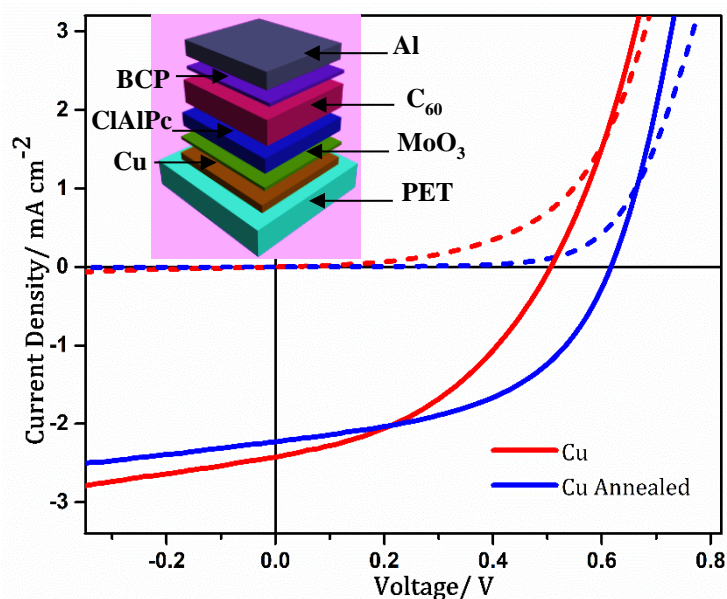


Figure 6.8: Representative current density–voltage characteristics in the dark and under one sun simulated solar illumination (100 mW cm^{-2} ; AM 1.5G) for devices with the architecture: Cu(11nm) / MoO_x (5 nm) / CIAIPc (20 nm) / C_{60} (40 nm) / BCP (5 nm) / Al (80 nm) with and without nano-holes in the Cu electrode. **Inset:** Schematic representation of the device architecture.

| Electrode | Champion J_{sc} / mA cm^{-2} | $J_{sc} \pm 1 \text{ SD}$ / mA cm^{-2} | $V_{oc} \pm 1 \text{ SD}$ / V | $FF \pm 1 \text{ SD}$ | %PCE $\pm 1 \text{ SD}$ |
|--------------|---|---|-------------------------------|-----------------------|-------------------------|
| Non-Annealed | 2.71 | 2.53 ± 0.09 | 0.48 ± 0.03 | 0.40 ± 0.02 | 0.49 ± 0.04 |
| Annealed | 2.65 | 2.44 ± 0.11 | 0.60 ± 0.02 | 0.49 ± 0.01 | 0.72 ± 0.05 |

Table 6.1: Summary of current density - voltage characteristics measured under one sun simulated solar illumination for devices with the architecture: Cu (11nm) / MoO_x (5 nm) / CIAIPc (20 nm) / C_{60} (40 nm) / BCP (5nm) / Al (80 nm) with and without nano-holes in the Cu electrode.

This conclusion is corroborated by the difference in the shape of the EQE spectra (Figure 6.9) from which it is evident that photons are converted to electrons in the external circuit

more efficiently for devices using the nano-hole electrode for wavelengths in the range of $\lambda = 600 - 800$ nm, which is the same range over which the far-field optical transparency is observed to be reduced. Indeed, the EQE is increased by $\sim 25\%$ over the wavelength range of $\lambda = 655 - 715$ nm, which coincides with the wavelength range over which the optical losses in Cu due to inter-band transitions and free electron damping are at a minimum (Figure 6.9) and so SPRs will be most intense. Conversely for $\lambda < 575$ nm the EQE is reduced in line with the reduction in far-field transparency for devices using the Cu nano-hole electrode. Normalizing the difference in EQE to the transparency (%T) (Figure 6.9 (b)) shows that the onset of enhanced absorption actually occurs very close to the minimum in the optical losses for Cu.

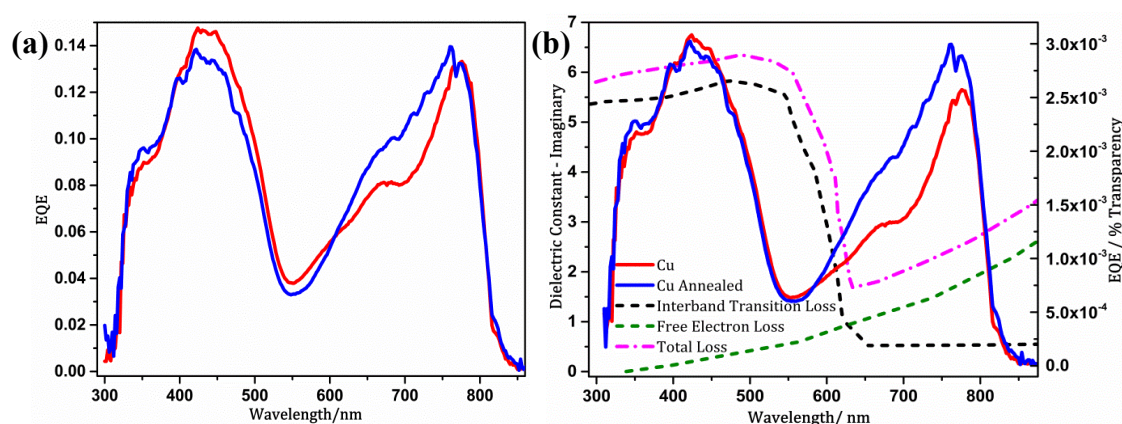


Figure 6.9: (a) Representative EQE for annealed (blue) and non-annealed (red) Cu electrodes with the device structure: Cu (11nm)/ MoO_x (5 nm) / ClAlPc (20 nm) / C₆₀ (40 nm) / BCP (5nm) / Al (80 nm); and (b) EQE/%T vs wavelength plot and imaginary component of the dielectric constant of Cu^[8] indicating inter-band transition losses and free electron losses.

Interestingly, devices using a nano-hole electrode also consistently exhibit a higher V_{oc} and FF (Figure 6.8 and Table 6.1). It is evident from Figure 6.8 that this difference stems from the earlier onset of dark current injection in devices using electrodes without nano-holes. Since Cu is known to diffuse aggressively into evaporated MoO_x films at room temperature this difference may stem from a difference in the energy level alignment at the electrode - ClAlPc interface due to filamentary strands of metallic Cu that extend partly or all the way to the surface of MoO_x at the grain boundaries thereby weakening the electronic functionality of the underlying Cu electrode.^{29,30} Conversely, as crystallinity is increased upon annealing, imparting increased lattice stability and reducing the thermodynamic drive for Cu diffusion into the neighbouring MoO_x layer, the Cu electrodes with apertures exhibit a higher V_{oc} . To test this hypothesis the crystallinity of the Cu electrodes before and after thermal annealing was probed using grazing angle

XRD, and the work function of Cu / MoO_x (5 nm) bilayer films were measured using the contact potential difference method (Kelvin probe measurements). It is evident from the XRD pattern (Figure 6.10) that the crystallinity is increased upon annealing because the intensity of the peak corresponding to reflection from the Cu (111) plane is more intense after annealing. The work function of the electrode/MoO_x bilayer is also significantly lower for the case in which the Cu electrode was not annealed; typical values were ~ 5.7 eV and ~ 5.1 eV for Cu electrodes with and without nano-holes respectively. Importantly, whilst this difference complicates the interpretation of device J_{sc} , it cannot explain the change in the shape of the EQE spectrum.

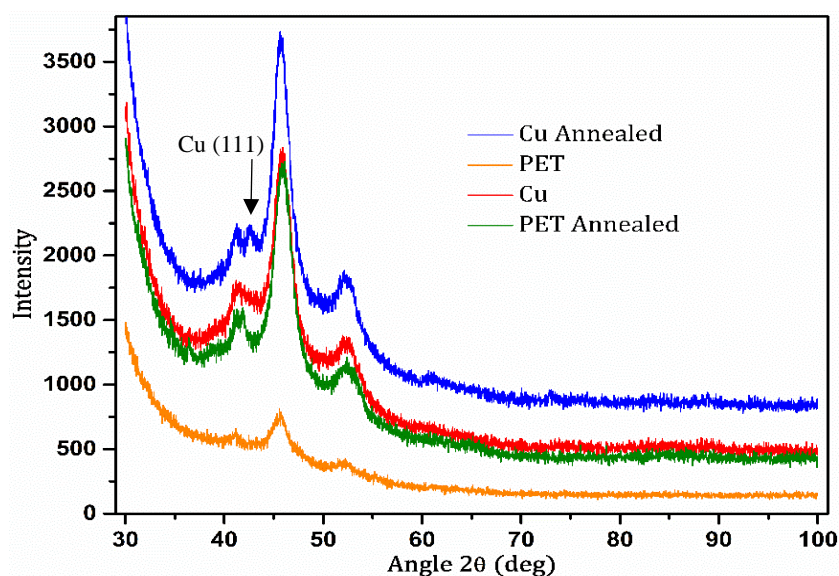


Figure 6.10: XRD pattern of Cu films (11 nm) deposited on PET substrates before and after annealing at 175°C for 10 min in vacuum. The pattern corresponding to the annealed Cu film has been offset for clarity.

To test the generality of the findings, OPVs were also fabricated using a BHJ, based on the narrow band gap polymer PCE10 in conjunction PC₇₀BM (100 nm) in place of ClAlPc:C₆₀. Importantly in this device structure a smaller proportion of the total photo-active layer thickness is in the region of intense near-field, near to the Cu electrode because the PCE10:PC₇₀BM BHJ system is thicker than the ClAlPc:C₆₀ bilayer, and unlike the ClAlPc:C₆₀ bilayer, the PCE10: PC₇₀BM BHJ absorbs strongly over a broad range of wavelengths, including in the range, $\lambda = 450\text{-}600$ nm where the Cu nano-hole electrode is not plasmon-active. Consequently, the J_{sc} in devices using nano-hole electrodes is lower compared to those that use a Cu electrode without nano-holes (Figure 6.11). However, the EQE in devices using the nano-hole electrode is still highest in that part of the spectrum where the electrode is least transparent, which corresponds to the

region over which Cu supports surface plasmonic excitations. It is also evident from Figure 6.11 that the onset of plasmon enhanced absorption occurs when the optical losses are a minimum and at the same wavelength as seen in the CIAIPc/C₆₀ bilayer OPVs; i.e. $\lambda = 590\text{-}600\text{ nm}$ (Figures 6.9 (b)).

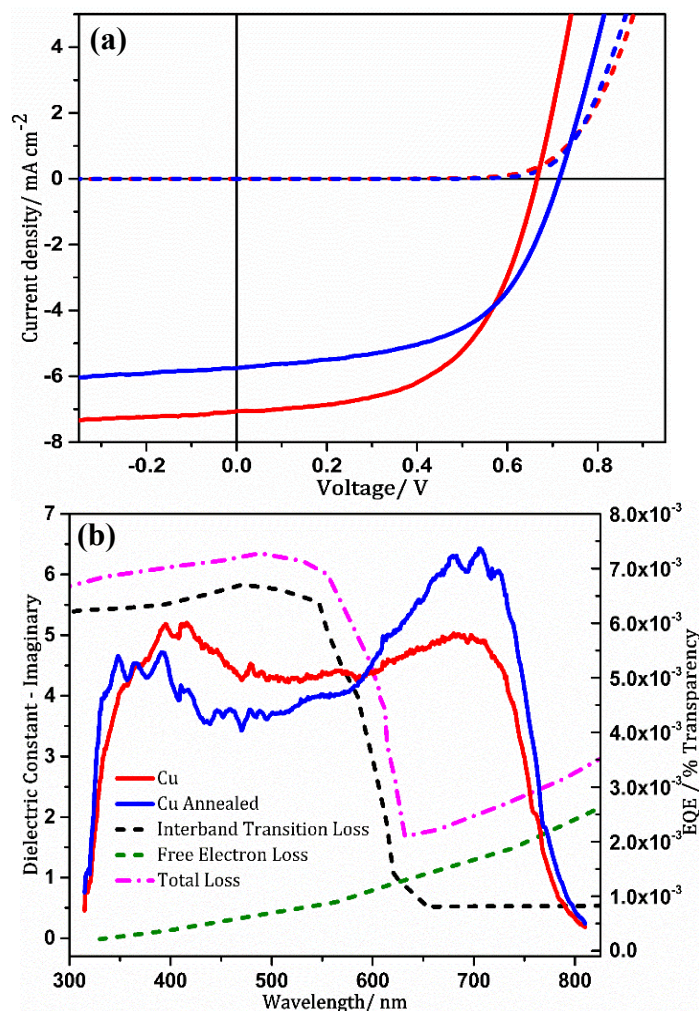


Figure 6.11: Representative (a) current density–voltage characteristics in the dark and under 1 sun simulated solar illumination for OPVs with the structure: Cu (11nm)/ MoO_x (5 nm)/ PCE10 - PC₇₀BM (100 nm) / BCP (5nm) / Al (80 nm); and (b) EQE/%T vs wavelength plot and imaginary component of the dielectric constant of Cu^[8] indicating inter-band transition losses and free electron losses.

To confirm the near-field nature of the light trapping mechanism, the thickness of the MoO_x layer was increased from 5 to 15 nm. The key device performance parameters are summarised in Table 6.2. It is evident from Table 6.2 that the effect of increasing the MoO_x layer thickness from 5 to 15 nm is much more pronounced for the devices with the nano-hole electrode, which is consistent with the exponential decay of the near-field intensity into the photo-active layer (Figure 6.6 (e)).

| Electrode | Thickness of MoO _x / nm | $J_{sc} \pm 1 \text{ SD}$ / mA cm ⁻² | $V_{oc} \pm 1 \text{ SD}$ / V | $FF \pm 1 \text{ SD}$ | $\%PCE \pm 1 \text{ SD}$ |
|--------------|------------------------------------|---|-------------------------------|-----------------------|--------------------------|
| Non-Annealed | 5 | 7.08 ± 0.16 | 0.65 ± 0.04 | 0.56 ± 0.02 | 2.78 ± 0.52 |
| Annealed | 5 | 6.16 ± 0.60 | 0.72 ± 0.02 | 0.56 ± 0.03 | 2.54 ± 0.35 |
| Non-Annealed | 15 | 6.31 ± 0.43 | 0.71 ± 0.03 | 0.57 ± 0.03 | 2.62 ± 0.34 |
| Annealed | 15 | 4.75 ± 0.36 | 0.74 ± 0.01 | 0.53 ± 0.03 | 1.91 ± 0.22 |

Table 6.2: Summary of current density - voltage characteristics of devices with the architecture; Cu (11nm)/ MoO_x (5 and 15 nm)/ PCE10 - PC₇₀BM (100 nm) / BCP (5nm) / Al (80 nm) with and without nano-holes in the Cu electrode, tested under 1 sun simulated solar illumination.

6.4 Conclusion

Collectively the findings reported in this chapter, provide compelling evidence that light trapped as surface plasmon-resonant excitations in an optically thin Cu electrode with a random array of sub-optical wavelength apertures can be efficiently coupled into an adjacent strongly absorbing organic semiconductor layer before the competing process of exciton quenching occurs. This study has focused on the demonstration of proof-of-principle in model OPVs, rather than optimisation of device performance. Based on the findings presented it may prove better to locate an electrode of this type at the back of the device so that the shorter wavelength photons can be substantially absorbed in the organic semiconductor before reaching the Cu electrode, since optical losses in Cu for $\lambda < 600$ nm are considerable.

6.5 References

- (1) Jang, Y. H.; Jang, Y. J.; Kim, S.; Quan, L. N.; Chung, K.; Kim, D. H. Plasmonic Solar Cells: From Rational Design to Mechanism Overview. *Chem. Rev.* **2016**, acs.chemrev.6b00302.
- (2) Karatay, D. U.; Salvador, M.; Yao, K.; Jen, A. K. Y.; Ginger, D. S. Performance Limits of Plasmon-Enhanced Organic Photovoltaics. *Appl. Phys. Lett.* **2014**, *105* (3), 033304.
- (3) Atwater, H. A.; Polman, A. Plasmonics for Improved Photovoltaic Devices. *Nat. Mater.* **2010**, *9* (10), 865–865.
- (4) Kuno, M. *Introductory Nanoscience : [Physical and Chemical Concepts]*; Garland Science, 2012.
- (5) Li, X.; Choy, W. C. H.; Huo, L.; Xie, F.; Sha, W. E. I.; Ding, B.; Guo, X.; Li, Y.; Hou, J.; You, J.; et al. Dual Plasmonic Nanostructures for High Performance Inverted Organic Solar Cells. *Adv. Mater.* **2012**, *24* (22), 3046–3052.
- (6) Niesen, B.; Rand, B. P.; Van Dorpe, P.; Cheyng, D.; Shen, H.; Maes, B.; Heremans, P. Near-Field Interactions between Metal Nanoparticle Surface Plasmons and Molecular Excitons in Thin-Films. Part I: Absorption. *J. Phys. Chem. C* **2012**, *116* (45), 24206–24214.
- (7) Goh, W. P.; Williams, E. L.; Yang, R. Bin; Koh, W. S.; Mhaisalkar, S.; Ooi, Z. E. Optimal Shell Thickness of Metal@Insulator Nanoparticles for Net Enhancement of Photogenerated Polarons in P3HT Films. *ACS Appl. Mater. Interfaces* **2016**, *8* (4), 2464–2469.
- (8) West, P. R.; Ishii, S.; Naik, G. V.; Emani, N. K.; Shalaev, V. M.; Boltasseva, A. Searching for Better Plasmonic Materials. *Laser Photonics Rev.* **2010**, *4* (6), 795–808.
- (9) Tang, Z.; Tress, W.; Inganäs, O. Light Trapping in Thin Film Organic Solar Cells. *Materials Today*. 2014, pp 389–396.
- (10) Uddin, A.; Yang, X. Surface Plasmonic Effects on Organic Solar Cells. *J Nanosci Nanotechnol* **2014**, *14* (2), 1099–1119.
- (11) Ferry, V. E.; Munday, J. N.; Atwater, H. A. Design Considerations for Plasmonic Photovoltaics. *Adv. Mater.* **2010**, *22* (43), 4794–4808.
- (12) Atwater, H. A. The Promise of Plasmonics A Technology That Squeezes Electromagnetic Waves into Minuscule Structures May Yield a New Generation of Superfast Computer Chips and Ultrasensitive Molecular Detectors. *Sci. Am.* **2009**, 2007–2010.

-
- (13) Reilly, T. H.; Van De Lagemaat, J.; Tenent, R. C.; Morfa, A. J.; Rowlen, K. L. Surface-Plasmon Enhanced Transparent Electrodes in Organic Photovoltaics. *Appl. Phys. Lett.* **2008**.
- (14) Stec, H. M.; Hatton, R. A. Plasmon-Active Nano-Aperture Window Electrodes for Organic Photovoltaics. *Adv. Energy Mater.* **2013**, *3* (2), 193–199.
- (15) Park, T. H.; Mirin, N.; Lassiter, J. B.; Nehl, C. L.; Halas, N. J.; Nordlander, P. Optical Properties of a Nanosized Hole in a Thin Metallic Film. *ACS Nano* **2008**, *2* (1), 25–32.
- (16) Schwind, M.; Kasemo, B.; Zorić, I. Localized and Propagating Plasmons in Metal Films with Nanoholes. *Nano Lett.* **2013**, *13* (4), 1743–1750.
- (17) Reilly, T.; van de Lagemaat, J.; Tenent, R. C.; Morfa, A. J.; Rowlen, K. L. Surface-Plasmon Enhanced Transparent Electrodes in Organic Photovoltaics. *Appl. Phys. Lett.* **2008**, *92* (24), 243304.
- (18) Hutter, O. S.; Hatton, R. A. A Hybrid Copper:Tungsten Suboxide Window Electrode for Organic Photovoltaics. *Adv. Mater.* **2015**, *27* (2), 326–331.
- (19) Chan, G. H.; Zhao, J.; Hicks, E. M.; Schatz, G. C.; Van Duyne, R. P. Plasmonic Properties of Copper Nanoparticles Fabricated by Nanosphere Lithography. *Nano Lett.* **2007**, *7* (7), 1947–1952.
- (20) Gong, C.; Leite, M. S. Noble Metal Alloys for Plasmonics. *ACS Photonics* **2016**, *3* (4), 507–513.
- (21) Hutter, O. S.; Stec, H. M.; Hatton, R. A. An Indium-Free Low Work Function Window Electrode for Organic Photovoltaics Which Improves with in-Situ Oxidation. *Adv. Mater.* **2013**, *25* (2), 284–288.
- (22) Grouchko, M.; Kamyshny, A.; Magdassi, S. Formation of Air-Stable Copper–silver Core–shell Nanoparticles for Inkjet Printing. *J. Mater. Chem.* **2009**, *19* (19), 3057.
- (23) Bellchambers, P.; Lee, J.; Varagnolo, S.; Amari, H.; Walker, M.; Hatton, R. A. Elucidating the Exceptional Passivation Effect of 0.8 nm Evaporated Aluminium on Transparent Copper Films. *Front. Mater.* **2018**, *5*:71.
- (24) Lal, N. N.; Zhou, H.; Hawkeye, M.; Sinha, J. K.; Bartlett, P. N.; Amaratunga, G. A. J.; Baumberg, J. J. Using Spacer Layers to Control Metal and Semiconductor Absorption in Ultrathin Solar Cells with Plasmonic Substrates. *Phys. Rev. B - Condens. Matter Mater. Phys.* **2012**, *85* (24), 245318.
- (25) Leznoff, C. C.; Lever, A. B. P. *Phthalocyanines : Properties and Applications*; 1989.
- (26) Kadish, K. M.; Smith, K. M.; Guillard, R. *The Porphyrin Handbook*; Academic Press,
-

2000.

- (27) Kröger, M.; Hamwi, S.; Meyer, J.; Riedl, T.; Kowalsky, W.; Kahn, A. Role of the Deep-Lying Electronic States of MoO₃ in the Enhancement of Hole-Injection in Organic Thin Films. *Appl. Phys. Lett.* **2009**, *95* (12), 10–13.
- (28) White, R. T.; Thibau, E. S.; Lu, Z.-H. Interface Structure of MoO₃ on Organic Semiconductors. *Sci. Rep.* **2016**, *6* (February), 21109.
- (29) Greiner, M. T.; Chai, L.; Helander, M. G.; Tang, W. M.; Lu, Z. H. Metal/Metal-Oxide Interfaces: How Metal Contacts Affect the Work Function and Band Structure of MoO₃. *Adv. Funct. Mater.* **2013**, *23* (2), 215–226.
- (30) Nguyen, D.-T.; Vedraïne, S.; Cattin, L.; Torchio, P.; Morsli, M.; Flory, F.; Bernède, J. C. Effect of the Thickness of the MoO₃ Layers on Optical Properties of MoO₃/Ag/MoO₃ Multilayer Structures. *J. Appl. Phys.* **2012**, *112* (May 2016), 063505.

Chapter 7

Optically Thin Copper Films as Top Electrodes for Top-illuminated Organic Photovoltaics

7.1 Background

Top-illuminated OPVs are an important emerging class of OPVs because they are well suited for integrating into automobile and building related application spaces. As discussed in chapter 5, top-illuminated OPVs require a thick reflective substrate electrode to serve as the bottom contact. Ag is the material of choice for both the bottom electrode and transparent top electrode in most reports on top-illuminated OPVs to date,¹⁻³ because it is relatively stable towards oxidation in air and has the lowest optical losses for metals in the visible region.^{4,5} However, regardless of the performance of these devices, the use of Ag as both the reflective bottom contact and the transparent top contact is questionable, since Ag is a costly metal⁶ and so such extensive use in an OPV seriously erodes the cost advantage of OPVs. The replacement of Ag with Cu as the reflective substrate electrode has already been successfully demonstrated⁷ in Chapter 5; a substitution that will contribute significantly towards reducing the bill of materials. As Cu has electrical properties comparable to that of Ag and as the oxidation of Cu in air can be slowed to provide remarkable stability in ambient conditions,⁸ this chapter focuses on investigating the possibility of using a thin Cu film as the transparent window electrode in top-illuminated OPVs.

Apart from the drawbacks of ITO for conventional architecture OPVs already discussed in Chapter 1, there is an additional complication related to its use in top -illuminated OPVs because it has to be deposited on top of the device by sputtering. Sputter deposition of ITO directly onto organic semiconductors, damages the organic material leading to poor device performance. Conversely, thin metal films, can be deposited by vacuum evaporation without damaging the underlying organic layer.

In this chapter an optically thin film of Cu is used as a top transparent window electrode in semi-transparent and top-illuminated OPVs and the device performance is compared with identical devices with an equally thin Ag film as the top electrode. The results presented in this chapter, represent ongoing work at the time of submission of this thesis.

7.2 Experimental Methods

Experimental details specific to the work presented in this chapter are as follows;

7.2.1 Substrate cleaning

Glass substrates of the required dimension and ITO coated glass substrates were cleaned as described in section 2.1 and 2.2.

7.2.2 Monolayer deposition:

A monolayer was deposited prior to evaporation of Ag by exposing the substrates to vapours of MPTMS at 50 mbar for 4 hours immediately after UV/O₃ treatment.

7.2.3 Molybdenum Bronze synthesis (H_yMoO_{3-z})

H_yMoO_{3-z} was synthesised by dispersing molybdenum powder (0.1 g) in ethanol (10 ml) by ultra-sonic agitation for 10 minutes. This solution was heated to 40 °C followed by addition of H₂O₂ (30%, 0.35 ml) under vigorous stirring. The solution turned yellow after 10 hours then blue after 48 hours. After 72 hours, the solution was removed from the heat, filtered through a 0.2 µm PTFE filter and dried using a rotary evaporator to yield the solid product which was dissolved in ethanol by ultrasonic agitation to give a 20 mg ml⁻¹ solution. This was used as the stock solution and was centrifuged at 10,000 rpm for 10 minutes before use.

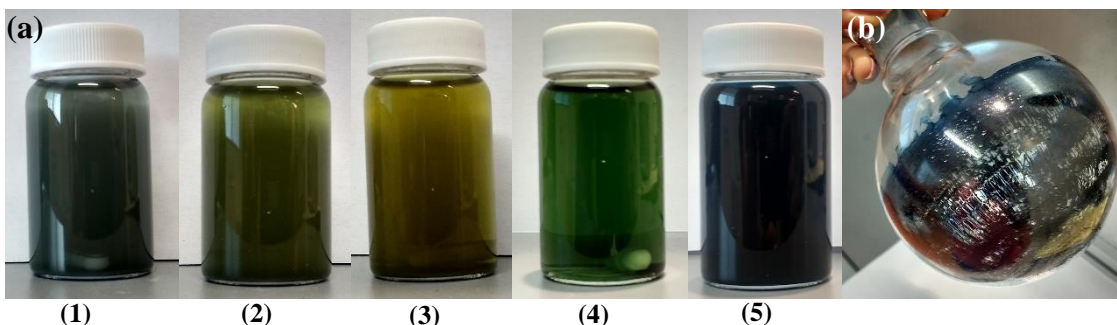


Figure 7.1: (a) The synthesis of H_yMoO_{3-x} showing the gradual change in the colour of the solution due to the change in oxidation state of Mo as the reaction progresses and (b) shows the isolated H_yMoO_{3-z} solid following rotary evaporation.

7.2.4 Fabrication of OPV Devices

Ag (85 nm at 1.0-1.2 Å s⁻¹) was deposited on cleaned glass substrates functionalised with a molecular monolayer. Polyethylenamine ethoxylated (PEIE) was spun from a 0.4% solution in 2-methoxyethanol at 5000 rpm for 60 seconds on to Ag or ITO to give a 10 nm film as the ETL. A PCE10 – PC₇₀BM solution was employed as the active layer. PCE10 and PC₇₀BM were mixed in 2:3 mass ratio to make a 35 mg ml⁻¹ solution in chlorobenzene (97%) and 1,8-diiodooctane (3%) and deposited by spin coating from a

static start at 4000 rpm for 120 seconds to form a photo-active layer having a thickness of 100 nm. These slides were left inside the evaporator overnight and a $\text{H}_y\text{MoO}_{3-z}$ solution having a concentration of 5 mg ml^{-1} was spun at 3000 rpm for 30 seconds followed by annealing in the glove box for 10 minutes at 80°C to form the HTL. Cu (11nm at $1.5\text{-}1.7 \text{ \AA s}^{-1}$) was deposited through a 0.06 cm^2 shadow mask as the top electrode.

7.2.5 Characterization of OPV devices

Current density-voltage (*JV*) testing was performed as described in section 2.17.

7.2.6 Fabrication of thin films of polydimethyl siloxane (PDMS)

Silicon wafers were cleaned in a similar manner to that described in 7.3.1 followed by UV/O₃ treatment for 15 mins. The wafers were then transferred to a desiccator and exposed to vapours of trichloro-perfluoro-octyl silane at 50 mbar for 2 hours immediately after UV/O₃ treatment. This surface functionalization facilitated easy peel off of the PDMS after curing. Sylgard 184 PDMS was mixed with the curing agent in 10:1 ratio and degassed gently until all air bubbles disappeared. This was then spun on surface modified Si wafers at 1000 rpm for 60 seconds followed by curing at 90°C for 1 hour for complete hardening. Once hardened, PDMS was spun on again and cured. This process was repeated 3 times to obtain a sufficiently thin PDMS layer ($\sim 200 \mu\text{m}$).

7.2.7 Optical transparency measurements

Far-field transmittance of different layers were measured over the wavelength range of 350 – 850 nm using a 150 mm Spectralon® Integrating Sphere coupled to a PerkinElmer® LAMBDA™ high performance UV/Vis spectrometer. Measurements were performed with reference to the substrate.

7.3 Results and Discussion

In the first instance semi-transparent OPV devices were fabricated on ITO with the architecture; ITO / PEIE (10 nm) / PCE10 – PC₇₀BM (100 nm) / $\text{H}_y\text{MoO}_{3-z}$ (10 nm) / Cu (11 nm) which enabled optimization of individual layers and preliminary understanding of how Cu would perform as a top electrode (Figure 7.2).

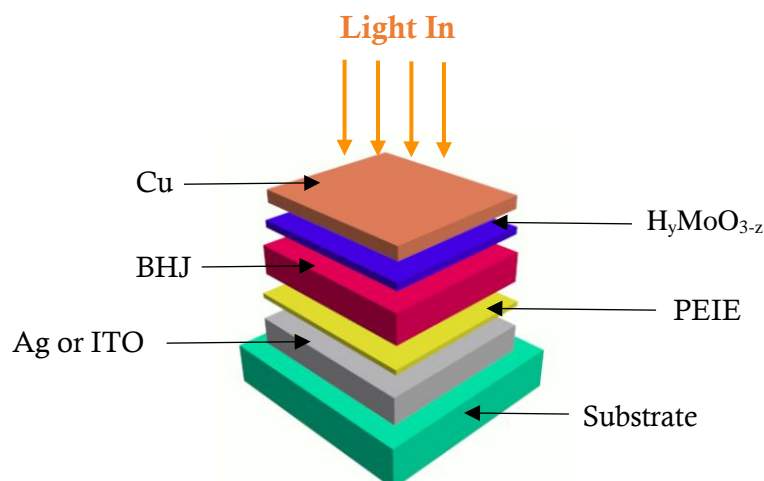


Figure 7.2: Schematic diagram of the device architecture used for this study

The J_{sc} of these devices is satisfactory considering that a significant portion of the light passes through unabsorbed. PEIE was used as the ETL^{9–11} and in order to ensure that a good balance between device J_{sc} and FF is achieved, the concentration of PEIE was varied from 0.2% (by weight) to 0.8% and it was found that as the amount of PEIE increased the J_{sc} increased gradually up to a PEIE weight of 0.6% but simultaneously the FF was reduced. Therefore, a PEIE concentration of 0.4% which gave a layer thickness of 10 nm was deemed suitable for this device architecture and resulted in a V_{oc} of 0.73 V and FF of 0.57 (Figure 7.3). H_yMoO_{3-z} synthesised according to the method outlined by Tyler *et al.*¹² was used as the HTL in place of vacuum evaporated MoO_x^{13,14} because this facilitates the fabrication of all layers except the top metal electrode by means of solution processing, making it more compatible towards scaling up.

As these devices are semi-transparent, they can be operated both as a top-illuminated device as well as an inverted device, such that the light enters through the ITO side. Thus, some of these devices were measured as inverted devices to demonstrate that the applicability of Cu as a top electrode is not limited to the top-illuminated device architecture. The inverted architecture was tested using higher PEIE concentrations (0.6%) as this system exhibited highest J_{sc} in top-illuminated devices. However as discussed previously for top-illuminated devices a PEIE concentration of 0.4% yielded the best performance and therefore 0.4% has been used in all OPV devices discussed in the proceeding sections of this chapter.

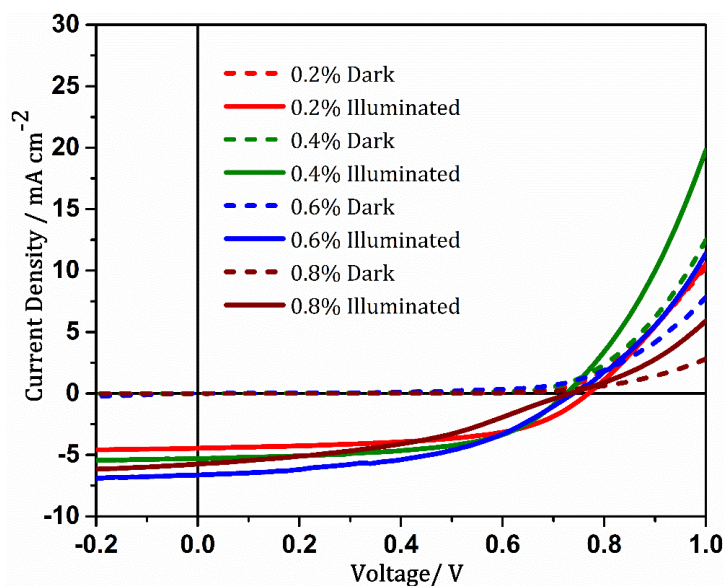


Figure 7.3: Representative current density - voltage (*JV*) characteristics measured under one sun simulated solar illumination (100 mW cm^{-2} ; AM 1.5G) for devices with the architecture: ITO / PEIE (10 nm) / PCE10 – PC₇₀BM (100 nm) / H_yMoO_{3-z} (10 nm) / Cu (11 nm).

| Device Architecture | Concentration of PEIE / % | $J_{sc} \pm 1SD$ / mA cm^{-2} | $V_{oc} \pm 1SD$ / V | $FF \pm 1SD$ | PCE $\pm 1SD$ / % |
|---------------------|---------------------------|--|----------------------|-----------------|-------------------|
| Top-illuminated | 0.2 | 4.33 ± 0.19 | 0.76 ± 0.01 | 0.55 ± 0.04 | 1.80 ± 0.10 |
| | 0.4 | 5.19 ± 0.20 | 0.73 ± 0.01 | 0.57 ± 0.04 | 2.16 ± 0.12 |
| | 0.6 | 6.04 ± 0.40 | 0.71 ± 0.02 | 0.46 ± 0.01 | 1.99 ± 0.19 |
| | 0.8 | 5.64 ± 0.17 | 0.73 ± 0.02 | 0.41 ± 0.02 | 1.69 ± 0.10 |
| Inverted | 0.6 | 10.70 ± 0.55 | 0.71 ± 0.01 | 0.49 ± 0.01 | 3.72 ± 0.21 |

Table 7.1: Summary of current density - voltage characteristics of devices with the architecture; ITO / PEIE (10 nm) / PCE10 – PC₇₀BM (100 nm) / H_yMoO_{3-z} (10 nm) / Cu (11 nm) tested under 1 sun simulated solar illumination (100 mW cm^{-2} ; AM 1.5G). The error bars represent ± 1 standard deviation ($\pm 1SD$) determined from the performance of 20 - 30 devices with identical architecture.

The stability of these semi-transparent devices was tested under constant illumination for 3 hours, both under ambient conditions exposed to atmospheric oxygen (Figure 7.4) and under N₂ (Figure 7.5) in the glove box. Device performance deteriorated rapidly when exposed to ambient air. This is attributed to the oxidation of the top electrode which is known to occur for unpassivated Cu films^{15–17} consistent with the large increase in device series resistance with time. Therefore, although the initial device PCE was ~2 %, in the time taken to transport the device in air to the stability testing rig, the PCE dropped to less than 1%. Consequently, the results given in Figure 7.3 show much lower initial *JV*

characteristics for time = 0 mins compared to the values reported in Table 7.1. Therefore, if these devices are to be used under an oxygen rich atmosphere some form of passivation or encapsulation will be essential to protect the top Cu electrode from oxidizing.

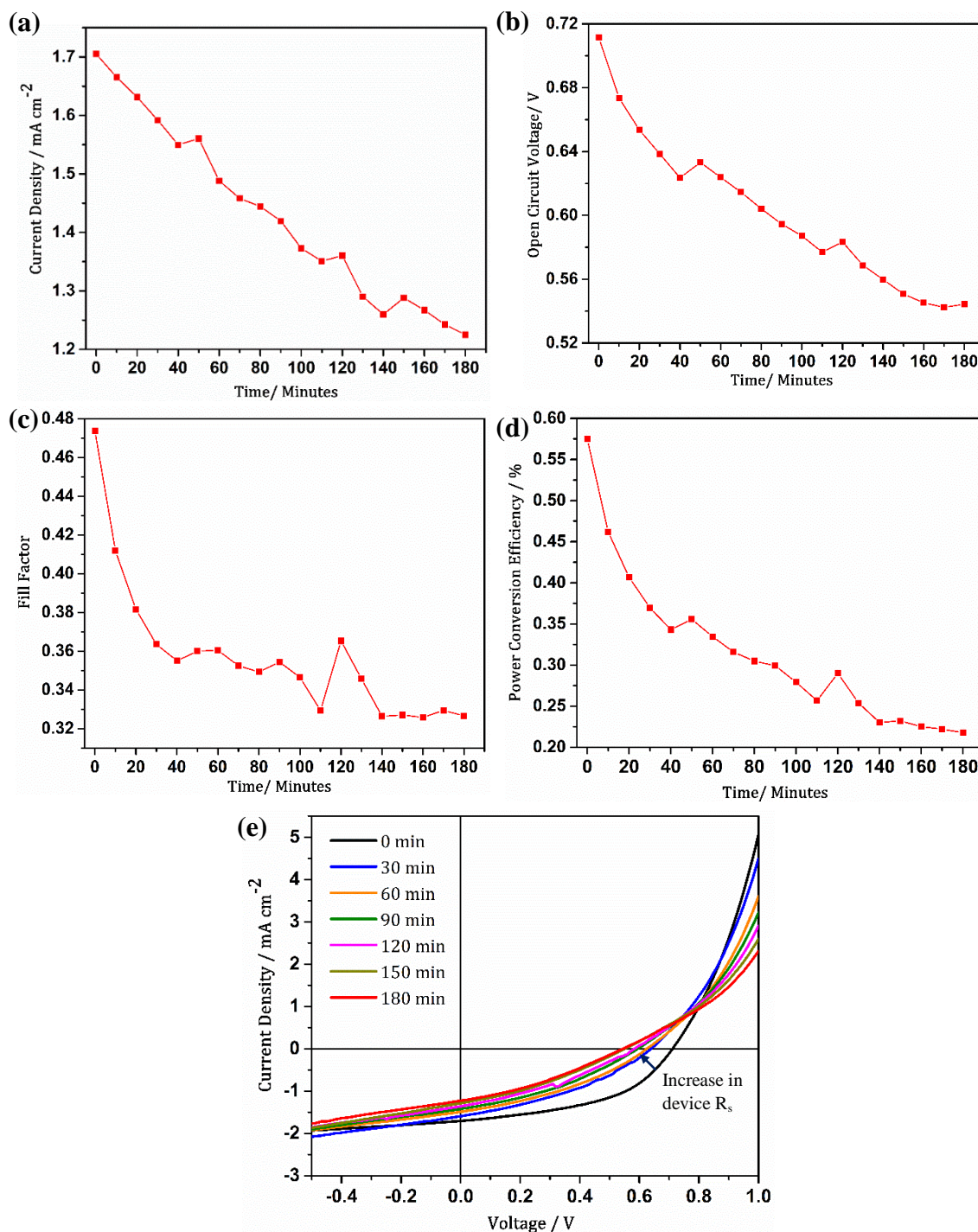


Figure 7.4: Variation in (a) J_{sc} ; (b) V_{oc} ; (c) FF; (d) PCE and (e) current density - voltage (JV) characteristics measured under constant illumination for 3 hours in air under one sun simulated solar illumination (100 mW cm^{-2} ; AM 1.5G) for devices with the architecture: ITO / PEIE (10 nm) / PCE10 – PC₇₀BM (100 nm) / H_xMoO_{3-z} (10 nm) / Cu (11 nm).

Conversely when the constant illumination experiment was performed under N_2 in the glove box, the devices exhibited good stability with negligible changes in J_{sc} and V_{oc} . Interestingly, the FF decreased slightly in the first few minutes and then gradually increased after $t = 40$ min and therefore the FF has remained at 0.54 both at $t = 0$ and $t = 180$ mins.

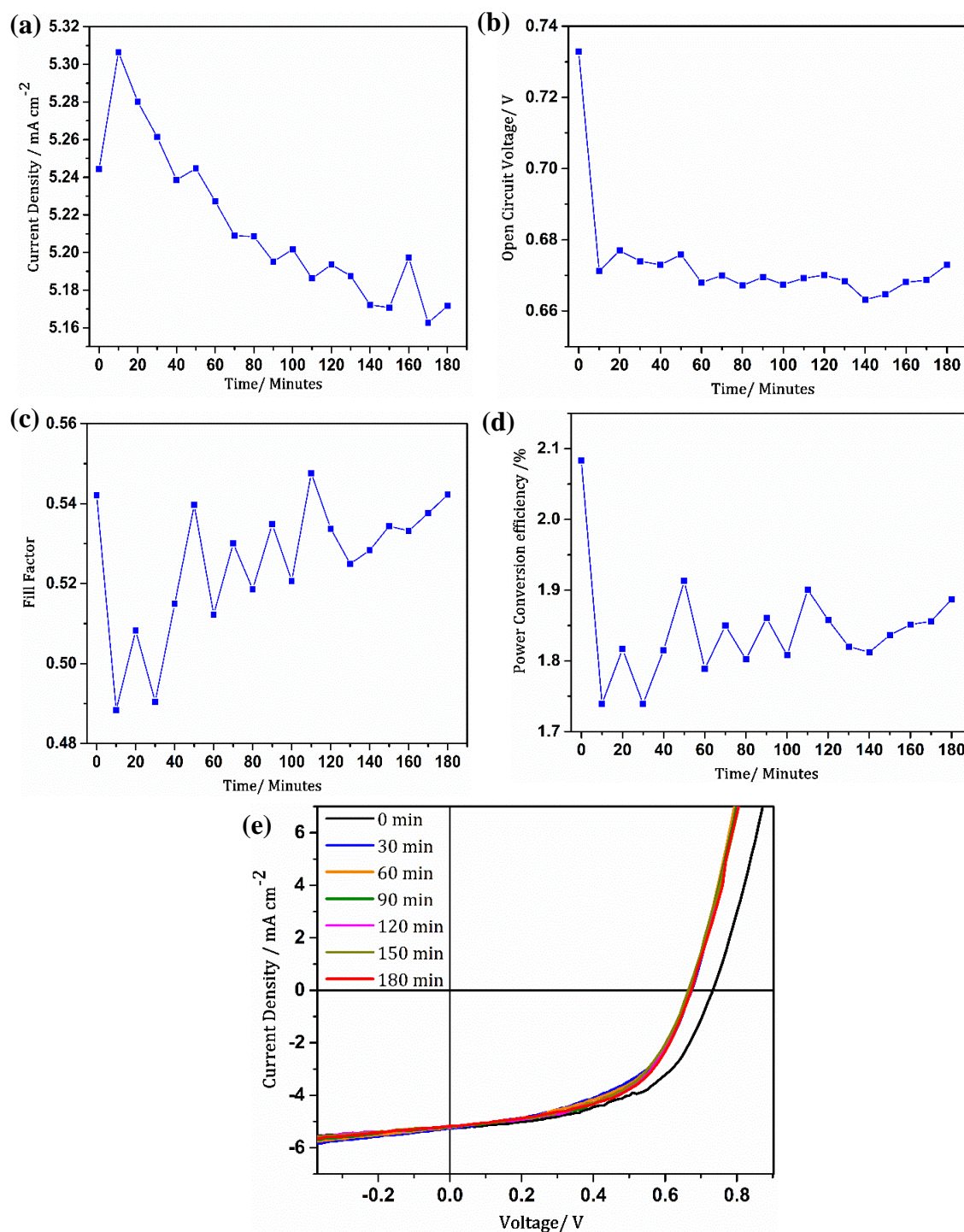


Figure 7.5: Variation in (a) J_{sc} ; (b) V_{oc} ; (c) FF ; (d) PCE and (e) current density - voltage (JV) characteristics measured under constant illumination for 3 hours in the glove box, under 1 sun simulated solar illumination (100 mW cm^{-2} ; AM 1.5G) for devices with the architecture: ITO / PEIE (10 nm) / PCE10 – PC₇₀BM (100 nm) / H₇MoO_{3-z} (10 nm) / Cu (11 nm).

In order to further increase the J_{sc} of these semi-transparent devices a thin layer of PDMS was laminated directly on top of the device. PDMS is an inert material with excellent viscoelastic properties¹⁸ and therefore can be laminated directly on the top surface of the device to achieve conformal physical contact without the need for any additional adhesive.² Additionally PDMS is hydrophobic and can therefore act as a barrier retarding ingress of air and moisture into the device. Furthermore, the low refractive index of PDMS (~1.4) enables gradual change in the refractive index when moving from air to PDMS / Cu / H_yMoO_{3-z} , facilitating an increment in the transmittance of the Cu / H_yMoO_{3-z} bilayer as evidenced from the data given in Figure 7.6.

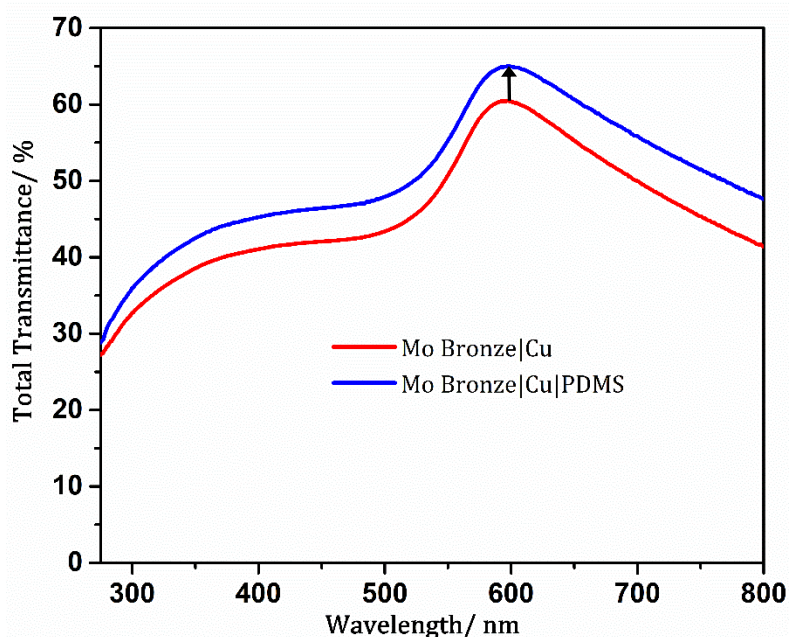


Figure 7.6: Total transmittance of H_yMoO_{3-z} (10 nm)/ Cu (11 nm) deposited on glass with and without a layer of PDMS.

Therefore, introduction of a thin layer of PDMS onto the device resulted in improved J_{sc} and FF with slight drop in the V_{oc} and an overall increment in the PCE of the device which was very prominent as the angle of the device holder was changed indicating that the enhancement is angle dependent (Table 7.2).

| Angle of Light Incidence/deg | Structure | $J_{sc} \pm 1SD$ / mA cm^{-2} | $V_{oc} \pm 1SD$ / V | $FF \pm 1SD$ | $PCE \pm 1SD$ / % |
|------------------------------|--------------|--|----------------------|-----------------|-------------------|
| 90° | Without PDMS | 5.19 ± 0.20 | 0.73 ± 0.01 | 0.57 ± 0.01 | 2.16 ± 0.12 |
| | With PDMS | 5.53 ± 0.28 | 0.72 ± 0.02 | 0.58 ± 0.01 | 2.22 ± 0.29 |
| 50° | Without PDMS | 1.42 ± 0.27 | 0.72 ± 0.02 | 0.58 ± 0.02 | 0.60 ± 0.30 |
| | With PDMS | 3.41 ± 0.17 | 0.74 ± 0.01 | 0.58 ± 0.01 | 1.44 ± 0.19 |

Table 7.2: Summary of current density - voltage characteristics of devices with the architecture; ITO / PEIE (10 nm) / PCE10 – PC₇₀BM (100 nm) / H_yMoO_{3-z} (10 nm) / Cu (11 nm) tested under 1 sun simulated solar illumination (100 mW cm⁻²; AM 1.5G) with and without a layer of PDMS laminated on top of the device. The error bars represent ± 1 standard deviation ($\pm 1SD$) determined from the performance of 10 - 20 devices with identical architecture.

This same device architecture used to fabricate semi-transparent devices was translated to top illuminated devices where the back contact was an 85 nm thick Ag film to provide adequate reflectance to redirect the unabsorbed light back into the device. The possibility of using an equally thick Cu film as the back contact in place of Ag has already been demonstrated in chapter 5, thus for simplicity a Ag bottom electrode was used for all devices reported in this chapter. In order to compare the performance of devices that use Cu as the top contact, identical devices were fabricated but with an 11 nm thick Ag electrode on top.

| Top Electrode | $J_{sc} \pm 1SD$ / mA cm^{-2} | $V_{oc} \pm 1SD$ / V | $FF \pm 1SD$ | $PCE \pm 1SD$ / % |
|---------------|--|----------------------|-----------------|-------------------|
| Ag | 12.24 ± 0.24 | 0.77 ± 0.01 | 0.57 ± 0.04 | 5.31 ± 0.23 |
| Cu | 10.55 ± 0.27 | 0.77 ± 0.01 | 0.60 ± 0.01 | 4.87 ± 0.20 |

Table 7.3: Summary of current density - voltage characteristics of devices with the architecture; Ag (85 nm) / PEIE (10 nm) / PCE10 – PC₇₀BM (100 nm) / H_yMoO_{3-z} (10 nm) / Ag or Cu (11 nm) tested under 1 sun simulated solar illumination (100 mW cm⁻²; AM 1.5G). The error bars represent ± 1 standard deviation ($\pm 1SD$) determined from the performance of 10 - 20 devices with identical architecture.

As evidenced by the device performance outlined in Table 7.3, it is clear that, Ag outperforms Cu as a top electrode primarily due to a higher J_{sc} . The higher J_{sc} arises from the higher transmittance of the Ag electrode compared to a Cu electrode of same thickness. However, it is noteworthy that the overall difference in performance is small; i.e. ~8%.

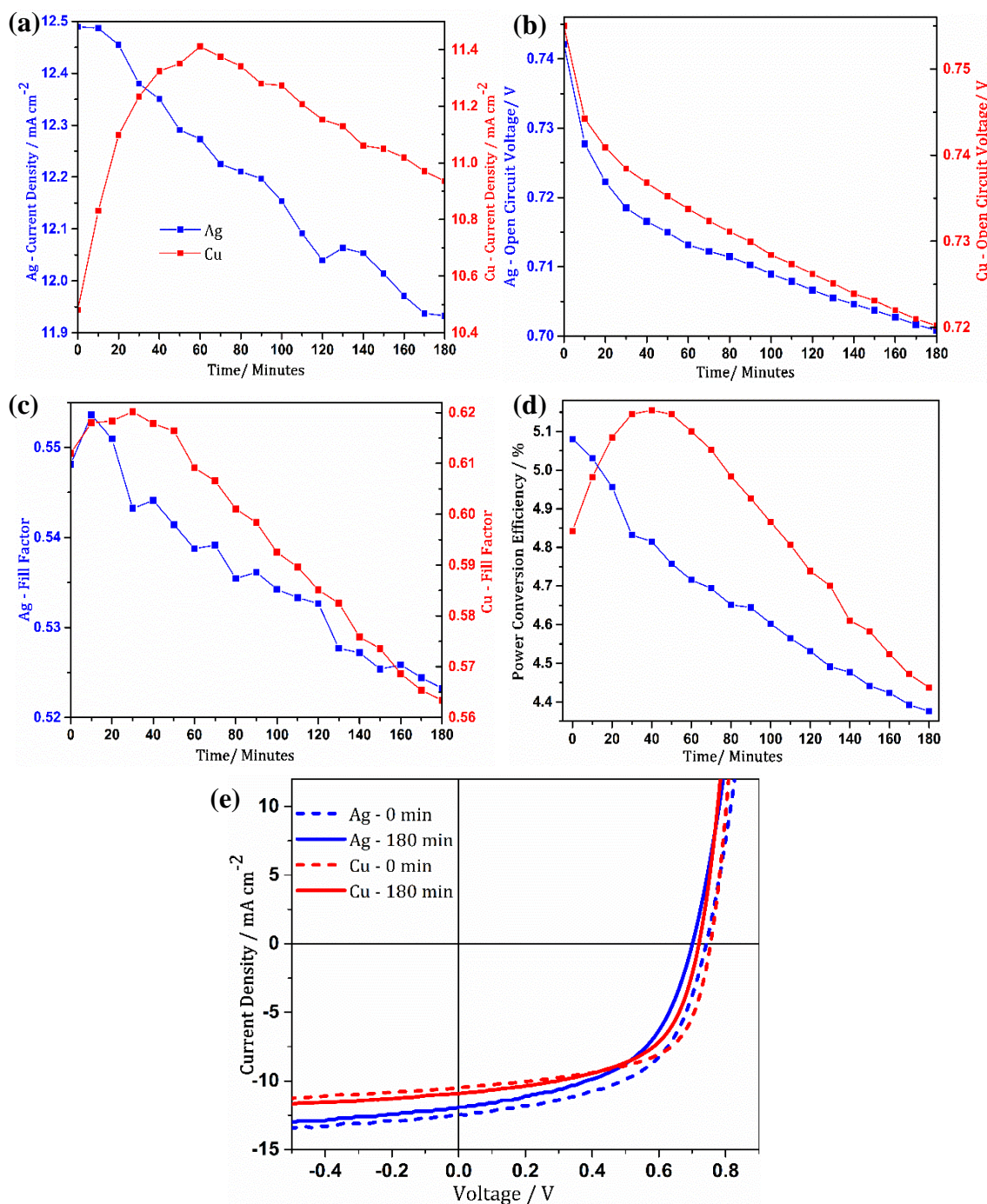


Figure 7.7: Variation in (a) J_{sc} ; (b) V_{oc} ; (c) FF; (d) PCE and (e) current density - voltage (JV) characteristics measured under constant illumination for 3 hours in the glove box, under 1 sun simulated solar illumination (100 mW cm^{-2} ; AM 1.5G) for devices with the architecture: Ag (85 nm) / PEIE (10 nm) / PCE10 – PC₇₀BM (100 nm) / H_yMoO_{3-z} (10 nm) / Ag or Cu (11 nm).

When these OPVs were subjected to constant illumination in a N₂ atmosphere in the glove box (Figure 7.7) the performance of both devices decreased but the rate of degradation of the OPV devices with Ag transparent electrodes were greatest with the PCE dropping from 5.08 to 4.40%. Ag electrodes are known to be unstable under illumination due to

the higher mobility of Ag resulting in cluster formation. This affects the Ag/ETL interface causing a drop-in performance of the device. Interestingly, for devices with a Cu top electrode the PCE decreased from 4.85 to 4.45 %, therefore at the end of the 3 hours these devices have outperformed the former marginally. The main reason behind this observation is the increase in J_{sc} in the first hour from 10.5 to 11.4 mA cm⁻² which has then gradually dropped at a low rate to 10.9 mA cm⁻². Thus, effectively there is a small improvement in J_{sc} contributing to an increment in the PCE but overall the PCE decreases as all other parameters degrade over the time period of 3 hours (Figure 7.7).

7.4 Conclusion

The use of an optically thin Cu electrode as the top contact in top-illuminated OPVs has been demonstrated in this chapter. It is shown that an enhancement in J_{sc} can be obtained by laminating a thin layer of PDMS onto the surface of the electrode. This may be further beneficial in the context of a Cu electrode which is susceptible to oxidation in air, as PDMS can behave as a barrier retarding the ingress of oxygen and moisture to a certain extent. The performance of top-illuminated devices with Ag and Cu as top electrodes have been compared and it is demonstrated that although devices with a Ag electrode exhibit a higher initial PCE, the devices with a Cu electrode are much more stable towards constant illumination.

7.5 References

- (1) Lin, H. W.; Chiu, S. W.; Lin, L. Y.; Hung, Z. Y.; Chen, Y. H.; Lin, F.; Wong, K. T. Device Engineering for Highly Efficient Top-Illuminated Organic Solar Cells with Microcavity Structures. *Adv. Mater.* **2012**, *24* (17), 2269–2272.
- (2) Ham, J.; Dong, W. J.; Park, J. Y.; Yoo, C. J.; Lee, I.; Lee, J. L. A Challenge beyond Bottom Cells: Top-Illuminated Flexible Organic Solar Cells with Nanostructured Dielectric/Metal/Polymer (DMP) Films. *Adv. Mater.* **2015**, *27* (27), 4027–4033.
- (3) Huang, J.; Li, C. Z.; Chueh, C. C.; Liu, S. Q.; Yu, J. S.; Jen, A. K. Y. 10.4% Power Conversion Efficiency of ITO-Free Organic Photovoltaics Through Enhanced Light Trapping Configuration. *Adv. Energy Mater.* **2015**, *5* (15), 4–9.
- (4) West, P. R.; Ishii, S.; Naik, G. V.; Emani, N. K.; Shalaev, V. M.; Boltasseva, A. Searching for Better Plasmonic Materials. *Laser Photonics Rev.* **2010**, *4* (6), 795–808.
- (5) Naik, G. V.; Shalaev, V. M.; Boltasseva, A. Alternative Plasmonic Materials: Beyond Gold and Silver. *Adv. Mater.* **2013**, *25* (24), 3264–3294.
- (6) Søndergaard, R. R.; Espinosa, N.; Jørgensen, M.; Krebs, F. C. Efficient Decommissioning and Recycling of Polymer Solar Cells: Justification for Use of Silver. *Energy Environ. Sci.* **2014**, *7* (3), 1006–1012.
- (7) Pereira, H. J.; Hatton, R. A. Copper Substrate Electrode for Efficient Top-Illuminated Organic Photovoltaics. *ACS Appl. Mater. Interfaces* **2018**, acsami.8b18453.
- (8) Bellchambers, P.; Lee, J.; Varagnolo, S.; Amari, H.; Walker, M.; Hatton, R. A. Elucidating the Exceptional Passivation Effect of 0.8 Nm Evaporated Aluminium on Transparent Copper Films. *Front. Mater.* **2018**, *5*:71.
- (9) Yang, X.; Wang, R.; Fan, C.; Li, G.; Xiong, Z.; Jabbour, G. E. Ethoxylated Polyethylenimine as an Efficient Electron Injection Layer for Conventional and Inverted Polymer Light Emitting Diodes. *Org. Electron. physics, Mater. Appl.* **2014**, *15* (10), 2387–2394.
- (10) Zhang, Y.; Chen, L.; Hu, X.; Zhang, L.; Chen, Y. Low Work-Function Poly(3,4-Ethylenedioxythiophene): Poly(Styrene Sulfonate) as Electron-Transport

- Layer for High-Efficient and Stable Polymer Solar Cells. *Sci. Rep.* **2015**, 5 (October 2014), 12839.
- (11) Li, P.; Wang, G.; Cai, L.; Ding, B.; Zhou, D.; Hu, Y.; Zhang, Y.; Xiang, J.; Wan, K.; Chen, L.; et al. High-Efficiency Inverted Polymer Solar Cells Controlled by the Thickness of Polyethylenimine Ethoxylated (PEIE) Interfacial Layers. *Phys. Chem. Chem. Phys.* **2014**, 16 (43), 23792–23799.
- (12) Tyler, M. S.; Walker, M.; Hatton, R. A. High-Performance Silver Window Electrodes for Top-Illuminated Organic Photovoltaics Using an Organo-Molybdenum Oxide Bronze Interlayer. *ACS Appl. Mater. Interfaces* **2016**, 8 (19), 12316–12323.
- (13) Xie, F.; Choy, W. C. H.; Wang, C.; Li, X.; Zhang, S.; Hou, J. Low-Temperature Solution-Processed Hydrogen Molybdenum and Vanadium Bronzes for an Efficient Hole-Transport Layer in Organic Electronics. *Adv. Mater.* **2013**, 25 (14), 2051–2055.
- (14) Soultati, A.; Douvas, A. M.; Georgiadou, D. G.; Palilis, L. C.; Bein, T.; Feckl, J. M.; Gardelis, S.; Fakis, M.; Kennou, S.; Falaras, P.; et al. Solution-Processed Hydrogen Molybdenum Bronzes as Highly Conductive Anode Interlayers in Efficient Organic Photovoltaics. *Adv. Energy Mater.* **2014**, 4 (3), 1–10.
- (15) Platzman, I.; Brener, R.; Haick, H.; Tannenbaum, R. Oxidation of Polycrystalline Copper Thin Films at Ambient Conditions. *J. Phys. Chem. C* **2008**, 112 (4), 1101–1108.
- (16) Gattinoni, C.; Michaelides, A. Atomistic Details of Oxide Surfaces and Surface Oxidation: The Example of Copper and Its Oxides. *Surf. Sci. Rep.* **2015**, 70 (3), 424–447.
- (17) Soon, A.; Todorova, M.; Delley, B.; Stampfl, C. Thermodynamic Stability and Structure of Copper Oxide Surfaces: A First-Principles Investigation. *Phys. Rev. B* **2007**, 75 (12), 125420.
- (18) Deguchi, S.; Hotta, J.; Yokoyama, S.; Matsui, T. S. Viscoelastic and Optical Properties of Four Different PDMS Polymers. *J. Micromechanics Microengineering* **2015**, 25 (9).

Chapter 8

Future Work

8.1 Fabrication of a plasmon-active transparent Cu electrode using polymer blend lithography

In Chapter 3, a method of fabricating a thin Cu film with a random distribution of circular holes was described.¹ In that work large holes were fabricated to improve the overall transparency of the Cu film. However, as corroborated with AFM images given in chapter 3, the size of the holes can be controlled by changing the concentration of the polymer blend solution. Therefore, this technique could be used to make apertures having a diameter smaller than the wavelength of light in order to generate plasmonic excitations. Compared to the method outlined in chapter 6, this method of fabricating small holes in Cu films has the advantage that no annealing is involved in the process.

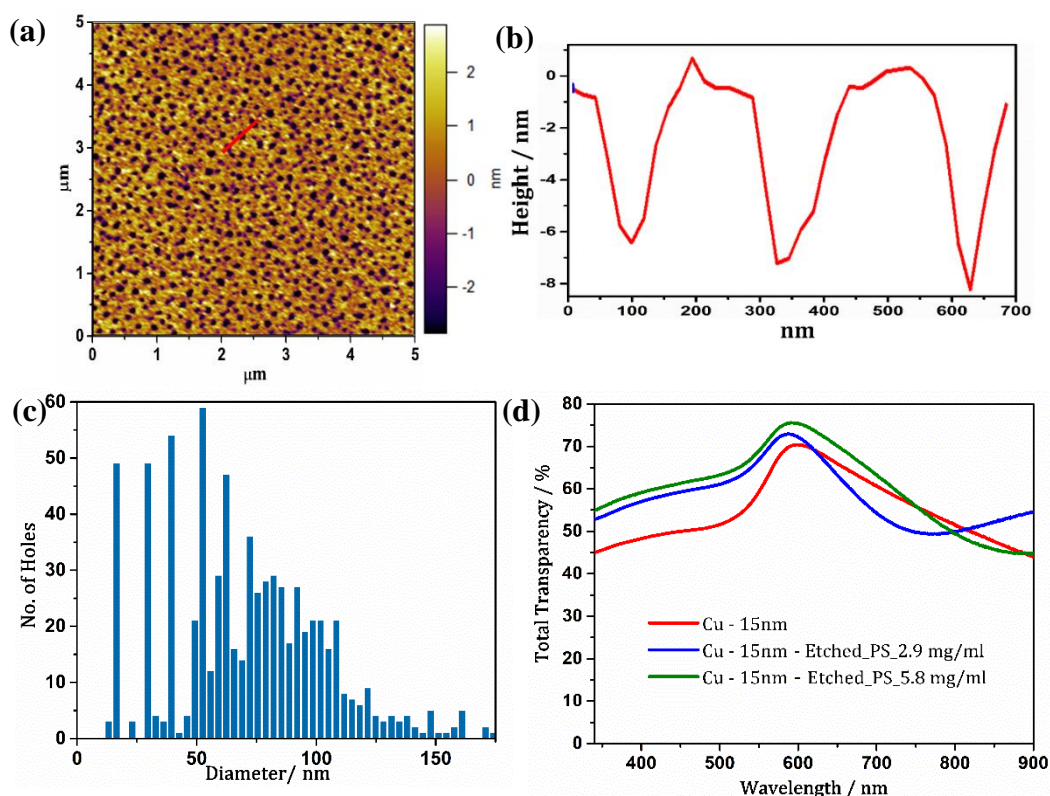


Figure 8.1: (a) A representative AFM image showing the morphology of a 15 nm thick Cu electrode with a random distribution of apertures fabricated using a polymer blend solution having a concentration of 2.9 mg ml^{-1} ; (b) shows a cross section of the AFM along the line shown in (a); (c) size distribution of (a); and (d) total transmittance spectra of Cu films with and without apertures.

Preliminary studies were conducted using a 15 nm thick Cu film deposited on glass, to identify the most suitable concentration of the polymer blend to fabricate small holes (Figure 8.1). Transparency measurements were performed to monitor the evolution of SPRs and when the etching was done using a blend solution having a concentration of 5.8 mg ml^{-1} a depression in the transparency spectrum was observed at $\lambda \geq 700 \text{ nm}$. This dip was further enhanced when the concentration was reduced to 2.9 mg ml^{-1} as shown in Figure 8.1(d). AFM images show a large density of very small holes with diameters $\leq 200 \text{ nm}$ which are suitable for a plasmon-active electrode. However as evident from the AFM cross section given in Figure 8.1(b), the holes do not appear to extend all the way down to the glass surface and are only 6 – 8 nm deep.

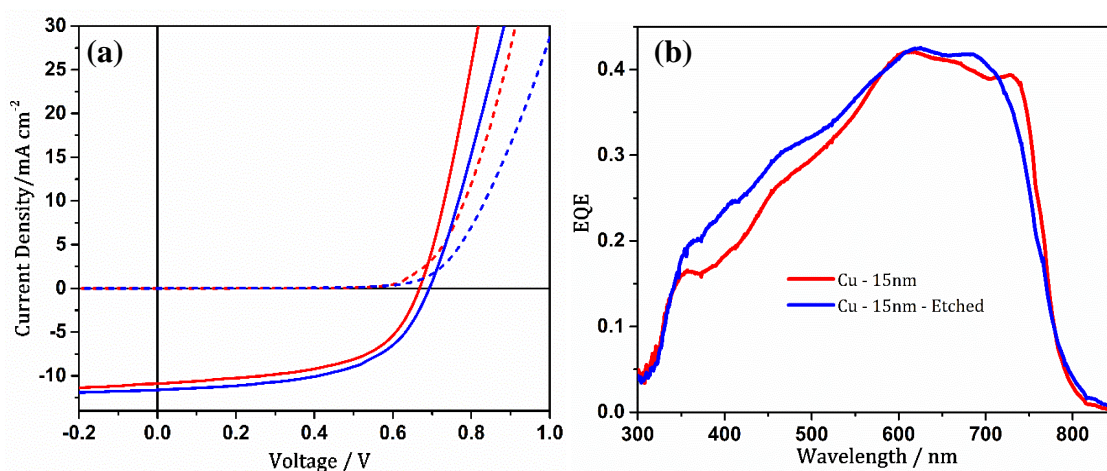


Figure 8.2: (a) Representative current density-voltage and (b) EQE data recorded under one sun simulated solar illumination (100 mW cm^{-2} ; AM 1.5G) for devices with the architecture: Cu (15 nm) with (blue) and without (red) apertures/ MoO_x (5 nm) / PCE10 – PC₇₀BM (100 nm) / BCP (5 nm) / Al (80 nm).

In order to test the electrode, devices with a conventional type architecture were fabricated, having an identical structure to those described in chapter 6; Cu (15 nm)/ MoO_x (5 nm)/ PCE10 - PC₇₀BM (100 nm) / BCP (5 nm) / Al (80 nm). Although the transparency spectrum showed a pronounced plasmonic effect for the Cu electrode with holes, device performance was similar to that of the reference with only marginal changes in J_{sc} (Figure 8.2(a)). However, the shape of the EQE is slightly different with improved photon to charge conversion at $\lambda \sim 350 - 570 \text{ nm}$ and $\lambda \sim 610 - 720 \text{ nm}$. The former can be attributed to the improved transparency in the short wavelength range owing to the removal of metal which contributes to a reduced absorption. However, in the region of $\lambda \sim 610 - 720 \text{ nm}$, the transparency of the Cu electrode with holes is much less compared to the planar electrode but still the EQE shows slightly higher efficiency in photon to charge

conversion. This therefore must be arising from the optical field enhancement as a result of light coupling due to the presence of apertures. This plasmon excitation decays rapidly as evidenced by a lower absorption edge of $\lambda \sim 700$ nm compared to ~ 750 nm for the devices that use a planar Cu electrode. Therefore, although a plasmonic effect is present it does not seem to contribute to any significant improvement in the overall device performance. Thus optimisation of the Cu/dielectric medium interface is essential in order to exploit the full potential of this electrode; i.e. to make use of the plasmon excitations to generate more excitons before it decays. Hence as plasmon excitations are distant dependent, the thickness of the MoO_x layer needs to be optimised for this particular electrode. Additionally the use of alternative material such as a thin layer of Al (0.8 nm) in place of MoO_x can be explored, as the CTL adjoining the metal must be sufficiently thin to harness the benefits of the light catching effect before the plasmon excitation relaxes whilst supporting charge extraction. Furthermore, the influence of hole depth on plasmon excitations need to be fully explored to understand the optimum depth of the hole for a given metal thickness that will be most beneficial for this type of electrode because although the holes do not extend the entire 15 nm there is still a significant plasmonic effect as evidenced by the transmittance spectrum given in Figure 8.1(d).

8.2 Fabrication of a plasmon-active reflective Cu electrode using polymer blend lithography

The results given in Chapter 6, suggest that it will be more beneficial to have the plasmon-active electrode at the back of the OPV device as a reflective electrode in a top-illuminated architecture rather than a transparent electrode.² This will facilitate absorption of shorter wavelength photons before reaching the Cu electrode because losses associated with Cu are significant at wavelengths ≤ 600 nm.²⁻⁴ This was investigated by repeating the process described in section 8.1 but with a thick Cu film of 45 nm and a higher concentration of the polymer blend (11.2 mg ml⁻¹) in order to make slightly large holes with low density. As the metal thickness is now high, during the complete etching of 45 nm, slight widening of the aperture may take place however, this can be mitigated by increasing the etchant concentration so that etching is completed fast.

For this electrode, the overall transparency is higher in the entire wavelength range of 300 – 900 nm, compared to an unpatterned electrode of equivalent thickness. Similar to the transparent plasmon-active electrode fabricated using polymer blend lithography, the improvement in transmittance at shorter wavelengths is due to the reduced absorption

caused by removal of metal to form apertures. In the longer wavelengths ranging from 600 – 900 nm the overall transmittance is still higher than the reference, but the extent of improvement is relatively lower. For instance, if the two curves were superimposed on one another, the overall transmittance increase at $\lambda \leq 600$ nm is much greater than at $\lambda \geq 600$ nm. Therefore, in this region there may be a complex interplay between plasmon excitations and reduction in reflectance caused by the presence of apertures as demonstrated in chapter 3.

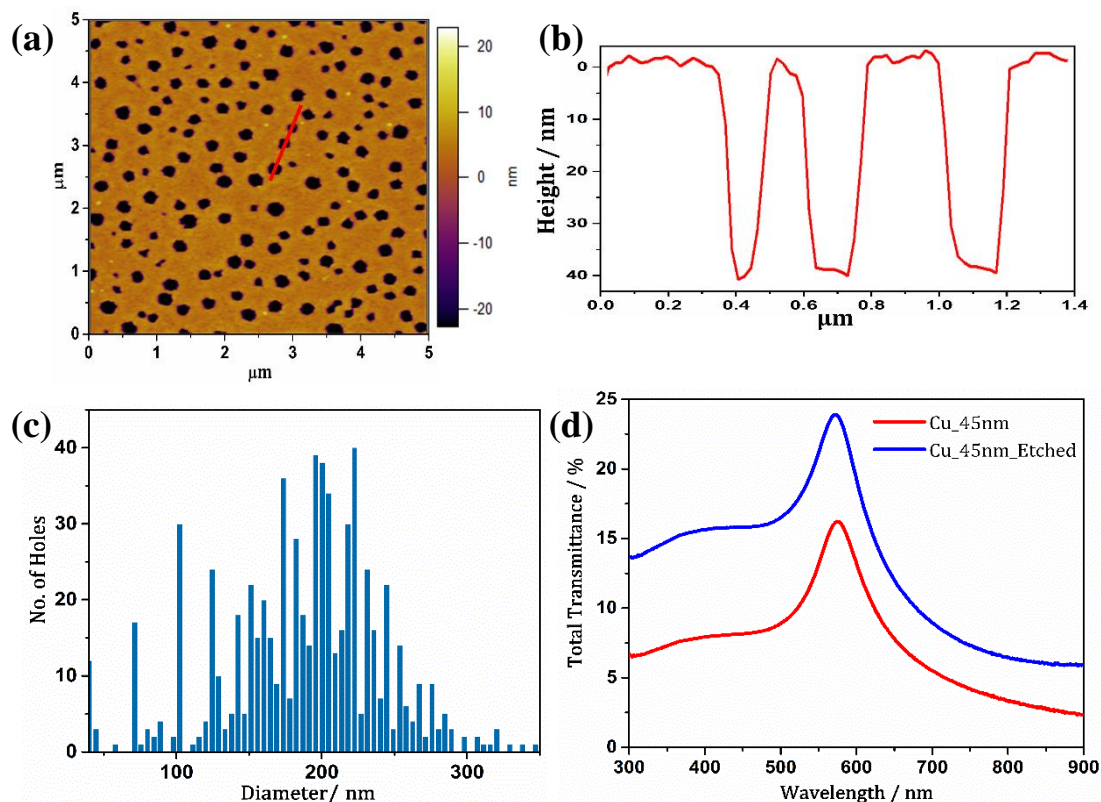


Figure 8.3: (a) A representative AFM image showing the morphology of a 45 nm thick Cu electrode with a random distribution of apertures fabricated using a polymer blend solution having a concentration of 11.2 mg ml^{-1} ; (b) shows a cross section of the AFM image along the line shown in (a); (c) size distribution of (a); and (d) total transmittance spectra of Cu films (45 nm) with and without apertures.

To investigate the applicability of this electrode, top-illuminated devices having the architecture, Cu (45nm)/ Al (0.8 nm)/ PCE10 - PC₇₀BM (100 nm) / MoO_x (10 nm) /Ag (11 nm) were fabricated. The JV characteristics given in Figure 8.4 depict that the J_{sc} in devices that use an electrode with apertures is comparable with the J_{sc} of devices that use an unpatterned back electrode. Conversely, the EQE shows a slight improvement in photon to charge conversion in the wavelength range of 400 to 600 nm in accordance with the transparency spectrum but at $\lambda \geq 600$ nm there is a drop in the EQE even though

the transparency is high compared to a planar Cu electrode in this wavelength range. However, as shown in Figure 8.4(b), a change in the shape of the EQE is indicative of a plasmonic effect and the drop in the intensity can be attributed to the fact that although there is light coupling and associated optical field enhancement in the vicinity of the holes, the plasmonic excitation may be undergoing rapid decay prior to the transfer of this energy to generate excitons.

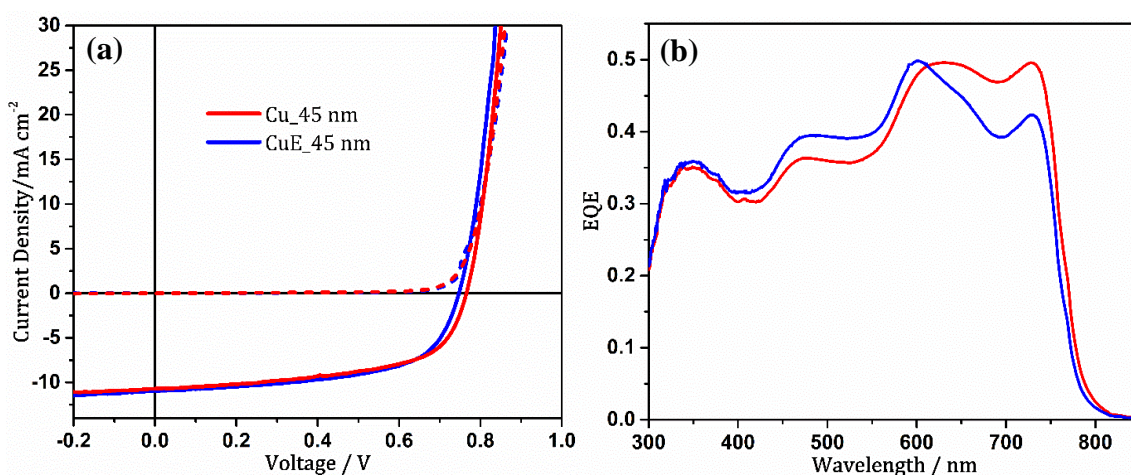


Figure 8.4: (a) Representative current density-voltage and (b) EQE data recorded under one sun simulated solar illumination (100 mW cm^{-2} ; AM 1.5G) for top-illuminated devices with the architecture: Cu (45 nm) with (blue) and without (red) apertures / Al (0.8 nm) / PCE10 – PC₇₀BM (100 nm) / MoO_x (10 nm) / Ag (85 nm).

Future work can focus on reflectance measurements of this electrode to investigate how the reflectance is altered upon introduction of holes to a thick Cu film and deduce the extent of plasmon-activity and reasons underlying the shape of the transmission spectrum given in Figure 8.2, especially at $\lambda \geq 600 \text{ nm}$. Following this, optimization of the hole size and density may be required for a thick electrode in order to obtain better light coupling.

Furthermore, as shown in Chapter 5, a thicker Cu electrode ($\sim 85 \text{ nm}$) which provides improved reflectance which is essential for good performance of a top-illuminated device and a thicker BHJ which is more suitable to use in conjunction with a Cu electrode can be used to obtain improved device performance since the reflectance of Cu drops at $\lambda \leq 600 \text{ nm}$.⁵

8.3 References

- (1) Pereira, H. J.; Reed, J.; Lee, J.; Varagnolo, S.; Dabera, G. D. R.; Hatton, R. A. Fabrication of Copper Window Electrodes with $\approx 10^8$ Apertures cm^{-2} for Organic Photovoltaics. *Adv. Funct. Mater.* **2018**, 28 (36), 1802893.
- (2) Pereira, H. J.; Hutter, O. S.; Dabera, G. D. M. R.; Rochford, L. A.; Hatton, R. A. Copper Light-Catching Electrodes for Organic Photovoltaics. *Sustain. Energy Fuels* **2017**, 1 (4), 859–865.
- (3) West, P. R.; Ishii, S.; Naik, G. V.; Emani, N. K.; Shalaev, V. M.; Boltasseva, A. Searching for Better Plasmonic Materials. *Laser Photonics Rev.* **2010**, 4 (6), 795–808.
- (4) Naik, G. V.; Shalaev, V. M.; Boltasseva, A. Alternative Plasmonic Materials: Beyond Gold and Silver. *Adv. Mater.* **2013**, 25 (24), 3264–3294.
- (5) Pereira, H. J.; Hatton, R. A. Copper Substrate Electrode for Efficient Top-Illuminated Organic Photovoltaics. *ACS Appl. Mater. Interfaces* **2018**, acsami.8b18453.

